Penn Center *for*
Musculoskeletal Disorders
UNIVERSITY *of* PENNSYLVANIA

18th Annual Scientific Symposium/Retreat

Wednesday, November 16, 2022
Smilow Rubenstein Auditorium/Commons
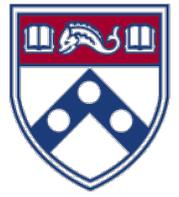8:15am-6:00pm
www.med.upenn.edu/pcmd/

Table of Contents

Penn Center for Musculoskeletal Disorders
Scientific Symposium Agenda

November 16, 2022
Smilow Rubenstein Auditorium ♦ University of Pennsylvania

08:15 – 09:20am | **Registration and Poster Set-up**

09:20 – 09:30am | **Welcome and Overview**
Louis J. Soslowsky, Ph.D.

09:30 – 10:30am | **Session I: Pilot Grantee Session** (Moderator: Maurizio Pacifici, Ph.D.)

- ♦ *Josh Baxter, PhD, "Towards Precision Rehabilitation for Achilles Tendon Ruptures."*
- ♦ *Riccardo Gottardi, PhD, "In Vivo Validation of a Continuous Gradient Porous Scaffold for Osteochondral Repair in a Rabbit Model."*
- ♦ *Kyu Sang Joeng, PhD, "Investigating the Function of mTORC1 Signaling in Tendon Using Mouse Genetic Models and Scaffold-Free 3D Tendon Constructs"*

10:30 – 11:15am | **Break and Poster Session (Even Numbered)**

11:15 – 12:15pm | **Session II: Affiliate Member Session** (Moderator: Mike Hast, Ph.D.)

- ♦ *Hannah Dailey, Ph.D., Lehigh University, "Virtual Mechanical Testing of Bone Fracture Healing"*
- ♦ *Ugur Ayturk, Ph.D., Hospital for Special Surgery, "A New, Injury-Activated Osteoprogenitor Population in the Musculoskeletal System."*
- ♦ *Kara L. Spiller, Ph.D., Drexel University, "Immunomodulatory Biomaterials for Regenerative Medicine."*

12:15 – 01:30pm | **Poster viewing and lunch (provided) in Smilow Commons**

01:30 – 02:30pm | **Session III: New Member Session** (Moderator: Lachlan Smith, Ph.D.)

- ♦ *Michael Mitchell, Ph.D., "Lipid Nanoparticles for Overcoming Biological Barriers to mRNA Delivery"*
- ♦ *Ernestina Schipani, M.D., Ph.D., "How Hypoxia and Mitochondrial Respiration Shape Up the Skeleton"*
- ♦ *Ottman Tertuliano, Ph.D., "Quantifying Length-Scale Dependent Toughening in Human Bone Fracture"*

02:30 – 03:15pm | **Break and Poster Session (Odd Numbered)**

03:15 – 04:15pm | **Keynote Speaker** (Moderator: Louis Soslowsky, Ph.D.)

"Navigating a Path to Understanding Drug Delivery in the Treatment of Arthritis"
Lori A. Setton, Ph.D., Lucy and Stanley Lopata Distinguished Professor and Chair of Biomedical Engineering
Professor of Mechanical Engineering & Materials Science and Orthopedic Surgery
Washington University in St Louis

04:15 – 04:30pm | **Final Comments Preceding Poster Session and Reception**

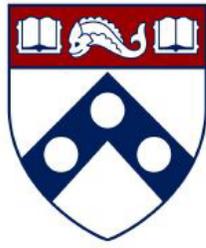04:30 – 06:00pm | **Poster Session, Presentation of Poster Awards and Reception in Smilow Commons**
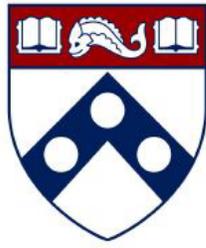
Center

Components

Center Overview

OVERVIEW OF THE PENN CENTER FOR MUSCULOSKELETAL DISORDERS

Director: Louis J. Soslowsky, PhD (soslowsk@upenn.edu)
Associate Director: Maurizio Pacifici, PhD (PacificiM@email.chop.edu)

Musculoskeletal-related conditions in the United States account for 132 million visits to physicians' offices, 29 million visits to emergency rooms, 15 million hospital outpatient visits, and cost over $850 billion each year. Further, musculoskeletal injuries in the United States cause workers to miss more than 440 million days of work annually. In fact, more than one in four Americans has a musculoskeletal impairment. With the widespread increase in athletic and recreational activities, and the increase of the elderly population at large, these numbers are expected to rise substantially. Musculoskeletal injuries represent a critical health concern which must be better understood and better treated. To do so, a dedicated and focused strategic effort is required that optimizes research translation from the bench to the bedside in an efficient and effective manner.

The Penn Center for Musculoskeletal Disorders (PCMD) will continue to enhance the research productivity of, and provide critical resources and programs to, investigators to address multidisciplinary research strategies for musculoskeletal problems. The overall goal of this Center is to promote cooperative interactions among investigators, accelerate and enrich the effectiveness and efficiency of ongoing research, foster new collaborations and new research, and ultimately, translate our research efforts into better and new therapies for musculoskeletal disorders. The central theme of the Center will continue to be "Musculoskeletal Tissue Injury and Repair". This theme is broad (as it includes all musculoskeletal tissue types, such as bone, cartilage, disc, ligament, meniscus, muscle, and tendon), focused (as takes advantage of commonalities in approaches across tissue types), and clinically significant (as it fosters development of assays, procedures and knowledge in preclinical animal and human models of translational relevance). It is important to note that our PCMD is not a "bone center" nor is it a "muscle center". Rather, it is truly a "musculoskeletal center" and has emerged as the recognized home for musculoskeletal research across the Penn campus and as a technical and intellectual resource for the broader Philadelphia musculoskeletal research community.

One focus of our Center is to translate research themes, approaches, and paradigms that are consistent across different tissues. Musculoskeletal tissues have much in common and their similarities are often overlooked when focus is restricted to a single tissue type. For example, the role of inflammatory cytokines is well studied in several tissue injury and repair scenarios; yet specific findings in one tissue-type are not always known and applied in other tissues. Similarly, the availability of technologies for imaging blood vessel formation in vivo to monitor healing in a given tissue is not always known and available to researchers focusing on other tissues. Given that approaches routinely used to evaluate mechanisms in one tissue could aid researchers in other areas, our Center will work to foster this critical cross-talk.

To provide a further focus for our Center, we will continue to develop programs with an emphasis on small animal models utilizing unique and sophisticated methods that can cross length scales to pre-clinical large animal models and human testing. Although large animal models for many human diseases exist and are essential for translational studies, small animals (e.g., mouse and rat) have become more commonly used for fundamental discovery of disease mechanism and initial therapeutic development due to availability of transgenic and knockout approaches and molecular tools, low cost, ease of handling and housing, and other practical issues. However, performing certain assays and experiments in mice and rats can be challenging and these difficulties often cannot be overcome in single investigator laboratories. The PCMD will provide unique expertise and sophisticated analytical tools to investigate musculoskeletal tissues across length scales.

Thus, the primary overall aims of this Center are to enhance and advance the research productivity of investigators in musculoskeletal tissue injury and repair by:

Aim 1: Providing innovation within critical resource core facilities in areas that cross disciplines, length scales, and hierarchies. These core facilities are μCT Imaging, Biomechanics, and Histology.

Aim 2: Developing a pilot and feasibility grant program for investigators, with direct mentorship, whereby new approaches, ideas, and collaborations can be developed prior to seeking extramural funding.

Aim 3: Developing educational and research enrichment programs spanning tissue types, research approaches, and paradigms, through which members can learn from national leaders and from each other.

High quality musculoskeletal research is currently being conducted by many groups at Penn. While many bring sophisticated approaches to bear on musculoskeletal problems, few groups have the required expertise and facilities to perform high quality and specialized assays in their own labs. Furthermore, most investigators are not aware of approaches utilized, and results obtained, in other tissues that may have direct relevance on their research questions. Ultimately, close cooperation, communication, and collaboration among researchers across musculoskeletal tissue types and from a wide variety of disciplines will significantly enhance the research of our members. The Center will provide opportunities to integrate multi-disciplinary techniques to determine mechanisms for tissue function, injury, degeneration, repair, and regeneration, with the ultimate goal of advancing the diagnosis, treatment, and prevention of diseases and injuries of the musculoskeletal system.

In addition to the specific features described in this proposal, there is an intangible feature of our Center that should not be overlooked. Although our musculoskeletal program is strong nationally, the Penn biomedical research community is large and diverse. As such, the Center serves as an essential mechanism to highlight our successes and the importance and excitement of musculoskeletal research across campus, as well as to institutional leadership. Having a strong voice for musculoskeletal researchers is critical to support our collective and individual research goals. In these ways, the Center - with essential support from the P30 - has become and remains an indispensable resource and advocate for our community.
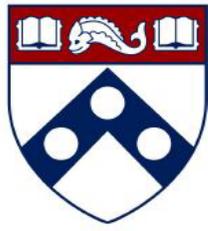
Core I

# Biomechanics

Biomechanics Core

Core Co-Directors: Robert Mauck, Ph.D. (lemauck@pennmedicine.upenn.edu) and Michael Hast, Ph.D. (hast@pennmedicine.upenn.edu)

Technical Director:

The overall objective of the Biomechanics Core is to develop and provide a wide range of innovative biomechanical approaches to evaluate musculoskeletal tissue function in the context of damage, repair, and regeneration, and to provide training and funding for new projects and collaborations utilizing these assays. Over the last decade, our Biomechanics Core at the Penn Center for Musculoskeletal Disorders (PCMD) has grown into a thriving resource for the University of Pennsylvania and Philadelphia area musculoskeletal research community. In this submission, we will further expand our services to meet the increased demand for specialized techniques and develop new and innovative methods that address the multi-scale mechanics of musculoskeletal tissues. These developments will provide customized services that enhance the research productivity of our members. The Specific Aims of the Biomechanics Core are:

- To provide guidance and training on the capabilities, advantages, and disadvantages of the various methodologies to assess musculoskeletal tissue biomechanical function through formal educational enrichment programs and one-on-one interactions

- To provide expertise and service for biomechanical assays of musculoskeletal tissues

- To develop innovative biomechanical testing techniques that will be applicable to Musculoskeletal research, and in particular those that provide information across tissue length scales

- To provide funding for the development of new projects and collaborations and to develop preliminary and/or feasibility data for investigators.

Successful completion of these aims will significantly enhance the environment and the capabilities of researchers at the University of Pennsylvania, leading to new approaches to address musculoskeletal disorders and new collaborations between Center faculties who may have not previously included biomechanical function approaches in their musculoskeletal research programs.
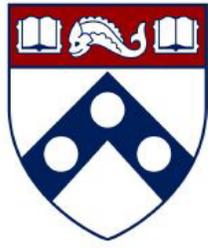
Core II

Histology

Histology Core

Overview and Mission

The mission of the Penn Center for Musculoskeletal Disorders (PCMD) Histology Core is to provide comprehensive, high quality histology services to musculoskeletal researchers at the University of Pennsylvania and the broader research community.

The Specific Aims of the core are:
- To provide guidance and training on the capabilities, advantages, and disadvantages of the various methodologies to assess musculoskeletal tissue structure and composition through formal educational enrichment programs and one-on-one interactions.
- To provide expertise and service for histological and histomorphometric assays of musculoskeletal tissues.
- To develop new histologically-based techniques that will be applicable to musculoskeletal research.
- To provide funding for development of new projects and collaborations and to develop preliminary and/or feasibility data for investigators.

Services Offered

The core offers a complete spectrum of services from sample preparation and processing, to sectioning, staining and analysis, with capabilities for paraffin, plastic and frozen histology. The core provides state of the art equipment in each of these areas, which can be accessed either on a self-service basis (upon completion of training) or a full-service basis through our full-time histology technician. Service fees are highly competitive, with significant subsidies offered for PCMD members.
- Consultation and protocol development (no charge for first 6 hours)
- Paraffin processing, embedding and sectioning
- Plastic processing and sectioning
- Frozen sectioning, including cryofilm method for undecalcified bone and teeth
- Routine histochemical staining
- Imaging and histoquantitation
- Training in histology techniques

If you are using the core for the first time, we highly recommend scheduling a meeting with one of the core co-directors and the core technician to discuss the scope of your project and specific needs.

We are very happy to provide letters of support for grant applications. To request a letter, please contact the core co-directors and provide the project title, a brief description of the project and core services you propose to use.

Please visit the core website for more information: www.med.upenn.edu/pcmd/histologymain.html

Co-Directors

Ling Qin, Ph.D. (Plastic and Frozen Histology)
Associate Professor of Orthopaedic Surgery
qinling@pennmedicine.upenn.edu
215 898 6697

Lachlan Smith, Ph.D. (Paraffin Histology)
Assistant Professor of Neurosurgery
lachlans@pennmedicine.upenn.edu
215 746 2169
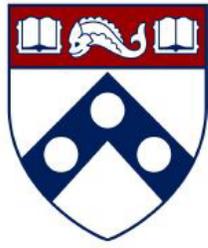
Core III

MicroCT

MicroCT Core

Director: X. Sherry Liu, Ph.D. (xiaoweil@pennmedicine.upenn.edu)

X-ray computed tomography (CT) imaging is an established and powerful tool to successfully analyze and clarify questions in musculoskeletal development, disease, injury and repair. In particular, the development of high-resolution micro-CT (μCT) over the last two decades has revolutionized the quantitative assessment of calcified and X-ray dense tissue morphology. With the capability of non-destructive, three-dimensional (3D) visualization of tissue structure, μCT has largely supplanted traditional histomorphometry and has become a gold standard for calcified tissue density and microstructure evaluation.

Due to the low intrinsic X-ray contrast of non-mineralized tissues, traditional applications of μCT in musculoskeletal research have been limited to mineralized tissue. However, the development of contrast-enhanced imaging methods has greatly broadened applications of μCT to include musculoskeletal soft tissues. This not only enables characterization of soft-tissue morphology, but also yields insight into tissue composition, such as glycosaminoglycan (GAG) density, which is essential for soft-tissue function and mechanics. Another important advance in the past decade is *in vivo* μCT imaging of living small animals, which enables longitudinal and non-invasive evaluation of changes in the same animal over time. This imaging strategy minimizes the number of animals required while enhancing statistical power. Further, high-resolution peripheral quantitative CT (HR-pQCT), a relatively recent μCT modality for clinical imaging of calcified tissue microstructure, has inaugurated a new era of non-invasive quantitative skeletal imaging and become a powerful tool for clinical research of musculoskeletal disorders. These new developments in μCT enable a detailed and quantitative understanding of the genetic influences on the skeleton, as well as modeling and remodeling events in hard and soft tissues during repair, treatment, and altered loading scenarios.

Over the past 4 years, our μCT Imaging Core (μCTIC) at the Penn Center for Musculoskeletal Disorders (PCMD) has grown into a thriving resource for the University of Pennsylvania and the region's musculoskeletal research community, serving a vibrant and growing base of 73 active PMCD faculty members and more than 170 trainees from their laboratories. The overall objective of the μCTIC is to develop and apply a wide range of standard and innovative μCT imaging approaches to evaluate musculoskeletal tissue development, disease, injury and repair, and to provide training and funding for new projects and collaborations utilizing these approaches.

The Specific Aims for the μCTIC are:

- To provide guidance and training on the capabilities, advantages, and limitations of using μCT imaging methods for musculoskeletal research through formal educational enrichment programs, online educational tutorials, and one-on-one interactions.

- To provide a range of μCT imaging resources, expertise, and services for the study of the structure, function, and physiology of the musculoskeletal system in laboratory animals and humans.

- To develop new μCT imaging-based techniques that support emerging needs and catalyze innovative musculoskeletal research.

- To provide funding for the development of novel, exploratory projects and collaborations, and to acquire preliminary and/or feasibility data for junior and senior investigators to seek external funding.

By implementing these Aims, the μCTIC will continue to serve as a unique and indispensable resource for researchers at UPenn, the Philadelphia region, and neighboring states, catalyzing innovative and high impact musculoskeletal research, and stimulating new collaborations between current and new PCMD members who may have not previously included μCT imaging approaches in their musculoskeletal research programs.
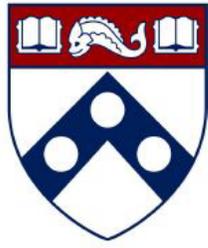
Pilot Grant Program

PENN CENTER FOR MUSCULOSKELETAL DISORDERS
PILOT AND FEASIBILITY GRANT PROGRAM

The Penn Center for Musculoskeletal Disorders has an ongoing Pilot and Feasibility Grant Program. Submissions should be related to musculoskeletal tissue injury and repair which is the broad focus of the Center and Grants are only eligible for Center members (if you are not a member but would like to become one, please contact pcmd@pennmedicine.upenn.edu). For more information on our Cores and Center in general, please see our web site at www.med.upenn.edu/pcmd . The next Center grant submission deadline is February 23, 2023.

Eligibility
- Only Full Center members are eligible. If you are not currently a member, please go to the link: http://www.med.upenn.edu/pcmd/memberinfo.shtml
- Categories of applicants include: 1) Established investigators with a proposal to test the feasibility of a new or innovative idea in musculoskeletal tissue injury and repair representing a clear and distinct departure from their ongoing research, 2) Established investigators with no previous work in musculoskeletal tissue injury and repair interested in testing the applicability of their expertise on a problem in this area, and 3) New investigators without significant extramural grant support as a Principal Investigator to develop a new project.
- Pilot and Feasibility Grants must use at least one of the Center's Research Cores.
- Pilot project awardees are eligible for one year, with a second year to be considered (budgets will be for $20-50,000 per year and timelines should be for one or two years). The second year of funding, the dollar amount of which would only be for up to half the year one budget, will be considered based on the progress report submitted after the first year of funding and funding availability in the Center. Please note that second year funding will often not be awarded, and when awarded, will be done so primarily to new investigators; second year funding to senior investigators will be quite rare.
- It is expected that these Pilot grants will lead to funding through other independent, extramural mechanisms. Therefore, the likelihood of future extramural funding will enter into the evaluation of these proposals.

Format
- Applications should be formatted loosely in the style of an NIH R03 grant (http://grants.nih.gov/grants/guide/pa-files/PA-18-488.html). The main body of the application (Specific Aims through Research Design and Methods-sections 4-7 below) is limited to five pages. The application should be in a single pdf file. The format should be:

  1) Cover Page (not NIH face page) with grant title, PI name (and co-PI name if applicable), affiliation, contact information
  2) Budget and brief justification (note that equipment is not allowed) (Please use form PHS398, Page 4)
  3) NIH Biosketch of PI (and co-PI if applicable) (in the new NIH format)
  4) Specific Aims
  5) Significance
  6) Innovation
  7) Approach
  8) Brief Statement of Category of Investigator per guidelines above
  9) Brief Statement of How this Funding will lead to other Extramural Funding
  10) Human Subjects and/or Vertebrate Animal Subjects (if applicable)
  11) Consultants (if applicable)
  12) Literature Cited
  13) Certification of Patient Oriented Research (if applicable)

The completed proposal are submitted via the PCMD website by going to the uploaded as a single PDF file.

Please do not hesitate to email pcmd@pennmedicine.upenn.edu with any questions or comments.

Awarded 2022-2023
Chider Chen, Ph.D., Department of Oral and Maxillofacial Surgery/Pharmacology, School of Dental Medicine: "mTOR Mediated Ribosome Biogenesis Regulates CD4+ T Cell Activation in Osteoporotic Mice"

Carla R. Scanzello, M.D., Ph.D., Department of Medicine, Perelman School of Medicine: "Biophysical Regulation of Macrophage Fate and Function in OA"

Eiki Koyama, D.D.S., Ph.D., Translational Research Program in Pediatric Orthopaedics, Division of Orthopaedic Surgery, CHOP: "The Molecular Mechanisms Underlying Osteophyte Onset and Growth and its Pharmacologic Intervention"

Awarded 2021-2022
Christop Thaiss, Ph.D., Department of Microbiology, Perelman School of Medicine: "Microbiome Control of Musculoskeletal Physiology"

Melike Lakadamyali, Ph.D., Department of Physiology, Children's Hospital of Philadelphia, and Perelman School of Medicine: "Chromatin Structural Regulation of Chondrocyte Fate in Cell Therapy"

Michael Hast, Ph.D., Department of Orthopaedic Surgery, Perelman School of Medicine: "Development of Load-Bearing Trauma Implants Using Bioresorbable Zinc Alloy Scaffolds"

Awarded 2020-2021
Kyu Sang Joeng, Ph.D., Department of Orthopaedic Surgery, Perelman School of Medicine: "The Function of Mtorc1 Signaling in the Regulation of the Provisional Matrix During Tendon Healing" *(awarded extramural funding from NIH/NIAMS R01AR079486)*

Patrick Seale, Ph.D., Department of Cell and Developmental Biology, Institute for Diabetes, Obesity and Metabolism, Perelman School of Medicine: "Fat and Synovial Tissue Development and Disease Remodeling in Joints" *(awarded extramural funding from NIH/NIAMS R21 AR078650-01A1)*

Josh R. Baxter, Ph.D., Department of Orthopaedic Surgery, Perelman School of Medicine: "Stimulating Muscle-Tendon Healing by Prescribing Mechanical Loading" (awarded extramural funding from R21 AR081497-01)

Awarded 2019-2020
Jaimo Ahn, M.D., Department of Orthopaedic Surgery, Perelman School of Medicine: "The Interplay of Notch Suppression and Hypoxia on Bone Regeneration"

Riccardo Gottardi, Ph.D., Department of Pediatrics, CHOP Pulmonary Medicine: "Impact of Scaffold Microporosity in Guiding Local Stem Cell Differentiation for Osteochondral Repair"

Lachlan Smith, Ph.D., Departments of Neurosurgery/Orthopaedic Surgery: "Emergent Nucleus Pulposus Cell Heterogeneity during Intervertebral Disc Development and Growth" *(awarded extramural funding from NIH/NIAMS R21AR077261)*

Awarded 2018-2019
Miltiadis Zgonis, M.D., Department of Orthopaedic Surgery, Perelman School of Medicine: "Development, Maturation, and Function of Meniscal Radial Elements"

Joel Boerckel, Ph.D., Departments of Bioengineering/Orthopaedic Surgery, Perelman School of Medicine: "Role of Yap/Taz in Osteoprogenitor Cell-Induced Angiogenesis for Vascularized Bone Repair" *(awarded extramural funding from NIH/NIAMS R01AR074948 and R01AR073809)*

Awarded 2017-2018
Nathaniel Dyment, Ph.D., Department of Orthopaedic Surgery, Perelman School of Medicine: "Murine Anterior Cruciate Ligament Reconstruction Model to Understand the Cellular Origins and Mechanisms of Repair" *(awarded extramural funding from NIH/NIAMS R01 AR076381)*

Yangqing Gong, Ph.D., Department of Medicine, Perelman School of Medicine: "Role of Plasminogen in Mesenchymal Stem Cell Function and Post-Injury Bone Regeneration"

Carla Scanzello, M.D., Ph.D., Department of Medicine, Perelman School of Medicine: "Importance of Macrophage Responses in Osteoarthritis" *(awarded extramural funding from NIH/NIAMS R01 AR075737and T21 RX001757)*

Susan Volk, V.M.D., Ph.D., D.A.C.V.S., Department of Small Animal Surgery, School of Veterinary Medicine: "The Regulatory Roles of Type III Collagen in the Cartilage Collagen Network: Implications for Osteoarthritis Prevention and Treatment" (*awarded extramural funding from NIH/NIGMS R01 GM124091*)

Awarded 2016-2017
Joseph Baur, Ph.D., Department of Physiology Institute for Diabetes, Obesity and Metabolism, Perelman School of Medicine: "Targeting Nad Metabolism in Muscular Dystrophy" *(awarded extramural funding from Elysium Health)*

Yongwon Choi, Ph.D., Department of Pathology and Lab Medicine, Perelman School of Medicine: "Cell Adhesion Regulation of Multiple-Myeloma Induced Bone Destruction"

X. Sherry Liu, Ph.D., Department of Orthopaedic Surgery and Bioengineering, Perelman School of Medicine: "Mechanical Consequences of Modeling- vs. Remodeling-Based Bone Formation" *(awarded extramural funding from the NSF Award #1661858)*

Hongtao Zhang, Ph.D., Department of Pathology and Lab Medicine, Perelman School of Medicine: "Novel Cartilage-Targeting Fc Fusion Proteins as Novel and Effective Treatments For Osteoarthritis"

Awarded 2015-2016
Yejia Zhang, M.D., Ph.D., Department of Physical Medicine and Rehabilitation, Perelman School of Medicine: "Inhibition of Adam-8 to Reduce Intervertebral Disc Degeneration" *(Awarded extramural funding from the VA Meri t; VA Competitive Pilot Fund)*

Oren Friedman, M.D., Department of Otorhinolaryngology, Perelman School of Medicine: "Effect Of Injury To Cartilage And Recovery Treatment With Fgf-18"

Harvey Smith, M.D., Department of Orthopaedic Surgery, Perelman School of Medicine: "Impact of Pre-Culture and In Vivo Remobilization on Engineered Disc Replacement" *(Awarded extramural funding from the VA RX002274-01A1)*

Tejvir Khurana, M.D., Ph.D., Department of Physiology, Perelman School of Medicine: "Role of the Il-15 / Il-15rα Axis in Modulating Muscle-Tendon-Bone Adaptation and Repair"

Awarded 2014-2015
Joshua F. Baker, M.D., MSCE, Department of Rheumatology & Epidemiology, Perelman School of Medicine: "Assessment of Intramyocellular Fat Accumulation in Rheumatoid Arthritis Using MR Spectroscopy" *(Awarded extramural funding from American Federation for Aging Research Foundation)*

Russ P. Carstens, M.D., Department of Renal-Electrolyte and Hypertension Division, Perelman School of Medicine: "Roles of Epithelial Splicing Regulatory Proteins in Craniofacial Development" *(awarded extramural funding NIH 1R56DE024749 and awarded R01 NIDCR)*

Foteini Mourkioti, Ph.D., Department of Orthopaedic Surgery, Perelman School of Medicine: "A Novel Molecular Mechanism in Chronic Skeletal Muscle Injury" *(awarded extramural funding R01AR075914 NIH/NIAMS)*

Chamith Rajapakse, Ph.D., Department of Radiology, Perelman School of Medicine: "Biomechanics of Hip Fracture Assessed by MRI" *(Awarded extramural funding from the NIH R01 AR068382)*

Awarded 2013-2014
X. Sherry Liu, Ph.D., Department of Orthopaedic Surgery, Perelman School of Medicine: "Structure and Strength Recovery in Post-Lactation Bone" *(awarded extramural funding from the NIH R03 AR065145 and NSF Career Award #1653216)*

Ling Qin, Ph.D., Department of Orthopaedic Surgery, Perelman School of Medicine: "Novel Anabolic Treatment for Radiation-Induced Osteoporosis" *(awarded extramural funding from the NIH R01AR066098)*

Lachlan Smith, Ph.D., Departments of Neurosurgery/Orthopaedic Surgery, Perelman School of Medicine: "Molecular Mechanisms of Failed Vertebral Bone Formation in Mucopolysaccharidosis VII" *(awarded extramural funding from the NIH R03 AR065142 and the MPS Society)*

Hansell H. Stedman, M.D., Department of Surgery, Perelman School of Medicine: "Molecular Pattern Recognition in Acute and Chronic Injury to Muscle and Myotendinous Junction" *(awarded extramural funding from the NIH R01NS094705)*

Awarded 2012-2013
Jason Burdick, Ph.D., Department of Bioengineering, School of Engineering and Applied Science: "Acelluar Fibrous Scaffolds for Stem Cell Recruitment and Cartilage Repair" *(awarded extramural funding from the NIH R01 EB008722)*

James L. Carey, M.D., MPH, Department of Orthopaedic Surgery, Perelman School of Medicine: "Development of a Large Animal Model of Osteochondritis Dissecans" *(awarded extramural funding from the NIH R01 EB008722)*

Andrew Kuntz, M.D., Department of Orthopaedic Surgery, Perelman School of Medicine: "Effects of Intra-Articular Glenohumeral Injection of a Nonsteroidal Anti-Inflammatory Drug on Shoulder Joint Mechanics in a Rat Model"

Arjun Raj, Ph.D., Department of Bioengineering, School of Engineering and Applied Science: "Single Cell Analysis of Molecular and Micromechanical Heterogeneity in Mesenchymal Stem Cells and Engineered Tissues"

Awarded 2011-2012
Struan F.A. Grant, Ph.D., Department of Pediatrics, Children's Hospital of Philadelphia and Perelman School of Medicine: "Utilization of ChIP-seq to Identify Genes Regulated by Osterix"

Motomi Enomoto-Iwamoto, DDS, Ph.D., Department of Orthopaedic Surgery, Children's Hospital of Philadelphia and Perelman School of Medicine: "Tendon Repair by Retinoic Acid Receptor Agonists" *(awarded extramural funding from the NIH R21 AR062193)*

Ian N. Jacobs, M.D., Department of Otorhinolaryngology: Head and Neck Surgery, Children's Hospital of Philadelphia and Perelman School of Medicine: "A Pilot Study for the Development of a Rabbit In-Vivo Tissue- Engineered Cartilage Graft for Pediatric Laryngotracheal Reconstruction" *(awarded extramural funding from The Triological Society)*

Awarded 2010-2011
Susan W. Volk, VM.D., Ph.D., Dipl ACVC, Department of Small Animal Surgery, School of Veterinary Medicine: "The Role of Type III Collagen in Bone Repair and Regeneration"

Jaimo Ahn, M.D., Ph.D., Department of Orthopaedic Surgery, Perelman School of Medicine: "Toward the Identification of Molecular Pathway Alterations in Aged Fracture Healing: A Pilot Study Utilizing a Genetic Model of Senescence" *(awarded extramural funding from the NIH R03 AG040670)*

Shannon Fisher, M.D., Ph.D., Department of Cell and Developmental Biology, Perelman School of Medicine: "Requirement for Osterix in Skull Formation and Maintenance of Adult Bone in Zebrafish" *(awarded extramural funding from the NIH R21 DE021509)*

Awarded 2010-2011 (Jointly with IOA)
Olena Jacenko, Ph.D., Department of Animal Biology, School of Veterinary Medicine: "Aging of the Hematopoietic Niche" *(awarded extramural funding from the NIH R01 DK088334-01)*

Eileen M. Shore, Ph.D., Departments of Orthopaedic Surgery and Genetics, Perelman School of Medicine: "Modulation of Progenitor Cell Differentiation through BMP Signaling" *(awarded extramural funding from the NIH R01 AR041916-15)*

Kurt D. Hankenson, DVM, Ph.D., Department of Animal Biology, School of Veterinary Medicine: "Notch Signaling in Bone Regeneration" *(awarded extramural funding from the DOD CDMRP)*

Awarded 2009-2010
Ling Qin, Ph.D., Department of Orthopaedic Surgery, Perelman School of Medicine: "Mechanisms of EGFR Action on Bone" *(awarded extramural funding from the NIH R01 DK095803)*

Steven Scherer, M.D., Ph.D., Department of Neurology, Perelman School of Medicine: "Are N-cadherin and L1 Adhesion Molecules Required for Recovery of Muscle Strength after Nerve Injury?"

Nader M. Hebela, M.D., Department of Orthopaedic Surgery, Perelman School of Medicine: "A Pre-Clinical Rodent Model of Intervertebral Disc Autograft Transplant" *(awarded extramural funding from the DOD/CDMRP/PROP OR090090)*

Awarded 2008-2009
Sunday O. Akintoye, BDS, DDS, MS, Department of Oral Medicine, School of Dental Medicine: "Orofacial Bone Marrow Stromal Cells Promote Bisphosphonate-Associated Jaw Osteonecrosis" *(awarded extramural funding from the NIDCR R21 DE022826)*

Margaret M. Chou, Ph.D., Departments of Cell and Developmental Biology, Perelman School of Medicine: "Mechanisms of TRE17/USP6 Function in the Etiology of Aneurysmal Bone Cyst" *(awarded extramural funding from the NIH-NCI R01 CA168452 and R21-CA18601)*

Kenneth W. Leichty, M.D., Department of Surgery, Perelman School of Medicine: "The Role of Inflammation in Regenerative Fetal Tendon Wound Healing" *(awarded extramural funding from the NIH DP2 DK083085)*

Kathleen M. Loomes, M.D., Department of Pediatrics, Children's Hospital of Philadelphia: "The Role of Jag1 in Osteogenesis"

Eileen M. Shore, Ph.D., Departments of Orthopaedic Surgery and Genetics, Perelman School of Medicine: "Analysis of an ACVR1 Knock-in Mouse Model for FOP*" (awarded extramural funding from the NIH R01 AR041916-15S1)*

Awarded 2007-2008
Sherrill L. Adams, Ph.D., Department of Biochemistry, School of Dental Medicine: "Collagen III-deficient Mice as a Model for Musculoskeletal Wound Repair"

Kurt D. Hankenson, DVM, Ph.D., Department of Animal Biology, School of Veterinary Medicine: "Regulation of Bone Formation by Novel Activators of Canonical Wnt Signaling"

Awarded 2006-2007
Robert J. Pignolo, M.D., Ph.D., Department of Medicine, Perelman School of Medicine: "Stem Cell Rescue of the Osteoporotic Phenotype in a Mouse Model of Accelerated Aging" *(awarded extramural funding from the NIH R01 AG028873)*

Robert L. Mauck, Ph.D., Department of Orthopaedic Surgery, Perelman School of Medicine "Meniscus Repair with a Novel Aligned Nanofiber Scaffold" *(awarded extramural funding from the NIH R01 AR056624 and the VA RR & D)*

Christopher S. Chen, M.D. Ph.D., Department of Bioengineering, School of Engineering and Applied Science: "Mechanotransduction in Mesenchymal Stem Cells" *(awarded partial funding as Co-Investigator on NIH P41 EB001046)*

Pedro K. Beredjiklian, M.D., Department of Orthopaedic Surgery, Perelman School of Medicine: "Role of Hyaluronic Acid Receptors in Tendon Healing" (*awarded extramural funding from the NIH R21 AR052393*)
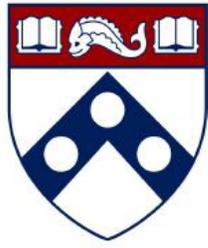
Penn Center *for* Musculoskeletal Disorders

UNIVERSITY *of* PENNSYLVANIA

Visiting Professorship Series
2022-2023

Visiting Professorship Series-Academic Year 2022-2023

Tuesday, May 2023, TBD

Tuesday, April 18, 2023, 1:30pm-2:30pm/CRB Austrian Auditorium
Title: Biomechanical & Energetic Factors Associated with Physical Activity Limitations in Osteoarthritis
Kharma C. Foucher, M.D., Ph.D., Associate Professor, Department of Kinesiology and Nutrition
Director, Biomechanics and Clinical Outcomes Laboratory, University of Illinois at Chicago

Tuesday, March 28, 2023, 1:30pm-2:30pm/CRB Austrian Auditorium
Title: From Bench to Human Trials: How did we get there?
Patrick Mooney, M.D., Ceo and Director
Christopher Natale, Ph.D., Co-Founder and VP, Research
Linnaeus Therapeutics

Tuesday, February 21, 2023, 130pm-2:30pm/CRB Austrian Auditorium
Title: Immunoengineering in the Musculoskeletal System
Jennifer Elisseeff, Ph.D., Morton Goldberg Professor; Wilmer Eye Institute and Biomedical Engineering
Translational Tissue Engineering Center; Board of Maryland's Technology Development Corporation (TEDCO)
Johns Hopkins University

Tuesday, January 24, 2023, 1:30pm-2:30pm/CRB Austrian Auditorium
Title: Life, Death and Transformation in the Transition Zone, Implications for Bone Healing
Ralph Marcucio, Ph.D., Professor of Orthopaedic Research; Director, Laboratory for Skeletal Regeneration
Orthopaedic Trauma Institute; Co-Director, Oral and Craniofacial Science Graduate Program, University of California, San Francisco

Tuesday, December 13, 2022, 1:30pm-2:30pm/CRB Austrian Auditorium
Title: The Physiology and Pathophysiology of FGF23 in Skeletal and Mineral Biology
Michael T. Collins, M.D., FASBMR
Senior Investigator; Chief, Section on Skeletal Disorders and Mineral Homeostasis; National Institute of Dental and Craniofacial Research, National Institute of Health

Wednesday, November 16, 2022, 8:15am-6:30pm/Smilow Rubinstein Auditorium/Commons
ANNUAL SCIENTIFIC SYMPOSIUM (all day event)
Keynote Speaker - Lori A. Setton, Ph.D., Lucy and Stanley Lopata Distinguished Professor & Chair of Biomedical Engineering, Washington University in St. Louis

Tuesday, October 25, 2022, 1:30pm — 2:30pm
Title: Biomanufacturing, Biomaterials and Biomechanics for Improved Treatment of Volumetric Muscle Loss Injuries
Chuanju Liu, Ph.D.
Professor and Director, Translational Orthopaedic Research Laboratory; Department of Orthopaedic Surgery and Cell Biology, NYU Grossman School of Medicine

Tuesday, September 20, 2022, 1:30pm — 2:30pm
Title: Building Tissues Engineering Complexity Through Biomaterial Design
Brendan A. Harley, Sc.D., Robert W. Schaefer Professor, Department of Chemical and Biomolecular Engineering, Cancer Center at Illinois (CCIL); Carl R. Woses Institute for Genomic Biology, University of Illinois at Urbana-Champaign

Visiting Professorship Series-Academic Year 2022-2023

Tuesday, May 17, 2022, 1:30pm-2:30pm/CRB Austrian Auditorium
https://bluejeans.com/163462521630/607111756539?src=join_info
(Co-Sponsored by Penn Health-Tech)
Title: Bringing Academic Discoveries from the Lab to the Market.
Katherine Reuther, Ph.D., Executive Director, Penn Health-Tech; Practice Associate Professor in Bioengineering
University of Pennsylvania

Tuesday, April 12, 2022, 1:30pm-2:30pm/CRB Austrian Auditorium
Title: Musculoskeletal Adaptation to Mechanical Loading.
Marjolein van der Meulen, Ph.D., James M. and Marsha McCormick Director of Biomedical Engineering
Swanson Professor of Biomedical Engineering; Meinig School of Biomedical Engineering, Cornell University

Tuesday, March 22, 2022, 1:30pm-2:30pm/CRB Austrian Auditorium
Title: Hypoxia and the Skeleton
Clare Yellowley, Ph.D., Professor of Anatomy, Physiology and Cell Biology, School of Veterinary Medicine
University of California, Davis

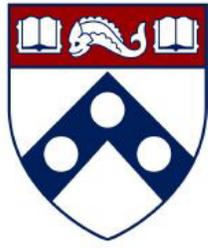**Tuesday, January 25, 2022, 1:30pm-2:30pm/Virtual Seminar Link**
https://bluejeans.com/428595277896/556211167641?src=join_info
Title: Advances in Regenerating Musculoskeletal Tissues
Warren L. Grayson, Ph.D., Professor of Biomedical Engineering and
Director, Laboratory for Craniofacial and Orthopaedic Tissue Engineering
Johns Hopkins University

Symposium Participants

Last Name	First Name	Email	Affiliation
Agnello	Kimberly	kagnello@vet.upenn.edu	UPenn Vet
Alexander	Carmel	carmel.alexander@temple.edu	Temple Univ Bioengineering
Angelozzi	Marco	angelozzim@chop.edu	CHOP Ortho
Arefin	Mohammed Shahriar	Tul18768@temple.edu	Temple Univ Bioengineering
Arnold	Alexandra	alexandra.arnold@temple.edu	Temple Univ Bioengineering
Aronson	Matthew	Mja5575@seas.upenn.edu	UPenn Bioengineering
Assi	Sereen	assi@seas.upenn.edu	UPenn Bioengineering
Ayturk	Ugur	ayturku@hss.edu	HSS Research Institute
Azar	Tala	talaazar@seas.upenn.edu	UPenn Ortho
Bakhri	Rania	rania.bakhri@temple.edu	Temple Univ Bioengineering
Barot	Dhvani	dhvani@vet.upenn.edu	UPenn Vet
Bautista	Catherine	cbaut@seas.upenn.edu	UPenn Bioengineering
Baxter	Josh	josh.baxter@pennmedicine.upenn.edu	UPenn Ortho
Bergstrom	Annika	abergs01@villanova.edu	Villanova Univ Engineering
Berlew	Erin	erin.berlew@pennmedicine.upenn.edu	UPenn Ortho
Bernstein	Elizabeth	Elizabeth.bernstein@pennmedicine.UPenn.edu	UPenn Ortho
Betts	Rebecca	rebecca.betts@pennmedicine.upenn.edu	UPenn Ortho
Binder-Markey	Ben	bb983@drexel.edu	Drexel Univ Physical Therapy
Bonelli	Hannah	hbonelli@seas.upenn.edu	UPenn Ortho
Boufidis	Dimitris	boufidis@seas.upenn.edu	UPenn Bioengineering
Boyes	Madeline	mboyes@vet.upenn.edu	UPenn Vet
Brewer	Leslie	lbrew@upenn.edu	UPenn Vet CORL
Brooks	Lauryn	lauryn.brooks@pennmedicine.upenn.edu	UPenn Ortho
Brown	Elizabeth	ebrown4@seas.upenn.edu	UPenn Bioengineering
Buckwalter	Grace	graceebuck@outlook.com	Temple Univ Bioengineering
Burrell	Justin	Burrellj@pennmedicine.UPenn.edu	UPenn OMFS
Cabrera	Gabriel	Tun91964@temple.edu	Temple Univ Ortho
Campbell	Nathan	campb302@purdue.edu	Purdue Univ Health and Kinesiology
Canonicco Castro	Maria	mjc7530@psu.edu	Penn State Biomedical Engineering
Capalbo	Margaret	mhc5270@psu.edu	Penn State Biomedical Engineering
Carey	James	james.carey@pennmedicine.upenn.edu	UPenn Ortho
Carlson	Jaclyn	jaclynca@upenn.edu	UPenn Ortho
Carroll	Chad	carrol71@purdue.edu	Purdue Univ Health and Kinesiology
Catheline	Sarah	cathelines@chop.edu	CHOP Surgery
Chan	Trevor	tjchan@seas.upenn.edu	UPenn Bioengineering
Chen	Chider	chenc10@upenn.edu	UPenn Dental Oral Surgery
Chia	Wai-Kit	waikit.chia@pennmedicine.upenn.edu	UPenn Radiology
Chu	Tiankuo	chutk@udel.edu	Univ of Delaware Mechanical Engineering
Ciuciu	Alexandra	axc497@students.jefferson.edu	Thomas Jefferson Univ Ortho
Cobbol	Kevin	Kevin.Cobbol@PennMedicine.UPenn.edu	UPenn Ortho
Collins	Joseph	jmcollin@seas.upenn.edu	UPenn Ortho
Connelly	Amanda	amanda.connelly@students.jefferson.edu	Thomas Jefferson Univ Ortho
Dailey	Hannah	hlr3@lehigh.edu	Lehigh Univ Mechanical Engineering
Daniels	Ryan	rydan@pennmedicine.upenn.edu	UPenn Ortho
De Jesus	Kelli	kmd119@students.jefferson.edu	Thomas Jefferson Univ Cell Biology/Regenerative Medicine
DiStefano	Michael	micdis@seas.upenn.edu	UPenn Ortho
Donahue	Joan	DonahueJ@pennmedicine.upenn.edu	UPenn CAMB
Duffy	Michael	mpduffy@upenn.edu	UPenn Ortho
Dyment	Nathaniel	dyment@pennmedicine.upenn.edu	UPenn Ortho
Eekhoff	Jeremy	jeremy.eekhoff@pennmedicine.upenn.edu	UPenn Ortho
Evans	Mary Kate	mkevans@seas.upenn.edu	UPenn Bioengineering
Fagan	Sophia	sfagan@upenn.edu	UPenn Vet Ortho
Fainor	Matthew	matthew.fainor@pennmedicine.upenn.edu	UPenn Ortho
Fan	Mingyue	mf988@drexel.edu	Drexel Univ Biomedical Engineering
Fang	Jiankang	jiankang.fang@pennmedicine.upenn.edu	UPenn Ortho

Last Name	First Name	Email	Affiliation
Farber	Daniel	daniel.farber@pennmedicine.upenn.edu	UPenn Ortho
Fernandez Iglesias	Angela	fernandeaf@chop.edu	CHOP Ortho
Freeman	Theresa	theresa.freeman@jefferson.edu	Thomas Jefferson Univ Ortho
Friday	Chet	Chet.Friday@Pennmedicine.upenn.edu	UPenn Ortho
Friedman	Ryan	friedmanr@chop.edu	CHOP Otolaryngology
Fung	Stephanie	fungs@chop.edu	CHOP Otolaryngology
Fung	Ashley	afung@seas.upenn.edu	UPenn Ortho
Gaesser	Angela	agaesser@upenn.edu	UPenn CAMB/DSRB
Gehret	Paul	gehretp@seas.upenn.edu	UPenn Bioengineering
Godshall	Stanton	sfg5423@psu.edu	Penn State
Gong	Wiley	wilegong24@ncs.charter.k12.de.us	Newark Charter School
Gottardi	Riccardo	gottardir@chop.edu	CHOP Pediatrics
Granquist	Eric	Eric.Granquist@pennmedicine.upenn.edu	UPenn Oral & Maxillofacial Surgery
Gullbrand	Sarah	sgullb@pennmedicine.upenn.edu	UPenn Ortho
Hallman	Mitchell	mitchell.hallman@pennmedicine.upenn.edu	UPenn Ortho
Hast	Michael	hast@pennmedicine.upenn.edu	UPenn Ortho
Henning	Elizabeth	ehenning@pennmedicine.upenn.edu	UPenn Ortho
Heo	Su Chin	heosc@pennmedicine.upenn.edu	UPenn Ortho
Hilliard	Rachel	rlhill@vet.upenn.edu	UPenn Vet
Hopster	Klaus	khopster@vet.upenn.edu	Veterinary Anesthesiology
Hu	Baofeng	baofeng.hu@pennmedicine.upenn.edu	UPenn Ortho
Hullfish	Todd	todd.hullfish@pennmedicine.upenn.edu	UPenn Ortho
Iyer	Keerthana	keerthana.iyer@pennmedicine.upenn.edu	UPenn
Jiang	Xi	jiangxi@pennmedicine.upenn.edu	UPenn
Jiang	Jason	th3jj1ang193@gmail.com	Conestoga High School
Joeng	Kyu Sang	joeng@pennmedicine.upenn.edu	UPenn Ortho
Johnson	Talayah	talayahj@seas.upenn.edu	UPenn Ortho
Johnston	Shira	shira.johnston@students.jefferson.edu	Thomas Jefferson Univ Ortho
Jones	Brandon	bcjones@seas.upenn.edu	UPenn Ortho
Jones	Erica	emjones7@pennmedicine.upenn.edu	UPenn Ortho
Kahle	Elizabeth	erk59@drexel.edu	Drexel Univ Biomedical Engineering
Kamalitdinov	Timur	timkam@seas.upenn.edu	UPenn Bioengineering
Kamona	Nada	nkamona@seas.upenn.edu	UPenn Radiology
Karvande	Anirudha	karvandea@chop.edu	CHOP Ortho
Katsura	Kei	kei.katsura@ucsf.edu	UPenn Genetics
Keith Lang	Sinaia	sinaiakl@sas.upenn.edu	UPenn Ortho
Khan	Mohd Parvez	mohd.khan@pennmedicine.umpenn.edu	UPenn Ortho
Kim	Dong Hwa	kimd1@pennmedicine.upenn.edu	UPenn Ortho
Kim	Minwook	kimm12@email.chop.edu	UPenn Ortho
Kim	Sung Yeon	sungyk@seas.upenn.edu	UPenn Ortho
Kneeland	Bruce	john.kneeland@pennmedicine.upenn.edu	UPenn Radiology
Kolasinski	Sharon	sharon.kolasinski@pennmedicine.upenn.edu	UPenn Medicine
Koo	Bonhyeock	Bonhyeock.Koo@penmedicine.upenn.edu	UPenn Ortho
Koyama	Eiki	koyamae@chop.edu	CHOP Ortho
Kumchai	Hattanas	hattanas.kumchai@jefferson.edu	Thomas Jefferson Univ Ortho
Kwok	Bryan	bk589@drexel.edu	Drexel Univ Biomedical Engineering
Kwon	Michelle	michelle.kwon@pennmedicine.upenn.edu	UPenn Ortho
Lang	Annemarie	Annemarie.Lang@Pennmedicine.upenn.edu	UPenn Ortho
Laslow	Brittany	Brittany.Laslow@Pennmedicine.upenn.edu	UPenn Ortho
Leahy	Thomas	tpleahy@upenn.edu	UPenn Ortho
Lee	Se-Hwan	se-hwan.lee@pennmedicine.upenn.edu	UPenn Ortho
Lee	Alexander	alexander.lee@pennmedicine.upenn.edu	UPenn Ortho
Lee	Wonsae	wonsae.lee@pennmedicine.upenn.edu	UPenn Ortho
Lee	Ji-Hyung	ji-hyung.lee@pennmedicine.upenn.edu	UPenn Ortho
Lefebvre	Veronique	lefebvrev1@chop.edu	CHOP Ortho
Lemmon	Elisabeth	elemmon@vet.upenn.edu	UPenn Ortho

Last Name	First Name	Email	Affiliation
Li	Jun	jun.li@pennmedicine.upenn.edu	UPenn Ortho
Li	Zizhao	lizizhao@seas.upenn.edu	UPenn Ortho
Li	Thomas	tl545@drexel.edu	Drexel Univ Biomedical Engineering
Liang	Qiushi	qiushil@seas.UPenn.edu	UPenn Bioengineering
Lim	Joohyun	limj@udel.edu	University of Delaware
Lin	Yu-Lieh	YuLieh.Lin@pennmedicine.upenn.edu	UPenn Ortho
Linardi	Renata	rlinardi@upenn.edu	UPenn Vet
Linus	Awuniji	awuniji.linus@temple.edu	Temple Univ Bioengineering
Liu	Yuchen	yl3358@drexel.edu	Drexel Univ Biomedical Engineering
Liu	X. Sherry	xiaoweil@pennmedicine.upenn.edu	UPenn Ortho
Long	Fanxin	longf1@chop.edu	CHOP Ortho
Lu	Jiawei	Jiawei.Lu@Pennmedicine.upenn.edu	UPenn Ortho
Madhu	Veda	vxm042@jefferson.edu	Thomas Jefferson Univ Ortho
Madi	Rashad	Rashad.madi25@gmail.com	UPenn Ortho
Mangine	Angela	amangine@upenn.edu	UPenn Vet
Maparu	Auhin	auhin.maparu@pennmedicine.upenn.edu	UPenn Ortho
Mauck	Robert	lemauck@pennmedicine.upenn.edu	UPenn Ortho
Meader	Julianne	julianne.meader@pennmedicine.upenn.edu	UPenn Ortho
Mehta	Amrita	mehtaa@chop.edu	CHOP Otorhinolaryngology
Mejias	Loreilys	loreilys.mejias@pennmedicine.upenn.edu	UPenn CAMB
Mitchell	Michael	mjmitch@seas.upenn.edu	UPenn Bioengineering
Moharrer	Yasaman	yasamanm@seas.upenn.edu	UPenn Ortho
Molin	Arnaud	molinan@chop.edu	CHOP Ortho
Montes de Oca	Anthony	asmontes@sas.upenn.edu	UPenn Ortho
Mourkioti	Foteini	fmour@pennmedicine.upenn.edu	UPenn Ortho
Mundy	Christina	matticolac@chop.edu	CHOP Ortho
Murphy	Lance	lance.murphy@pennmedicine.upenn.edu	UPenn Ortho
Nadruz	Veridiana	vnadruz@upenn.edu	Upenn Vet
Newton	Joseph	josebr@seas.upenn.edu	UPenn Ortho
Nguyen	VU	vunguyen@pennmedicine.upenn.edu	UPenn Rheumatology
Nijsure	Madhura	mnijsure@seas.upenn.edu	UPenn Bioengineering
Nixon	Jacob	jacobnix@seas.upenn.edu	UPenn Ortho
Nuss	Courtney	cnuss@pennmedicine.upenn.edu	UPenn Ortho
Orozco	Brianna	brianna.orozco@pennmedicine.upenn.edu	UPenn Ortho
Ortved	Kyla	kortved@vet.upenn.edu	UPenn Vet Clinical Studies
Ottone	Olivia	oko002@students.jefferson.edu	Thomas Jefferson Univ Ortho
Pacifici	Maurizio	pacificim@chop.edu	CHOP Ortho
Panebianco	Christopher	christopher.panebianco@pennmedicine.upenn.edu	UPenn Ortho
Paschall	Lauren	lnp55@psu.edu	Penn State Biomedical Engineering
Patel	Neil	nrp46@drexel.edu	Drexel Univ Biomedical Engineering
Patten	Jennifer	tul00628@temple.edu	Temple Univ Bioengineering
Pedaprolu	Krishna	kup225@psu.edu	Penn State BME
Peterson	Ben	Bep15@psu.edu	Penn State BME
Pleshko	Nancy	npleshko@temple.edu	Temple Univ Bioengineering
Pletcher	Joshua	Joshua.pletcher@temple.edu	Temple Univ Bioengineering
Pyle	Sienna	scpyle@seas.upenn.edu	UPenn Ortho
Qin	Ling	qinling@pennmedicine.upenn.edu	UPenn Ortho
Querido	William	william.querido@temple.edu	Temple Univ Bioengineering
Rajagopal	Karthikeyan	Karthikeyan.Rajagopal@pennmedicine.upenn.edu	UPenn Ortho
Rajapakse	Chamith	chamith@pennmedicine.upenn.edu	UPenn Radiology
Rajpar	Ibtesam	ibtesam.rajpar@jefferson.edu	Thomas Jefferson Univ Ortho
Ramteke	Pranay	pranay.ramteke@jefferson.edu	Thomas Jefferson Univ Ortho
Rao	Daya	daya.rao@gmail.com	Thomas Jefferson Univ Ortho
Reyes	Camila	c.reyeslauriani@gmail.com	Purde Univ Health/Kinesiology
Risbud	Makarand	makarand.risbud@jefferson.edu	Thomas Jefferson Univ Ortho
Roberts	Doug	doug.roberts@pennmedicine.upenn.edu	UPenn Ortho

Last Name	First Name	Email	Affiliation
Rodrigues	Mariana	marianarodrigues2798@gmail.com	UPenn Ortho
Rowe	Matthew	mmrowe@seas.upenn.edu	UPenn Pulmonary
Rux	Danielle	ruxd@chop.edu	CHOP Ortho
Sang	Wen	wsang1@villanova.edu	Villanova Univ MEAM
Santillian	Jaime	jaime.santillan@pennmedicine.upenn.edu	UPenn Ortho
Sao	Kimheak	kxs489@students.jefferson.edu	Thomas Jefferson Univ Ortho
Scanzello	Carla	cscanz@pennmedicine.upenn.edu	CMC VA Medical Center
Schipani	Ernestina	Ernestina.Schipani@Pennmedicine.upenn.edu	UPenn Ortho
Sedigh	Ashkan	Ashkan.sedigh@jefferson.edu	Thomas Jefferson Univ Ortho
Setton	Lori	setton@wustl.edu	WUSTL Bioengineering
Sharma	Riti	Ritis@seas.upenn.edu	UPenn MEAM
Sharp	Emily	ees015@seas.upenn.edu	UPenn Bioengineering
Shaughnessy	Kelly	shaughnesk@chop.edu	CHOP Ortho
Shore	Eileen	shore@pennmedicine.upenn.edu	UPenn Ortho
Singh	Prerana	prs67@drexel.edu	Drexel University
Smith	Lachlan	lachlans@pennmedicine.upenn.edu	UPenn Ortho
Smith	Carly	carly.smith9620@gmail.com	Thomas Jefferson Univ Ortho
Smith	Harvey	harvey.smith@pennmedicine.upenn.edu	UPenn Ortho
Smith	Anna	annasmi@vet.upenn.edu	UPenn Vet
Smith	Kyra	kwys@seas.upenn.edu	UPenn Bioengineering
Song	Ke	ke.song@pennmedicine.upenn.edu	UPenn Ortho
Soslowsky	Lou	soslowsk@upenn.edu	UPenn Ortho
Spiller	Kara	kls35@drexel.edu	Drexel Univ Biomedical Engineering
Spitsin	Sergei	spitsins@upenn.edu	UPenn Pathology
Stoeckl	Brendan	bstoeckl@pennmedicine.upenn.edu	UPenn Ortho
Sun	Wei	Wei.Sun@pennmedicine.upenn.edu	UPenn Ortho
Szczesny	Spencer	ses297@psu.edu	Penn State Biomedical Engineering
Tamburro	Margaret	margaret.tamburro@pennmedicine.upenn.edu	UPenn Ortho
Tang	My	mymy.tang@pennmedicine.upenn.edu	UPenn Ortho
Tang	Waixing	waixing@pennmedicine.upenn.edu	UPenn Ortho
Tertuliano	Ottman	oat@seas.upenn.edu	UPenn MEAM
Thurlow	Nat	nthurlow@seas.upenn.edu	UPenn Bioengineering
Tomlinson	Ryan	ryan.tomlinson@jefferson.edu	Thomas Jefferson Univ Ortho
Tsingas	Maria	maria.tsingas@students.jefferson.edu	Thomas Jefferson Univ Ortho
Usimaki	Alexandra	ausimaki@upenn.edu	UPenn Vet
Vining	Kyle	viningk@upenn.edu	UPenn Dental
Volk	Susan	swvolk@vet.upenn.edu	UPenn Vet
Vu	Brian-Tinh	bdvu@seas.upenn.edu	UPenn Bioengineering
Wagner	Margaret	magwag@seas.upenn.edu	UPenn Bioengineering
Wang	Liyun	lywang@udel.edu	Univ of Delaware Mechanical Engineering
Wang	Bin	bin.wang@jefferson.edu	Thomas Jefferson Univ Medicine
Wasi	Murtaza	murtaza@udel.edu	Univ of Delaware Mechanical Engineering
Watkins	Amanda	Watkinsa@upenn.edu	UPenn CPM
Weiss	Stephanie	weisssn@gmail.com	UPenn Ortho
Whitaker	Ricardo	rw688@drexel.edu	Drexel Univ Biomedical Engineering
Wilson	Christalle	tul09017@temple.edu	Temple Univ Bioengineering
Woods	Madison	woodsmad@sas.UPenn.edu	UPenn Ortho
Xu	Xiaoyu	xiaoyu.xu@pennmedicine.upenn.edu	UPenn Ortho
Xu	Karen	klxu@seas.upenn.edu	UPenn Bioengineering
Xue	Lulu	lulxue@seas.upenn.edu	UPenn Bioengineering
Yang	Yanmei	yanmei.yang@jefferson.edu	Thomas Jefferson Univ Medicine
Zhang	Chenghao	chenghao.zhang@pennmedicine.upenn.edu	UPenn Ortho
Zhang	Yejia	yejiazhang07@gmail.com	Upenn Rehab
Zhang	Ellen	yzhang98@seas.upenn.edu	UPenn Ortho
Zhou	Yilu	yilu.zhou@pennmedicine.upenn.edu	UPenn Ortho
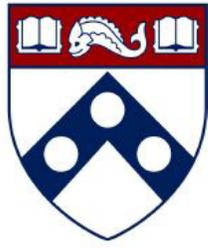
Speaker Abstracts

Towards Precision Rehabilitation for Achilles Tendon Ruptures

Josh R Baxter, PhD
Assistant Professor of Orthopaedic Surgery

Orthopaedics is fundamentally a load transfer problem. Managing loads before someone suffers injury is a major challenge that requires fundamental shifts in how we live, work, and train. But patients typically seek treatment after suffering an injury. Treating musculoskeletal injuries is an opportunity to improve care by precisely managing tissue loading. My lab is exploring strategies to mitigate the severity of chronic Achilles tendon disease – called tendinopathy – and maximize recovery from acute Achilles tendon ruptures. In this talk I will describe a novel small animal dynamometer that we developed with the support of a PCMD Pilot Grant. We developed this tool to assess joint-level function in an established rat Achilles tendon rupture model. Importantly, our lab has already collected and published joint-level function data from a cohort of Penn Medicine patients who suffered acute Achilles tendon ruptures and received non-surgical treatment. We validated this dynamometer by simulating this non-surgical care in a cohort of rats and found that the functional deficits – measured as ankle work deficits – between the injured and uninjured sides were similar in both shape and magnitude between rats (34%) and humans (38%). By building confidence in this small animal dynamometer, we can now *quantify* functional outcomes and *prescribe* precision rehabilitation loading profiles in a controlled and validated preclinical model. We then tested the isolated effects of surgically repairing an acute Achilles tendon rupture compared to non-surgical treatment in the same rat model. Surgically repairing the tendon rupture mitigated functional deficits – particularly in ankle plantar flexion where patients often complain of reduced strength that limits their ability to enjoy activities like hiking and sports. Our findings support surgical treatment because it prevents excessive plantar flexor work deficits compared to non-surgical care. Some patients are not candidates for surgical treatment because of comorbidities, fear of surgery, or wound healing complications. We are now using this small animal dynamometer to prescribe rehabilitation loading following the injury and initial treatment to identify therapeutic mechanical loads that we hope to translate to future clinical trials.

In vivo validation of a continuous gradient porous scaffold for osteochondral defect repair in a rabbit model

Kyra W.Y. Smith[1,2], Soheila Ali Akbari Ghavimi[2], Stephanie Logterman[2], Paul M. Gehret[1,2], Gioacchino Conoscenti[3], Valerio Brucato[3], Vincenzo La Carrubba[3], J. Todd Lawrence[2], Riccardo Gottardi[1,2]

[1]University of Pennsylvania, Philadelphia, PA, [2]Children's Hospital of Philadelphia, Philadelphia, PA, [3]University of Palermo, Italy

gottardir@chop.edu

Disclosures: Nothing to disclose

INTRODUCTION: Osteochondral defects, characterized by damage to the articular cartilage and the subchondral bone, are a major health concern affecting 60% of patients who undergo knee surgery [1]. Current standards of care include microfracture, which only creates fibrocartilaginous scar tissue, or osteochondral transplant, which suffers from limited donor supply [2]. Tissue engineering thus represents an exciting alternative, but a key hurdle is the tendency of engineered cartilage to ossify [3]. To overcome this limitation, we developed a porous osteochondral scaffold in which specific pore sizes are tailored to promote chondrogenesis on one side and osteogenesis on the opposite side. The scaffold is made of Poly(L-Lactide) (PLLA) and the pore dimensions vary along a continuous gradient to prevent delamination from the cartilage side (~70μm pore diameter, pro-chondrogenic) to the bone side (~200μm pore diameter, pro-osteogenic). We used an established biphasic bioreactor [4] that allows parallel chondrogenic and osteogenic differentiation of each side of the osteochondral constructs which were then tested *in vivo* in an osteochondral defect rabbit model.

METHODS: *Engineering of the osteochondral constructs:* Scaffolds of PLLA were fabricated by Thermally Induced Phase Separation to form a continuous gradient of pore sizes along the sample thickness (***Fig. 1A***), as described in a previous ORS abstract by Gottardi et al. [5]. Cylindrical scaffolds (diameter=4mm, height=6mm) were uniformly seeded with 200K rabbit mesenchymal stem cells (MSCs) harvested from the marrow of rabbit donors and expanded in growth medium (DMEM, 2% Penicillin/Streptomycin/Fungizone (PSF), 10% Fetal Bovine Serum (FBS)). Seeded scaffolds were placed in the biphasic bioreactor for osteochondral differentiation (***Fig. 1B***). The small pore side of the scaffold was perfused in the upper chamber of the bioreactor at flow rate of 1.4μL/min with chondrogenic medium (DMEM, 2% PSF, 10ng/mL TGF-β3, 1% insulin-transferrin-selenium (ITS), 50 μg/mL L-ascorbic acid 2-phosphate (AA), 40μg/mL L-proline, 0.1μM dexamethasone), and the larger pore side was perfused in the lower chamber at the same rate with osteogenic medium (DMEM, 2% PSF, 10% FBS ,0.1μM dexamethasone, 50μM AA, 10mM β -glycerophosphate, 10nM 1α, 25-Dihydroxyvitamin D3).

Osteochondral constructs characterization: Constructs were assessed for chondrogenic and osteogenic morphology via Alcian Blue and Alizarin Red staining, respectively (***Fig. 1D,E***). The top third (cartilage) and the bottom third (bone) of the constructs were separated and analyzed via RT-qPCR for chondrogenesis (*COL2A1, ACAN, SOX9*) and osteogenesis (*RUNX2, IBSP, SPP1*) (***Fig. 1F,G***), or underwent mechanical testing (bulk modulus: 20% compression at 0.01%/s, dynamic modulus: 10 sinusoidal compressions at 1Hz) using a custom compression tester at the Penn Biomechanics Core (***Fig. 1C***) [6].

In vivo implantation of engineered osteochondral constructs: Bilateral osteochondral repair was performed on 21 female rabbits (New Zealand White, 3.5-4.5kg) for a total of 42 knees (IACUC: Children's Hospital of Philadelphia). The experimental groups were: (i) empty defects (negative control), (ii) acellular scaffolds, (iii) non-differentiated MSC-seeded scaffolds, (iv) pre-differentiated engineered osteochondral constructs (see previous section). In brief, the trochlea was exposed, a surgical drill was used to create a cylindrical osteochondral defect 4mm wide and 6mm deep, and the scaffold was press-fit into the defect with the large pore side (bone) facing the marrow cavity and the small pore side (cartilage) facing the joint space. After three months, the rabbits were euthanized, the knees were examined for gross appearance, integration, and repair, then excised for microCT and histology to assess differentiation and integration, and for RNAscope to asses spatial distribution of gene expression across the implanted constructs.
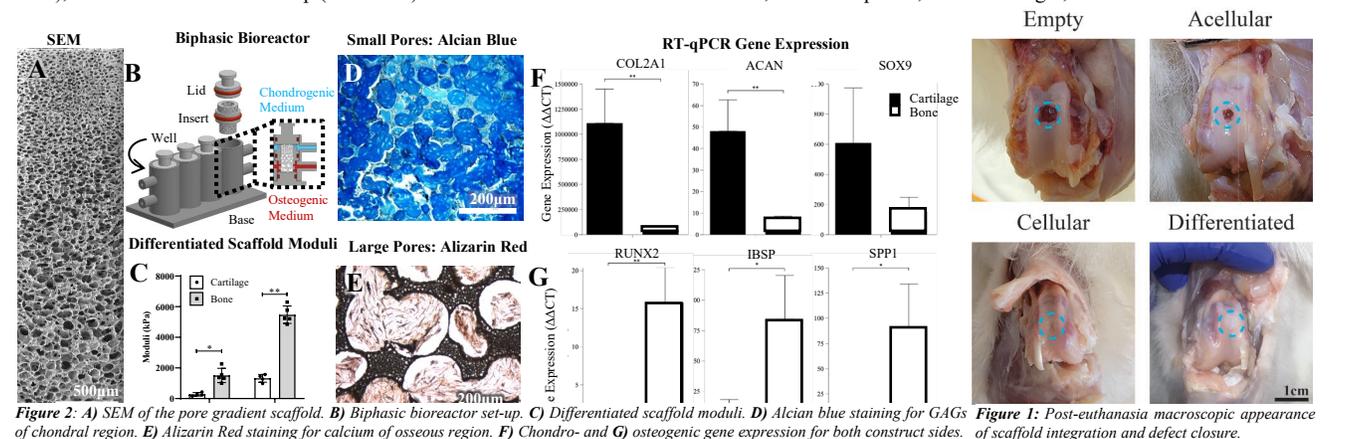
RESULTS: Pre-surgical characterization of the scaffold shows that after differentiation, there is significant difference in both the bulk and dynamic moduli between the chondral and osseous regions of the scaffold, approaching native articular cartilage values (***Fig. 1B***). Strong glycosaminoglycan presence and expression of chondrogenic genes was observed in the chondral region (***Fig. 1D,F***), while strong calcium production and expression of osteogenic genes in the osseous region (***Fig. 1E,G***). At the end of the three-month healing period, all rabbits were ambulating normally and showed no signs of pain or distress. Healed osteochondral defects exhibited complete defect closure and integration in the cellularized and differentiated groups, and non-closures in most empty and acellular groups (***Fig. 2***). Additionally, differentiated scaffolds display shiny white surfaces typical of hyaline cartilage. There was only one scaffold extrusion event. Ongoing examinations by microCT show both cartilaginous and trabecular repair in healed defects, proving successful biphasic morphologies, and initial gene expression distributions in the *in vivo* model suggest specific chondrogenic and osteogenic differentiation analogous to *in vitro* results.

DISCUSSION: Our continuous pore gradient scaffold avoids the risk of delamination common with biphasic models and promotes dual chondro- and osteogenic differentiation to align with the osteochondral bilayer in the knee. Small pores promote chondrogenic differentiation by mimicking mesenchymal condensation [7], while large pores promote osteogenic differentiation [8]. Construct maturation within the dual-flow bioreactor allows the simultaneous differentiation of each tissue types within a monolithic structure ready to be implanted. Application of the scaffold to an *in vivo* rabbit model confirms success of scaffold integration and osteochondral tissue healing suggesting significant promise for clinical translatability.

SIGNIFICANCE: With this work we explored the use of local pore geometry to replicate developmental processes that drive chondrogenesis thus establishing a powerful approach for robust cartilage engineering. The effectiveness of our engineered osteochondral construct to repair a rabbit osteochondral defect shows tremendous promise for this this technology to heal osteochondral defects and provide a solution to a major health problem.

REFERENCES: [1] Graham*, Orthop. Nurs.*, 237-239, 2017. [2] Howel et al., *Curr. Rev. Musculoskelet. Med.*, 60-66, 2021. [3] Saka et al., *Regen. Med. Res.*, 2019. [4] Ianetti et al., *PLoS One*, 1-25, 2016. [5] Gottardi et al., *ORS Proceedings*, 2016. [6] Patel et al., *Tissue Eng. Part C Methods*, 593-608, 2019. [7] Nava et al., *J. Appl. Biomater. Funct. Mater.*, e223-e229, 2016. [8] Lin et al., *Int. J. Mol. Sci.*, 326, 2019.

Figure 2: A) SEM of the pore gradient scaffold. B) Biphasic bioreactor set-up. C) Differentiated scaffold moduli. D) Alcian blue staining for GAGs of chondral region. E) Alizarin Red staining for calcium of osseous region. F) Chondro- and G) osteogenic gene expression for both construct sides.

Figure 1: Post-euthanasia macroscopic appearance of scaffold integration and defect closure.

Investigating the function of mTORC1 signaling in tendon using mouse genetic models and scaffold-free 3D tendon constructs

Kyu Sang Joeng
Assistant Professor of Orthopaedic Surgery

The limited understanding of the regulatory mechanisms underlying tendon cell maturation and fibrovascular scar formation hinders the development of effective treatment modalities for tendon diseases. We have demonstrated that mTORC1 (mechanistic target of rapamycin complex 1) signaling is a critical regulator for postnatal tendon development and constitutive activation of mTORC1 signaling caused fibrovascular scar-like phenotypes in tendons. However, the precise mechanisms by which mTORC1 regulate tendon cell maturation and fibrovascular scar formation are not known. To investigate the function of mTORC1 in tendon cell maturation, we analyzed the morphological maturation of tendon cells in the tendon-specific mTORC1 loss-of-function (*Scx-Cre;Raptor$^{fl/fl}$*) and gain-of-function (*Scx-Cre;Tsc1$^{fl/fl}$*) mouse models. To exam the function of mTORC1 in the differentiation of tendon progenitors into the *Col1(2.3)-GFP-positive cells*, we generated *Scx-Cre;Raptor$^{fl/fl}$; Col1 (2.3)-GFP* (loss-of-function) and *Scx-Cre;Tsc1$^{fl/fl}$;Col1 (2.3)-GFP* (gain-of-function) mouse models. The results from these studies suggested that mTORC1 signaling inhibits early differentiation of tendon progenitors into Col1a1-expressing tenocytes and morphological maturation.

Stat3 is a transcription factor and plays a crucial role in fibrosis and inflammation via the regulation of cell proliferation and ECM organization. Interestingly, previous studies showed that Stat3 can be activated by mTORC1 signaling. To genetically determine Stat3 as a mediator of mTORC1 function in fibrovascular scar formation in tendons, we performed a genetic rescue experiment by generating three types of the tendon-specific deficient mouse: 1) *Scx-Cre; Tsc1$^{fl/fl}$* (tendon-specific mTORC1 gain-of-function mouse model), 2) *Scx-Cre; Stat3$^{fl/fl}$* (tendon-specific Stat3 knockout mouse model), and 3) *Scx-Cre; Tsc1$^{fl/fl}$; Stat3$^{fl/fl}$* (tendon-specific Tsc1 and Stat3 double knockout mouse model for rescue experiment). Stat3 deletion partly rescued fibrovascular scar-like phenotype such as neovascularization, inflammatory cell infiltration, disorganized collagen organization caused by constitutive activation of mTORC1 signaling. Our genetic data suggest that Stat3 partially mediates mTORC1 function in fibrovascular scar formation.

Standard two-dimensional (2D) cell culture has been widely used for *in vitro* studies to understand molecular mechanisms. However, tenocyte phenotype is not well-maintained in monolayer culture, and it is difficult to study ECM organization and morphological maturation of cells without a 3-dimensional (3D) environment. To overcome this limitation, we developed a scaffold-free, three-dimensional (3D) tendon culture system using mouse tendon cells. The 3D tendon constructs exhibited tissue maturation similar to the postnatal mouse tendon, including decreased cell density, increased thickness, and elongated cells between highly aligned extracellular matrix. The 3D tendon culture system is also feasible for genetic manipulation using adenovirus. Overall, the results suggest that the 3D tendon culture system using mouse tendon cells is a reliable *in vitro* system to study underlying biological mechanisms that regulate cellular and matrix maturation in postnatal tendon development.

Virtual Mechanical Testing of Bone Fracture Healing

Hannah Dailey, PhD
Assistant Professor of Mechanical Engineering & Mechanics
Lehigh University (Bethlehem, PA)

Web: https://engineering.lehigh.edu/faculty/hannah-dailey
Twitter: @DaileyOrthoLab

Abstract: Bone fracture healing is a mechanoregulated process that gradually restores the mechanical integrity of an injured bone by forming an adaptive, functionally graded new material called *callus* at the fracture line. In humans, the recovery process after a bone fracture usually lasts at least several months. However, in some patients, healing does not proceed successfully after the first surgery, resulting in a condition called *nonunion*. Nonunions are notoriously difficult to treat, in part because diagnosis requires subjective assessment of clinical signs and the visual appearance of callus on X-rays. Early diagnosis could transform nonunion care, but due to the lack of definitive biomarkers for failed healing, most patients wait at least 6-9 months before receiving an intervention. To address this clinical need, we have developed a technique for measuring what really matters in bone healing—the mechanical integrity of the healing bone—using subject-specific finite element models built from low-dose computed tomography (CT) scans. In this seminar, Dr. Dailey will describe how the techniques for virtual mechanical testing were developed and validated in ovine tibial osteotomy models. She will also present case studies of clinical application, where we have successfully used virtual mechanical tests to detect delayed healing of tibial fractures and structurally insufficient bone formation associated with comorbidities such as smoking.

A New, Injury-Activated Osteoprogenitor Population in the Musculoskeletal System

Ugur Ayturk, Ph.D.

C-type lectin domain family 3, member b (Clec3b) is necessary for the healing of skin, connective tissue and bone injuries in mice. Recent single cell RNA-seq studies on bone, muscle, ligament and fat have shown that Clec3b expression is unique to a specific set of mesenchymal cells in the musculoskeletal system. These cells also express Pdgfra, Sca1 and Cd34, and are predicted to be progenitors by computational lineage algorithms. However, the in vivo fate, precise location and function of Clec3b+ cells remain unclear. To fill this knowledge gap, we generated a tamoxifen-inducible Clec3b.creERT2 allele using CRISPR-Cas9 knock-in strategy. We hypothesized that Clec3b-expressing cells give rise to osteoblasts and contribute to bone formation in vivo. Analysis of Clec3b.creERT2; Ai14.R26.tdTomato mice showed Clec3b+ cells primarily in skeletal muscle, as well as the peripheral layers of periosteum and connective tissues, but not in bone marrow or growth plate. Further, Clec3b+ cells remained osteogenically inactive and did not give rise to osteoblasts or osteocytes during the first 3 months of life. Yet, monocortical drill hole injury, as well as stabilized and nonstabilized fractures mobilized Clec3b-lineage cells to become chondrocytes, osteoblasts, osteocytes and marrow stromal cells. To distinguish the injury-responsiveness of periosteal- and muscle-based Clec3b+ cells, we performed calvarial drill hole surgeries, as Clec3b+ cells are exclusively located in outer periosteum of parietal bones and do not interface with muscle. Although Clec3b+ cells participated in cranial callus formation, they maintained a fibroblast-like morphology and did not give rise to bone-lining cells or osteocytes. These data suggest that Clec3b+ cells in skeletal muscle but not periosteum contribute to bone healing following injury. Consistent with this, our analysis of recently published scRNA-seq data showed that Clec3b is a highly specific marker for Prx1-lineage fibroadipogenic progenitors. We therefore tested whether Clec3b+ muscle cells are also capable of heterotopic ossification through pharmacologic and genetic activation of BMP-signaling. Both approaches indicated participation of Clec3b-lineage cells in ectopic mineralization. Altogether, our data show that Clec3b+ cells participate in both bone repair and pathologic mineralization of muscle tissue, but not musculoskeletal growth or remodeling. Studying Clec3b+ cells may therefore suggest collective strategies to treat fractures and heterotopic ossification.

Immunomodulatory Biomaterials for Regenerative Medicine
Kara L. Spiller, PhD
School of Biomedical Engineering, Science, and Health Systems
Drexel University

The inflammatory response plays a major role in the body's response to injury, disease, or implantation of a biomaterial. When the inflammatory response functions normally, it can be a powerful force that promotes tissue repair and regeneration, but when it goes awry, disease takes hold and healing is impaired. The goal of the Biomaterials and Regenerative Medicine Laboratory at Drexel University is to understand the mechanisms by which the inflammatory response orchestrates successful tissue regeneration and to develop novel biomaterial strategies that apply these principles to situations in which tissue regeneration is impaired. In particular, we focus on the behavior of the macrophage, which can rapidly change behavior in response to environmental stimuli to promote inflammation, vascularization, tissue deposition, or remodeling. Through their dynamic phenotypic changes, macrophages function as major regulators of healing. In this talk, we will focus on our work to investigate the role of macrophage phenotype in angiogenesis and wound healing, with applications in novel biomaterials design and biomarker development.

Biosketch:

Dr. Kara Spiller is a Professor in Drexel University's School of Biomedical Engineering, Science, and Health Systems. Her research interests include the role of immune cells in tissue regeneration, the design of immunomodulatory biomaterials, and international engineering education. Her research is funded by the NIH, the NSF, and private foundations. Her awards include a Fulbright fellowship, the NSF CAREER award, and the United States nomination for the ASPIRE prize.

Lipid Nanoparticles for Overcoming Biological Barriers to RNA Delivery

Michael J. Mitchell, Ph.D.[1]

[1]Department of Bioengineering, University of Pennsylvania, Philadelphia, PA

Recent years have witnessed tremendous developments and breakthroughs in the field of RNA-based therapeutics and vaccines. The distinct mechanisms of exogenous RNAs and analogs, including messenger RNAs, small interfering RNAs, microRNAs, and antisense oligonucleotides, have brought them unprecedented potential to treat a variety of pathological conditions. However, the widespread application of RNA therapeutics and vaccines is hampered by their intrinsic features (e.g., instability, large size, and dense negative charge) and formidable host barriers. Development of safe and efficient vectors is key for successful delivery and translation of RNA therapeutics and vaccines. In this talk, I will discuss our efforts towards the development of new lipid nanoparticles (LNPs) that enable the delivery of RNA therapeutics and vaccines to target cells and tissues *in vivo*. Furthermore, I will describe new therapeutic strategies utilizing these LNPs for (i) mRNA delivery to bone for regenerative medicine applications, (ii) in vivo reprogramming of immune cells, and (ii) in utero mRNA delivery for treating disease before birth.

How Hypoxia and Mitochondria Shape up the Skeleton

Ernestina Schipani

Department of Orthopaedic Surgery, University of Pennsylvania, Perelman School of

Medicine, Philadelphia, 19104, PA, USA.

Hypoxia occurs not only in pathological conditions like cancer and ischemia and in a variety of physiological settings in the adult organism, but also during normal embryonic development. In the inner portion of the fetal growth plate, which is an avascular tissue originating from mesenchymal progenitor cells, chondrocytes experience physiological hypoxia. Hypoxia-Inducible Transcription Factor-1α (HIF1α), a crucial mediator of cellular adaptation to hypoxia, is an essential survival and differentiation factor for fetal growth plate chondrocytes. In my talk, I will discuss our current understanding of the survival and differentiation functions of HIF1α in skeletal development.

Ottman A. Tertuliano,
AMA Family Assistant Professor
Mechanical Engineering and Applied Mechanics
University of Pennsylvania

Title: Quantifying length-scale dependent toughening in human bone fracture

Abstract:
Natural composite materials such as bone exhibit a combination of these properties exceeding that of their constituents, a feat generally credited to their hierarchal structure, down to the nanoscale. In this talk, we will demonstrate the use of micro and nanoscales site-specific microstructural characterization and mechanical experiments to probe the strength, deformation, and fracture behavior of human bone. We will demonstrate an *in situ* SEM/nanoindentor methodology, that enables 3-point bending fracture experiments with observation and measurement of crack growth and toughening behavior at nano and micrometer scales. We will discuss the crack initiation and growth mediated by underlying fibril microstructure (~50 nm) in bone under static and fatigue loading, and place it in the context of hierarchical toughening up to the macro/organ level (500+ um) fracture. These results open the door for understanding the dynamic mechanical adaptation of bone tissue at small length scales

Navigating a Path to Understanding Drug Delivery in the Treatment of Arthritis

Lori A Setton, Ph.D.
Lucy and Stanley Lopata Distinguished Professor & Chair of Biomedical Engineering
Washington University in St. Louis

Research and development have advanced clinical use of protein and small molecule drugs that can modify the progression and symptoms of osteoarthritis and inflammatory pain, including mediators of TNF-alpha and the NF-kappa B pathway. Systemic administration of these drugs can have serious side effects that motivate use of local drug delivery strategies, such as intra-articular injection, to prolong drug residence time and decrease serum exposure. Our laboratory both develops *in situ* forming drug depots for sustained drug delivery to the joint over time and constructs computational models of drug clearance to understand governing processes. Here we will review the synthesis and design of intra-articular drug depots, and show evidence that drugs retain substantial bioactivity and disease-modifying effects in vivo. We further describe our ex vivo models to advance an understanding of factors affecting drug transport in the joint space towards the goal to design optimal drug delivery strategies.
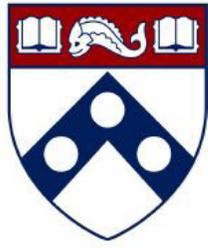
Biomechanics Abstracts

Knockdown of Decorin and Biglycan Immediately Following Tendon Injury Significantly Alters Gene Expression and Fibril Morphology, with Minimal Effects on Mechanical Properties

Joseph B. Newton[1], Stephanie N. Weiss[1], Christelle Darrieutort-Laffite[1,2], Courtney A. Nuss[1], David E. Birk[3], Louis J. Soslowsky[1]

[1]McKay Orthopaedic Research Laboratory, University of Pennsylvania, Philadelphia, PA, [2]Rheumatology Department, Nantes University Hospital, France
[3]Department of Molecular Pharmacology and Physiology, University of South Florida, Tampa, FL

josebr@seas.upenn.edu

Disclosures: Joseph B. Newton(N), Stephanie N. Weiss(N), Christelle Darrieutort-Laffite(N), Courtney Nuss(N), David E. Birk(N), Louis J. Soslowsky(N)

INTRODUCTION: Tendon consists of highly organized collagen fibrils with small leucine rich proteoglycans (SLRPs) bound to the fibril surface. Two of these SLRPs, decorin (Dcn) and biglycan (Bgn) play important roles throughout tendon growth, aging, and repair as regulators of fibrillogenesis and matrix assembly [1]. Biglycan is highly expressed in the immediate response to tendon injury and early stages of tendon growth, but decreases dramatically during remodeling and in mature tendons, while decorin is present throughout these processes [2]. However, the roles of decorin and biglycan in the initial injury response in aged tendons are unknown. Therefore, the objective of this study is to evaluate the differential roles of decorin and biglycan through their knockdown at the time of injury in aged mice. We hypothesized that induced knockdown of decorin and biglycan expression, individually and in a double knockdown, would impair the healing response compared to wild type mice leading to reduced improvement in tendon mechanical properties post injury, altered gene expression profiles, and changes in collagen fibril diameter distributions. As the predominant SLRP in tendon, we hypothesized that knockdown of decorin would result in greater impairment as biglycan expression is minimal in mature tendons.

METHODS: Study Design: Female $Dcn^{+/+}/Bgn^{+/+}$ control (WT, n=48), $Dcn^{flox/flox}$ (I-$Dcn^{-/-}$, n=32), $Bgn^{flox/flox}$ (I-$Bgn^{-/-}$, n=32), and compound $Dcn^{flox/flox}/Bgn^{flox/flox}$ (I-$Dcn^{-/-}/Bgn^{-/-}$, n=32) mice with a tamoxifen inducible Cre (B6.129-Gt(ROSA)26Sortm1(cre/ERT2)Tyj/J, Jackson Labs) were utilized [3] (IACUC approved). At 300 days old, Cre excision of conditional alleles was induced in all mice via two (injured mice) or three (uninjured mice) consecutive daily IP injections of tamoxifen. WT mice (n=16) were designated as uninjured controls and remaining mice were divided into 3- or 6-week post-injury groups to represent the early and later remodeling healing phases (n=16/genotype/time point). At time of induction, mice in injury groups underwent bilateral patellar tendon injury surgery and were sacrificed 1-, 3- or 6-weeks later. Uninjured groups were sacrificed at 330 days old. Mechanical Testing Protocol: The patellar tendon-bone complex from one limb of each animal in the 3- and 6-week post-injury groups was dissected and prepared for mechanical testing (n=10-14/genotype/time point) [4]. Tendons were subjected to a testing protocol: preconditioning, stress relaxations at 3, 4, and 5% strains, and a quasi-static ramp to failure. Tendon elastic mechanical properties were calculated from the ramp to failure test and stain lines were used for optical strain tracking. Percent relaxation was quantified for each stress-relaxation. Transmission Electron Microscopy (TEM): For TEM, patellar tendons from animals in the 6-week post-injury group were fixed, embedded in epon, sectioned at 75nm, and imaged at 60,000x. Collagen fibril distributions were quantified from images in the healing region (n=4/genotype). Gene: Injured patellar tendons from animals in the 1-, 3-, and 6-weeks post injury groups were isolated for RNA extraction and cDNA reverse transcription. Pre-amplified cDNA was loaded into a Fluidigm 96.96 Dynamic Array with Taqman assays to probe expression levels of 96 target genes relevant for tendon healing (n=4/genotype/time point). Statistics: For mechanics, one-way ANOVAs with Bonferroni corrections were conducted for 3- and 6-week post-injury groups. For gene expression, the same tests were conducted for 1-, 3-, and 6-week post injury groups. Fibril diameter distributions were compared using Kolmogorov-Smirnov tests. Significance was set at $p \le 0.05$.

RESULTS: Decorin and biglycan expression showed efficient knockdown (Fig 1A). Tendon cross-sectional area was decreased in the I-$Dcn^{-/-}$ group vs WT (Fig 1B). Midsubstance modulus was increased in I-$Bgn^{-/-}$ vs WT (Fig 1C). No differences were found in max stress and percent relaxation (not shown). Fibril distributions were different between all groups at 6-weeks post-injury (Fig 2). At 1-week post-injury, I-$Bgn^{-/-}$ had increased expression of genes related to collagen and non-collagenous matrix synthesis, inflammation, and cell-ECM interactions compared to WT tendons (Table 1). 3- and 6-weeks post-injury reveals I-$Dcn^{-/-}$ tendons have reduced expression of genes related to collagen synthesis, non-collagenous matrix synthesis, matrix remodeling, inflammation, and cell-ECM interactions compared to WT, I-$Bgn^{-/-}$ and I-$Dcn^{-/-}/Bgn^{-/-}$ groups (Table 1).

Figure 1: A) Knockdown of decorin and biglycan resulted in a significant reduction in expression levels. B) A significant decrease in cross-sectional area (CSA) was found comparing I-Dcn$^{-/-}$ to WT tendons 6-weeks post-injury. C) A significant increase in midsubstance modulus was found in I-Bgn$^{-/-}$ tendons compared to WT at 3-weeks post-injury. Bars indicate significance at $p \le 0.05$. Dashed line denotes uninjured WT values.
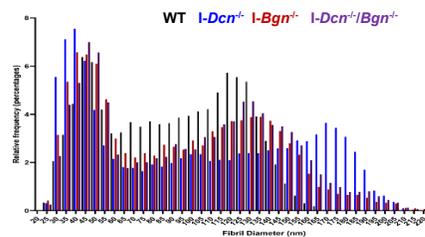
Figure 2: Relative frequency of fibril diameter taken from TEM.

	1-Wk				3-Wk				6-Wk			
UP / Down	WT	I-*Dcn⁻/⁻*	I-*Bgn⁻/⁻*	I-*Dcn⁻/⁻/Bgn⁻/⁻*	UP / Down	WT	I-*Dcn⁻/⁻*	I-*Bgn⁻/⁻*	I-*Dcn⁻/⁻/Bgn⁻/⁻*	UP / Down	WT	I-*Dcn⁻/⁻*	I-*Bgn⁻/⁻*	I-*Dcn⁻/⁻/Bgn⁻/⁻*
WT			Col1a2, Postn, Ly6a, Itgb1, Ltbp1, Ly6a, Ltbp1	TNF, Tlr2, P2x7	WT			Elastin		WT			Col3a1	Ccl5
I-*Dcn⁻/⁻*	Col2a1		Col1a1		I-*Dcn⁻/⁻*		Col12a1, Kera, Fbn2, Fbln4, Thbs2, Tnc		Col12a1, Thbs4, Tnc, Txnb, MMP3, Mkx, Itgb1	Col12a1, Col11a1, Col12a1, Kera, Fbn2, Thbs2, Tnc, Txnb, MMP14, Sox9, Itgb1, Pge2, Igf1	I-*Dcn⁻/⁻*		Fmod, Kera, Timp3, Runx2, Mkx		Fmod, Timp3, Mkx	Thbs4, Timp3, Mkx, Ctgf, Bmp2
I-*Bgn⁻/⁻*				TNF, P2x7	I-*Bgn⁻/⁻*		IL10	IL10		I-*Bgn⁻/⁻*				
I-*Dcn⁻/⁻/Bgn⁻/⁻*	Col2a1				I-*Dcn⁻/⁻/Bgn⁻/⁻*		Ly6a	Timp3	Ltbp1	I-*Dcn⁻/⁻/Bgn⁻/⁻*				

Table 1: Gene expression summary table. Genes listed are significantly increased in the column group relative to the row group.

DISCUSSION: Our study supports the differential roles of decorin and biglycan throughout healing. At 1-week, most changes in gene expression were found in I-$Bgn^{-/-}$ tendons suggesting that biglycan plays a critical role during the inflammatory phase of healing. [2]. At 3-weeks, gene expression changes were found in I-$Dcn^{-/-}$ tendons that were not fully maintained at 6-weeks post-injury. Decorin and biglycan have been shown to be involved in matrix assembly, inflammation, and growth factor activity during healing [4,5]. Both single and double knockdown of biglycan and decorin led to tendons with a smaller fibril diameter 6-week post injury, further highlighting the role of these SLRPs in fibrillogenesis [6]. Surprisingly, these changes were not reflected in mechanical properties, with only an increase in midsubstance modulus 3-weeks post-injury in I-$Bgn^{-/-}$ tendons vs WT. Contrary to our hypotheses, knockdown at the time of injury did not lead to differences in mechanical properties 6-weeks post-injury. These results may suggest a more limited role of decorin and biglycan during later stages of healing in aged mice. Future work is necessary to elucidate the roles of decorin and biglycan at the later stages of healing.

SIGNIFICANCE: This study highlights the differential roles of biglycan and decorin in gene expression and fibril structure during healing in aged mice and suggests that biglycan has a larger role in the early phases of healing, while decorin is more pronounced at 3- weeks post injury.

REFERENCES: [1] Chen et al., *FEBS J*, 280, 2013. [2] Dunkman et al., *Ann Biomed Eng*, 42, 2014. [3] Robinson et al., *Matrix Biol*, 64, 2017. [4] Connizzo et al., *J Biomech Eng*, 135, 2013. [5] Iozzo et al., *J Biol Chem, 286,* 2011. [6] Hildebrand et al., *Biochem J*, 302, 1994.
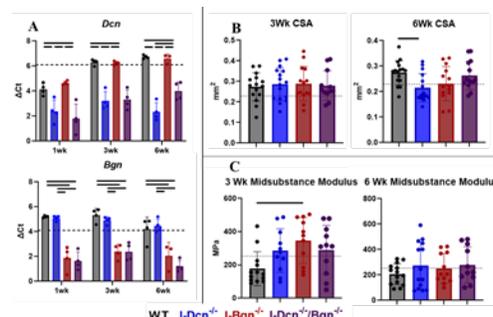
Collagen III Deficiency Alters Mechanical Properties and Decreases Regulation of Fibrillogenesis Following Injury in Female Murine Tendons

Carlson JA[1], Weiss SN[1], Volk SW[2], Soslowsky LJ[1]

[1]McKay Orthopaedic Research Laboratory, University of Pennsylvania, Philadelphia, PA, [2]School of Veterinary Medicine, University of Pennsylvania, Philadelphia, PA

Disclosures: Carlson JA (N), Weiss SN(N), Volk SW(N), Soslowsky LJ (N)

INTRODUCTION: Patients with vascular Ehlers-Danlos syndrome (*v*EDS), a rare genetic disease caused by *Col3A1* mutations, are well-known for severe vascular complications and early death. However, tendon rupture and dysfunction contribute to patient morbidity[1-4], supporting a critical role of collagen III (Col3) in tendon homeostasis and maintenance. Col3 is essential in homeostasis and healing of other collagen I (Col1)-rich tissues (e.g., skin[5], meniscus[6], and bone[7]) due to its role regulating fibrillogenesis, extracellular matrix (ECM) organization, and the formation of cross-links and scar tissue[5,6]. Therefore, the objective of this study was to define the role of Col3 in both tendon homeostasis and in response to injury, regulating collagen fibril deposition and resultant alterations in tendon mechanics. We hypothesized that a reduction in Col3 would result in a more robust, stiffer provisional matrix early in tendon healing, with smaller diameter fibrils when compared to wild-type tendons.

METHODS: Female wild-type (WT) Balb/cJ and heterozygous *Col3a1*^{+/-} mice at 30 days of age (n=48) were used (IACUC approved). Injured mice underwent bilateral patellar tendon injury surgery[8] and were sacrificed 1-week (1w) post-injury in the early proliferative phase of healing. Uninjured sex, strain and age-matched mice were also examined. *Transmission Electron Microscopy (TEM):* Tendons for TEM (n=4/group) were fixed *in situ* and processed[10] to analyze fibril structure. *Mechanics:* Patella-patellar tendon-tibia complexes were prepared for mechanical testing (n=12/group)[11]. Tendons were subjected to a viscoelastic testing protocol[10,12] consisting of: 1) preconditioning, 2) stress relaxation at strain levels of 2%, 3% and 4%, 3) a sinusoidal frequency sweep (10 cycles at 0.1, 1, 5, and 10 Hz) at each strain level, 4) return to gauge length, and 5) ramp to failure. *Statistics.* Two-way repeated measures ANOVAs with post-hoc Bonferroni tests were used to assess the effects of genotype, injury and their interaction on quasistatic and viscoelastic properties. Collagen fibril diameter distributions were compared by genotype using Kolmogorov-Smirnov tests. Significance was set at p≤0.05 (solid lines) and trends at p≤0.1 (dotted lines).

RESULTS: Following injury, tendon cross-sectional area was increased in both WT and *Col3a1*^{+/-} tendons with *Col3a1*^{+/-} tendons having a larger area than WT tendons (trend) following injury (Fig. 1). *Col3a1*^{+/-} tendons had increased failure load and stiffness (Fig. 2A,B) 1w post-injury when compared to WT tendons, with no differences in uninjured tissues. A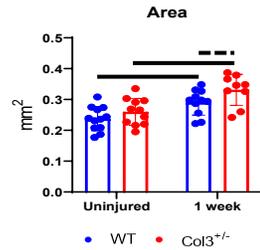dditionally, WT tendons had a lower failure load and modulus (trend) 1w post-injury when compared to uninjured, while there was no effect of injury in *Col3a1*^{+/-} tendons (Fig. 2A,C). Failure stress (Fig. 2D) was decreased in both genotypes 1w following injury. Additionally, TEM analysis showed a shift to smaller diameter fibrils post-injury in both genotypes (Fig. 3). Finally, distinctly different distributions for WT and *Col3a1*^{+/-} fibrils post-injury were seen, with *Col3a1*^{+/-} tendons having a larger population of smaller and larger fibrils, and WT tendons having a less pronounced peak and more flat distribution (Fig. 3).

DISCUSSION: Our study shows that Col3 deficiency alters both mechanical properties and matrix structure 1w post-injury in a murine patellar tendon injury model in novel and previously unexplored ways. Tendon area increases following injury as healing tissue is deposited into the wound site. The trend toward increased area of *Col3a1*^{+/-} tendons compared to WT tendons post-injury is consistent with an increased deposition of provisional matrix, secondary to increased activation of fibroblasts in *Col3a1*^{+/-} tendons, as decreased Col3 has been shown to cause increased activation[5]. Decreases in failure stress in both genotypes following injury is due to increases in area without concurrent increases in failure load, indicating poor quality tissue following injury in both genotypes as would be expected 1w post-injury. Additionally, TEM analysis showed a more densely packed provisional matrix with

Figure 1. Tendon cross-sectional area was increased post-injury in both genotypes when compared to uninjured tendons.
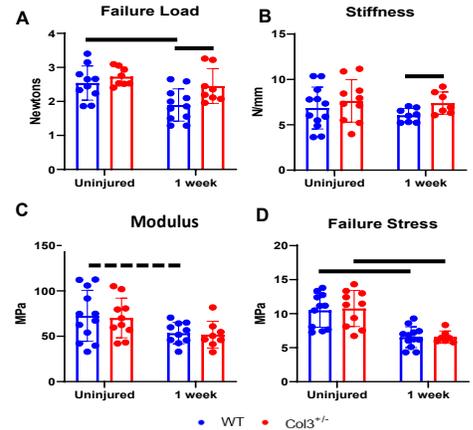

Figure 2. Failure load and stiffness was increased in *Col3a1*^{+/-} tendons 1w post-injury compared to WT. Failure stress was decreased in both genotypes following injury.
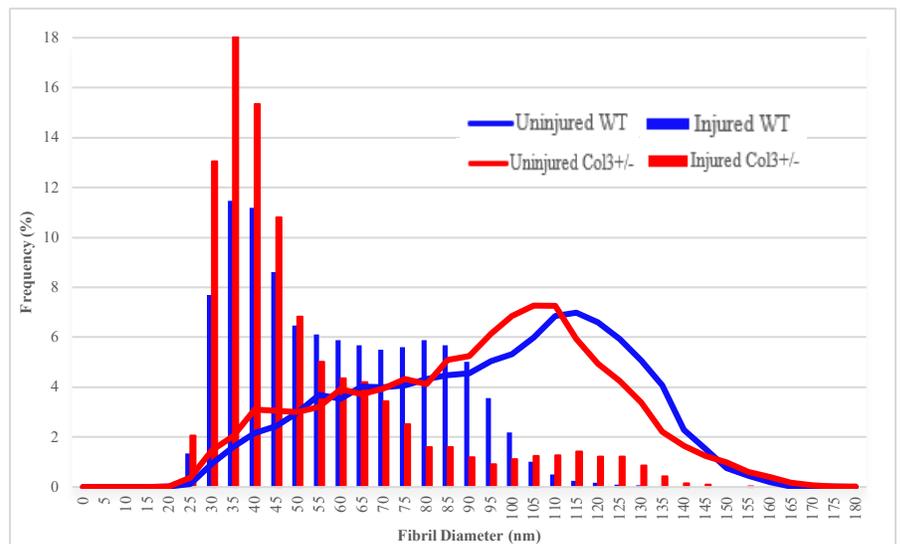

Figure 3. Smaller fibrils were seen in both genotypes following injury. *Col3a1*^{+/-} tendons post-injury had a larger population of smaller fibrils and larger fibrils when compared to WT. Uninjured: line graph, Injured: bar graph.

smaller fibrils following injury in *Col3a1*^{+/-} tendons likely explaining increased stiffness and further indicating a hypersecretory state of myofibroblasts for Col1 post-injury. Lastly, the highly skewed fibril diameter distribution with an extended right tail in *Col3a1*^{+/-} tendons indicates dysregulation in fibrillogenesis when compared to WT tendons post-injury. An increased population of larger fibrils reveals increased lateralization of fibrils in *Col3a1*^{+/-} tendons, which is expected as Col3 presence decreases lateral growth during fibrillogenesis[13]. Notably, while *Col3a1*^{+/-} tendons have increased failure load following injury compared to WT tendons at this time point, the poor quality of healing tissue quantified in this study supports the likelihood of an important role of Col3 in dictating cellular activity and healing potential. Based on these findings, we will examine later time points to understand how fibril growth continues into later stages of healing, along with alterations to the cellular population and activity. Importantly, we will also further evaluate the role of Col3 using a novel conditional Col3 knockdown model to understand the unique temporal role of Col3 throughout healing and more specifically, to rigorously analyze the targeted role of Col3 by evaluating the dose response in an otherwise normal matrix.

SIGNIFICANCE: Col3 is crucial during early wound healing, affecting matrix structure and function, likely influencing long-term healing. Elucidating the mechanistic role of Col3 throughout healing will provide the necessary foundation for developing Col3-inspired therapies that optimize tendon healing and will ultimately have a profound impact on tendon healing, thereby decreasing healthcare expenditures and improving patient quality of life.

REFERENCES: [1] Cooper et al. *Vet Path.* 2010. [2] Maffulli et al. *Br J Sports Med.* 2002. [3] Ong et al. *Lancet.* 2010. [4] Byers et al. *Am. J. Med. Genet.* 2017. Review. [5] Volk et al. *Cells Tissues Organs.* 2011. [6] Wang et al. *Matrix Biol.* 2020. [7] Miedel et al. *J Orthop Res.* 2015. [8] Beason et al. *J. Biomech*, 2012. [10] Dunkman et al. *Matrix Biol.* 2013. [11] Kjaer et al. *J. Anat.* 2006. [12] Miller KS, et al. *J Biomech Eng.* 2012. [13] Liu et al. *Proc Natl Acad Sci USA.* 1997.

The Mechanosensor Focal Adhesion Kinase Regulates Cell Shape and Tendon Development

Thomas P. Leahy[1,2], Srish S. Chenna[1,2], Louis J. Soslowsky[1,2], Nathaniel A. Dyment[1,2]
[1]McKay Orthopaedic Research Laboratory, University of Pennsylvania, PA
[2]Department of Bioengineering, University of Pennsylvania, Philadelphia, PA
tpleahy@seas.upenn.edu

Disclosures: Thomas P. Leahy (N), Srish S. Chenna (N), Louis J. Soslowsky (N), Nathaniel A. Dyment (N),

INTRODUCTION: Throughout development and postnatal growth, resident tendon cells respond to mechanical cues from the nascent tendon extracellular matrix (ECM) to regulate tissue properties. Focal adhesion kinase (FAK, gene: *Ptk2*) is an intracellular protein kinase that regulates the actin cytoskeleton and cell-ECM adhesions. In tendon cells, FAK activity is required for tenogenic gene expression in response to growth factor stimulation and mechanical stretching.[1–3] In addition, pharmacological inhibition of FAK in explanted tendons significantly attenuates ECM to nuclei strain transmission.[4] Despite these known roles for FAK in tendon, the mechanism by which FAK activity regulates cell mechanotransduction as well as the role of FAK-dependent mechanotransduction in tendon development remain unknown. Therefore, the objective of this study was to evaluate the regulatory role of FAK in (1) tendon cell-ECM mechanical interactions and in (2) tendon development. We hypothesized that (1) FAK activity regulates tendon cell *in vitro* focal adhesion morphology and cell spreading behavior, and that (2) reduced FAK expression will negatively impact tendon development.

METHODS: *In Vitro* **Cell Culture**: Tail tendon cells were isolated from P30 WT male and female mice (3 mice in 2 independent experiments; n = 30 cells/treatment/mouse). Cells were cultured on fibronectin-coated coverslips and treated with a FAK inhibitor (10 µM PF-573228; FAK-I) or vehicle (DMSO) control. Immunofluorescence staining was performed to quantify cell morphology and pFAK localization 6 hours post-treatment. *In Vivo* **Mouse Model**: Tendon targeted FAK knockout (Scx-Cre;FAK^F/F; FAK-KO) mice were generated.[5] Achilles tendons (ATs), flexor digitorum longus tendons (FDLs), and patellar tendons (PTs) from P30 male and female FAK-KO and WT littermate controls were used for gene expression analysis, paraffin histology, and viscoelastic mechanical testing. Gene Expression: RNA was isolated from tendons to evaluate *Ptk2* expression using Taqman assays, with *Abl1* as a

housekeeping control (n=6/genotype/sex). Paraffin Histology: Whole ankle and knee joints were fixed, decalcified, paraffin embedded, and sectioned in the sagittal plane (n=5/genotype/sex). Hoechst nuclear staining was used to quantify cell density and nuclear aspect ratio (nAR). Overall tissue morphology was evaluated via toluidine blue staining. Viscoelastic Mechanics: Tendon cross-sectional areas (CSAs) were measured (n=7-9/genotype/sex), and tendons were subjected to a viscoelastic mechanical testing protocol (preconditioning, viscoelastic stress relaxation and dynamic frequency sweep, and a quasi-static ramp to failure).

RESULTS: *In Vitro* **Cell Culture**: FAK-I treated cells developed pronounced cell protrusions compared to DMSO treated cells (Fig. 1A). While cell area was not different between groups (Fig. 1B), FAK-I treated cells had significantly higher cell compactness values relative to DMSO treated cells (Fig. 1C), which is indicative of the increased protrusion phenotype. Focal adhesions were closer

Figure 1. A) Representative images of DMSO and FAK-I treated tail tendon cells. Scale: 50 µm. B) Cell area, C) cell compactness, D) focal adhesion distance to the cell periphery, and E) pFAK-Paxillin correlation coefficient quantifications of DMSO and FAK-I treated tail tendon cells. Data was analyzed with t-tests comparing groups. Bars represent sig. diff. between groups ($p < 0.05$).

to the cell periphery and colocalized less with pFAK staining in FAK-I treated cells relative to DMSO treated cells (Fig. 1D-E). *In Vivo* **Mouse Model**: Ptk2 expression was reduced in all FAK-KO tendons relative to WT tendons, thereby validating our conditional knockout mouse model (Fig. 2). FAK-KO tendons were not remarkably distinct from WT tendons histologically, and there were no differences between groups in quantified cell density or nAR (data not shown). Interestingly, FAK-KO tendons were consistently smaller compared to WT tendons (Fig. 3A), while there was no difference in animal body weight (body weight data not shown). Despite the decreased size in all FAK-KO tendons, stiffness was only decreased in PTs (Fig. 3B), and modulus was generally comparable and, in fact, superior in ATs (Fig. 3C). Failure properties of FAK-KO tendons demonstrated decreased maximum load in the AT and PT, while maximum stress was increased in the FDL (Fig. 3D-E). Viscoelastic stress relaxation was not different between groups (data not shown), though dynamic modulus was increased in all FAK-KO tendons relative to WT tendons at all frequencies evaluated (1Hz dynamic modulus data shown as representative in Fig. 3F).

Figure 2. *Ptk2* expression for ATs, FDLs, and PTs from WT and FAK-KO tendons. Data was analyzed with t-tests comparing groups. Bars represent sig. diff. between groups ($p < 0.05$).

DISCUSSION: Consistent with our hypothesis, inhibition of FAK activity in tendon cells significantly affected focal adhesion morphology and cell spreading behavior. Taken together with our previous results demonstrating attenuated ECM to nuclear strain transmission with reduced FAK activity,[4] these findings help explain FAK's regulatory role on tenogenic gene expression.[1–3] In our *in vivo* model, all tendons from FAK-KO mice were smaller, which is consistent with our hypothesis and indicates that FAK plays an essential role in tendon development. Interestingly, structural properties were not consistently reduced, and material properties were comparable or increased in FAK-KO tendons relative to WT tendons, potentially indicating changes in matrix assembly.

SIGNIFICANCE: Due to the mechanical role and mechano-responsiveness of tendons, defining the key transductive pathways that regulate cell and tissue properties will be critical to better understand disease and to develop improved therapies. Our results indicate that FAK-dependent tendon cell mechanotransduction may drive tissue assembly during growth and development.

REFERENCES: 1. Liu *et al.*, Stem Cells Int, 2018; 2. Xu *et al.*, J Cell Physiol, 2012; 3. Li *et al.*, J Orthop Res, 2019; 4. Leahy *et al.*, ORS Annual Meeting, 2022; 5. Beggs *et al.*, Neuron, 2003;
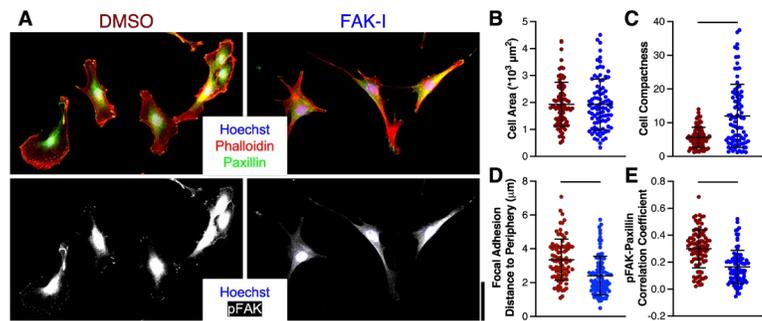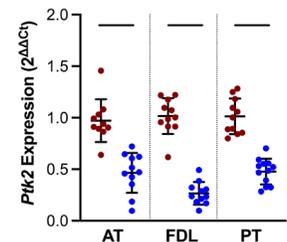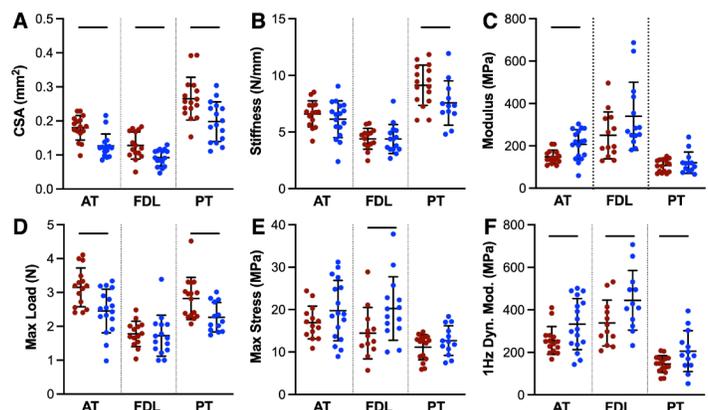
Figure 3. A) Cross-sectional area (CSA), B) stiffness, C) modulus, D) maximum load, E) maximum stress, and (F) 1Hz dynamic modulus measurements for WT and FAK-KO tendons. Data was analyzed with t-tests comparing groups. Bars represent sig. diff. between groups ($p < 0.05$).

Surgically repairing Achilles tendon ruptures restores plantar flexor function better than non-surgical treatment in a rat model

My M. Tang[1], Courtney A. Nuss[1], Natalie Fogarty[1], Josh R. Baxter[1]
[1] Department of Orthopaedic Surgery, University of Pennsylvania, Philadelphia, Pennsylvania, USA
Email of Presenting Author: mymy.tang@pennmedicine.upenn.edu

Disclosures: No conflicts of interest, financial or otherwise, are declared by the authors.

INTRODUCTION: Achilles tendon ruptures have increased by a factor of 10 in the past three decades, causing long-term functional deficits in nearly 2 out of 3 patients [1]. Despite the increasing demand for non-surgical treatment of acute Achilles tendon ruptures, rigorous preclinical studies that test the isolated effects of surgical and non-surgical treatment on plantar flexor functional deficits are lacking [2]. Previous studies have established mechanistic link between muscle-tendon structural changes and functional deficits but do not directly test the functional implications of surgical versus non-surgical treatment. Recent small animal experiments suggest that non-surgical treatment results in superior Achilles tendon biomechanics and healing, but none has been able to directly link muscle-tendon structural deficits with plantar flexor functional deficits to obtain measurements that are clinically translatable to patients. This study presents two competing objectives: 1) to develop a small animal joint dynamometer that quantifies joint functional deficits that can be directly translated to similar measurements made in patients and 2) to test the effects of surgical and non-surgical treatments for acute Achilles tendon ruptures using an established rat model.

METHODS: We surgically induced an acute Achilles tendon rupture in 18 adult male Sprague Dawley rats (weight: 439 +\- 46 g) and randomly assigned half of the animals to undergo a surgical repair while the rest to non-surgical treatment. Then, all animals completed 2-weeks of joint immobilization in plantarflexion followed by 2-weeks of unrestricted cage activity to stimulate the early habitation stages in patients. We quantified plantar flexor torque across the range of ankle motion in 20-degree increments from 60 degrees dorsiflexion to 60 degrees plantarflexion using a custom-developed small animal dynamometer with 15 seconds of rest over 3 sets of contractions. Hypothesis 1 compared plantar flexor work deficits between animals treated non-surgically and our prior report of patients treated non-surgically. Hypothesis 2 tested the effects of rupture and initial treatment (surgical vs. non-surgical) on plantar flexor function using one-tailed t-tests.

RESULTS SECTION: Rats that were non-surgically treated experienced a 35% deficit in plantar flexor work (**Figure 2**), which compares closely to our published data set of patients treated non-surgically that experienced a 38% deficit in plantar flexor work. Both non-surgically (30-51% deficits, p<.001) and surgically repaired (19-29%, p<.05) animals suffered plantar flexor deficits (**Figure 3**) based on our findings. However, rats that received non-surgical treatment had 11-35% greater functional deficits compared to surgically repaired animals (p<.01).

DISCUSSION: We found that our rat model closely mimics the plantar flexor deficits observed in patients. Using this clinically relevant functional assay, we then tested the effects of surgical and non-surgical treatment on plantar flexor function. Our study poses several limitations with the surgical incision used to transect the tendon resulting in increased inflammatory response compared to spontaneous Achilles tendon ruptures and with the open approach to repairs not directly resemble the typical treatment in patients. Despite this, our model closely mimics that of the natural human injury. This is seen in our findings, where it was found that surgically repairing the ruptured Achilles tendon mitigates functional deficits, particularly in plantarflexion, which is critical for preserving patient function.

SIGNIFICANCE/CLINICAL RELEVANCE: Our findings support surgically repairing acute Achilles tendon ruptures when restoring plantar flexor function is a clinical priority.

IMAGES AND TABLES:

Figure 1: Clinically translational ankle dynamometry.

Figure 2: Similar plantar flexor deficits found between rat (left) experiments and patient (right) observational study.

Figure 3: Reduced plantar flexor torque across the ankle range of motion in animals in repaired and non-repaired groups with non-surgical treatment group experiencing 11-35% greater functional deficits compared to surgically repaired animals.

REFERENCES: [1] Lantto+, *Scand JMed Sci Sports,* 2015; [2]Huttunen+. *Am J Sports Med*, 2014

Molecular Augmentation of the Microniche of Human Osteoarthritic Chondrocytes by Biomimetic Proteoglycans

Elizabeth R. Kahle[1], Colette E. Trouillot[1], X. Lucas Lu[2], Michele S. Marcolongo[3], Lin Han[1]

[1]Drexel University, Philadelphia, PA; [2]Univeristy of Delaware, Newark, DE; [3]Villanova University, Villanova, PA.

Disclosures: None.

INTRODUCTION: In articular cartilage, chondrocytes are surrounded by the 2-4 μm thick, structurally distinctive pericellular matrix (PCM). The PCM plays crucial roles in mediating the biophysical and biological signals between chondrocytes and the extracellular matrix (ECM) [1]. In osteoarthritis (OA), degeneration of the PCM is one leading event of disease initiation, contributing to disrupted chondrocyte mechanotransduction and downstream deleterious metabolic changes, and as a result, the irreversible breakdown of cartilage [2]. Molecular engineering of the PCM integrity and mechanobiological functions thus holds the potential for modulating chondrocyte mechanosensitive activities and attenuating disease progression during degeneration [1]. Recently, our group has synthesized a suite of biomimetic proteoglycans (BPGs), which are composed of natural chondroitin sulfate bristles (CS) and a poly(acrylic acid) (PAA) backbone. These molecules mimic the nano-architecture and water uptake of native proteoglycans [3]. We have demonstrated that BPG10, a ~170 kDa mimic with ~7-8 CS bristles attached onto a 10 kDa PAA core (Fig. 1a), can passively diffuse through all zones of bovine cartilage *in vivo* and *ex vivo*, preferentially localize in the PCM and territorial-ECM (T-ECM), and effect the local mechanical and mechanobiological status of the PCM through adhesive interactions with native matrix molecules, such as aggrecan [4-6]. To conceptualize the clinical relevance of BPG10 as a potential therapeutic agent for OA, this study aimed to determine the localization and mechanical effects of BPG10 on *ex vivo*, early OA cartilage from human donors. In the present study, we demonstrate the ability to use BPG10 to modulate, to varying degrees, the micromechanical properties of both the PCM and nearby territorial matrix (T-ECM) of mildly degenerated cartilage.

METHODS: *Sample preparation.* BPG10 was synthesized and fluorescently labeled as previously described [7]. Four-mm-thick, cylindrical femoral cartilage plugs were harvested from $n = 4$ Collins Grade 0-1 arthritic donors (IRB #1503003490) and incubated in 1× PBS with or without 10 mg/mL fluorescently tagged BPG10 for 24 hrs. *Histology and immunofluorescence (IF) imaging.* Samples were fixed, paraffin-embedded, sagittally sectioned (6 μm), and stained for either collagen VI antibody (col VI, Fitzgerald 70R-CR009x) to identify the PCM (Fig. 1a) or Safranin-O/Fast Green (Saf-O/FG) to determine gross-level morphological changes among donor specimens (Fig. 1b). Loss of sulfated glycosaminoglycan (sGAG) ($t_{sGAG\ loss}$) was assessed by measuring the thickness of cartilage regions devoid of sGAGs on cartilage surface ($n \geq 60$ measurements from each donor). *IF-guided AFM.* Following diffusion of BPG10, unfixed cartilage plugs were sectioned into ~ 8 μm-thick sagittal sections in OCT via Kawamoto's film-assisted cryo-sectioning [8]. Using col VI-guided AFM nanomechanical mapping, we quantified the micromodulus, E_{ind}, of the PCM and T-ECM using a microspherical tip ($R \approx 2.25$ μm, $k \approx 0.6$ N/m) and an MFP-3D AFM (Asylum Research) (Fig. 2) [4]. *Statistics.* Data from each donor were pooled per experimental condition (control v. BPG10-treated) for the PCM or T-ECM and analyzed via paired t-test with the Holm-Bonferroni correction at the significance level of $\alpha = 0.05$.

RESULTS: When infiltrated into degenerative human cartilage, BPG10 was found to be concentrated in the PCM and nearby T-ECM domains, as illustrated by the co-localization of BPG10 and collagen VI, a biomarker of PCM [9](Fig. 1a). This co-localization was pronounced in donor tissue 16L and 4R, while a more overall diffuse signal was observed in donors 12R and 11R (Fig. 1a). Saf-O/FG histology indicated a reduction in sGAG staining (t_{sGAG}) in the superficial zones of all tissues, with more severe degeneration indicated in donors 11R and 12R (105 ± 16 μm and 84 ± 25 μm, respectively, mean ± std) and milder degeneration in 16L and 4R (45 ± 10 μm and 62 ± 12 μm, respectively, mean ± std, Fig. 1b). Localization of BPG10 in the PCM of OA cartilage resulted in an increase in E_{ind} of the PCM of donors 16L, 11R, 12R, and 4R by 109%, 140%, 58%, and 32%, respectively (mean percent increase, Fig. 2b). In addition, T-ECM also exhibited a moderate increase in the micromodulus of donors 16L, 11R, 12R, and 4R by 52%, 64%, 39%, and 32%, respectively (mean percent increase, Fig. 2b). When E_{ind} was pooled across donors, BPG10 was able to significantly increase the modulus of both the PCM ($p = 0.024$) and T-ECM ($p = 0.005$) of OA cartilage despite the range in levels of degeneration as well as heterogeneity of BPG10 distribution present in each donor.

DISCUSSION: This study demonstrates the use of biomimetic proteoglycans as a novel molecular therapy to engineer degenerative human PCM (Fig. 2b) through its preferred localization within the PCM (Fig. 1a). The micromechanics of the PCM is an early casualty of post-traumatic OA (PTOA) initiation due to aggravated enzymatic degradation of native matrix molecules, such as aggrecan, in this region [2, 10]. As the highly negatively charged microenvironment of the PCM is essential for maintaining normal chondrocyte mechanotransduction [11], the impairment of PCM leads to disruption of chondrocyte mechanosensitive activities, as evidenced by the significantly altered $[Ca^{2+}]_i$ signaling in murine PT-OA cartilage [2]. When localized in the PCM of healthy cartilage, BPG10 not only directly increases the negative fixed charge density (through the highly negatively charged CS bristles), but provides additional physical linkages with existing matrix molecules (such as aggrecan), thereby strengthening the integrity of the already partially degraded PCM [4]. Our results on human OA cartilage further showed that even in the partially degraded environments, in which loss of proteoglycans is evident by Saf-O/FG histology (t_{sGAG}), BPG10 retains its capability of localizing within the PCM and augmenting the local micromechanics of PCM (Figs. 1,2). Thus, our results provide direct molecular and biomechanical evidence that BPG10 can molecularly engineer the chondrocyte's immediate cellular micro-niche not only in intact cartilage, but also in those with a range of matrix degradation in early OA, and thus, has the potential to serve as a minimally invasive molecular therapy candidate to slow or prevent OA progression by restoring the immediate micromechanical niche of chondrocytes.

SIGNIFICANCE: This study demonstrates that biomimetic proteoglycans (BPGs) can be used to mechanically bolster the pericellular microniche of mildly degraded cartilage from human OA donors, indicating its clinical potential as a molecular therapy candidate for early osteoarthritis treatment.

References: [1] Guilak+ 2018. [2] Chery+ 2020. [3] Prudnikova+ 2019. [4] Kahle+ 2022. [5] Phillips+ 2019a. [6] Phillips+ 2019b. [7] Prudnikova+ 2018. [8] Kawamoto+ 2014. [9] Poole+ 1988. [10] Chambers+ 2001. [11] Guilak+ 2006.
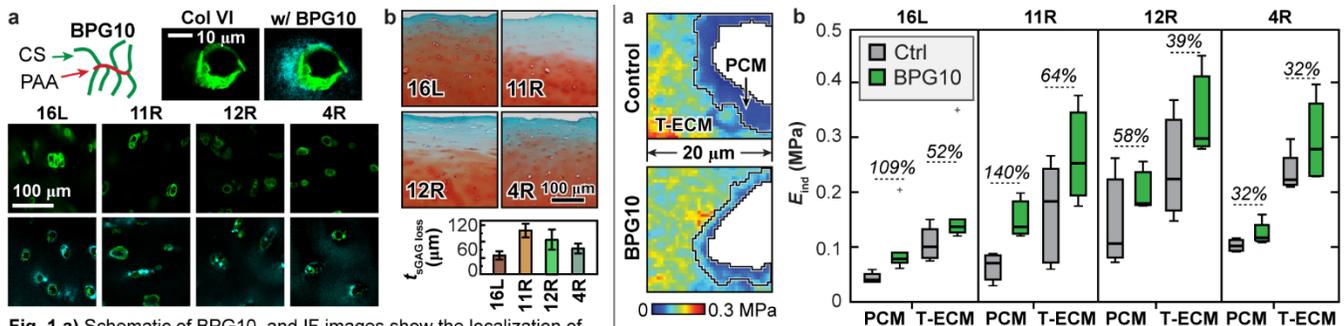
Fig. 1 a) Schematic of BPG10, and IF images show the localization of BPG10 in the PCM (denoted by collagen VI signal) of human OA cartilage from Collins Grade 0-1 ($n = 4$ donors: 16L, 11R, 12R, 4R) with some diffusive presence of BPG10 in the territorial ECM (T-ECM). b) Saf-O/FG histology shows varying degress of sGAG loss on cartilage surface ($t_{sGAG\ loss}$) (mean ± std from ≥ 60 measurments per donor).

Fig. 2 a) Representative modulus maps from control and BPG10-diffused (BPG10) femoral human cartilage plugs. b) IF-AFM reveals mechanical reinforcement of PCM and T-ECM in early-OA human cartilage from all donor tissues by the infiltration of BPG10 ($n \geq 500$ moduli points for each box and whisker plot with mean of percent increase in modulus for each donor).

Intervertebral Disc and Facet Crosstalk in a Rabbit Puncture Model of Disc Degeneration

Brianna S. Orozco[1,2], Matthew Fainor[1,2], Victoria Muir[1], Sonal Mahindroo[2,3], Sachin Gupta[1,2], Jason Burdick[4], Robert L. Mauck[1,2], Harvey E. Smith[1,2], Sarah E. Gullbrand[1,2]

[1]University of Pennsylvania, Philadelphia, PA; [2]Corporal Michael J. Crescenz VA Medical Center, Philadelphia, PA; [3]Bonaventure University, St. Bonaventure, NY [4]University of Colorado – Boulder, Boulder, CO

INTRODUCTION: 28.5% of adult Americans suffer from lower back pain[1], which is frequently associated with degeneration of both the intervertebral discs and the adjacent diarthrodial facet joints. These structures form what is referred to as the three-joint complex of the spine, working in concert to resist large magnitude axial loads and constrain range of motion to non-injurious levels[2]. Despite the inherent mechanical linkage between these spinal structures, crosstalk between the disc and facets during degeneration remains severely understudied. Our previous work has established that needle puncture of the lumbar intervertebral disc in rabbits compromises disc mechanical function and leads to progressive disc degeneration[3]. In this study, we seek to uncover how altered disc mechanics associated with varying severities of disc injury can elicit degenerative changes in the adjacent facet joints.

METHODS: Following IACUC approval, eight New Zealand White male rabbits (~3 kg, ~3 months of age) underwent surgery to puncture the lumbar intervertebral discs. For three rabbits, two levels between L23 and L67 were punctured with a 16G needle, and animals were euthanized at 4 weeks[3]. In the five remaining rabbits, four levels between L23 and L67 were punctured, two using a 16G needle and two using a 21G needle, with animals euthanized at 10 weeks. Following euthanasia, motion segments were dissected into discs and adjacent facets. Healthy control motion segments (n=6) were obtained from animals that did not undergo spinal surgery. Additional healthy rabbit spinal motion segments were punctured *ex vivo* with either a 16G or 21G needle to assess the acute effects of needle puncture on disc mechanics (n=6 per needle gauge). All discs (n=3-5 experimental, n=6 control) underwent tension-compression and creep mechanical testing, as previously described[3], and were scanned in a μCT to evaluate osteophyte volume. The adjacent paired facet articular surfaces at each level were subject to creep indentation testing to determine articular cartilage mechanical properties[4]. Both discs and facets were processed for paraffin histology and stained with Safranin-O/Fast Green. All disc and facet histology were scored using a 3-scorer consensus system according to the OARSI scoring system for rabbit cartilage[6] and the ORS Spine Section/JOR Spine intervertebral disc scoring system[7], respectively. All data was analyzed using an ANOVA with a Tukey's post-hoc test or a Kruskal-Wallis post-hoc test.
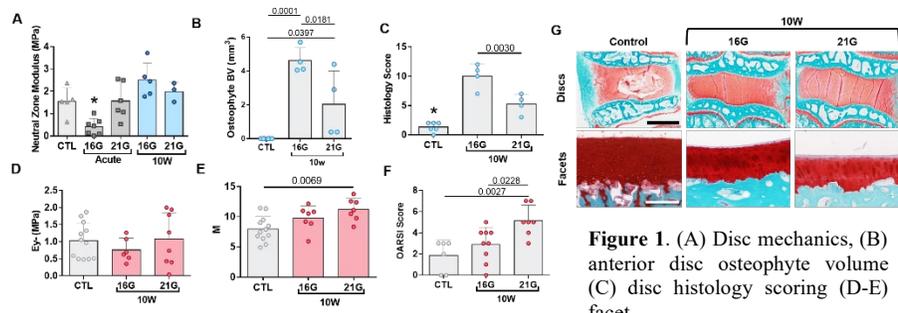

Figure 1. (A) Disc mechanics, (B) anterior disc osteophyte volume (C) disc histology scoring (D-E) facet cartilage mechanics, (F) facet histology scoring, and (G) representative Safranin-O/Fast Green histology (disc scale bar = 2 mm, facet scale bar = 200 μm). * = p<0.5 compared to all groups.
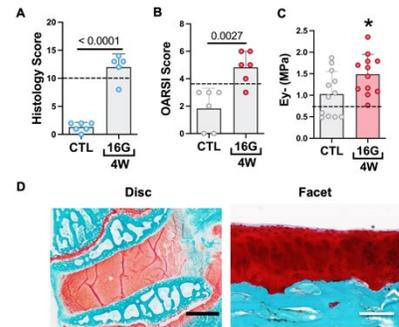
RESULTS: Biomechanical testing of vertebral body-disc-vertebral body segments demonstrated that as time progressed *in vivo*, disc range of motion decreased, accompanied by increase in neutral zone modulus (**Figure 1A**). Anterior osteophyte formation was higher in the 16G group compared to the control 21G group (**Figure 1B**). Disc degeneration was most severe in 16G puncture group at 10-week time point, evident by significant increase in histologic score compared to controls and the 21G group (**Figure 1C, G**). While no significant differences in facet cartilage compressive modulus were observed at 10 weeks, there was an increase in M, nonlinear strain-dependent flow-limited constant, in 21G facet group compared to controls (**Figure 1D-E**). Unexpectedly, facet degeneration was most severe in 21G puncture group at 10-week time point, as evidenced by OARSI scoring (**Figure 1F**). Next, we examined an earlier timepoint for the 16G puncture group to ascertain if more severe facet degeneration was evident earlier in time course of disc degeneration. At 4 weeks, discs were significantly degenerative compared to controls (**Figure 2A, D**), as were the adjacent facets (**Figure 2B, D**), as evidenced by histologic scoring. Facet cartilage compressive modulus was significantly higher at 4 weeks compared to 10-weeks (**Figure 2C**).

Figure 2. (A) Histology Score, (B) OARSI Score, (C) Compressive Modulus, and (D) representative Safranin-O/Fast Green histology (scale bar = 2 mm, scale bar = 200 μm). * = p<0.5 16G 4W group comparison to controls and 16G 10W. Dashed line =

DISCUSSION: Our results demonstrate that acute disc injury compromises disc mechanical function, leading to degeneration of the disc, the severity of which is dependent on needle diameter. Disc degeneration was accompanied by early-stage degenerative changes in the adjacent facet joints, which were primarily driven by altered disc mechanical function. 16G punctured discs rapidly degenerated and progressively stiffened over time *in vivo*, due to the development of large anterior osteophytes[3]. The partial recovery of the facet cartilage health observed from 4 to 10 weeks may have been due to off-loading in the facet joints, concurrent with prior studies of off-loading in the knee joint[7]. Osteophyte formation was less severe in 21G needle puncture discs. These discs exhibited milder degenerative changes than 16G puncture discs, creating a mechanical environment where aberrant loading across the motion segment was likely sustained over a longer period. This may explain why the facets in the 21G disc puncture group were among the most degenerative samples. Overall, our work suggests that altered disc mechanics can induce facet degeneration, but further work is needed to define the time course of facet osteoarthritis following alterations in disc mechanics.

SIGNIFICANCE: This work links our knowledge of disc degeneration with facet osteoarthritis, allowing for a better understanding of the progression of whole motion segment degeneration, which can aid in informing the development and evaluation of novel regenerative strategies.

REFERENCES: [1] USBJI *BMD,* 2020. [2] Yong-Hing+*Orthopaedic Clinics of North America*, 1983 [3]Ashinsky+ *Osteoarthritis and Cartilage*, 2019. [4] Meloni+ *Tissue Engineering Part A*, 2017 [5] Laverty+ *Osteothritis and Cartilage*, 2010. [6] Gullbrand+ *JOR Spine*, 2021. [7] Karamchedu+ *American Journal of Sports Medicine*, 2021

Determining Region-Specific Mechanical and Structural Differences in Aging Mouse Supraspinatus Tendons

Michael S. DiStefano[1], Biao Han[1], Patrick L. Paglia-Garcés[1], Stephanie N. Weiss[1], Snehal S. Shetye[1], Andrew F. Kuntz[1], Louis J. Soslowsky[1]

[1]McKay Orthopaedic Research Laboratory, University of Pennsylvania, PA

micdis@seas.upenn.edu

INTRODUCTION: Damage, degeneration, and injury occur disproportionately in regions of high and complex stress, such as at the insertion site of the supraspinatus tendon of the shoulder, particularly in the aging population[1]. Recent studies in aged patellar tendons demonstrated an inferior response to load, reduced elastic and viscoelastic mechanical properties, and altered fibril structure[2]. However, despite its complex loading, region-specific mechanical and structural differences in aging mouse supraspinatus tendon remain unknown. Therefore, the objective of this study was to elucidate region-dependent mechanical and structural differences in mouse supraspinatus tendon with aging. We hypothesized that aging would result in region-specific mechanical and structural changes, such as inferior elastic and viscoelastic mechanical properties and altered collagen fibril morphology, with larger alterations expected at the insertion site due to the increased complexity and functional demands[3] in this region.

METHODS: <u>Animals:</u> Forelimbs were collected from male wildtype mice sacrificed at either 300 (P300, n=20) or 570 (P570, n=20) days of age, respectively (IACUC approved). <u>Mechanics:</u> Mice for mechanical testing were frozen at -20°C until test day. Mice were thawed and the supraspinatus tendon-humerus complex from the left limb of each mouse was dissected clean. Stain lines were applied for optical strain tracking of the insertion and midsubstance regions and a laser device was used to measure cross-sectional area. The myotendinous junction was placed between two sandpaper tabs with cyanoacrylate. The humerus was secured in polymethyl methacrylate and the construct was mounted on a material testing machine (Instron 5848). Testing was conducted in a phosphate buffered saline bath at 37°C. Each sample was preloaded to 0.025N. The testing protocol consisted of 10 cycles of preconditioning, followed by stress relaxations at 3%, 5%, and 7% strain. Following each stress relaxation, frequency sweeps of 10 cycles at 0.1, 1, 5, and 10 Hz were performed. Following a 10-minute rest, a quasistatic ramp-to-failure was completed. Viscoelastic parameters dynamic modulus (E*), phase shift (tan δ), and percent relaxation were quantified for each stress relaxation and frequency sweep. Elastic parameters stiffness and modulus were also calculated. <u>Transmission Electron Microscopy (TEM):</u> Supraspinatus tendons (n=8/age group) were isolated, fixed, and embedded in epon resin blocks. 85nm sections were cut using an ultramicrotome, stained with uranyless and phosphotungstic acid, and imaged at 60,000x using a transmission electronic microscope (JEOL 1010). Fibril diameter frequency distribution and fibril density were quantified. <u>Statistics:</u> Elastic properties were compared using two-way ANOVAs across age and region followed by Bonferroni post-hoc tests. Viscoelastic properties were compared using two-way ANOVAs across age and strain levels followed by Bonferroni post-hoc tests. Fibril diameter distributions were compared using Kolmogorov-Smirnov tests.

RESULTS: <u>Region-Dependent Elastic Mechanics (Fig. 1A-C):</u> As expected, all samples failed at their insertion sites. Cross-sectional area was greater in the insertion region than in the midsubstance in both ages. Stiffness and modulus were lower for the insertion region than the midsubstance in the P300 and P570 groups. Midsubstance modulus had an interaction and decreased with age. <u>Viscoelastic Mechanics (Fig. 1D-F):</u> Although there were no interactions between viscoelastic properties and age, the viscoelastic response was preserved with aging across strain levels. Specifically, dynamic modulus was greater at 5 and 7% strain relative to 3% strain with aging. Additionally, percent relaxation and phase shift were not altered across strain levels with aging. <u>Fibril Morphology (Fig. 2):</u> Consistent with previous studies[4], fibril size distributions were different across region and age with smaller diameter fibrils at the insertion compared to the midsubstance within each age group. Moreover, insertion region fibrils had narrower distributions compared to the midsubstance fibrils whereas midsubstance fibrils demonstrated typical bimodal distributions for both age groups. Interestingly, aging resulted in a shift towards smaller diameter fibrils in the midsubstance region.

DISCUSSION: This study investigated the regionally dependent mechanical and structural differences in aging mouse supraspinatus tendons. Supporting our hypothesis, detrimental mechanical and structural changes were observed at the insertion of supraspinatus tendons. Insertion region elastic mechanical properties were less than those at the midsubstance. Additionally, insertion region fibril size distributions shifted towards smaller fibril diameters. Previous studies in superficial digital flexor tendons demonstrated that mechanical properties and fibril diameter distributions can differ from the bone-tendon junction to the myotendinous junction[5]. Multiscale regression analyses have shown that the one of the strongest predictors of structure-function relationships at the insertion and midsubstance regions were mediators[6] of the relationship between fibril diameter and mechanical properties[6]. Contrary to our hypothesis, aging did not have a large influence on regional and whole tendon elastic and viscoelastic mechanical properties but did influence fibril morphology. Our results also agree with previous studies relating mechanical function to fibril morphology. Specifically, with increased loading, smaller diameter fibrils were not able to withstand the same loading and likely suffered early damage, resulting in inferior mechanical properties[3]. Our results support these previous findings and may further explain why supraspinatus tears predominantly occur at the tendon's insertion on the humeral head[7]. Future studies will build on these results by elucidating additional region-specific multiscale structural, functional, and compositional mechanisms in aging supraspinatus tendons.

SIGNIFICANCE: This study demonstrates critical region-specific mechanical and structural differences in aging mouse supraspinatus tendons.

REFERENCES: 1. Buckwalter et al., J Bone Joint Surgery, 2003. 2. Dunkman et al., Matrix Biol, 2013. 3. Connizzo et al., Interface Focus, 2016. 4. Connizzo et al., J Orthop Res, 2016. 5. Watanabe et al., Connect Tissue Res, 2007. 6. Connizzo et al., J Biomech Eng, 2016. 7. Bell et al., J Orthop Res, 2015.
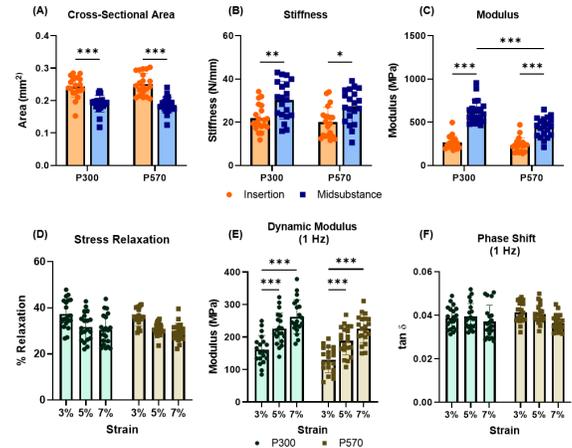
Figure 1. Elastic and viscoelastic mechanical properties. Insertion regions exhibited significantly greater (A) cross-sectional area while midsubstance regions had significantly greater (B) stiffness and (C) elastic modulus for both age groups. Elastic modulus was (C) significantly reduced with aging. Viscoelastic properties were conserved with aging with no differences across strain level in (D) stress relaxation and (F) phase shift and similar significant differences across strain levels in (E) dynamic modulus in both age groups. Data as mean ± standard deviation (*p≤0.05, **p≤0.01, ***p≤0.001)
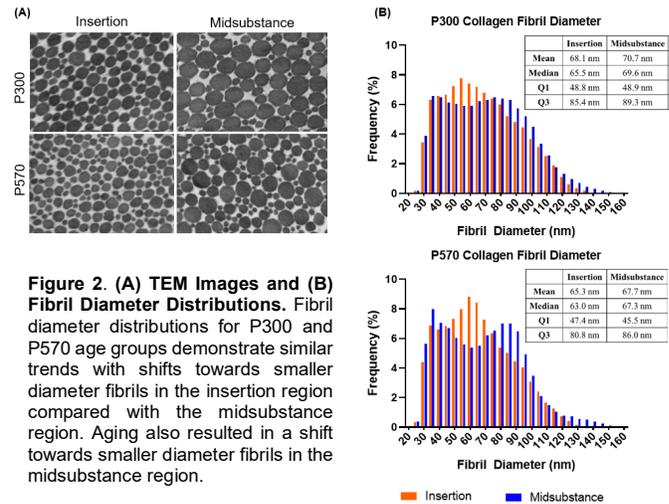

Figure 2. (A) TEM Images and (B) Fibril Diameter Distributions. Fibril diameter distributions for P300 and P570 age groups demonstrate similar trends with shifts towards smaller diameter fibrils in the insertion region compared with the midsubstance region. Aging also resulted in a shift towards smaller diameter fibrils in the midsubstance region.

Investigating the Influence of Osteocyte Lacunar Morphology and Perilacunar Tissue Properties on Local Mechanical Environment of Lacunae Using Finite Element Modeling

Wen Sang[1], Ani Ural[1]

[1]Department of Mechanical Engineering, Villanova University, 800 Lancaster Avenue, Villanova, PA

ABSTRACT

Osteocyte lacunar morphology and perilacunar tissue properties are modified by physiological and pathological processes such as aging, diseases, treatments, and lactation. These modifications can influence osteocyte mechanosensitivity and the remodeling process as they may alter the mechanical environment around lacunae. However, changes in local mechanical environment cannot be easily measured experimentally. Therefore, the goal of this study is to evaluate how the modifications in lacunar morphology and the perilacunar tissue properties influence the local deformation around lacunae using finite element (FE) modeling.

This study developed a new approach to generate 3D FE models of lacunar networks under tensile loading based on experimental data from the literature (Fig. 1a). Five FE model groups were created that evaluated the influence of osteocyte lacunar density (Lc.D), volume (Lc.V), and orientation (Lc.Φ), as well as perilacunar modulus (Pl.E), and perilacunar size (Pl.S) on the deformation of the local bone matrix. In each group, one of the properties was varied while the others remained constant. The amount of highly strained elements (1.5 times the applied strain) was evaluated for all models to assess the local deformation around lacunae.

The simulation results showed annular strain concentration regions around lacunae (Fig. 1b). The highly strained regions around lacunae (E.Vol) (i) increased linearly and doubled as Lc.D was doubled (Fig. 1c), (ii) increased linearly by four times as the Lc.V was doubled (Fig. 1d), (iii) increased exponentially as the orientation of the long axis of the lacunae deviated away from the loading direction (Fig. 1e), (iv) increased exponentially by about four times with a 25% reduction in Pl.E to 15 GPa compared to the bulk elastic modulus (20 GPa) (Fig. 1f); and (v) increased only by ~13.8% as Pl.S increased from 2 μm to 7 μm.

In summary, the simulation results showed that modifications in the osteocyte lacunar morphology and perilacunar tissue properties can significantly alter local tissue deformation around lacunae which may impact osteocyte mechanosensitivity. The modeling approach presented here can be used to gain a better understanding of how mechanosensitivity of osteocytes are influenced by physiological and pathological processes that alter osteocyte lacunar morphology and perilacunar tissue properties.
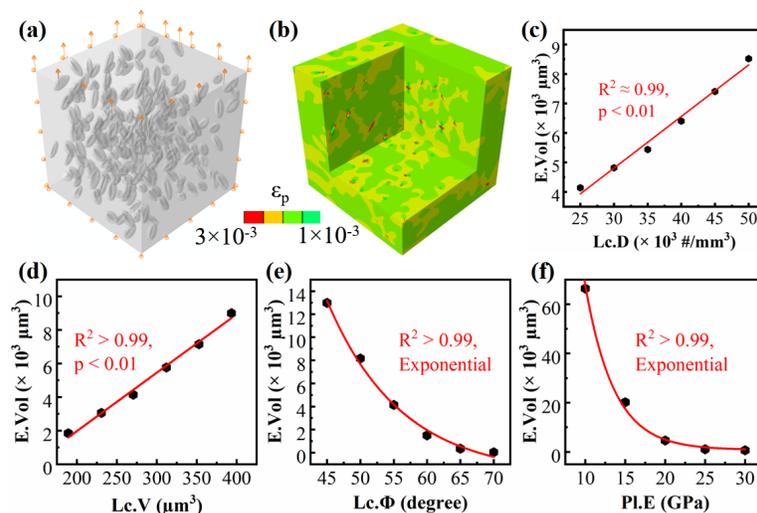
Figure 1: **(a)** A sample 3D FE model of osteocyte lacunar network. **(b)** Representative strain distribution in the models. Variation in highly strained elements with **(c)** lacunar density, **(d)** lacunar volume (Lc.V), **(e)** lacunar orientation (Lc.Φ), and **(f)** perilacunar modulus (Pl.E).

Mechanoactive Anti-Inflammatory Drug Delivery to Meniscus Defects

Lemmon EA[1,2,3], Locke RC[1, 2,3], Stoeckl BD[1, 2,3], Jenk AC[1,2,3], Hast MW[1, 3], Mauck RL[1,2,3]

Departments of [1]Orthopaedic Surgery and [2]Bioengineering, University of Pennsylvania, Philadelphia, PA, [3]Translational Musculoskeletal Research Center, Philadelphia VA Medical Center, Philadelphia, PA

elemmon@vet.upenn.edu

Disclosures: EAL (None), RCL (None), BDS (None), ACJ (None), MWH (None), RLM (4, 5, 8)

Introduction: The meniscus, a crucial load-bearing structure in the knee, is commonly injured and heals poorly after surgical intervention. A contributing factor to this poor healing may be the presence of inflammatory cytokines in the wound environment.[1] In vitro studies have shown that these cytokines inhibit migration of meniscus fibrochondrocytes (MFCs) and prevent tissue repair.[2,3] Notably, IL1β receptor antagonist (IL-1Ra) can block the negative effects of IL1β in meniscus tissue explants in vitro by promoting tissue integration.[4] Despite these promising results, application of such factors at therapeutically relevant levels to meniscus injuries in a localized and sustained manner remains a challenge. To address this need, we developed a hybrid meniscus tear augmentation strategy that incorporates a clinically approved fibrin tissue adhesive and IL-1Ra-loaded mechanoactive microcapsules (MAMCs).[5] We queried whether the clinical formulation of IL-1Ra (Anakinra) delivered from MAMCs could rescue MFC migration following IL1β exposure and whether orthotopic delivery in fibrin would enable progressive release in the context of a longitudinal vertical meniscus tear subjected to physiologic loading.

Methods: <u>MAMC Fabrication:</u> Thick-shelled (thickness: 2.49+/-0.05um diameter: 33.56+/-0.88um) MAMCs were fabricated as previously described containing either IL-1Ra or bovine serum albumin (BSA-MAMCs).[5] <u>2D Migration Assay:</u> Confluent MFC monolayers were treated with 10 ng/ml of IL1β for 24 hrs. At day 1 (48 hrs), bMFCS were treated with 100 ng/ml soluble IL-1Ra or ~100ng/ml IL-1Ra derived from the supernatant of MAMCs after mechano-activation using a pestle **(Fig 1A)**.[5] Monolayers were scratched at this time with a 200uL pipet tip. At 8 hrs post-scratch, images were obtained (Nikon), and % closure was calculated (ImageJ). Results from MAMC anti-inflammatory delivery were compared to MFCs treated with soluble IL-1Ra, intact MAMCs added to the media, and untreated controls. <u>Fibrin-MAMC Mechanical Characterization:</u> BSA MAMCs (25 μL, ~2,000) were suspended in 75 μL of fibrin adhesive (Tisseel™) and cross-linked into cylindrical plugs for 5 minutes. Cylindrical plugs were either cross-linked alone or between meniscus tissue segments. Next, constructs were uniaxially compressed at a strain rate of 0.5%/sec to a defined load (0, 3, 10, or 45N) and imaged for % full **(Fig 2C)**. <u>Fibrin-MAMC Culture:</u> Fibrin MAMC constructs were incubated at 37ºC for up to 14 days, and % full was determined on days 0, 7, and 14. <u>In Situ Mechano-Activation:</u> ~10mm longitudinal meniscus tears were created in the avascular inner zone of the medial meniscus in cadaveric porcine knees. Defects were filled with ~10,000 BSA-MAMCs suspended in 200μL of fibrin adhesive. The BSA-MAMC containing adhesive was allowed to crosslink for 5 minutes prior to closure of the tear with a vertical suture. A universal test frame (TA Instruments) was used to apply 10-400N for either 100 or 1800 cycles at 1Hz **(Fig 3A-B)**.[6] Joints were dissected and tears imaged to calculate % full BSA-MAMCs (n>100) **(Fig 3C-E)**. <u>Statistical</u> <u>Analyses:</u> For migration studies, 1-way ANOVA was used. For all other assays, 2-way ANOVA with repeated measures and Sidak's correction was used.

Results: MFCs exposed IL-1β showed a decrease in migration **(Fig 1B)**. Addition of soluble IL-1Ra restored migration and % wound closure to control levels, as did the supernatant of activated IL-1Ra-loaded MAMCs **(Fig 1B)**. When combined with fibrin adhesive, incubated BSA-MAMCs showed a significant decrease in % full on day 7, compared to day 0, with no further loss through day 14 **(Fig 2B)**. Under uniaxial compression, BSA-MAMCs showed a load dependent rupture profile, and meniscus tissue segments moderately protected BSA-MAMCs from rupture with increased load. **(Fig 2C-D)**. With in situ testing, fibrin+BSA-MAMCs placed in meniscus tears **(Fig 3A-B)** remained in place and showed progressive rupture with increasing cycle number **(Fig 3C-E)**.

Discussion: Our findings show that the migration deficits in IL1β-treated MFCs can be rescued by treatment with IL-1Ra at the time of challenge (scratch). Treatment with IL-1Ra derived from ruptured MAMCs had comparable efficacy in rescuing migration (vs. soluble IL-1Ra), supporting the idea that therapeutics encapsulated in MAMCs retain biologic activity. When suspended in fibrin, BSA-MAMC % full remained consistent between one and two weeks suggesting that this material may be a useful drug carrier for local delivery with extended release in the long-term. When mechanically loaded (both in direct compression and in situ under physiologic models), BSA-MAMCs progressively released their contents as loading and/or cycles increased. These data indicate that BSA-MAMCs can be mechanically activated when encapsulated within tissue adhesive hydrogels and delivered within meniscus tears under physiologic loading. Future work will further characterize the mechanoactivation and degradation of drug-loaded MAMCs in large animal meniscus repair models.

Significance/Clinical Relevance: We developed a novel drug delivery system and evaluated its potential for meniscus repair using a clinically translatable fibrin gel as a carrier material. Our findings show that loaded MAMCS can deliver anti-inflammatory drugs and rescue migratory capacity of MFCs in vitro. Combined with fibrin gel, loaded MAMCs can be localized in a meniscus defect where they mechano-activate with increasing load. This system has the potential to improve clinical treatment by delivering multiple, mechanoactivated biologics directly to the repair site to improve outcomes for otherwise irreparable meniscus tears.

References: 1. Fernandes+ *Biorheol,* 2002; 2. Riera+ *Arthr Res Ther,* 2011; 3. Wilusz+ *JOR,* 2008; 4. McNulty+ *Arthritis Rheumatol*, 2007; 5. Peredo+ *Biomaterials*, 2021; 6. Bansal+ *Orthop. J. Sports Med*, 2021.
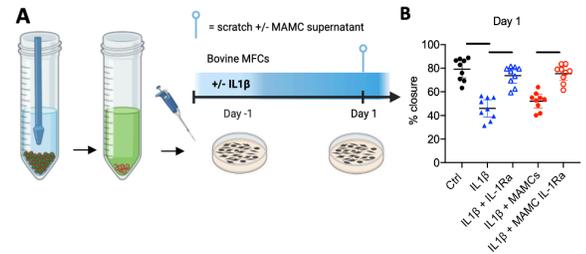
Fig 1. (A) Schema of IL-1Ra-loaded MAMC supernatant treatment following IL1β treatment and scratch., (B) % scratch closure at 8 hrs post-scratch for each treatment group (see Methods). Mean +/- SD, n=9/group, bars indicates difference between groups.
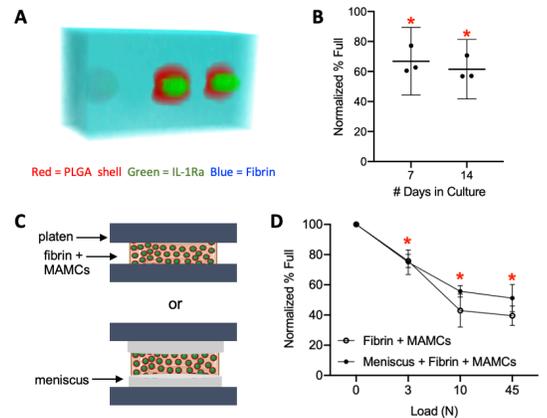

Fig 2. (A) 3D rendering of loaded MAMCs cross-linked in fibrin adhesive. (B) % full BSA-MAMCs incubated at 37C in fibrin over 14 days. (C) Uniaxial compression schema (D) % full BSA-MAMCs at 0, 3, 10, and 45N load. Mean +/- SD, n=3/group, asterisk indicates difference vs. day 0 (B) or 0N group (D).
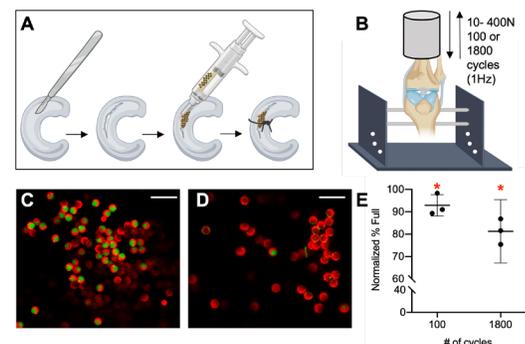

Fig 3. (A) Schematic of vertical tear with fibrin+MAMC delivery and (B) in situ loading rig. Fibrin+MAMC images after loading for (C) 100 and (D) 1800 cycles of 10-400N compressive loading @ 1Hz). (E) % full MAMCs after 100 and 1800 cycles of loading. Mean +/- SD, n=3/group, asterisk indicates difference vs. 0 cycles of loading. Scale bar 100 μm.

Toll-Like Receptor 4 Signaling In Osteoblasts Is Required For Load-Induced Bone Formation

Ibtesam Rajpar[1], Gaurav Kumar[2], Paolo M. Fortina[2], Ryan E. Tomlinson[1,3]

[1] Department of Orthopaedic Surgery, Thomas Jefferson University, Philadelphia, PA
[2] Department of Cancer Biology, Thomas Jefferson University, Philadelphia, PA
[3] Department of Oral and Maxillofacial Surgery, Thomas Jefferson University, Philadelphia, PA

During skeletal development, expression of the neurotrophin nerve growth factor (NGF) leads to the establishment and survival of afferent sensory nerves that express neurotrophic tyrosine kinase receptor type 1 (TrkA), the high affinity receptor for NGF. In adulthood, NGF is expressed by mature osteoblasts following mechanical loading and signals through TrkA receptors in resident sensory nerves to support load-induced bone formation. However, the regulation of NGF in osteoblasts following loading is not well understood. In this study, we sought to determine whether osteoblastic expression of toll-like receptor 4 (TLR4), a key receptor in the NF-κB signaling pathway, is required to initiate NGF-TrkA signaling to support skeletal adaptation following mechanical loading. Specifically, we hypothesized that the loss of TLR4 signaling in bone would result in diminished load-induced bone formation due to decreased NGF expression in osteoblasts following loading. First, we show that NF-κB inhibition reduces NGF expression following axial forelimb compression. Similarly, TLR4+ periosteal cells are increased after mechanical loading. Next, we generated a novel mouse model (CKO) in which *Tlr4* was selectively removed in the mature osteoblast lineage. Although CKO mice have normal skeletal mass and strength in adulthood, the loss of osteoblastic *Tlr4* expression results in significant reductions in periosteal lamellar bone formation following axial forelimb compression. Furthermore, we demonstrate that the upregulation of *Ngf* following application of fluid shear stress to calvarial osteoblasts is significantly reduced by NF-κB and TLR4 inhibitors. Finally, RNA sequencing demonstrated that the deficits in load-induced bone formation in CKO mice can be attributed to dysregulated inflammatory signaling. In total, our study reveals a novel role for TLR4 in skeletal adaptation to mechanical loading in bone, which may enable new therapeutic strategies for diseases of low bone mass and provide new targets for musculoskeletal pain relief.

Naproxen decreases bone toughness in a COX2-independent manner, reduces osteocyte dendrite number, and impairs perilacunar canalicular remodeling

Alexandra Ciuciu[1], Ryan E. Tomlinson,PhD[1]

[1]Thomas Jefferson University, Philadelphia, PA

Non-steroidal anti-inflammatory drugs (NSAIDs) inhibit the activity of cyclooxygenase (COX) enzymes, COX1 and/or COX2, which produce prostaglandins that cause pain, fever, and inflammation. Previous work has shown that loss of prostaglandin E2 (PGE2) signaling due to NSAID use before exercise decreases strain adaptive bone remodeling[1]. Likewise, a recent analysis of US Army personnel revealed a high correlation between NSAID use and stress fracture incidence, with the highest correlation observed in naproxen users[2]. We also observed that administration of naproxen, but not aspirin, to mice for 15 days reduced load-induced bone formation, significantly decreased bone toughness, and diminished stress fracture repair[3]. Both naproxen and aspirin are non-selective NSAIDs (inhibit both COX1 and COX2), thus these results suggest that naproxen's effects in bone are COX-independent. To test this hypothesis, we used Ptgs2-Y385F mice, which harbor a point mutation that inactivates the cyclooxygenase activity of COX2, but preserves the peroxidase activity. Here naproxen sodium (10.9 mg/kg) or vehicle (DI water) was administered through drinking water for 15 days, starting 24 hours before experimentation. Each mouse was subjected to six bouts of non-damaging uniaxial forelimb compression using a 2 Hz rest-inserted sinusoidal waveform with a peak force of 3 N for 100 cycles to induce lamellar bone formation. Mice received calcein on day 5 and alizarin red on day 12, with drinking water refreshed every 2-3 days. Right femurs were stored at -20°C in PBS-soaked gauze before microCT analysis and three-point bending. Left femurs and tibias were fixed with 10% NBF overnight, decalcified in 14% EDTA at 4°C for 10 days, sunk in 30% sucrose, and embedded in OCT before sectioning. Both loaded and non-loaded forelimbs were harvested, fixed in 10% NBF, embedded in polymethyl methacrylate (PMMA). By microCT, we observed that Ptgs2-Y385F mice have comparable bone geometry to wild-type (WT) littermates, and naproxen treatment did not alter bone geometry of either genotype. Three-point bending demonstrated that naproxen treatment caused a significant decrease in bone toughness in WT, heterozygous, and Ptgs2-Y385F mice, suggesting a COX2-independent mechanism of naproxen on bone toughness. Sections stained with Phalloidin F-Actin and imaged at 63X using confocal microscopy revealed that naproxen-treated osteocytes in WT male mice had a trend of lower average number of dendrites per osteocyte (p=0.076; Figure 1A-C). Standard dynamic histomorphometry revealed that Ptgs2-Y385F mice have a muted response to loading due to their defective COX2 and that naproxen treatment was associated with decreased
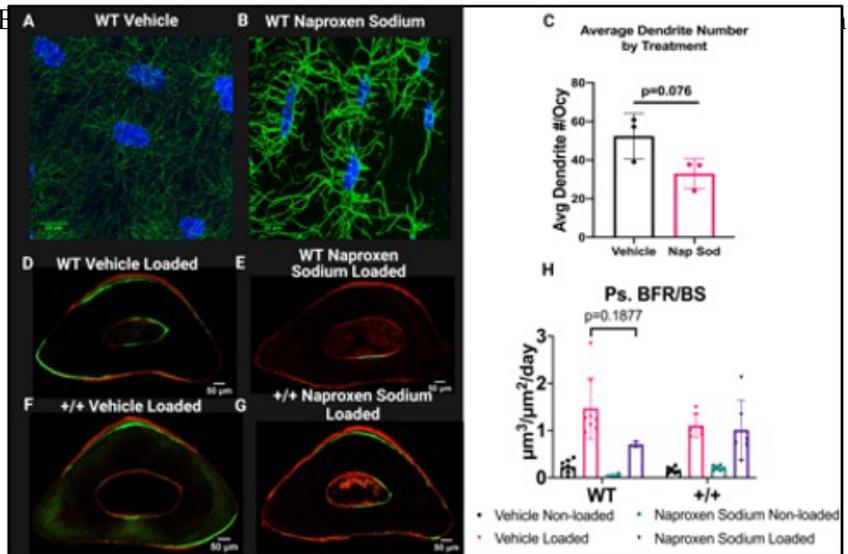

Figure 1: Naproxen sodium treatment decreases the average number of dendrites per osteocyte and decreases load induced bone formation in a COX2-dependent manner.
A-C) 63X confocal images of phalloidin-stained cortical bone sections and quantifications of the average number of dendrites per osteocyte (n=3). D-G) Representative dynamic histomorphometry images of ulna-mid diaphysis sections from D) WT vehicle, E) WT naproxen sodium, F) Ptgs2-Y385F vehicle, and G) Ptgs2-Y385F naproxen sodium treated and loaded mouse forelimbs. H) Quantification of periosteal BFR/BS for loaded and non-loaded forelimbs. Naproxen sodium does not significantly affect Ptgs2-Y385F periosteal BFR/BS but may decrease WT load response (n=2-8).

periosteal bone formation rate per bone surface in WT mice, but not in Ptgs2-Y385F mice (p=0.1877; Figure 1D-H), suggesting a COX2-dependent mechanism of NSAIDs on load-induced bone formation. In total, these results support the hypothesis that naproxen decreases bone toughness through a mechanism that is independent of COX2 cyclooxygenase inhibition, and that naproxen also acts on osteocytes to decrease dendritic network connectivity. These observations provide novel insights into how NSAIDs influence fracture risk through their actions on osteocytes.

References:
1. Kohrt, W. M. et al. Timing of ibuprofen use and bone mineral density adaptations to exercise training. J. Bone Miner. Res. 25, 1415–1422 (2010).
2. Hughes, J. M. et al. Nonsteroidal Anti-Inflammatory Drug Prescriptions Are Associated With Increased Stress Fracture Diagnosis in the US Army Population. J. Bone Miner. Res. 34, 429–436 (2019).
3. Park, J., Fertala, A. & Tomlinson, R. E. Naproxen impairs load-induced bone formation, reduces bone toughness, and diminishes woven bone formation following stress fracture in mice. Bone 124, 22–32 (2019)

Evaluation of additively manufactured bioresorbable trauma implants in a rat femur fracture model

Anna N. Smith, My My Tang, Richa Gupta, Tim D. Teinturier, Stephanie N. Weiss, Anna M. Massie, Michael W. Hast

Department of Orthopedic Surgery, Perelman School of Medicine, University of Pennsylvania, Philadelphia, PA (Smith, Tang, Gupta, Teinturier, Weiss, Hast)
Department of Clinical Sciences of Advanced Medicine, School of Veterinary Medicine, University of Pennsylvania, Philadelphia, PA (Massie)

Many veterinary orthopaedic interventions rely upon metallic implants to bear mechanical loads during healing. However, this approach can lead to stress shielding and metal implants remain within the body permanently. 3-D printed bioresorbable polymers, such as PLGA, can be tuned to change mechanical properties and alter degradation kinetics to improve healing. However, little is known about the temporal mechanical behavior of such implants. The aim of this study is to determine how the degradation of novel, 3-D printed, implants affect bone healing at clinically relevant timepoints (4-16 weeks) using a rat femur osteotomy model. We hypothesize that the bone formation will be accelerated in the resorbable implant group compared to controls. In this ongoing experiment, we expect to see substantial callus formation beginning in the resorbable group by the 4-week timepoint, but do not expect to see these changes until 8-weeks in the control group. We expect to see early cartilage bone formation in addition to high levels of osteoblastogenesis beginning in the resorbable group at the 4-week timepoint. We also expect bones treated with resorbable implants to demonstrate higher torsional strength than the control group at the 8 and 16-week timepoints. Preliminary results from in vitro testing demonstrate that mechanical strength of the bioresorbable implants is maintained from the 0 to 8-week timepoints but significantly decreases at the 16-week timepoint. Results from this study will guide the design and development of patient specific PLGA devices that may shift the paradigms of veterinary orthopaedic surgery.

Can *in vivo* tendon morphology and biomechanical properties be predicted from serum factors in people with pre-diabetes and type 2 diabetes?

Nathan WC Campbell[1], Shivam H Patel[1], Chinonso E Emenim[1], Dominick O Farino[1], Joseph V Rispoli[2], Craig J Goergen[2], Jacob M Haus[4], and Arman Sabbaghi[3] and Chad C Carroll[1]

[1]Department of Health and Kinesiology, [2]Weldon School of Biomedical Engineering, [3]Department of Statistics, Purdue University, West Lafayette, IN; [4]School of Kinesiology, University of Michigan, Ann Arbor, MI.
carrol71@purdue.edu

Introduction: Altered biomechanical properties are a clinical challenge for millions suffering from diabetes. However, the impact of type 2 diabetes and the transition from pre-diabetes to type 2 diabetes on tendon biomechanical and morphological properties are not well described. Further, knowing that many tendinopathies go undetected, a reliable systemic bloodborne surrogate of tendon properties would allow clinicians to identify at-risk patients, recommend interventional strategies, and quickly assess the progress of interventions. Therefore, our primary objective was to probe for relationships between *in vivo* tendon biomechanics, morphology, inflammatory markers, and standard clinical parameters. A secondary objective was to determine the effect of diabetes and pre-diabetes on tendon biomechanical and morphological properties compared to healthy controls without diabetes.

Methods: Using ultrasound and magnetic resonance imaging (MRI), we determined *in vivo* patellar tendon modulus, tendon cross-sectional area (CSA), and T1 signal in healthy controls (n=14, Age:45±5y, BMI:24±1, HbA1c:5.3±0.1%), individuals with pre-diabetes (n=14, Age:54±5y, BMI:29±2, HbA1c:5.7±0.1), and individuals with type 2 diabetes (n=13, Age:55±3y, BMI:33±2, HbA1c:6.7±0.3). Live ultrasound imaging during isometric ramped contractions was used to determine patellar tendon strain. Patellar tendon CSA was used in conjunction with strain to determine modulus. A basic metabolic, HbA1c, and lipid panel were completed. Plasma c-peptide, IL-1β, IL-6, IL-8, TNF-α, adiponectin, leptin, IGF-1, and C-reactive protein (CRP) were evaluated using enzyme immunoassay. Variables were assessed for possible correlations to tendon modulus, CSA, and signal with simple linear regression in Prism. We also performed variable selection via elastic net regularization. Variables selected by the elastic net were used to develop linear regression models to predict in vivo tendon outcomes. To address our secondary objective, healthy controls, individuals with pre-diabetes, and people with type 2 diabetes were compared using a one-way ANOVA. Residual diagnostics were performed to assess the validity of the model assumptions of normality and constant variance. This project was approved by the Purdue University Institutional Review Board, Protocol#: 17100199832.

Results: Age was not different across groups (p>0.05). BMI was greater in persons with type 2 diabetes than in healthy control (p<0.05). HbA1c was greater in persons with type 2 diabetes compared to healthy controls (p<0.0001) and those with pre-diabetes (p=0.0008). Serum IL-1β, IL-8, TNF-α, adiponectin and IGF-1 were not different between groups (p>0.05, Table 1). In contrast, serum c-peptide, IL-6, leptin, and CRP were greater in those with type 2 diabetes than in healthy controls (p<0.05, Table 1). Serum CRP was also greater in those with pre-diabetes than in healthy controls (p<0.05). From the metabolic and lipid panels, glucose (controls: 90±3, pre-diabetes: 99±4, type 2 diabetes: 124±9 mg/dl) and HOMA-IR (controls: 1.5±0.2, pre-diabetes: 2.3±0.4, type 2 diabetes: 4.2±1.0) were greater in those with type 2 diabetes compared to healthy controls (p<0.05). HDL levels were lower in persons with type 2 diabetes (p<0.05; 49±4 mg/dl) compared to healthy controls (63±5) and pre-diabetes (58±4). No other differences were noted from the metabolic and lipid panels. After normalization to body weight, we found that patellar tendon CSA was lower in people with type 2 diabetes compared to controls but not those with pre-diabetes (Figure 1). Signal intensity (mean grey value) was not different between groups (Figure 2). The differences in tendon modulus did not reach statistical significance in our small pilot sample (Figure 3).

With simple linear regression, we found that serum HbA1c (r=-0.313, p=0.05), HOMA-IR (r=-0.371, p<0.05), c-peptide (r=-0.439, p=<0.0001), IL-6 (r=-0.336, p<0.05), leptin (r=-0.708, p<0.0001), adiponectin (r=-0.299, p<0.05), HDL (r= 0.417, p=0.008), creatinine (r=0.420, p<0.05), and GFR (r=-0.431, p<0.05) were associated with body weight normalized tendon CSA. Further, c-peptide (r=0.383, p<0.05), leptin (r=0.403, p<0.05), and BMI (r=0.360, p<0.05) were predictors of tendon MGV. Lastly, we found that patellar tendon modulus was correlated with chronological age (r=-0.365, p<0.05) and MGV (r=0.376, p<0.05). Using the elastic net, the best predictive model for body weight normalized CSA (p<0.05) included BMI, leptin, and group (R^2= 0.6123). Group indicators alone were poor predictors of tendon CSA (R^2= 0.1584, p<0.05). For MGV, including all main effects predicted ~50% (R^2=0.5376, p=0.06) of the variation in tendon MGV, which was a better model than including only group predictors (R^2= 0.0457, p=0.16). For modulus, we consider all main effects and groups in our model. This approach resulted in an R^2=0.4944, which was greater than the fit achieved when only considering group (R^2=0.0869).

Discussion: Our group comparisons imply that systemic inflammation is apparent even in pre-diabetes, as indicated by a 6-fold increase in CRP levels. Surprisingly, the greater CRP levels with pre-diabetes were not accompanied by significant differences in HbA1c or HOMA-IR compared to healthy controls. These preliminary data also provide evidence that some blood-based variables could give reliable estimates of *in vivo* tendon properties in humans. However, our models do not account for all the variance in tendon properties; thus, it is likely that additional serum factors may influence tendons. Increasing our sample size is needed to strengthen our initial findings and may improve the ability of the elastic net to select variables. Our long-term goal is to use this approach to identify biomarkers that modulate tendon health. Given the relationships noted in this preliminary analysis, it would be prudent to utilize cell culture or *ex vivo* models to explore the impact of these variables on tendon or tendon cells. In the future, we will use more advanced T2* mapping procedures, which are better predictors of *in vivo* tendon degeneration and biomechanical properties.
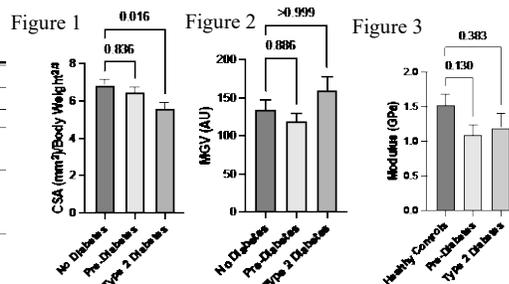
Significance: Type 2 diabetes is a significant risk factor for developing tendon complications, which are often challenging to treat and impart a considerable burden to individuals and society. The mechanisms contributing to tendon complications with diabetes are poorly understood and often go undetected until significant degeneration has occurred. Our findings provide novel targets that may contribute to changes in tendon properties with diabetes. Further, our preliminary correlation analysis suggests that several blood-based variables could predict *in vivo* tendon properties in humans.

Table 1

Figure 1

Figure 2

Figure 3

Collagen XI Deficiency Increases Collagen Fibril Deformation and Sliding in Developing Mouse Patellar Tendon

Jaime A. Santillan, Biao Han, Jeremy D. Eekhoff, Stephanie N. Weiss S., Louis J. Soslowsky

McKay Orthopaedic Research Laboratory, University of Pennsylvania, Philadelphia, PA

Jaime.santillan@pennmedicine.upenn.edu

Stickler syndrome is a genetic disorder caused by a mutation in the COL11A1 gene and is characterized by eye abnormalities, hearing loss, and joint problems [1,2]. Collagen XI co-assembles with collagens I and II during heterotypic fibril formation and therefore its disruption leads to abnormal extracellular matrix development [3]. Further, deficiency of collagen XI disturbs tendon structure, causing nuclear disorganization and degradation of mechanical properties [4]. However, how nanoscale mechanisms contribute to the weakened structure of collagen XI deficient tendon is unknown. To this end a tendon-targeted Collagen XI Knockout mice model was created. We hypothesized that tendon-targeted knockout of collagen XI would result in increased deformation and sliding of collagen fibrils. Accordingly, we mechanically tested three different genotypes : Male wild-type control (WT) mice, $Scx\text{-}Cre;Col11a1^{floxwtx}$ heterozygous (HET) mice, and $Scx\text{-}Cre;Col11a1^{flox/flox}$ knockout (KO) mice, to characterize their mechanical properties and determine the suitable % of low and high strain to be used for each group. There was no significant difference between the control group and the other genotypes. However, Knockout tendons were significant longer compared to HET and WT. This study provides evidence about the regulatory role of collagen XI in developing tendon; but also, further investigation is necessary to elucidate the role of collagen XI in the fibril deformation mechanisms in developing patellar tendon.

REFERENCES: [1] Printzlau et al. Cleft Palate Craniofac J, 2004. [2] Cattalini et al. Pediatr Rheumatol Online J, 2015. [3] Linsenmayer et al. J Cell Biol 1993. [4] Sun et al. Matrix Biology 2020. [5] Connizzo BK et al. J Biomech 2014.

Exploring methods for long-term, daily monitoring of Achilles tendon loading outside clinical or laboratory settings.

Authors: Michelle P. Kwon[1], Madison Woods[1], Todd J. Hullfish[1] , Josh R. Baxter[1].
[1]McKay Orthopaedic Research Laboratory, University of Pennsylvania, Philadelphia, PA

Abstract: Rehabilitation loading is critical to promote tissue healing following musculoskeletal injuries. Laboratory techniques accurately quantify these biomechanical loads, but only quantify loading in controlled settings. Monitoring the loads and motion that patients experience throughout daily living is necessary to improve rehabilitation strategies that promote healing and restore function. Measuring patient biomechanics outside clinical and laboratory spaces is now possible thanks to advances in affordable wearable sensor technology. Yet, there continue to be obstacles including subject compliance, and collecting usable data when deploying complex sensors over long periods of time. Our lab is exploring ways to better understand everyday human loading for Achilles tendon healing and the capability to monitor tendon loading for prolonged durations. We developed a comprehensive system to monitor tendon loading with laboratory grade sensors for two weeks. Subjects wore instrumented shoe insoles (Loadsol, Novel) to approximate Achilles tendon loading and an inertial measurement unit (AX6, Axivity) to measure daily movement. We supplemented these measurements using Redcap surveys, accessible instructions, and auto-uploading capabilities to bolster compliance. We found users correctly wore and logged data with a capture rate of greater than 59.9%. These continuously collected tendon loading data are the first of its kind to quantify Achilles tendon loading profiles in everyday activities. Our findings are encouraging and bolster the feasibility of monitoring Achilles tendon loading to first understand tendon healing and then prescribe therapeutic tendon loading. Our framework to monitor Achilles tendon loading brings laboratory-quality assessments to real-world settings, fundamentally changing how mechanistic clinical research can be done. Our ongoing research is optimizing this framework to minimize the burden on both patients and providers while maximizing measurement fidelity and data integrity. We also expect this framework to be easily adapted to other orthopaedic injuries that need improved post-operative rehabilitation guidance like rotator cuff tears and long bone fractures.

TITLE:

A Validated Open-Source Digital Image Correlation Algorithm for Measuring Local Tissue Strains in Tendon Explants

AUTHORS AND AFFILIATIONS:

Stanton Godshall[1], Krishna Pedaprolu[1], Erica Vasti[1], Faezeh Eskandari[2], Spencer E. Szczesny[1,3]

[1] Department of Biomedical Engineering, Pennsylvania State University, University Park, PA
[2] Department of Biomedical Engineering, Amirkabir University of Technology, Tehran, Iran
[3] Department of Orthopaedics and Rehabilitation, Pennsylvania State University, Hershey, PA

ABSTRACT:

There is considerable scientific interest in understanding the strains that tendon cells experience in situ and how these strains influence tissue remodeling. Based on this interest, several analytical techniques have been developed to measure the local tissue strains within tendon explants during loading. However, in several cases the accuracy and sensitivity of these techniques were not reported and none of the algorithms are publicly available. This has made it difficult for more widespread measurement of local tissue strains in tendon explants. Therefore, the objective of this project was to create a validated analysis tool for measuring local tissue strains in tendon explants that is readily available and easy to use. Specifically, we adapted a publicly available Augmented Lagrangian Digital Image Correlation (ALDIC) algorithm for measuring two-dimensional strains by tracking the displacements of cell nuclei within mouse Achilles tendons under uniaxial tension. Additionally, we validated the accuracy of the calculated strains by analyzing digitally transformed images as well as by comparing the strains with values determined from an independent technique (i.e., photobleached lines). Finally, we also incorporated a technique that reconstructs the reference image using the calculated displacement field, which can be used to assess the accuracy of the algorithm in the absence of known strain values or a secondary measurement technique. We found that the algorithm is capable of measuring strains up to 0.1 with an accuracy of 0.00015. Our technique for comparing a reconstructed reference image with the actual reference image successfully identified samples that had erroneous data and indicated that, in samples with good data, approximately 85% of the displacement field was accurate. Finally, the strains measured in mouse Achilles tendons was consistent with prior literature. Therefore, we believe that this algorithm is a highly useful and adaptable tool for accurately measuring local tissue strains in tendons.

Loading Levels in Patellar Tendon, Quadriceps Tendon, and Patellofemoral Joint Across 35 Rehabilitation Exercises

*Ke Song[1], Rodrigo Scattone Silva[2], Todd J. Hullfish[1], Andrew L. Sprague[3], Karin Grävare Silbernagel[2], Josh R. Baxter[1]
[1]University of Pennsylvania, Philadelphia, PA, [2]University of Delaware, Newark, DE, [3]University of Pittsburgh, Pittsburgh, PA
*Email of Presenting Author: ke.song@pennmedicine.upenn.edu

INTRODUCTION: Patellar and quadriceps tendinopathy and patellofemoral pain are prevalent knee joint pathologies, particularly affecting physically active individuals. Yet state-of-the-art knee rehabilitation protocols often rely on clinician perspectives, potentially leading to suboptimal recovery outcomes. Progressive loading promotes tissue healing, but the loading levels in knee tendons and the patellofemoral joint have not been quantified for most common rehabilitation exercises. As such, clinicians need more quantitative evidence to refine knee rehabilitation plans that progress therapeutic loading and suit patient-specific recovery goals. We recently developed a "Loading Index" based on loading peak, impulse, and rate to define overall loading "tiers" in the Achilles tendon during various exercises [1]. In this study, our goal was to establish a Loading Index to quantify, compare, rank, and categorize loading levels in the patellar tendon, quadriceps tendon, and patellofemoral joint across 35 common clinical knee rehabilitation exercises and routine activities.

METHODS: We recruited 20 healthy adult subjects (10F, 25.9 ± 5.7 years, body mass index = 24.1 ± 2.6 kg/m^2) who had no self-reported knee pain or injury, and obtained their informed consent for this IRB-approved study. We recorded motion data of each subject performing 35 knee rehabilitation or routine exercises (**Figures 1-3**), and calculated knee flexion angles and moments using an inverse dynamics biomechanical model. Next, we estimated load in the patellar tendon, quadriceps tendon, and patellofemoral joint based on the knee flexion angles and moments, using effective tendon moment arms and force relationships among the 3 knee structures defined in literature [2-4]. We normalized each knee structure load by subject weight, zeroed negative force components to account for physiologically one-way loading, then calculated their peak, impulse, and rate metric during each exercise. We calculated the Loading Index of each exercise as a weighted sum of the group-average of each loading metric [1]. For knee tendons, we set 50% Loading Index weight on loading peak, 30% on impulse, and 20% on rate, similar to our Achilles tendon study [1]. For patellofemoral joint, we set 50% weight on loading peak and 50% on impulse based on our perspective on their relative clinical importance. To compare the overall loading levels in each knee structure across all 35 exercises, we ranked their Loading Indices in an ascending order, then categorized them into 3 equally-divided tiers, from Tier 1 (low, i.e. < 0.333) to Tier 3 (high, i.e. > 0.667).

RESULTS: Overall loading levels in each knee structure varied substantially across exercises (**Figures 1-3**). Most rehabilitation exercises fell into Tier 2 (0.333 < Loading Index < 0.667), suggesting they provide moderate knee loading. Few exercises provide low-level loading (Tier 1) that resembles routine walking, while single-leg decline squat was the only exercise that generate highest-level loading in all 3 knee structures (Tier 3). For many exercises with moderate or high loading levels, loading peak, impulse, and rate varied between fast-speed exercises (e.g. run-and-cut) and long-duration exercises (e.g. Spanish squat). Loading ranks were generally similar among the 3 knee structures, yet for quadriceps tendon and patellofemoral joint forces, there is a notable bias towards higher Loading Index for high knee flexion exercises. Notably, exercises with long duration and high knee flexion (e.g. squats) saw a relative shift up the ranks while many fast-speed but short-duration exercises (e.g. running and jumping) moved down the ranks substantially.

DISCUSSION: Our results show that most rehabilitation exercises feature a moderate level of knee structure loading, while few exercises provide low level of loads that resemble walking, or loading with both high magnitude and long duration. Exercises with a moderate level of knee structure loading provide the most diverse opportunities for patient-specific rehabilitation planning, as clinicians can simplify protocols and choose mechanically similar exercises that best suit patient needs and abilities during rehabilitation. Conversely, the scarcity of low-loading exercises suggest that clinicians should use caution when prescribing early-stage exercises to avoid tissue over-loading that poses risks of healing complication. While many fast exercises feature high level patellar tendon loading, exercises with high knee flexion often generate higher quadriceps tendon and patellofemoral joint loading. We thus recommend clinicians differentiate loading profiles among the 3 knee structures and adjust rehabilitation strategies to progress therapeutic loading on the healing knee structure.

CLINICAL RELEVANCE: To our knowledge, this study is the first to quantify loading in three knee structures across a large collection of exercises in the same cohort. Our findings provide straightforward tools for clinicians to design rehabilitation protocols that prescribe progressive therapeutic loading while suiting patient-specific recovery needs, and set a benchmark for future research on complex and chronic knee pathologies.

REFERENCES: [1] Baxter+ *Med Sci Sports Exerc* 2020 [2] Van Eijden+ *J Biomech* 1986 [3] Bretcher+ *Gait Post* 2002 [4] Dandridge+ *J Orthop Res* 2022
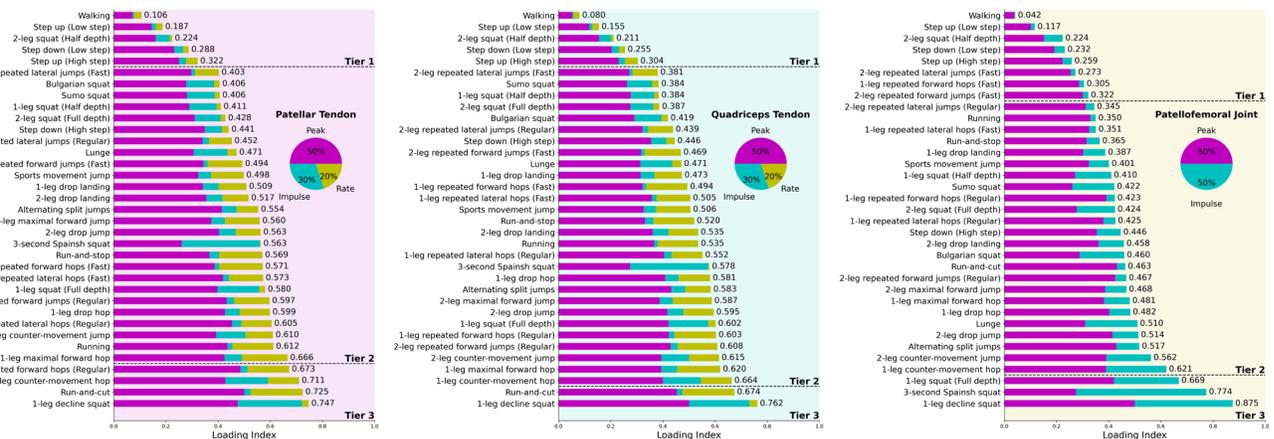
Figures 1-3. Loading Indices ranked for patellar tendon, quadriceps tendon, and patellofemoral joint forces across 35 rehabilitation exercises, categorized low (Tier 1), moderate (Tier 2), and high (Tier 3). Loading Index weights for patellar and quadriceps tendons are 50% on loading peak, 30% on impulse, and 20% on rate. Weights for patellofemoral joint are 50% on loading peak and 50% on impulse.

Collagen XII is a Critical Regulator of Tendon Function: Development of a Conditional Mouse Model

Ashley K. Fung[1,2], Mei Sun[3], Louis J. Soslowsky[1], David E. Birk[3]

[1]McKay Orthopaedic Research Laboratory, University of Pennsylvania, Philadelphia, PA
[2]Department of Bioengineering, University of Pennsylvania, Philadelphia, PA
[3]Department of Molecular Pharmacology and Physiology, University of South Florida, Tampa, FL
afung@seas.upenn.edu

Disclosures: Ashley K. Fung (N), Mei Sun (N), Louis J. Soslowsky (N), David E. Birk (N)

INTRODUCTION: Collagen XII is a fibril-associated collagen with interrupted triple helices (FACIT) that regulates collagen fibril assembly, and mutations in *Col12a1* result in myopathic Ehlers-Danlos Syndrome (mEDS). Patients with mEDS experience excess weakness at birth, hypermobile distal joints, and an absence of deep tendon reflexes [1], indicating impaired tendon function due to the absence of collagen XII. Tendons in a global *Col12a1$^{-/-}$* knockout mouse model demonstrated disrupted grip strength and tendon fiber structure as well as disordered tenocyte organization [2]. However, secondary effects due to involvement of bone and muscle may occur in this model, and the isolated role of collagen XII in tendon has not been elucidated. To address this limitation, the objective of this study was to create and characterize a conditional *Col12a1*-null mouse model to target collagen XII knockout in tendons using a Scleraxis-Cre driver. We hypothesized that tendon-targeted knockout of *Col12a1* expression would impair tendon function.

METHODS: <u>Model Development:</u> A promoter-driven knockout embryonic stem (ES) cell line was obtained from the KOMP Repository (ID: CSD29388, *Col12a1*$^{tm2a(KOMP)Wtsi}$). ES cell clones were injected into wild-type C57BL/6-Albino blastocysts, and resulting chimeric mice were backcrossed to produce mice with the targeted allele, *Col12a1$^{+/ta}$*. *Col12a1$^{+/ta}$* mice were bred with FLPe mice (B6; SJL-Tg(ACTFLPe) 9205Dym/J, Jackson Labs) to excise the FRT flanked neo sequences. The resulting offspring were crossbred with C57BL/6 mice for 6 generations and then inter-crossed to obtain conditional knockout mice, *Col12a1$^{flox/flox}$*. *Col12a1$^{flox/flox}$* mice were bred with Scleraxis-Cre (*Scx-Cre*) mice to obtain tendon-targeted heterozygous (Het, *Col12a1$^{+/\Delta ten}$*) and homozygous (KO, *Col12a1$^{\Delta ten/\Delta ten}$*) collagen XII knockout mice. <u>Gene & Protein Expression:</u> *Col12a1* expression and collagen XII content were assessed in flexor digitorum longus (FDL) tendons from mice at day 10 using qPCR and Western blots, respectively. <u>Immunofluorescence:</u> FDLs were dissected, fixed in 4% paraformaldehyde, embedded in optimal cutting temperature compound, and sectioned in the transverse plane at 5 μm thickness. Immunofluorescence staining of collagen XII was performed using a rabbit anti-mouse Col XII antibody (KR33, 1:500 dilution) with a donkey anti-rabbit Alexa Fluor 568 (1:200 dilution) secondary antibody. <u>Grip Strength:</u> Using a grip strength meter, mice were lowered toward the grip platform and upon grasping, mice were pulled away steadily until the grip was broken. The force applied just before the mouse lost its grip was recorded as the peak force. <u>Tendon Mechanics:</u> FDL tendons from day 60 mice were dissected from the foot, cleaned of excess tissue, and mechanically evaluated as described [3]. Tensile testing was performed using the following protocol: preconditioning, stress relaxation at 5% strain, and a ramp to failure at a rate of 0.5%/s. <u>Statistics:</u> One-way ANOVAs with Tukey post-hoc tests were conducted. Significance was set at $p \le 0.05$.

RESULTS: *Col12a1* expression was reduced in *Col12a1$^{\Delta ten/\Delta ten}$* KO mice compared to Cre- littermate control (Ctrl) mice though baseline expression, determined from traditional collagen XII knockout mice [2], was not reached in KO mice (**Fig. 1A**). Furthermore, the α1(XII) chain was present at comparable levels in the control group: Cre-, *Scx-Cre* and *Col12a1$^{flox/flox}$* mice (data not shown). Collagen XII content was lower in Het mice and just above background in KO mice compared to Ctrl (**Fig. 1B**). Collagen XII immunofluorescence localization demonstrated efficient knockdown in the tendon proper but not in the surrounding peritenon as expected (**Fig. 1C**). For joint function, female KO mice had reduced forelimb grip strength compared to Het (**Fig. 2A**) while male KO mice had reduced strength compared to Ctrl mice (**Fig. 2B**). At the tendon level, FDLs from day 60 male and female KO mice exhibited a reduction in mechanical properties. There was no difference in cross-sectional area (data not shown), but stiffness and modulus were both decreased in KO FDLs compared to Ctrl (**Fig. 2C, D**).

DISCUSSION: The overall goal of this study was to create a conditional *Col12a1*-null mouse model and target collagen XII knockout to tendons using a scleraxis-Cre driver. In FDLs of tendon-targeted *Col12a1$^{\Delta ten/\Delta ten}$* KO mice, both mRNA and protein expression levels were decreased but did not reach the baseline levels of global collagen XII knockout mice. This suggests that cells from a non-tendon lineage are not targeted as expected, and collagen XII immunofluorescence indicates that the surrounding peritenon population likely contributes to the above baseline expression levels. Furthermore, in the absence of *Col12a1* expression and therefore collagen XII, *Col12a1$^{\Delta ten/\Delta ten}$* KO mice have impaired mechanics, as evidenced by reduced forelimb grip strength and FDL tendon mechanical properties. Reduced grip strength is consistent with joint function in the global *Col12a1$^{-/-}$* knockout model, but interestingly, FDL tendon mechanical properties deviated from previous findings. In the global *Col12a1$^{-/-}$* knockout model, FDLs had larger cross-sectional area and greater stiffness with no difference in tendon material properties [2]. In this study, however, there were no differences in FDL cross-sectional area in KO mice, but stiffness was significantly decreased, resulting in inferior tendon elastic modulus. Differences in mechanical properties suggest that collagen XII is a critical regulator of tendon structure-function, and the contrasting findings from the global knockout model may be a result of secondary effects, such as those due to muscle and bone. Additionally, collagen XII knockout did not exhibit sex-specific effects with similar trends in grip strength and tendon mechanics for both male and female mice. Future studies are necessary to elucidate sex-specific roles of collagen XII in tendon structure and determine the biological mechanisms underlying changes in tendon structure-function. In conclusion, grip strength and tendon mechanical changes in the tendon-targeted *Col12a1$^{\Delta ten/\Delta ten}$* model support that collagen XII is a critical regulator of tendon function.

SIGNIFICANCE: Through development of a tendon-targeted collagen XII knockout mouse model, this study demonstrates the critical role of collagen XII in regulating joint and tendon function. Elucidating guiding mechanisms will provide the foundation to leverage the role of collagen XII in therapeutic strategies, providing support for treatments that address conditions such as myopathic Ehlers-Danlos syndrome.

REFERENCES: [1] Zou et al., Hum Mol Genet, 2014 [2] Izu et al., Matrix Biology, 2021 [3] Sun et al., Matrix Biology, 2020.
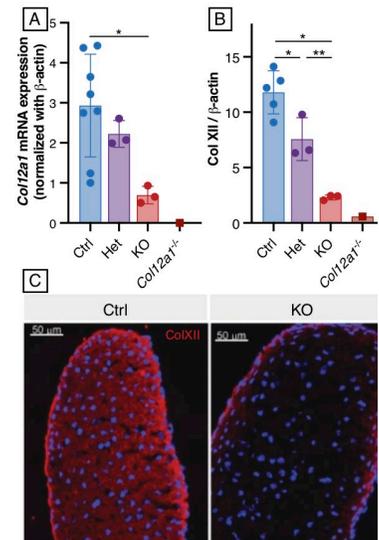
Figure 1: A) *Col12a1* and B) collagen XII expression were significantly reduced in *Col12a1$^{\Delta ten/\Delta ten}$* KO tendons compared to Ctrl though still above the baseline level established from conventional *Col12a1$^{-/-}$* mice. C) Efficient collagen XII knockdown was achieved in the tendon proper of KO tendons but not the surrounding peritenon. (*$p \le 0.05$, **$p \le 0.01$)
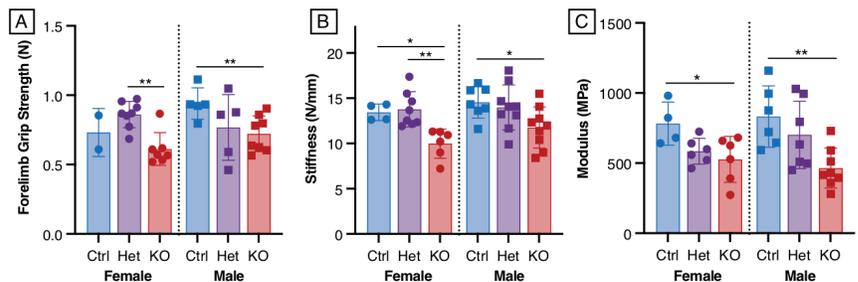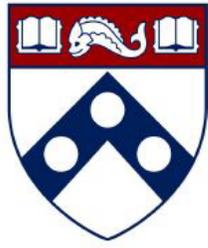

Figure 2: Forelimb grip strength was significantly reduced in A) female *Col12a1$^{\Delta ten/\Delta ten}$* KO mice compared to *Col12a1$^{\Delta ten/+}$* Het and in male *Col12a1$^{\Delta ten/\Delta ten}$* KO mice compared to Ctrl. FDL tendon B) stiffness and C) modulus were significantly reduced in *Col12a1$^{\Delta ten/\Delta ten}$* KO compared to Ctrl in both female and male mice. (*$p \le 0.05$, **$p \le 0.01$)

Micro CT Abstracts

Non-Muscle Myosins are Critical Regulators of Skeletal and Connective Tissue Formation

Mary Kate Evans[1], Tonia K. Tsinman[1], Ellie Ferguson[1], Xi Jiang[1], Joel Boerckel[1], Lin Han[2], Eiki Koyama[3], Robert L. Mauck[1], Nathaniel A. Dyment[1]

[1]University of Pennsylvania, [2]Drexel University, and [3]Children's Hospital of Philadelphia, Philadelphia, PA

mkevans@seas.upenn.edu

Disclosures: RL Mauck (*5, 4Web Medical; 8, JOR Spine*), No other disclosures.

INTRODUCTION: Tendon entheses often insert into bony eminences which are protrusions on the ends of long bones that increase the mechanical advantage during ambulation. Bony eminences and the entheses attached to them are often referred to as an attachment unit. External forces (i.e. muscle contraction) are required for attachment unit growth and development; however, cells also experience internal (cell-mediated) forces generated via actomyosin contractility [1-2]. Time lapse imaging of drosophila embryos has shown that non-muscle myosin (NM-II) mediated forces drive the cell shape changes required for morphogenesis, but the role of NM-II mediated forces in attachment unit development is largely unknown [3]. To determine the extent to which actomyosin contractility governs attachment unit development, we chose to ablate the predominant NM-II isoforms in mesenchymal tissues, NM-IIA and NM-IIB, which are encoded by the Myh9 and Myh10 genes respectively, in either all limb mesenchyme or targeted to tendinous tissue [4]. We hypothesized that NM-II ablation in both mesenchymal cells and tendinous tissues would disrupt attachment unit growth and maturation.

METHODS: All animal work was approved by the UPenn IACUC. <u>Mouse Models</u>: Myh9$^{f/f}$;Myh10$^{f/f}$ mice were crossed with either Prrx1Cre or ScxCre to target all limb mesenchyme or to restrict ablation to tendinous tissues, respectively. Because homozygous double knockouts did not appear with the Prrx1Cre driver at birth, suggesting embryonic lethality, we analyzed Prrx1Cre;Myh9$^{f/wt}$;Myh10$^{f/f}$ (Prrx1Cre Myh9^{HET} Myh10^{KO}) and Prrx1Cre;Myh9$^{f/f}$;Myh10$^{f/wt}$ (Prrx1Cre Myh9^{KO} Myh10^{HET}) mice. The ability of a single allele of either gene to rescue embryonic lethality reinforced previous findings that Myh9 and Myh10 are mutually compensatory; therefore, we only analyzed ScxCre;Myh9$^{f/f}$;Myh10$^{f/f}$ double knockouts (ScxCre dKO). <u>Micro-CT</u>: Prrx1Cre Myh9^{HET} Myh10^{KO}, Prrx1Cre Myh9^{KO} Myh10^{HET}, and ScxCre dKO mice were sacrificed at 5 weeks of age along with Cre-negative littermate controls (n=3 per genotype) and tissues were scanned at 10μm resolution. <u>Histology Sample Preparation</u>: Knees, ankles, and shoulders from ScxCre dKO and Cre-negative littermate control mice were harvested, fixed in formalin, cryo-embedded, and serially sectioned in the longitudinal plane (n=3 per genotype). <u>Staining</u>: Sections were stained for alkaline phosphatase (AP) activity with ELF97 endogenous phosphatase fluorescent substrate, counterstained with Hoechst-33342 (nuclei), and imaged by brightfield and polarized light microscopy. <u>Image quantification</u>: AP intensity as a percent of total enthesis area was recorded based on a minimum threshold in Fiji. <u>Statistics</u>: Control and mutant groups were compared via Student's t-tests (p<.05). Data presented as Mean ± SD.

RESULTS: <u>NM-II is critical for appendicular skeletal development</u>. To assess the roles of NM-IIA and NM-IIB in appendicular skeletal development we conditionally ablated Myh9 and Myh10 with Prrx1Cre. Physical examination of Prrx1Cre Myh9^{HET} Myh10^{KO} mice at 5 weeks of age revealed a marked shortening of the forelimbs coinciding with impaired mobility. Interestingly, these limb shortening and ambulation defects were less severe in Prrx1Cre Myh9^{KO} Myh10^{HET} mice, indicating that NM-IIB is more dominant than NM-IIA in limb formation. Micro-CT reconstruction showed severe abnormalities in the Prrx1Cre Myh9^{HET} Myh10^{KO} mutants (**Fig. 1**) including, a subluxed patella (P), missing trochlear groove (TG), and unfused tibia and fibula (T) (100% penetrance). These abnormalities are also present in the hindlimb of Prrx1Cre Myh9^{KO} Myh10^{HET} mice; however, these mice display some, albeit incomplete fusion of the tibia and fibula. In the forelimb of Prrx1Cre Myh9^{HET} Myh10^{KO} mice, the deltoid tuberosity (DT) was missing, the humeral head and scapula were misshapen, and the spine of the scapula (S) was absent. In the Prrx1Cre Myh9^{KO} Myh10^{HET} mice, the humeral head, scapula, and spine of the scapula appeared normal and the deltoid tuberosity was present; however, it was severely misshapen. <u>NM-II regulates tuberosity development and mineralization</u>. To target NM-II ablation more in the tendon than the adjacent cartilage anlagen, we created ScxCre dKO mice. These mice display a strikingly similar shoulder phenotype to the Prrx1Cre Myh9^{KO} Myh10^{HET} mice, with a misshapen tuberosity, despite no other apparent skeletal defects (**Fig. 2**). Further investigation into the mineralization of several tendon entheses demonstrated a severe lack of mineral apposition at the tibial tuberosity enthesis (2.09 ± 2.87% vs. 9.81 ± 2.84%, p = 0.03) (**Fig. 3**), with disorganized mineralization in the Achilles and supraspinatus tendons.

DISCUSSION: Despite the well-known role of applied (external) loading in the development of the attachment unit, the role of cell-mediated (internal) forces in attachment unit development is unknown. We show that mice retaining a single copy of either Myh9 or Myh10 in limb mesenchyme demonstrate similar abnormalities to mice lacking skeletal muscle contraction. The differences in skeletal defects observed, depending on which gene remains active, highlights the differential roles of Myh9 and Myh10 in tuberosity and bone formation. Additionally, we show that NM-II ablation in tendons disrupts deltoid tuberosity formation and yielded markedly reduced mineral apposition in the distal patellar tendon enthesis. Interestingly, ScxCre dKO mice phenocopy the deltoid tuberosity defects found in Prrx1Cre Myh9^{KO} Myh10^{HET} mice but are less severe than Prrx1Cre Myh9^{HET} Myh10^{KO} mice. Therefore, we will investigate allele dosages in Scx Cre mutant mice to determine the cell autonomous roles of NM-IIA and NM-IIB in attachment unit development. These results also raise the question of whether defects in tuberosity development are due to a defect in mechanotransduction or rather disrupted cell patterning during tuberosity initiation and growth. Future studies will seek to address these important questions.

SIGNIFICANCE: Establishing how cell intrinsic mechanical forces regulate tissue patterning and matrix production and organization of dense connective tissues will provide benchmarks for success and novel druggable targets for future therapies to treat disease.

REFERENCES: 1. Blitz, *Dev Cell*, 2009; 2. Thomopoulos, *JOR*, 2007; 3. Franke, *Current Biology*, 2005; 4. Shutova, *Biokhimiia*, 2018.
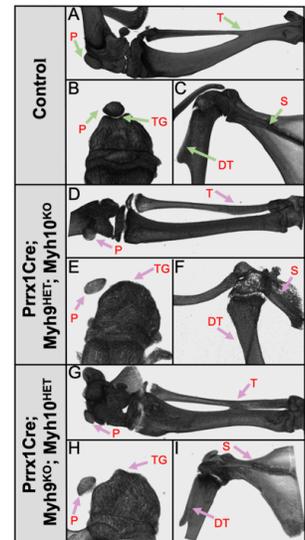
Figure 1: NM-II is critical to long bone and tuberosity formation. 3D μCT renderings of the hindlimb (A), frontal view of the knee (B), and shoulder joint (C) of control samples with arrows denoting important skeletal features that are lacking or abnormal in the Prrx1Cre Myh9^{HET} Myh10^{KO} (D-F) and Prrx1Cre Myh9^{KO} Myh10^{HET} (G-I) mutants. P: patella, TG: trochlear groove, T: tibia-fibula fusion, DT: deltoid tuberosity, S: spine of scapula.
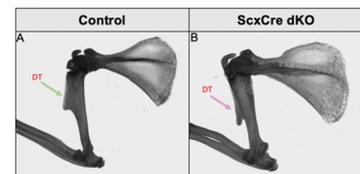

Figure 2: μCT images illustrating the misshapen deltoid tuberosity (DT) in ScxCre Myh9^{KO} Myh10^{KO} (B) compared to controls (A).
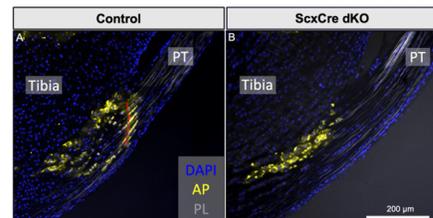

Figure 3: ScxCre Myh9^{KO} Myh10^{KO} mice (B) have disrupted mineral deposition within the distal patellar tendon enthesis as seen by reduced AP activity compared to controls (A). PT: patellar tendon, AP: Alkaline phosphatase, PL: Polarized light. Tide mark (red line).

Type V Collagen Plays an Essential Role in the Development of Knee Articular Cartilage and Meniscus

Bryan Kwok[1], Mingyue Fan[1], David E. Birk[2], Robert L. Mauck[3], Nathaniel A. Dyment[3], Eiki Koyama[4], Lin Han[1]

[1]Drexel University, Philadelphia, PA; [2]University of South Florida, Tampa, FL;
[3]University of Pennsylvania, Philadelphia, PA; [4]The Children's Hospital of Philadelphia, Philadelphia, PA.

Disclosures: RL Mauck (8, *JOR Spine*), no other disclosures.

INTRODUCTION: The extracellular matrix (ECM) of articular cartilage is characterized by a porous network of type II collagen fibrils that entrap aggrecan aggregates [1]. The meniscus, the loading counterpart of cartilage, is a fibrocartilage mainly consisting of collagen I fibers, with minor collagen II content [2]. Collagens V and XI are regulatory collagens that serve as the nucleation cores for initiating fibrillogenesis of collagens I and II, respectively [3, 4]. To date, little is known about how these two regulatory collagens work in concert to regulate initial development and growth of the knee joint that encompasses both hyaline and fibrocartilage. Such knowledge could provide a crucial benchmark for designing novel regenerative strategies to repair and restore the function of degenerative joints [5]. This study aims to elucidate the role of collagen V by assessing the development phenotype of cartilage and meniscus resulting from targeted knockout of *Col5a1* gene in the knee joint.

METHODS: *Immunofluorescence (IF)* and *RNA-scope* were applied to C57BL/6J murine knees to assess the distributions of collagens V and XI at embryonic (E17.5), newborn (P0) and adult (P90) ages. *Conditional Col5a1 knockout mice* (*Col5a1^{f/f}/Gdf5Cre*, or *Col5a1^{cKO}*) were established by crossing *Col5a1^{f/f}* mice [6] with joint-specific *Gdf5Cre* mice [7]. Knee joints were harvested from 3 and 8 months of age (P90 and P240) *Col5a1^{cKO}* and control *Col5a1^{f/f}* mice. We applied *histology* and *μCT* imaging to assess cartilage and meniscus morphology, cell morphology, sGAG staining, and subchondral bone structure, as well as *AFM-nanoindentation* to quantify the indentation modulus, E_{ind}, of the loading regions of articular cartilage and meniscus via a microspherical tip ($R \approx 5$ μm, $k \approx 8.9$ N/m) [8]. Mann-Whitney U tests were applied to detect differences in E_{ind} between genotypes at $\alpha = 0.05$.

RESULTS: In WT mice, at both E17.5 and P0, as expected, we detected strong staining for collagen XI in epiphyseal cartilage (Fig. 1a, EC) and collagen V in meniscus (Fig. 1a, M). Surprisingly, articular cartilage showed higher staining for collagen V than for collagen XI (Fig. 1a). This finding was also validated by gene expression at P0 using RNA-scope (Fig. 1b), with *Col5a1* enrichment in the articular vs. epiphyseal cartilage and vice versa for *Col11a1*. In adult joints, staining of both collagens V and XI were low, with collagen V mainly localized to the pericellular domain of superficial layer cells (Fig. 1a). Corroborating the important role of collagen V in developing articular cartilage and meniscus, we found profound developmental defects in both young adult (P90) and middle-aged (P240) *Col5a1^{cKO}* mice. In P90 mice, loss of collagen V resulted in a much smaller meniscus (Fig. 2a). For articular cartilage, although we did not detect changes in tissue thickness or sGAG staining, chondrocytes appeared to undergo aberrant clustering in *Col5a1^{cKO}* group (Fig. 2a). Notably, both cartilage and meniscus of *Col5a1^{cKO}* mice had significantly reduced modulus relative to control, indicating impaired matrix integrity and mechanical functions with loss of collagen V (Fig. 2b). μCT analysis showed aberrant calcification in joints, with a loss of expected ossification at the horns of lateral meniscus in P90 *Col5a1^{cKO}* joints, and excessive osteophyte formation in P240 joints, which is a sign of severe osteoarthritis (OA) [9] (Fig. 3).

DISCUSSION: This study highlights a crucial role for collagen V in the development and maintenance of articular cartilage. For years, the consensus has been that the fibrillar collagen network of hyaline cartilage consists of collagen types II, IX and XI [10], with collagen XI being highly expressed at embryonic and neo-natal stages [11]. While the high expression of collagen XI is confirmed in developing epiphyseal cartilage, we show here for the first time, that developing articular cartilage is rich in collagen V, but not in collagen XI (Fig. 1). The importance of collagen V in cartilage integrity is further highlighted by aberrant cell clustering and reduced tissue modulus in young adult *Col5a1^{cKO}* mice (Fig. 2). Recent studies have suggested that collagen V may regulate stem cell quiescence in muscle through the Notch-Col V-CALCR axis [12]; it is thus possible that collagen V may play a similar role in regulating progenitor cell fate in developing articular cartilage. Collagen V is present at low concentrations in young adult cartilage, and according to our recent study, induced knockout of *Col5a1* during post-natal growth led to no clear phenotype in articular cartilage [13]. Thus, the role of collagen V in regulating articular cartilage integrity is most likely limited to early embryonic and neo-natal stages, and the observed phenotype in *Col5a1^{cKO}* mice is due to cell and/or tissue defects resulting from the lack of collagen V in early development.

The reduced size, modulus and absence of horn ossification in *Col5a1^{cKO}* menisci (Figs. 2, 3) also suggest a crucial role of collagen V in the developing meniscus. The reduction of meniscus size cannot be explained by the canonical role of collagen V in regulating collagen I fibril assembly [14]. In early development, articular cartilage and meniscus are both initiated from *Gdf5*-expressing progenitors in the interzone [15]. Given the high expression of collagen V in this region, it is possible that collagen V regulates the activities of progenitors that give rise to multiple joint tissues, including the meniscus. In fact, the osteophytes in P240 *Col5a1^{cKO}* knees (Fig. 3) support the importance of collagen V in overall joint health and maintenance. Meanwhile, lack of collagen XI in this region suggests that collagen V may be more crucial than collagen XI in the initial development of articular cartilage, while collagen XI could be essential for the development of epiphyseal cartilage and secondary ossification. Building on these results, our ongoing studies aim to elucidate the mechanisms by which collagen V regulates cartilage and meniscus integrity, and delineate the roles of collagen V versus XI in initial joint development.

SIGNIFICANCE: This study is the first to highlight an essential role for collagen V in the development of articular cartilage and meniscus, which represents an expansion of our knowledge of the cartilage matrix, which had largely focused on collagen II/IX/XI fibrils. Our results provide a basis to delineate the roles of collagens V and XI in knee development, and to test the potential of collagen V as a candidate for improving cartilage regeneration.

References: [1] Han+ 2011. [2] Vanderploeg+ 2012. [3] Wenstrup+ 2004. [4] Wu+ 1995. [5] Wang+ 2022. [6] Sun+ 2011. [7] Rountree+ 2004. [8] Wang+ 2020. [9] Felson+ 2005. [10] Eyre 2001. [11] Mendler+ 1989. [12] Baghdadi+ 2018. [13] Chandrasekaran+ 2021. [14] Birk 2001. [15] Shwartz+ 2016.
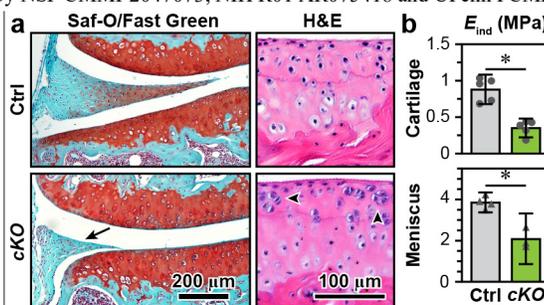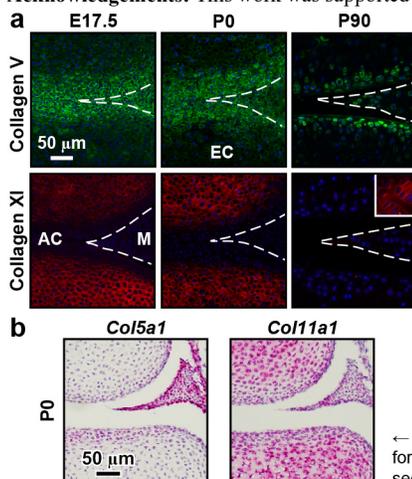
Fig. 2 a) Representative Saf-O/Fast Green and H&E histology shows the reduced meniscus size (black arrow) and aberrant chondrocyte clustering (black arrowheads) in *Col5a1^{cKO}* (*cKO*) mice relative to the control at P90. **b)** Nanoindentation modulus of cartilage and meniscus at P90 (mean ± 95% CI, $n \geq 3$, *: $p < 0.05$ via Mann-Whitney test).
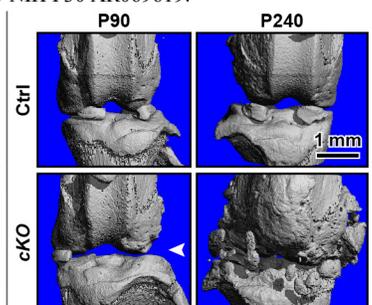
Fig. 3 Reconstructed 3D μCT images of knee joints from *Col5a1^{cKO}* (*cKO*) and control mice at P90 and P240 (white arrowhead: absence of meniscus horn ossification at P90, repeated for $n \geq 3$ mice).

← **Fig. 1 a)** Immunofluorescence (IF) images of collagens V and XI in WT mice at E17.5, P0 and P90 (Inset: positive control for collagen VI at the growth plate). **b)** RNA-scope of *Col5a1* and *Col11a1* expressions at P0. Images were taken on sagittal sections of murine knee joints (AC: articular cartilage, EC: epiphyseal cartilage, M: meniscus).

SDC4 plays an important role in the homeostasis of lumbar spine

Kimheak Sao[1], Makarand V. Risbud[1]

[1]Department of Orthopaedic Surgery, Cell Biology & Regenerative Medicine Graduate Program, Thomas Jefferson University, Philadelphia, PA

INTRODUCTION: Syndecan 4 (SDC4) is a heparan sulfate proteoglycan that shows enriched expression in the intervertebral disc. Importantly, further induction in SDC4 levels by pathological stimuli, such as inflammatory cytokines TNF-a and IL-1b, are linked to intervertebral disc degeneration and osteoarthritis [1, 2]. Previous studies have shown that SDC4 promotes aggrecan degradation by aiding ADAMTS-5 activity in an inflammatory setting. Deletion of SDC4 protects mice from proteoglycan loss and reduces severity of osteoarthritis-like cartilage destruction [2]. While SDC4's role has been described to accelerate degenerative processes in the disc and articular cartilage, its role in healthy disc tissue maintenance has not been explored. A goal of this study is to investigate the effects of SDC4 deletion on disc health during aging.

METHODS: C57BL/6 wildtype (WT) and SDC4 global deletion mice at 6, 11-12, and 20-24-months are collected for this study. Coronal sections of the lumbar were evaluated by Safranin-O/Fast Green, Picrosirius Red, quantitative immunohistochemistry, and mechanical loading. Four lumbar levels (L3-S1) from each timepoint and genotype (n = 6-9 mice) were scored by $\geq$ 3 blinded graders using a modified Thompson scale. Micro-computed tomography (microCT) analysis of the spines was performed to investigate the effects of SDC4 deletion on vertebral bone. All mouse experiments were performed under protocols approved by the Institutional Animal Care and Use Committee (IACUC) of Thomas Jefferson University.

RESULTS: Characterization of SDC4 global deletion in discs and vertebrae were done to determine its function in disc tissue homeostasis. Quantitative-histological analyses of lumbar discs show prolonged protection of NP tissue health in SDC4 null mice at 6 month.. Picrosirius red showed similar collagen fiber thickness between KO and WT at 6 and 20-24-months mutant mice. Interestingly, microCT analysis revealed altered bone morphology in SDC4 null mice at all timepoints with significant decreases in lumbar bone mineral density, volume, cross-sectional thickness, and trabecular thickness. Furthermore, immunohistochemistry revealed lower osteoblastic activity.

CONCLUSION: Our results show that SDC4 deletion mildly protects lumbar disc tissue under normal physiological spinal loading at the 6m timepoint. Interestingly, SDC4 null mice vertebrae bone parameters showed early development of osteopenia in comparison to WT, demonstrating SDC4's involvement in bone health and potential consequences of its deletion. Further, immunohistochemistry revealed lower osteoblastic activity, which could contribute to the loss of bone parameter. We suspect that these bone parameter changes could affect how the disc experiences loading.

SIGNIFICANCE: SDC4's function is tissue-dependent: its deletion has potential early protective effects on disc degeneration but may negatively affect bone health.

REFERENCES:
1. Wang, J., et al., *TNF-alpha and IL-1beta promote a disintegrin-like and metalloprotease with thrombospondin type I motif-5-mediated aggrecan degradation through syndecan-4 in intervertebral disc.* J Biol Chem, 2011. **286**(46): p. 39738-49.
2. Echtermeyer, F., et al., *Syndecan-4 regulates ADAMTS-5 activation and cartilage breakdown in osteoarthritis.* Nat Med, 2009. **15**(9): p. 1072-6.

Beneficial Effects of Yoda1 Treatment on Adult Mice Vertebrae

Jason Jiang[1#], Wiley Gong[2#], Tiankuo Chu[3], Murtaza Wasi[3], Rosa Guerra[3], Liyun Wang[3*]

[1]Conestoga High School, 200 Irish Road, Berwyn, PA, USA
[2]Newark Charter School, 200 McIntire Drive, Newark, DE, USA
[3]Department of Mechanical Engineering, University of Delaware, Newark, DE, USA
[#]equal contribution and presenting co-first authors:
th3jj1ang193@gmail.com; wilegong24@ncs.charter.k12.de.us
*Corresponding author: lywang@udel.edu

DISCLOSURES: The authors have declared no conflicts of interest.

INTRODUCTION: Bone metastasis occurs in 70% of all breast cancer metastatic cases [1], causing reduced bone quality, severe pain, and bone fractures, reducing the overall survival rate [2]. Exercise decreases the risk of breast cancer occurrence and recurrence, improves bone strength, and enhances patient tolerance to cancer treatments [3]. Therefore, exercise is promoted as an adjuvant therapeutic in treating metastatic breast cancers [4]. However, exercise is implausible for some patients due to osteoporosis, risk of unintended injury, or many other underlying factors [5]. Yoda1 is a small-molecule activator of mechanosensitive Piezo1 ion channels, the most abundant calcium ion channels on osteocytes [6]. Yoda1 treatment has been proven promote anabolic responses that lead to new bone formation in young mice [6]. The objective of this study was to examine the in vivo effects of Yoda1 using female skeletally mature mice. We hypothesized that the Yoda1 treatment would protect or increase the skeletal integrity of the adult mice.

METHODS: To verify the protective effects of Yoda1 on the mature skeletal system, we randomly assigned twenty-eight 8 to 9 month old adult mice with various strain backgrounds (Balb/c, C57BL/6J and MTMG) into 2 groups receiving either Yoda1 or DMSO Vehicle (n = 17 and 11 respectively). The animal experiment protocol was approved by the University of Delaware Institutional Animal Care and Use Committee.

Yoda1 treatment: Yoda1 dissolved in DMSO and 30% (w/v) 2-hydroxypropyl beta cyclodextrin (2-HPBC) was administered via intraperitoneal (IP) injection at a dose of 5 mg/kg body weight, and the same volume of the DMSO and 30% 2-HPBC solution was given to vehicle groups. The mice received Yoda1 or vehicle treatment 5 days per week for 4 weeks.

In vivo Micro-CT: Mice were scanned using a SkyScan® 1276 scanner at 7-μm resolution, 50 kV, 200μA, with 990ms exposure, 0.8° rotation step, and a 0.5mm aluminum filter on Week 0 and 4 as published [7]. The 2D projections were reconstructed in NRecon®. Then, the 6th caudal tail vertebrae were isolated in Dataviewer® and registered to a vertical orientation through a custom-made Python script. Following the registration, two regions of interests were selected for analysis of the trabecular and cortical bone regions, which were located 30-80 slices (0.21-0.56 mm) and 200-250 slices (1.4-1.75 mm) respectively above the growth plate at the distal end (**Fig. 1**). Standard bone histomorphometry indices were obtained using batch processes in CTan®, including trabecular bone volume fraction (Tb.BV/TV, %), trabecular number (Tb.N, #/mm), trabecular thickness (Tb.Th, mm), and trabecular spacing (Tb.Sp, mm), trabecular bone mineral density (Tb.BMD), cortical polar moment of inertia (pMOI, mm^4), cortical thickness (Ct.Th, mm), cortical area (Ct.Ar), and tissue mineral density (TMD).

Statistical analysis: Student's t tests were performed to determine the significance ($p < 0.05$) of the changes incurred by the Yoda1 vs. vehicle treatment over the 4 week observed period.

Fig. 1. The schematic of the workflow. **(A)** The scout view of a mouse's lower body, with the 6th caudal vertebra highlighted. **(B)** Side view of the 6th caudal vertebra, reconstructed from 3D microCT scans. The two analysis regions are shown. **(C)** A 2D cross-section in the cortical analysis region. **(D)** A 2D cross-section in the trabecular analysis region.

RESULTS: After 4 weeks, the vehicle-treated mice showed an average 0.004 ± 0.010 mm^4 increase in cortical pMOI of the 6th caudal vertebra, while the Yoda1-treated mice showed a 2.5 times greater increase over the same time period (0.010 ± 0.007 mm^4, p = 0.08, Fig. 2A). The trabecular BV/TV data follows a similar trend, with the vehicle group seeing a small increase in the bone volume fraction ($0.75\% \pm 4.7\%$) and the Yoda1 group showing a nearly 5 times higher increase ($3.85\% \pm 4.2\%$, p = 0.08, Fig. 2B).

DISCUSSION: The objective of the study was to test the effect of Yoda1 treatment on skeletally mature mice. The pMOI and BV/TV data from the cortical and trabecular analyses demonstrate that Yoda1 treatment has a positive effect on vertebral bone structure and bone formation. This finding supports our hypothesis that Yoda1 treatment protects and increases the skeletal integrity of adult mice. Whereas previous studies showed that Yoda1 promoted bone formation in younger mice [6], this study tested the vertebral responses of older mice to Yoda1 treatment. Experiments from our lab also showed positive responses in other skeletal sites including tibiae and femurs [7]. These discoveries confirm that activation of mechanosensitive Piezo1 ion channels in osteocytes through Yoda1 treatment leads to enhanced bone formation regardless of the age of animal. These mouse studies suggest that Piezo1 activation through Yoda1 or other agonists could be a new mechanism for treating age-related osteoporosis or preventing bone degradation in patients with cancers, fractures, or diabetic bone diseases, and potentially even astronauts in microgravity. It may also be utilized alongside conventional exercise or targeted physical therapy.

Fig. 2. Beneficial effects of Yoda1 on vertebrae of 8-9 month old mice (n = 14 mice/group). **(A)** Cortical pMOI (week 4 – week 0). **(B)** Trabecular BV/TV (week 4 – week 0). Yoda1 vs. Vehicle: p = 0.08 (Student's t test)

SIGNIFICANCE/CLINICAL RELEVANCE: This study represented an initial attempt to test the potential of Yoda1 as an "exercise pill" to enhance bone structure and strength for elderly and metastatic breast cancer patients.

REFERENCES: [1]. Chen M,T et al. 2017, [2]. D. Miller MPH et al. 2022, [3]. L.W. Jones et al. 2016, [4]. C.M. Alfano et al. 2012, [5]. Meghan W et al. 2009, [6]. Xuehua Li et al. 2019. [7] Wasi et al. 2022. ASBMR.
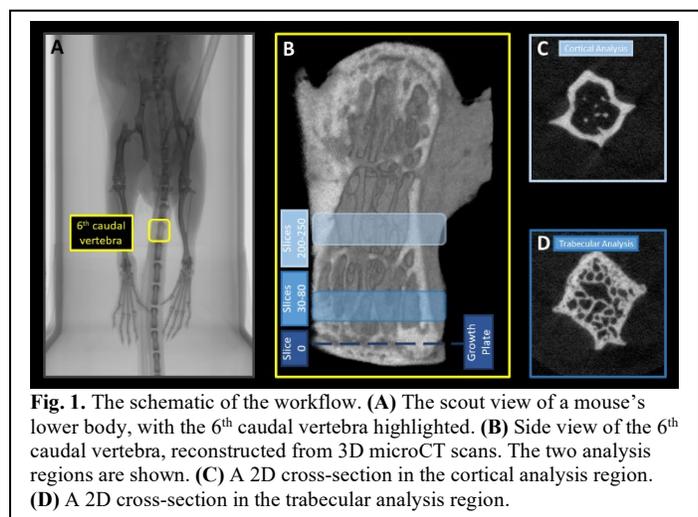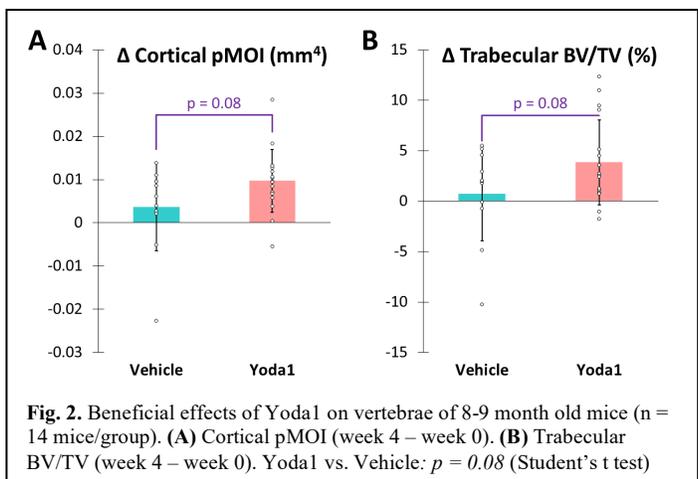
Yoda1 Protects Cortical Bone in Aged Mice Bearing Breast Cancer

Murtaza Wasi1, Tiankuo Chu1, Jinhu Xiong2, Lidan You3, Liyun Wang1
1. Department of Mechanical Engineering, University of Delaware; 2. Department of Orthopaedic Surgery, University of Arkansas Medical Sciences. 3. Department of Mechanical and Industrial Engineering, University of Toronto.

Upon the metastasis of breast cancer to bone, the 5-year overall survival rate drastically reduces from 90% to about 24%. In addition, elderly breast cancer patients and survivors are at higher risk of bone fractures because their skeletons most likely have already been compromised with aging-related osteoporosis and adverse side effects from cancer treatments. Previously we showed that moderate physical activity suppressed breast cancer-induced osteolysis in young adult mice[1]. However, bone formation by mechanical loading is diminished in aged mice[2]. To restore the protective effects of loading on aged bones, we need to enhance the responses of aged skeleton towards exercise. Piezo1 ion channels are the most abundant calcium channels in osteocytes, and can be activated by mechanical force and agonist Yoda1[3]. We hypothesized that Yoda1-augmented mechanical loading could better preserve skeletal integrity in aged mice with and without breast cancer.

Aged female C57BL/6J mice (66-week-old, Jackson Laboratory) received 1000 Py8119 breast cancer cells in 20 uL PBS in each of the two tibiae using a 30G1/2 syringe. Only tibiae shown successful injections into tibial metaphysis (examined under microCT) were randomly assigned to the four experimental groups (n = 5-9 per group): Vehicle-Nonloaded, Vehicle-Loaded, Yoda1-Nonloaded, Yoda1-Loaded. The non-tumor mice of both sexes (36- to 78-week-old) were randomly selected to receive either Yoda1 or vehicle treatment (n = 12-13 per group) and their left tibiae were subjected to tibial loading with the right tibiae as non-loaded control. Yoda1 was administered via intra-peritoneal injection at a dose of 5mg/kg body weight 1 hour prior to the loading session. Vehicle solution was injected in a similar fashion. For tibial loading, the mice were anesthetized to receive cyclic uniaxial compression on one tibia with a 4.5N peak load, 4Hz, 300 (tumor groups) or 600 cycles per day (non-tumor groups), 5 day/week for a duration of 4 weeks. In vivo uCT scans were performed using a Bruker SkyScan® 1276 scanner weekly or biweekly as published[1]. The sequential scans were reconstructed, registered (to week 0), and analyzed for the changes of polar moment of inertia of the tibial midshafts (Ct.pMOI), a key structural index of mechanical integrity.

In aged mice without tumor, tibial loading (4.5N) alone did not affect cortical pMOI over the duration of the study, while Yoda1 alone or in combination of tibial loading significantly elevated pMOI relative to the group receiving no treatment (Fig. 1A). In the aged mice with tumor, loading alone did not significantly slow the decline of pMOI in the Vehicle treated mice (Fig. 1B), in contrast to our previous finding in young-adult mice. Amazingly, Yoda1 alone or in combination of loading not only reversed the decline of pMOI but also induced net increases of Ct.pMOI at Week 3, and Week 4 (Fig. 1B). Analysis of the proximal metaphysis and tumor burden is ongoing.

This study demonstrated the potential benefits of Yoda1-based interventions in improving the skeletal integrity in aged mice with and without breast cancer metastasis.
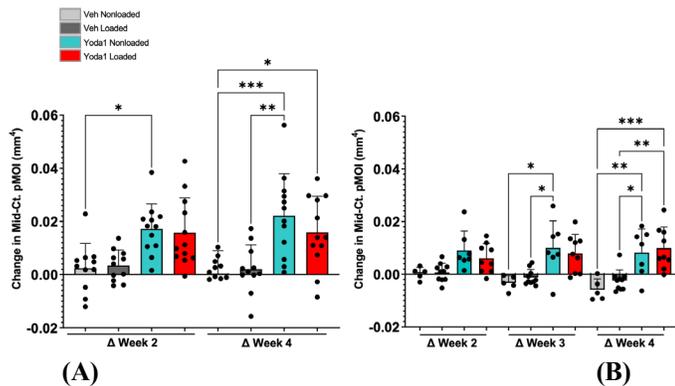

Figure 1: The effects of Yoda1 and tibial loading on the midshaft cortical polar moment of inertia (Ct.pMOI) of aged mice without (A) or with metastatic breast cancer (B). Sample size: n=5-12 per group. One way ANOVA with post hoc Tukey tests (*, $p \leq 0.05$; **, $p \leq 0.01$, ***, $p \leq 0.001$)

References:
1. Wang, S. *et al.* Moderate tibial loading and treadmill running, but not overloading, protect adult murine bone from destruction by metastasized breast cancer. *Bone* **153**, 116100 (2021).
2. Holguin, N., Brodt, M. D. & Silva, M. J. Activation of Wnt Signaling by Mechanical Loading Is Impaired in the Bone of Old Mice. *J. Bone Miner. Res.* **31**, 2215–2226 (2016).
3. Syeda, R. *et al.* Chemical activation of the mechanotransduction channel Piezo1. *Elife* **4**, 1–11 (2015).

Effects of Yoda1-augmented whole-body vibration on adult skeleton after radiotherapy

Tiankuo Chu[1], Jason Jiang[2], Wiley Gong[3], Murtaza Wasi[1], Rosa Guerra[1], Shubo Wang[1], Lidan You[4], Liyun Wang[1]
[1]Department of Mechanical Engineering, University of Delaware, Newark, DE, USA
[2]Conestoga High School, 200 Irish Road, Berwyn, PA, USA
[3]Newark Charter School, 200 McIntire Drive, Newark, DE, USA
[4]Department of Mechanical & Industrial Engineering, University of Toronto, Canada
Email of Presenting Author: chutk@udel.edu

DISCOLSURES: The authors have declared no conflicts of interest.

INTRODUCTION: Bone metastasis makes up 70% of all breast cancer metastatic cases [1], resulting in adverse skeletal-related event (SRE) such as reduced bone quality, severe pain, and bone fractures as well as the overall survival rate being drastically reduced [2]. Exercise is proven to be beneficial for breast cancer patients, reducing the risk of breast cancer occurrence and recurrence, improving bone quality and strength, and enhancing the tolerance to cancer treatments [3]. Therefore, exercise is promoted as an adjuvant therapeutic in treating metastatic breast cancers [4]. But routine aerobic or strength exercise is challenging for elderly patients due to age-related osteoporosis and tendency of unintended injury [5]. Whole-body vibration (WBV) is believed to be safer and easier-to-perform than regular activity because WBV impacts lower acceleration on ankle (0.3-0.4g) than walking and running (1.2-2g), and WBV shows overall wellness benefits for elderly metastatic patients including bone protection [6]. However, recent studies suggest that WBV is inefficient in reducing bone lose in postmenopausal women due to adverse skeletal effects of hormonal treatments and radiotherapy such as decreased mechano-sensitivity and increased osteocytes apoptosis [7]. Hence, there is a need to enhance the responses of mature skeletons to WBV. Yoda1 is a small-molecule activator of mechanosensitive Piezo1 ion channels, which are the most abundant calcium ion channels on osteocytes, and Yoda1 treatment can reduce osteoclast differentiation and promote anabolic responses, leading to new bone formation in vivo [8]. The objective of this study was to examine the in vivo effects of Yoda1-augmented WBV using the female skeletal matured mice receiving radiation. We hypothesized that Yoda1-augmented WBV would protect skeletal integrity in adult mice after radiotherapy.

METHODS: To verify the protective effects of Yoda1 and/or WBV in the mature skeletal system, we randomly assigned twenty-eight 8 to 9-month-old adult mice with various strain background (Balb/c, C57BL/6J and MTMG) into 4 groups receiving either Yoda1 or DMSO Vehicle and subjected to WBV or Ground according to their polar moment of inertia (pMOI) at week 0 (n = 5 to 9 per group). Animal experiment protocol was approved by University of Delaware Institutional Animal Care and Use Committee. Radiation: We applied a clinically relevant dosing regimen (8 Gy twice with three days apart) on the right tibiae of mice with the left as the non-radiation control. Live-dead assay: In a separate pilot study, bone marrow from radiated and non-radiated tibiae (n =4) was collected via centrifuge out of the bones 24 h after radiation therapy, and the viability of the marrow nucleated cells was determined by staining with calcein-AM (live dye) and ethidium bromide (dead dye) and confocal microscopy. Yoda1 treatment: Yoda1 dissolved in DMSO and 30% (w/v) 2-hydroxypropyl beta cyclodextrin (2-HPBC) was administered via intraperitoneal (IP) injection one day after radiation at a dose of 5 mg/kg body weight, and the same volume of the DMSO and 30% 2-HPBC solution was given to vehicle groups. WBV: 1 h after Yoda1/Vehicle injection, mice were subjected to for 2 sessions of 7.5 min WBV at 12 Hz, 0.25 g, with a 7.5 min rest period in between. The ground groups were kept in cages. Treatment frequency and duration: The mice received Yoda1/WBV treatments 5 days per week for up to 4 weeks. In vivo Micro-CT: Mice were scanned using a SkyScan 1276 scanner at 7-μm resolution on Week 0, 2, and 4 as published [9], from which the changes of bone structure in tibial mid-shaft (0.35 mm above the tibiofibular junction) were derived and compared among groups. Statistical analysis: Mixed Model and one-way ANOVA were separately chosen to do comparison within and between groups. For conservativeness, pairwise comparisons using Tukey HSD post hoc test were performed.

RESULTS: 24 hours after the 2nd radiation exposure, radiated marrow cells showed a trend of decreased viability ($p = 0.06$) compared with the non-radiation group (Fig. 1A). Surprisingly, the ground control mice all showed positive changes of mid-shaft pMOI (increased bending resistance) regardless of radiation/non-radiation or Yoda1/vehicle treatments (Fig. 1B). Among the mice receiving WBV, those receiving vehicle treatment or radiation showed negative changes of pMOI (decreased bending resistance), while Yoda1 treatment neutralized this negative effect in non-radiated bones, and even increased pMOI in the radiated bones ($p = 0.03$, Fig. 1C).

DISCUSSION: As we expected, radiotherapy of 2x 8 Gy did increase cells apoptosis acutely, possibly due to radiation induced DNA double-strand breaks (DSBs) [10] and release of reactive free radicals (ROS) [11] (Fig. 1A). In contrast with the positive skeletal effects of Yoda1 on young mice [12], we did not find additional skeletal benefits of Yoda1 on adult mice compared with vehicle treated ground control mice. Although Yoda1-augmented WBV appeared to be beneficial in adult mice after radiation compared with vehicle-treated mice, Yoda1 alone didn't produce noticeable beneficial effects, possibly due to the reduced mechano-sensitivity of the mature skeletal system. It remains unclear why some mice showed decreased pMOI under vibration even without radiation. The small sample size might be a reason. The frequency of our WBV device (12 Hz) was more than 2-fold lower than the ones used in clinical studies (30 Hz), resulting > 4-fold higher vertical displacements that might have induced stress experienced by the mice. Ongoing work on histology and cellular assays will provide insights on the overall effects of Yoda1 and WBV alone or combined when applied after radiotherapy. The WBV parameters will be further optimized before the treatment strategy being tested in aged mice with breast cancer.

SIGNIFICANCE/CLINICAL RELEVANCE: This study represented an initial attempt to test the potential of Yoda1-augmented whole-body vibration as an adjuvant strategy in treating older metastatic breast cancer patients with compromised skeleton.

REFERENCES: [1]. Chen M,T et al. 2017, [2]. D. Miller MPH et al. 2022, [3]. L.W. Jones et al. 2016, [4]. C.M. Alfano et al. 2012, [5]. Meghan W et al. 2009, [6]. Margaret M et al. 2021, [7]. Marin-Cascales, E et al. 2018, [8]. Xuehua Li et al. 2019, [9]. Chun-Yu Lin et al. 2022, [10]. Shubo Wang et al.2021, [11]. Chandra, A et al. 2017, [12]. Kondo H et al. 2010
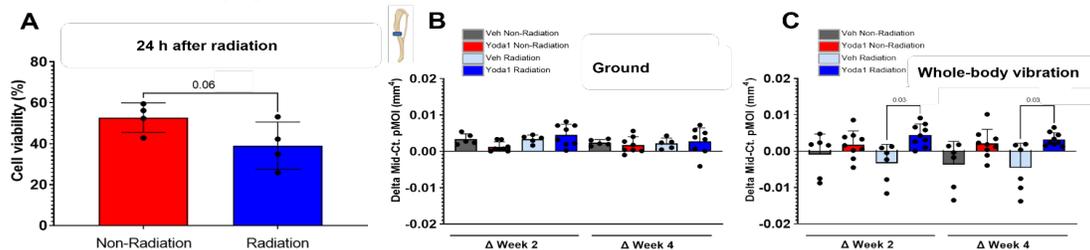
Fig. 1. The effects of Yoda1-augmented WBV (12 Hz, 0.25 g) on the skeletal integrity of adult mice (31 to 36 weeks) receiving radiotherapy. (A) Radiation resulted in decreased viability of marrow nucleated cells 24 hours after in vivo exposure. (B) For ground control groups, there were no additional beneficial effects of Yoda1-based interventions. (C) In contrast, for WBV groups, the benefit of preserving bone pMOI was seen in Yoda1 treated mice only after radiation ($p < 0.05$).
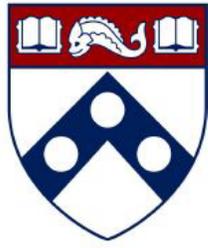
Histology Abstracts

GLUT1 is redundant in hypoxic and glycolytic nucleus pulposus cells of the intervertebral disc

Shira N. Johnston[1,2,#], Elizabeth Silagi[1,2,3,#], Vedavathi Madhu[1], Duc H. Nguyen[1,2], Irving M. Shapiro[1,2], Makarand V. Risbud[1,2]

[1]Department of Orthopaedic Surgery, Sidney Kimmel Medical College, Thomas Jefferson University, Philadelphia, PA, USA
[2]Graduate Program in Cell Biology and Regenerative Medicine, Jefferson College of Life Sciences, Thomas Jefferson University, Philadelphia, PA, USA
[3]Current affiliation - Department of Neuroscience, Dana Farber Cancer Institute, Harvard Medical School, Boston, MA, USA
[#]Have contributed equally to this work

INTRODUCTION:

Glycolysis is central to homeostasis of nucleus pulposus (NP) cells in the avascular intervertebral disc. Since the glucose importer, GLUT1, is a well-established phenotypic marker of NP cells, we hypothesized that it is vital for development and post-natal maintenance of the disc. Despite the well-studied importance of glucose availability and consumption on NP cell viability *in vitro*, few studies have elucidated the correlation between glucose consumption and disc degeneration *in vivo*. This is due to the complexity of studying solute transport and metabolite concentrations in animal models or by using genetic techniques. Studies have shown enriched expression of GLUT1 in human NP and that GLUT3 and GLUT9 levels were lower than GLUT1. These results suggest that GLUT1 expression may be required for health and maintenance of the intervertebral disc with age. Mouse models of Glut1 loss of function in growth plate and articular cartilage demonstrate that Glut1 function is required for cartilage homeostasis, particularly relating to cell proliferation, matrix production and resistance to injury and osteoarthritis. Since GLUT1-mediated glycolytic metabolism plays a fundamental role in many tissues including bone and cartilage homeostasis, we surmised that loss of GLUT1 expression in the NP would impact both disc development and age-related maintenance.

METHODS:

In vivo: Glut1$^{f/f}$ mice were crossed with K19^{CreERT} to delete GLUT1 in keratin19-expressing cells. The spines of 9-month-old (9M) K19^{CreERT}; Glut1$^{f/f}$ (Glut1cKO^{K19}) (n=7 mice) and GLUT1$^{f/f}$ (WT) (n=7-8 mice) mice were analyzed. Additionally, Glut1$^{f/f}$ mice were crossed with FoxA2^{Cre} to delete GLUT1 in FoxA2-expressing cells. The spines of P7 and 14-week-old FoxA2^{Cre}; Glut1$^{f/f}$(Glut1cKO^{FoxA2}) (n=5 or 9 mice/t.p.) and Glut1$^{f/f}$ (WT) (n=5 or 11 mice/t.p) mice were analyzed. Lumbar and caudal discs were sectioned in the mid-coronal plane and morphological changes were evaluated by Safranin-O/Fast Green staining, aspect ratio, and grades of degeneration were quantified using modified Thompson scheme. Picrosirius Red and polarized light quantitative microscopy and quantitative immunohistochemistry were used to measure compositional changes. μCT imaging of the spinal column was performed to quantitively assess vertebral morphology and changes in disc height. Microarray and RT-PCR were used to determine transcriptomic changes in Glut1cKO^{K19} NP tissue. Western blot was used to evaluate protein expression and confirm RT-PCR findings. In addition, previously generated E15.5 NP of FoxA2^{Cre}; HIF-1α$^{f/+}$ and FoxA2^{Cre}; HIF-1α$^{f/f}$ mice were used to assess expression of GLUT1 and GLUT3. All animal studies were performed in accordance with protocols approved by the Institutional Animal Care and Use Committee (IACUC) of Thomas Jefferson University. *In vitro:* Rat NP cells were isolated and maintained in DMEM with 10% FBS and antibiotic. Cells were treated with specific GLUT1 inhibitors (BAY-876 or WZB-117) or with a GLUT1,2,3 inhibitor (GLUTOR) for up to 72 hours. Seahorse was used to determine the effects using GLUT1 inhibitor, or Glutor, on ECAR and OCR, while substrate dependent Seahorse experiments evaluated glutamine metabolism and fatty acid oxidation under GLUT1 or GLUT1,2,3 inhibition. Glucose utilization was assessed by 2-deoxyglucose uptake assay. NP cell viability after treatment was done using Calcein AM cell viability assay out to 72 hours. All *in vitro* experiments were done in 4-6 biological replicates with 4 technical replicates/experiment/group.

RESULTS SECTION:

In vivo: Successful deletion of GLUT1 in NP cells in skeletally mature mice (9M Glut1cKO^{K19}) was verified by RT-PCR showing a ~95% reduction in mRNA levels in NP and by Western blot showing loss of GLUT1 protein. Histological analysis of Glut1cKO^{K19} mice showed NP specific loss of GLUT1 did not affect NP and AF cell morphology, cell number, or disc structure at 9M of age. Additionally, quantitative immunohistochemistry, μCT, assessment of AF lamellae, microarray, and RT-PCR of Glut1cKO^{K19} mice showed loss of GLUT1 did not have adverse effects on intervertebral disc health and no change in mRNA expression of *Glut3, Glut9, Sglt1*. Histological analysis of Glut1cKO^{FoxA2} mice showed NP specific loss of GLUT1 did not affect NP and annulus fibrosus cell morphology, cell number, or disc structure at postnatal day 7 (p7) nor at 14-weeks (14wks) of age. Interestingly, the NP of E15.5 FoxA2^{Cre}; HIF-1α$^{f/f}$ mice showed both loss of GLUT1 and GLUT3. *In vitro:* Although short term inhibition (1 h) of GLUT1 using BAY-876 and WZB-117 did impact ECAR indicating initial impact on NP glycolysis, long term (24 h) inhibition of GLUT1 did not affect glycolytic or oxidative metabolism in NP cells. Glucose uptake and cell viability was only impacted when using Glutor (a GLUT1,2,3 inhibitor), but not when using GLUT1 specific inhibitors. Substrate dependent Seahorse experiments with glucose + glutamine or BSA-palmitate were used to assess the effects of effects on glutamine metabolism and fatty acid oxidation respectively, with NP cells treated with Glutor for 24 hours prior to Seahorse assessment. The resulting substrate dependent Seahorse data showed that loss of GLUT1/3 function did not result in NP cells switching to glutamine or fatty acid oxidation, and glucose import through GLUT1/3 is indispensable for NP cell metabolism.

DISCUSSION:

Contrary to other skeletal tissues, both conditional and inducible loss of GLUT1 expression in the NP did not instigate notable degenerative changes in the discs of developing perinatal mice or in skeletally mature mice. Surprisingly, microarray analysis of global transcriptomic changes in NP tissue isolated from conditional GLUT1 knock-out mice did not uncover any differentially regulated genes besides *Slc2a1* (encoding GLUT1) – a finding which suggests NP cells are refractory to loss of GLUT1. In fact, long-term GLUT1 inhibition had no effect on the rates of NP glycolytic flux or oxidative metabolism since NP cells potentially mitigate the loss of GLUT1 function by rewiring glucose import through GLUT3. Importantly, our findings suggest that under glucose limiting conditions resulting from inhibition of GLUT1/3, NP cells do not undergo metabolic reprogramming to use alternative substrates, such as glutamine and fatty acids. These findings provide the first evidence of functional redundancy in GLUT transporters in a physiologically hypoxic intervertebral disc and underscore the importance of glucose as the indispensable metabolic substrate for NP cells. Overall, our study provides the first evidence of functional redundancy in GLUT transporters in a physiologically hypoxic NP compartment of the intervertebral disc and highlights its uniquely different niche than other skeletal tissue like articular and growth plate cartilage. Importantly, our findings underscore the importance of glucose as the indispensable metabolic fuel for NP cells and provides vital baseline for any cell-based therapies aimed at restoring the function of degenerating disc.

SIGNIFICANCE:

Glucose import into hypoxic nucleus pulposus cells is critical for maintaining glycolysis and intervertebral disc health, however import through GLUT1 is surprisingly redundant as another high-capacity glucose transporter, GLUT3, appears sufficient to compensate for loss of GLUT1 function; and, under glucose limiting conditions, NP cells do not switch to utilizing glutamine or fatty acid palmitate as metabolic substrates for mitochondrial oxidation. These findings contrast with the critical role that GLUT1 plays in the development and homeostasis of bone and cartilage.

ACKNOWLEDGEMENTS:

Roles of TNFAIP8 family in intervertebral disc degeneration

Zuozhen Tian [1], Lutian Yao [1], Alec Sandroni[1], Honghong Sun [1], Ling Qin [1], Yejia Zhang [1, 2]
[1]Perelman School of Medicine, University of Pennsylvania;
[2]Corporal Michael J. Crescenz Veterans Affairs Medical Center, Philadelphia, PA

INTRODUCTION: The TNFa-induced protein-8 (TNFAIP8, also known as TIPE) family of molecules comprises four members: TNFAIP8 and TIPEs1-3. Since the first description of these proteins, their roles in fine-tuning inflammation and in directing leukocyte migration have been described in several organ systems. However, their relationship to intervertebral disc degeneration (IVD) is unknown.

METHODS: TIPE2 has been shown to direct leukocyte migration (Fayngerts, Wang et al. 2017) and we have preliminary evidence that TNFAIP8 participates in this process as well. Here, we studied tail IVDs in TNFAIP8 and TIPE2 double knockout (dko) mice and their wild type littermates (age 20-33 weeks), with the adjacent intact discs as controls. Macrophages were identified by immunostaining of the F4/80 antigen (EMR1), a known marker for cells of monocyte-macrophage lineage (antibody: Cell Signaling Rabbit mAb #70076). CXCL1 (known to attract leukocytes) gene expression was examined by Real Time PCR.

RESULTS. In the injured annulus fibrosus (AF) of wild type (WT) mice, macrophages were easily detectable by F4/80 staining (n=8 mice). In comparison, there was only faint staining in the outer edge of the AF, near the needle entry site (Figure 1, red arrow; n=10 mice). There was minimal staining at the outer edge of the AF, in the intact IVDs of both WT and TNFAIP8/TIPE2 dko mice (Figure 1). Cxcl1 gene expression was upregulated in the injured discs of the WT mice and dko mice compared with adjacent intact controls (n=8 and 10 mice, respectively; p<0.05), but there were no significant differences between the injured discs of the mutant mice and WT mice, with regard to gene expression (p>0.05).

DISCUSSION: We found elevated gene expression of chemokines in the injured discs in both WT and mutant mice, but fewer F4/80 stained cells in the injured AF of the mutant mice, suggesting that the leukocyte is a primary 'target' of the mutation. Future studies include quantifying macrophages in the AF tissues, and correlating IVD morphology and mouse behavior, to further delineate the roles of TIPE molecules in IVD inflammation and degeneration.

Figure 1. TIPE/TIPE2 double knock out (dko) mouse shows reduced macrophage recruitment compared with wild type (WT) mouse. Red arrow: direction of injury to the annulus fibrosus (AF). **Bar:** 50 µm. **Blue dotted line in intact discs** outlines the border of AF and nucleus pulposus (NP).

SIGNIFICANCE/CLINICAL RELEVANCE: Macrophages, found in diseased human IVDs (Nakazawa, Walter et al. 2018, Shamji, Setton et al. 2010) may be of pathophysiological significance.

REFERENCES:

1. Fayngerts SA, et al. Direction of leukocyte polarization and migration by the phosphoinositide-transfer protein TIPE2. Nat Immunol. 2017 Dec;18(12):1353-60. PMCID: PMC5690821.

2. Nakazawa KR et al. Accumulation and localization of macrophage phenotypes with human intervertebral disc degeneration. Spine J. 2018 Feb;18(2):343-56. PMCID: PMC5815908.

3. Shamji MF, et al. Proinflammatory cytokine expression profile in degenerated and herniated human intervertebral disc tissues. Arthritis Rheum. 2010 Jul;62(7):1974-82. PMCID: PMC2917579.
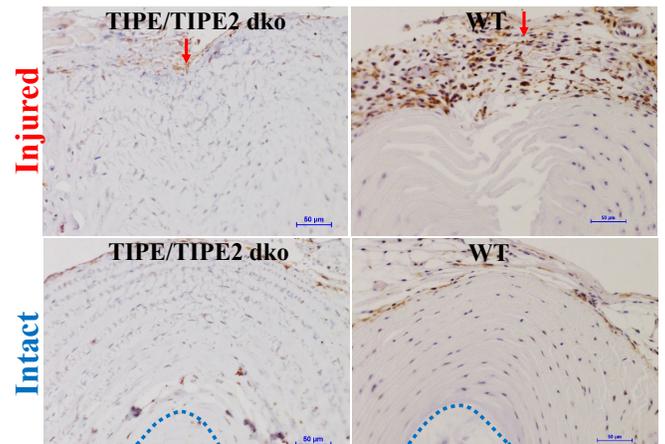
ADAM8 Inactivation Retards Intervertebral Disc Degeneration in Mice

Zuozhen Tian[1], Frances S. Shofer, PhD[2], Mingyue Fan[4], Alec Z. Sandroni[1], Lutian Yao, MD[3,5], Lin Han, PhD[4], Ling Qin, PhD[3], Motomi Enomoto-Iwamoto, DDS, PhD[6], Yejia Zhang, MD, PhD[1,3,7]

[1]Departments of Physical Medicine & Rehabilitation, [2]Emergency Medicine, and [3]Orthopedic Surgery, Perelman School of Medicine, University of Pennsylvania; Philadelphia, PA.

[4]School of Biomedical Engineering, Science & Health Systems, Drexel University, Philadelphia, PA.

[5]Department of Orthopaedics/Sports Medicine and Joint Surgery, First Affiliated Hospital, China Medical University, Shenyang, Liaoning, China.

[6]Department of Orthopedics, University of Maryland School of Medicine, Baltimore, MD.

[7]Section of Rehabilitation Medicine, Corporal Michael J. Crescenz Veterans Affairs Medical Center, Philadelphia, PA.

Introduction. Previously, ADAM8 and its proteolytic product, fibronectin fragments, were found elevated in degenerative human IVDs.[1] The annulus fibrosus (AF) tissue of 3-month-old mice with ADAM8 inactivated (the *Adam8^EQ* mice) was slightly enhanced than WT controls.[2] In this study, middle aged mice were examined in the current study to better model human intervertebral disc (IVD) degeneration.

Methods. Intact lumbar spine IVD and injured coccygeal discs were compared between 10-month-old *Adam8^EQ* and age-matched wild type (WT) control mice.

Methods. Ten-month-old mouse lumbar spines were examined histologically. The mouse coccygeal (Co) IVDs at Co3/4 and Co5/6 were injured with a 26G needle, Co4/5 and Co6/7 served as intact controls. RNA was extracted from Co3/4 and 4/5 IVDs, and gene expression was determined by real-time PCR. Co5/6 and 6/7 were used for histochemical staining. Safranin O and Picrosirius Red stained sections were analyzed for proteoglycan density and collagen fiber size. Collagen fibril size was further measured by scanning electron microscopy.

Results. The intact IVDs of middle aged *Adam8^EQ* mouse had higher proteoglycan content and reduced aggrecan degradation compared with those of WT mice (n=24 and 15; p<0.05). Scanning electromicroscopy (SEM) revealed that the AF were thicker in the *Adam8^EQ* than in WT control mice (p=0.043). *Adam8^EQ* mouse AFs also contain a lower proportion of large collagen bundles (p<0.05). Interestingly, type II collagen gene expression is higher in the injured coccygeal IVDs of *Adam8^EQ* mice than in WT controls (p<0.01).

Significance. ADAM8-inactivation resulted in more proteoglycans and thicker AF in the normal IVDs. Inhibition of this enzyme may be considered a novel strategy to retain extracellular matrix and prevent IVD degeneration.

References.
1.Ruel N *et al. Spine*. 39(16): 1274–1279 (2014).
2.Zhang Y *et al. Sci Rep.* 11, 1804 (2021).

Inflammation Alters Inner Zone but Not Outer Zone Meniscus Cell Migration via Nanoscale Histone Reorganization

Yize Zhang[1], Yujia Zhang[1], Zizhao Li[1], Se-Hwan Lee[1], Lucy Hederick[2], Joel D Boerckel[1], Robert L Mauck[1], and Su-Jin Heo[1]
[1]University of Pennsylvania, Philadelphia, PA; [2]Northwestern University, Evanston, IL

Disclosures: Yize Zhang (N), Yujia Zhang (N), Zizhao Li (N), Se-Hwan Lee (N), Lucy Hederick (N), Joel D Boerckel (N), Robert Mauck (8), Su-Jin Heo (5)

INTRODUCTION: Meniscus tears are the most common knee injuries and insufficient meniscus repair can lead to osteoarthritis and adversely impact activities of daily living. Appropriate cell migration to the wound sites is required for the proper healing. During healing, increases in pro-inflammatory cytokines in the wound environment are observed, which inhibits repair [1]. It is widely understood that cells in the inner vs outer meniscus zones have different phenotypes [2]. However, differences in cell migration behaviors of the two different meniscus cell types and how they respond to inflammatory conditions are not well understood. Previous studies have shown that histone modifications in cell nuclei (e.g., tri-methylation of lysine 27 on histone H3, H3K27me3) change during the migration of various cell types [3]. However, whether such epigenetic mechanisms impact meniscus cell migration and its 'zonal-dependency' remain unexplored. Thus, we explored how inflammatory conditions affect the migration of inner and outer zone meniscus cells and further investigated the epigenetic mechanism underlying this response.

METHODS: Inner or outer zone meniscus cells were harvested from juvenile (< 3 months) bovine menisci (**Fig. 1a**). Wound closure assays (WCA) were performed on cells (Passage 1) seeded in 12-well dishes with imaging taken via brightfield 0 and 12 hours after scratch (**Fig. 1b**) with/without treatment with tumor necrosis factor-alpha (TNF-α, 10 nM). Wound closure was quantified by the percent closure of a predefined area at the time of scratch using Image J. To investigate how meniscus cell migration alters H3K27me3 (a marker of transcriptional suppression or condensed heterochromatin) levels in cells at the migration "front" (**Fig. 2a**) or on the migration "back" (10 cell-layers behind the "front") (**Fig. 2a**). At each time point, cells were fixed and immunofluorescence for H3K27me3 (Cell Signaling) was performed using a confocal microscope (Zeiss) and quantified using Image J. Further, to investigate the role of the histone methyltransferase, EZH2 (a histone methyltransferase that catalyzes H3K27me3) in meniscus cell migration, WCBs were performed with inner or outer zone meniscus cells treated with GSK343 (a selective EZH2 inhibitor, 2~14 μM). Finally, to investigate how cell migration and/or TNF-α treatment alters nanoscale chromatin organizations, cells were fixed at each time point and immunostained for histone-H2B (H2B, Proteintech.) Cells were then incubated with secondary antibodies custom labeled with activator-reporter dye pairs (Alexa Fluor 405-Alexa Fluor 647, Invitrogen) for super-resolution stochastic optical reconstruction microscopy (STORM) imaging (Nanoimager, ONI) [4]. H2B staining and Voronoi cluster analysis-based chromatin density and distribution were determined using our established protocols [4]. All experiments were performed in triplicates with 3 different donors. Statistical analyses were performed via ANOVA with Tukey's post hoc testing.

RESULTS: No significant differences were observed in the baseline migration of inner zone (Inner Cell-Ctrl) and outer zone (Outer Cell-Ctrl) meniscus cells (**Fig. 1c**). When inner (Inner Cell-TNF-α) and outer cells (Outer Cell-TNF-α) were treated with the pro-inflammatory cytokine TNF-α, only inner meniscus cells decreased in migration compared to their untreated control (**Fig. 1c**). At 1 hour after scratch, when the "front" cells had just started to migrate, the intensity of H3K27me3 in inner cells located at the "front" (Inner Cell-Front) was higher than in inner cells located at the "back" (Inner Cell-Back) (**Fig. 2b**). The intensity gradually increased as cell migrated (**Fig. 2b**) and cells located further from the migration front slowly caught up to the migration front level during the 12-hour migration period (**Fig. 2b**). More interestingly, the average baseline level of H3K27me3 in the inner cells was higher than in the outer cells during migration (**Fig. 2b**). When the cells were treated with GSK343 to decrease the EZH2 activity, cell migration speed decreased in the inner cells, but not in the outer cells (**Fig. 2c**). Consistently, H2B STORM images revealed that cell migration increased nanoscale chromatin condensation in the inner cells while it significantly decreased in outer cells (**Fig. 3a, b**). Most interestingly, with TNF-α treatment, inner meniscus cells showed a much more significant decrease in chromatin compaction in response to TNF-α, compared to outer meniscus cells. (**Fig. 3c**).

DISCUSSION: In this study, we demonstrated that the inner meniscus cell migration is more sensitive to the pro-inflammatory cytokine TNF-α than the outer meniscus cell migration. It is known that H3K27me3 (which is catalyzed by EZH2 inducing chromatin condensation) is required for cell migration [3]. In this study, interestingly, we found that chromatin condensation (mediated by H3K27me3) is accompanied by only the inner meniscus cell migration, and the TNF-α treatment results in chromatin relaxation decreasing only the inner cell migration speed (but not the outer cell migration). These findings indicate that the responses of meniscus cells to inflammatory conditions are meniscus-zone dependent and rely on different epigenetic mechanisms. To further understand how inflammatory conditions differentially alter epigenetic signaling and migration in inner and outer meniscus cells, current studies are focused on profiling changes in chromatin accessibility using ATAC-Seq and understanding the impact of histone modifications through ChIP-Seq during meniscus cell migration under inflammatory conditions.

SIGNIFICANCE: Our data shows that inner and outer meniscus cells have different epigenetic mechanisms for cell migration under inflammatory conditions. This study may inform new directions in whole meniscus tissue engineering and novel epigenetic therapeutics for zonal-specific meniscus repair strategies.

REFERENCES: [1] Hennerbichler +, Osteoarthr. Cartil. 2007; [2] Furumatsu+, Connect. Tissue Res. 2011; [3] Gerlitz+, J. Cell Sci. 2010; [4] Heo+, Nature BME. 2022.
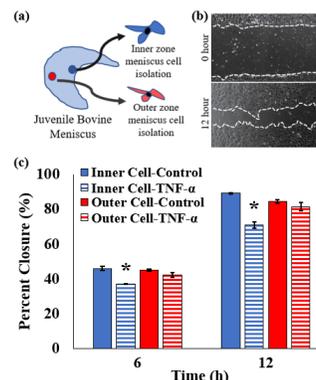
Figure 1: (a) Schematic showing isolation of inner and outer zone meniscus cells (from 3 different donors). (b) WCA images and (C) results quantified as percent wound closure over time (n=6/group, *: p<0.05 vs. Control).
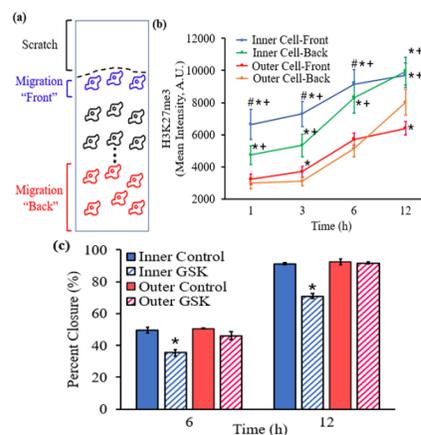
Figure 2: (a) A schematic showing H3K27me3 immunofluorescence intensity measurements in cells located at the migration front (Front) vs. at 10 cell-layers behind the migration front (Back) and (b) quantifications (n>100/group, *: p<0.05 vs. Outer Cell-Back, +: p<0.05 vs. Outer Cell-front, #: p<0.05 vs. Inner Cell-Back). (C) Inner vs outer meniscus cell migration with/without treatment with an EZH2 inhibitor (GS, 10 μM, n=6/group, *: p<0.05 vs. Control).
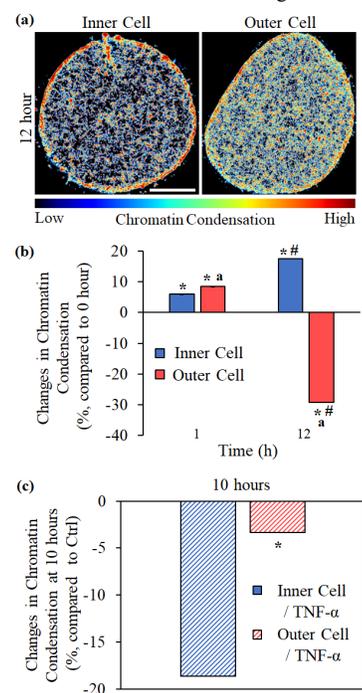

Figure 3: (a) Representative H2B-STORM images (bar = 5μm) and (b) percent change in chromatin condensation in nuclei at the migration "front" (n=7/group, *: p<0.05 vs. Ctrl 0h, a: p<0.05 vs. Inner, #: p<0.05 vs. 1h). (c) Percent change in chromatin condensation in the inner or outer cell nuclei with TNF-α treatment at the 10-hour time point during the cell migration (normalized to non-treated controls), *: p<0.05 vs. Inner Cell/TNF-α).

Loss of mitochondrial fusion protein OPA1 disrupts cell organelles integrity leading to NP tissue degenerative phenotype in mice

Miriam Hernandaz-Meadows[1], Vedavathi Madhu[1], Paige K Boneski[3], Yunping Qiu[4], Irwin Kurland[4], Makarand V. Risbud[1,2]

[1]Department of Orthopaedic Surgery, Thomas Jefferson University, Philadelphia, PA
[2]Cell Biology and Regenerative Medicine Graduate Program, Thomas Jefferson University, Philadelphia, PA
[3]Department of Neuroscience, Mayo Clinic, Jacksonville, FL
[4]Einstein-Mount Sinai Diabetes Research Center (ES-DRC) Albert Einstein College of Medicine, Bronx, NY

Introduction: Nucleus pulposus (NP) cells of the intervertebral disc lack tissue vascularity, and therefore reside in a hypoxic environment and depend on glycolytic metabolism for energy production. Due to its unique niche, the NP is believed to contain few functional mitochondria. We recently showed that NP cells possess functional and well-networked mitochondria. As highly dynamic organelles, mitochondrial number and mass is regulated through constant fusion and fission events. Previously we have shown that HIF-1α regulates mitochondrial morphology, number, and mitophagy in hypoxic NP cells by modulating the levels of DRP1 and OPA1, key fission and fusion proteins respectively, and mitophagy receptor BNIP3. Since mitochondria function is fundamentally tied to its ultrastructure, alternations in the number, size, and shape lead to functional deficits and disease states. It has been shown that mitochondrial morphology and dynamics are altered in several degenerative, metabolic diseases and aging. Recently, we have shown in two independent studies that loss of HIF-1α and BNIP3 results in altered mitochondrial morphology which leads to dysregulation of mitochondrial functions in NP cells. In the present study, we directly modulated the inner mitochondrial membrane fusion protein OPA1 in NP tissue using *in vivo* and *in vitro* loss of function approach and investigated the consequences on disc health during aging.

Methods: To understand the functions of OPA1 *in vivo*, we postnatally deleted OPA1 in NP compartment using Krt19CreERT and characterized the spinal phenotype of OPA1f/f: Krt19CreERT (OPA1cKO) and OPA1f/f (WT) mice at 20 months. Lumbar spines from WT and OPA1cKO mice were decalcified, and mid-coronal disc sections were stained with Safranin O/Fast Green/Hematoxylin and visualized using light microscopy. Modified Thompson scoring was performed on mice of both genotypes. To gain mechanistic insights into the contribution of OPA1 in organelle morphology and metabolism we studied primary rat NP cells transduced with ShOPA1 and ShCtrl lentivirus. Using confocal microscopy, we explored the role of OPA1 on organelles morphology including mitochondria in transduced NP cells cultured. In addition, we performed metabolomic flux analysis using [1,2]-13C-glucose and 13UC-glutamine labeling followed by GC-MS to measure the derivatized metabolites and the data were analyzed with MassHunter Quantitative Analysis software.

Results: OPA1cKO mice evidenced compromised disc health at 20 months, as there was significantly higher Modified Thompson grading. Expression levels of NP cell phenotypic marker CA3 and an abundant proteoglycan in the disc, aggrecan, were not affected; however, chondroitin sulfate a major component of aggrecan, and pro-inflammatory cytokine IL-6 expression was significantly increased in cKO mice. As OPA1 is mainly studied in context of mitochondria as it is localized to the mitochondrial inner membrane, interestingly, we noted that loss of OPA1 resulted in structural changes to organelles in addition to mitochondria. Specifically, we observed fragmented Golgi apparatus, enlarged early endosomes, and altered peroxisomes compared to ShCtrl. [1,2]-13C-glucose labeling studies demonstrated decreased glycolytic and PDH flux, whereas palmitate and steric acid flux was significantly increased in ShOPA1 cells. In addition, 13UC-glutamine labeling exhibited decreased TCA cycle intermediates citrate, fumarate, malate, and aspartate suggesting that altered organelles morphology contribute to the reformed metabolism.

Discussion: Altered mitochondrial morphology and dynamics are linked to several degenerative, metabolic diseases and aging. Our studies show that loss of OPA1 in aging mice NP tissue increased IL-6 expression which is one of the major pro-inflammatory cytokines associated with intervertebral disc degeneration and lower back pain. Interestingly, chondroitin sulfate level was significantly increased in the OPA1cKO mice and chondroitin sulfate shown to have anti-inflammatory activity and subdues IL-6 induction. Further, in vitro studies suggested that OPA1 is necessary to maintain organelles morphology as mitochondria physically interacts with other organelles. We further showed that OPA1 is one of the key regulators of NP cells glycolytic and mitochondrial metabolism. Taken together data suggests that OPA1 is vital for maintaining the integrity of organelles and therefore, NP cell/tissue homeostasis.

Significance: Our studies reveal that OPA1 is not only critical for mitochondria morphology and function, but it is also critical for multi-organelles structure/function homeostasis in NP cells.

Driving Osteogenesis in Composite Biomaterials Using Tunable Hydroxyapatite Surface Modifications

Matthew Fainor[1,2], Janai Augustin[2,3], Harvey E. Smith[1,2], Robert L. Mauck[1,2], Sarah E. Gullbrand[1,2]
[1]University of Pennsylvania, Philadelphia, PA; [2]Corporal Michael J. Crescenz VA Medical Center, Philadelphia, PA; [3]City College of New York, NYC, NY
Disclosures: MF – Matthew.Fainor@pennmedicine.upenn.edu (N), JA (N), HES (N), RLM (8), SEG (6)

INTRODUCTION: Satisfactory clinical outcomes following spinal fusion can range from 46% [1] to 82% [2]. To make spinal interventions more successful, hydroxyapatite (HA) has been commonly used to modify titanium and PEEK spinal fusion cages [3], as well as biodegradable polymeric implants [4]. Our lab has previously created a protocol for creating robust, scalable, and tunable HA surface coatings on poly(caprolactone) (PCL) scaffolds through direct immersion in SBF, which can upregulate markers of osteogenesis in mesenchymal stem cells *in vitro* [5]. Because of its ability to induce osteogenesis in a spatially controlled manner, hydroxyapatite surface coating has also been combined with other biomaterials in composite tissue engineered scaffolds, such as gradient [6] or zoned [7] polymeric ligament replacements. However, this approach has yet to be explored for tissue engineering applications in the spine, such as inducing localized osteogenesis in the endplate region of a whole, tissue engineered disc replacement. We hypothesized that HA coating would enhance osteogenesis in acellular scaffolds implanted *in vivo* and that this would not affect the chondrogenic maturation of adjacent cell-seeded regions during *in vitro* culture.

METHODS: PCL scaffolds (rat vertebra: 5 mm in diameter x 5 mm in height; goat endplate: 16 mm diameter x 1.5 mm in height) were fabricated according to a previously established salt-leaching protocol [8]. Rat vertebra- or goat endplate-sized scaffolds were then hydrolyzed in 2M NaOH for 24 hours and immersed in 10X or 40X SBF, respectively, for 7 days. The formation of HA crystals was characterized using μCT and SEM imaging. Hydrolyzed PCL or HA-coated PCL scaffolds were then implanted into the caudal intervertebral disc space of athymic rats (n = 3/group) following total discectomy, according to a previously described IACUC approved surgical method [9]. Rats were euthanized 15 weeks post-implantation and vertebral body—implant—vertebral body segments were dissected. HA-coated PCL or uncoated PCL scaffolds were also used in the fabrication of endplate-modified Disc-like Angle Ply Structures (eDAPS) (n = 3) to be used as total tissue engineered disc replacements [10], as previously described [11]. eDAPS were cultured in chemically defined media with TGF-β3 with constant agitation for 10 weeks. Each rat tail and half of each eDAPS was embedded in OCT and cryosectioned in the sagittal plane to a thickness of 18 μm using the Kawamoto tape method [12] for immunohistochemical detection of osteocalcin and osteopontin. Following cryosectioning, each rat tail and the second half of each eDAPS was processed for paraffin histology. 10 μm and 15 μm sections, respectively, were stained with Hematoxylin/Eosin, Alcian Blue/Picrosirius Red, Red Green Blue Trichrome, and Mallory Heidenhaim Trichrome.

RESULTS: The formation of robust and homogeneous hydroxyapatite crystals was observed on HA-coated scaffolds (**Figure 2A&B**). Scaffolds were successfully implanted into rat tail caudal disc spaces (**Figure 1A**). After 15 weeks *in vivo*, all scaffolds were fully cellularized (**Figure 1B**). This cellularization led to increased deposition of osteopontin and osteocalcin (**Figure 1C-D**) as well as increased staining for unmineralized bone (**Figure 1E-F**) throughout HA-coated scaffolds. HA coating of acellular endplates did not induce mineralization in, or affect the maturation of, the adjacent cell-seeded NP and AF analogs during *in vitro* culture of the tissue engineered disc composite (**Figures 2A&B**).

DISCUSSION: Our results suggest that the use of tunable SBF-based HA coating can promote higher levels of osteogenesis *in vivo*. After 15 weeks *in vivo*, this upregulation of osteogenic protein deposition did not however lead to full osseointegration in any of the samples. The presence of concentrated areas of unmineralized bone tissue within HA-coated implants suggests that bone may continue to form over longer periods of time. Results from other *in vivo* trials assessing the use of HA coating on scaffolds vary widely [13]. Although our implants were fully cellularized after 15 weeks,
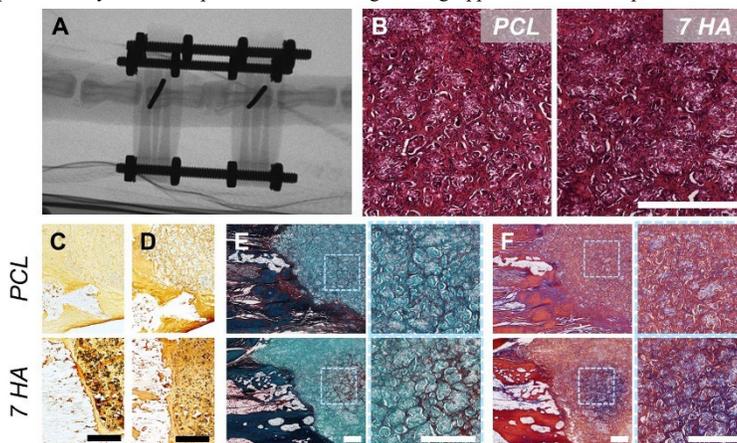

Figure 1. (A) Surgical X-ray showing HA-coated scaffold implantation and fixation. 15-weeks post-implantation: (B) H+E staining of implant centers (500μm), (C) osteopontin IHC (1mm), (D) osteocalcin IHC (1mm), (E) Red Green Blue Trichrome (500μm), and (F) Mallory-Heidenhaim (500μm) (Left: native bone; Right: implant).
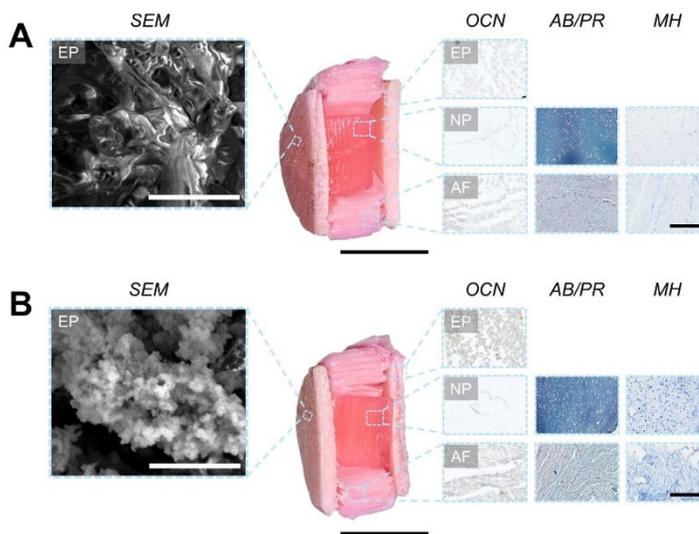

Figure 2. eDAPS fabricated with (A) uncoated or (B) HA-coated PCL endplate analogs. From left to right: representative SEM (15μm), macroscopic eDAPS sagittal cross-section (6mm), osteocalcin (OCN), Alcian Blue/Picrosirius Red (AB/PR), and Mallory Heidenhaim Trichrome (MH) staining (500μm) of the endplate (EP), nucleus pulposus (NP), and annulus fibrosus (AF) regions of the eDAPS.

the 106 μm pore size of our PCL scaffolds is likely too small to allow for short-term remodeling. Pursuing angiogenic-coupled-osteogenesis has been suggested as a more successful strategy for inducing bone deposition and could be achieved by introducing a combination of pore sizes (around 100μm and 300μm) [14-15]. Furthermore, our results demonstrate that the use of HA coating in a composite biomaterial does not negatively influence non-HA-coated cellular components, even if those components have a large surface contact area with the HA crystals. Optimization of scaffold morphology for angiogenesis in combination with SBF-based HA coating will likely increase the success of discrete bone formation in applications that require multi-tissue regeneration.

SIGNIFICANCE: Understanding how hydroxyapatite influences osseointegration of composite biomaterials is critical to the success of strategies that seek to regenerate multiple tissues simultaneously, such as a large multi-component tissue-engineered disc replacement.

REFERENCES: [1] Wetzel+ *Spine,* 1994. [2] Thomsen+ *Spine,* 1997. [3] Rao+ *Orthopaedic Surgery,* 2014. [4] Chuenjitkuntaworn+ *J Biomed Mater Res A,* 2010. [5] Fainor+ *ORS 2022*, Paper #0390. [6] Chen+ *ACS Biomater Sci Eng*, 2021. [7] Olvera+ *ACS Biomater Sci Eng*, 2020. [8] Kim+ *Acta Biomater, 2020*. [9] Martin+ *Sci Rep*, 2017. [10] Gullbrand+ *Sci Transl Med*, 2018. [11] Gullbrand, *Acta Biomater,* 2018. [12] Kawamoto+ *Stain Technology, 1986.* [13] Surmenev+ *Curr Opin in Biomed Eng,* 2019. [14] Karageorgiou+ *Biomaterials,* 2005. [15] Liu+ *Mater Sci Eng C,* 2020

Ectopic ossification of the temporomandibular joint (TMJ) in a murine model of Osteogenesis Imperfecta

Joohyun Lim, Carolina Leynes, Brian Dawson, Brendan Lee

Department of Biological Sciences, University of Delaware, Newark, DE 19716
Department of Molecular and Human Genetics, Baylor College of Medicine, Houston, TX 77030

Temporomandibular disorders (TMDs) derive from abnormalities in the temporomandibular joint (TMJ) and adjacent connective tissues that cause severe orofacial pain and reduced range of motion. TMDs negatively affect the quality of life in an estimated 10 million individuals in the U.S. alone which creates an immense healthcare burden. However, the mechanistic basis underlying TMDs are poorly understood. Here, we report a murine model of osteogenesis imperfecta (OI) which displays aberrant bone formation in the tendon-bone interface (TBI) of TMJ due to defects in the posttranslational modification and cross-linking of collagen I. The lysyl hydroxylase 2 (LH2) complex, which consists of LH2 and FKBP10, is required for telopeptide lysyl hydroxylation of procollagen I and, hence, collagen cross-linking. Loss-of-function mutations in *FKBP10* causes OI with joint contracture. In addition, we recently reported that tendon-specific deletion of *Fkbp10* causes postnatal joint deformities and impaired locomotor function which corroborates the phenotypic spectrum observed in patients. Interestingly, conditional deletion of *Fkbp10* also induced abnormal ossification in TMJ that increases mandibular condyle length and width at 6 and 18 months-of-age, despite normal mandibular development. The ectopic bone formation in TMJ of *Fkbp10*-deficient mice was triggered by ectopic bone growth in the TBI at 1.5 months-of-age. Interestingly, abnormal bone growth in *Fkbp10* mutants coincided with a significant increase in αSMA-expressing cell populations in the TBI. Furthermore, these αSMA-positive cells rapidly contributed to ectopic bone growth in a localized manner, indicating that *Fkbp10* is likely required for preventing abnormal differentiation of this cell population. Collectively, the data suggests that posttranslational modification of the collagen matrix is critical for postnatal tissue homeostasis of the TMJ, in part through regulating a unique population of cells in the TBI. (Funding: F32AR070612, P01 HD070394, HD024064, U54HD083092).

Loss of hypoxia-inducible factor 1α in the presomitic mesoderm alters the process of somitogenesis and causes spine and rib abnormalities reminiscent of Jarcho-Levin Syndrome

Brittany M. Laslow[1], Matthew J. Anderson[2], Mohd Parvez Khan[1], Mark Lewandoski[2] and Ernestina Schipani[1]

[1]Department of Orthopaedic Surgery, Perelman School of Medicine, University of Pennsylvania, Philadelphia, PA, USA
[2]Genetics of Vertebrate Development Section, Cancer and Developmental Biology Lab, National Cancer Institute, National Institutes of Health, Fredrick, MD, USA

Low levels of oxygen, known as hypoxia, occur naturally in various tissues and cells during the development of mammalian embryos. The transcription factor hypoxia-inducible factor 1α (HIF1) controls the cellular response to these hypoxic conditions. It has previously been reported that somites, the blocks of mesodermal cells that give rise to the vertebral bodies, are hypoxic environments.

Since vertebrae and ribs originate from the somites during embryonic development, changes in the HIF pathway could lead to abnormalities in the their development of . To investigate the role that HIF1 plays in somitogenesis and spine development, we conditionally inactivated HIF1 in the presomitic mesoderm (PSM) using TCre mice. TCre$^{(+)}$;HIF-1α$^{(flox/null)}$ mice stained with Alcian blue/Alizarin red at ages E18.5 exhibited several abnormalities associated with the spine and ribs. They showed abnormal curvature of the spine due to misshapen vertebrae, specifically fused vertebrae, hemi-vertebrae and butterfly vertebrae. Ribs displayed fusions, bridging between two ribs, forked ribs, and an additional rib on one or both sides. To determine whether these malformations were due to the previously known fact that lacking HIF1 alters endochondral bone development, we inactivated HIF1 in chondrocytes using Col2a1Cre mice. Col2a1Cre$^{(+)}$;HIF-1α$^{(flox/flox)}$ mice did not show the phenotypes observed in the TCre$^{(+)}$;HIF-1α$^{(flox/null)}$ mice indicating that the rib and vertebral abnormalities were not due to a failure in endochondral bone development. Since HIF1 is a survival factor for hypoxic cells, TUNEL assay was conducted on paraffin sections of the somites and did not show any signs of cell death, removing dying cells as a reason for impaired somitogenesis. Whole mount in situ hybridization of TCre$^{(+)}$;HIF-1α$^{(flox/null)}$ mice using the Uncx4.1 riboprobe showed that the somite segmentation process was altered.

The spine and rib abnormalities in the TCre$^{(+)}$;HIF-1α$^{(flox/null)}$ mice bear a resemblance to phenotypes observed in human patients with Jarcho-Levin Syndrome. Since 25% of individuals with Jarcho-Levin have mutations in several components of the Notch pathway, we investigated whether TCre$^{(+)}$;HIF-1α$^{(flox/null)}$ mice have altered expression of these Notch pathway genes. Whole mount in situ hybridization revealed altered expression of Notch components Delta-like 1, Hes7, Lfng, and Mesp2 in the PSM of mice lacking HIF1.

Our study reveals that HIF-1α is essential for development of the spine and rib and plays a key role in regulating the Notch pathway during the process of somitogenesis. Follow up experiments are needed to completely understand the relationship between HIF1 and the Notch pathway and in general, the role of HIF1 in somitogenesis.

Assessment of New Bone Formation in a Cyclic Treatment Regimen of Parathyroid Hormone-related Peptide (PTHrP) with and without an Intervening Antiresorptive

Tala Azar, Kruti Desai, Justin Leggin, Wenzheng Wang, Nathaniel Dyment, X. Sherry Liu
McKay Orthopaedic Research Laboratory, Department of Orthopaedic Surgery, University of Pennsylvania,
Philadelphia, PA; talaazar@seas.upenn.edu

Bone mineral density rapidly decreases upon withdrawal from anabolic agents despite their potent effect on promoting bone formation. Our previous studies in ovariectomized (OVX) rats demonstrated an extended anabolic period (EAP) during the first week of PTHrP discontinuation, supporting the use of a cyclic treatment regimen with repeated cycles of on and off PTHrP treatment. We hypothesized that cyclic treatment would induce new bone formation on quiescent surfaces during a new PTHrP treatment cycle and induce an EAP during off PTHrP periods. Furthermore, adding an antiresorptive (alendronate, ALN) during off PTHrP periods would inhibit bone resorption.

OVX rats were given two cycles of 3 wk PTHrP followed by either 3 wk VEH (n=5) or ALN (n=6) and calcein green (G), alizarin complexone (red/R), and tetracycline (yellow/Y) in the sequence of G-G-R-R-Y at wks 0 (start of treatment), 3, 6, 9, and 12 (2 days before sacrifice, Fig A). Using tibial cryosections, dynamic histomorphometry was performed for cycle 1 ON (C1-ON, 1st to 2nd G), C1-OFF (2nd G to 1st R), C2-ON (1st to 2nd R), and C2-OFF (2nd R to Y, Fig B). Only 3% of all active bone formation sites during C2-ON were independent of active sites during C1-ON (Fig C-D), suggesting that a new cycle of PTHrP induced minimal new bone formation on quiescent surfaces. During C1-ON (Fig E-G), there was an 86% and 106% greater mineralizing surface (MS/BS) and bone formation rate (BFR/BS) in cyclic PTHrP-ALN *vs.* PTHrP-VEH, suggesting that ALN minimized withdrawal-induced bone loss during the 1st off PTHrP period. Contrarily, there was a 33% greater C2-ON MS/BS in cyclic PTHrP-VEH *vs.* PTHrP-ALN (Fig H-J), suggesting that ALN may blunt the anabolic effect of PTHrP. In both C1-OFF and C2-OFF, new bone deposition was drastically greater in cyclic PTHrP-VEH *vs.* PTHrP-ALN (Fig K-M, N-P), indicating a blunting effect of ALN on the EAP of PTHrP. Nevertheless, the antiresorptive effect of ALN overcame its blunting effect, resulting in a 50% greater BV/TV and a trend towards increased total new bone formation from the start to the end of treatment in cyclic PTHrP-ALN *vs.* PTHrP-VEH (Fig Q-R).

In conclusion, multiple cycles of PTHrP treatment induce mineralization almost completely on existing new bone formation sites and extended the treatment duration by inducing an EAP. Furthermore, adding ALN during the off PTHrP period minimizes bone resorption but may blunt mineralization during the EAPs and new cycles of PTHrP.
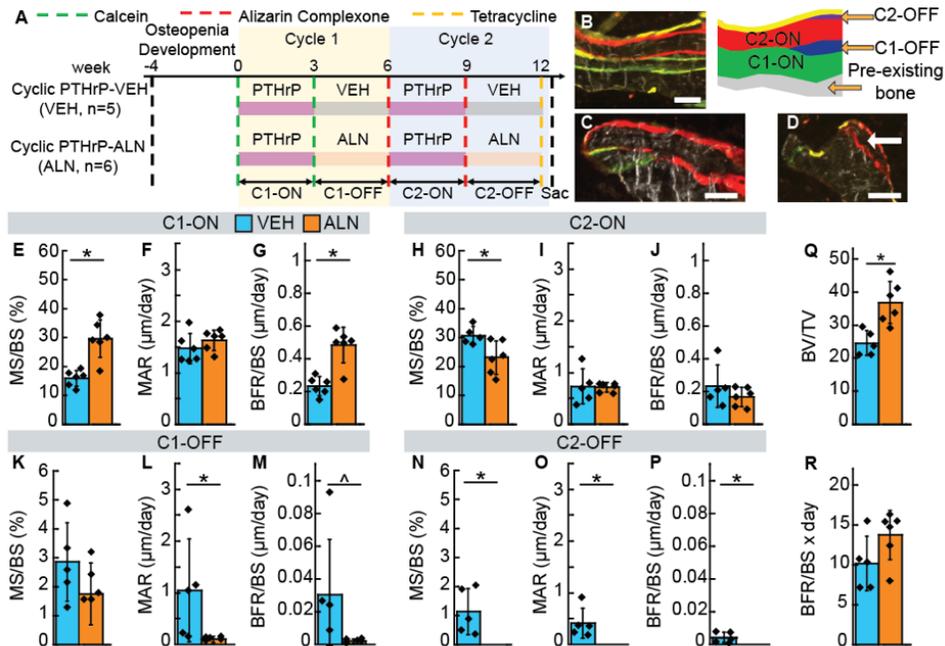
(A) Study design. C1-ON: cycle 1 PTHrP; C1-OFF: cycle 1 VEH or ALN; C2-ON: cycle 2 PTHrP; C2-OFF: cycle 2 VEH or ALN. (B) Image and schematic showing the four quantified, double-label areas on pre-existing bone. (C) The majority of bone formation during C2-ON was adjacent to or right on formation sites generated during C1-ON. (D) In rare occasions, a new formation site generated during C2-ON was independent of sites generated during C1-ON. Scale bars: 50 μm. (E-P) Mineralizing surface (MS/BS), mineral apposition rate (MAR), and bone formation rate (BFR/BS) for C1-ON (E-G), C2-ON (H-J), C1-OFF (K-M), and cycle 2-OFF (N-P). *: p<0.05 and ^: p<0.1. (Q) Bone volume fraction and (R) total new bone formation for both groups.

Biphasic Role of Hedgehog Signaling in Tunnel Integration Following ACL Reconstruction

Timur B. Kamalitdinov[1], Keitaro Fujino[1,2], Sinaia Keith Lang[1], Xi Jiang[1], Rashad Madi[1], Mary Kate Evans[1], Miltiadis H. Zgonis[1], Andrew F. Kuntz[1],
Nathaniel A. Dyment[1]
[1]University of Pennsylvania, Philadelphia, PA, [2]Osaka Medical College, Osaka Prefecture, Japan.
timkam@seas.upenn.edu

Disclosures: AF Kuntz (5 - Integra Lifesciences, Orthofix, Inc., FX Shoulder; 9 - Orthopaedic Research Society, Phoenix Shoulder Society, American Shoulder and Elbow Surgeons, American Board of Orthopaedic Surgery). No other disclosures.

INTRODUCTION: Zonal enthesis formation involves anchoring collagen fibers, creating proteoglycan-rich fibrocartilage, and mineralizing part of this fibrocartilage. During development, Hedgehog (Hh) signaling promotes fibrocartilage production and maturation, leading to these distinct zones [1]. Despite this important developmental role, it is not known whether the Hh pathway plays a similar function in adult tendon-to-bone repair. Utilizing a murine anterior cruciate ligament reconstruction (ACLR) model, where tendon-to-bone integration occurs more readily than in direct tendon-to-bone repair models [2,3], this study aims to address this gap in knowledge. Our objective is to genetically and pharmacologically stimulate the Hh pathway in α-smooth muscle actin (αSMA)-expressing bone marrow stromal cells (bMSCs), which give rise to zonal fibrocartilaginous attachments [2], to promote tunnel integration. Our central hypothesis is that the Hh pathway promotes zonal fibrocartilage formation in the adult, similar to its role in growth and development.

METHODS: All animals and procedures were approved by UPenn's IACUC. Experimental Design. ACL reconstructions were performed on 45 transgenic mice. Genetic Hh Activation Study. αSMACreERT2 mice [4] were crossed with constitutively active SmoM2 mice [5] (Gt(ROSA)26Sor$^{tm1(Smo/EYFP)Amc}$/J) to yield SMACre;SmoM2 (SmoCA) mice with increased Hh signaling and Cre-negative controls. Mice were sacrificed at 28 days post-surgery and assigned to cryohistology (n = 10-13/group). Tamoxifen injections (80 mg/kg) were given on the day of surgery and every other day thereafter for a total of five injections to constitutively activate Smo in αSMA-expressing cells. Pharmacologic Hh Activation Study. Mice received either Hh agonist (20mg/kg Hh-Ag1.5 [6]) or PBS injections 5X per week. Mice were sacrificed at 28 days post-surgery and assigned to cryohistology (n = 7/group). A subset of mice received EdU and Hh agonist every day and tamoxifen on days 0, 3, and 5 post-surgery, were sacrificed at 7 days post-surgery, and assigned to cryohistology (n = 4-5/group). Calcein and Demeclocycline were given 7 and 1 day before sacrifice, respectively, to help define the mineralized fibrocartilage (MFC) zones of attachments in the 28 days post-surgery mice. ACL Reconstruction. The ACL was excised near the femoral insertion. Bone tunnels were drilled with 27G needles. A tail tendon autograft was passed through the tunnels and anchored to the femoral and tibial outer cortices with stainless steel washers [2,3]. Mineralized Cryohistology. Knees were fixed in formalin, embedded, sectioned undecalcified with cryofilm, and imaged on the Zeiss Axio Scan.Z1. Image Quantification. MFC area/total length (Fig. 1A), percentage of tunnel length containing MFC (Fig. 2C), and percentage of MFC produced in the last week (Fig. 3A) were measured to assess the extent and timing of zonal integration at day 28. EdU+ cells in the expanding marrow (excluding bone) were measured to assess amplification of the progenitor pool at day 7 (Fig. 2A). Statistics. Treated and control groups were compared via Student's t-tests (p < 0.05). Data presented as mean ± SD.
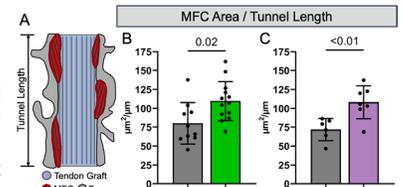

Fig. 1: Hh promoted MFC formation after 28 days.

Fig. 2: Hh promoted progenitor pool proliferation, leading to a greater percentage of the tunnel length containing MFC.

Fig. 3: Genetic Hh stimulation promoted MFC formation in the last week.

RESULTS: Hh Pathway Positively Regulated Tunnel Integration. When targeting the αSMA-expressing amplifying progenitor pool, SmoCA mice had 36% greater MFC compared to controls at day 28 (Fig. 1B, p = 0.02). Mice that received Hh agonist for four weeks had 50% more MFC (Fig. 1C, p < 0.01) compared to controls at day 28. Hh Pathway Activation Increased Progenitor Pool Proliferation Leading to More Attachments. Since Hh-stimulated mice showed greater MFC formation at 28 days, we next sought to identify the mechanism that led to this improved integration: increased number of attachments along the tunnel length or increased mineral apposition within each attachment. Hh agonist treated mice had 52% greater percentage of EdU+ cells in the expanding marrow after 7 days compared to controls (Fig. 2B, p = 0.03), resulting in an 18% increase in cell density (4682 ± 144 vs 3970 ± 260 cells/mm^2, p < 0.01). Likely because of the increased progenitor pool proliferation, we found that 17% more of the tunnel length contained MFC in the SmoCA mice (Fig. 2D, p < 0.01) and 23% more in Hh agonist-treated mice (Fig. 2E, p = 0.02) compared to respective controls after 28 days. Hh Pathway Activation Increased MFC Area in the Last Week. To determine if Hh stimulation yielded continued MFC production during later stages of tunnel integration, we measured the percentage of MFC produced in the last week (MFC between mineral labels given on days 20 and 27, Fig. 3A) compared to total MFC. The percentage of MFC produced in the last week was markedly increased in the SmoCA mice compared to controls (Fig. 3B, p < 0.01) while Hh agonist-treated mice had no difference (Fig. 3C, p = 0.21).

DISCUSSION: Following ACL reconstruction, bMSCs must expand and infiltrate the periphery of the tendon graft, then assemble collagen and zonal fibrocartilage to properly anchor the tendon to adjacent bone. Similar to enthesis development, we demonstrated that Hh signaling promoted mineralized fibrocartilage formation (Fig. 1). Since Hh signaling also promotes proliferation of several cell types, including bMSCs, we then tested whether this increase in MFC formation was due to an increase in the number of attachments from increased proliferation of the bMSC progenitor pool (Fig. 2), or an increase in the amount of MFC per attachment (Fig. 3). Our results indicate that Hh promotes both of these stages of tendon-to-bone integration. First, agonist treatment increased proliferation in the expanding marrow during the first week, resulting in more MFC along the tunnel length (i.e., more attachment sites). Additionally, there was more MFC produced in the last week in the SmoCA mice, indicating that Hh is promoting fibrocartilage cell differentiation and maturation. Interestingly, agonist treatment did not affect mineralization in the last week, which may be caused by desensitization of cells to agonist treatment [7] or limited diffusion of the systemically delivered agonist to the dense MFC that is within the tunnels at later stages of the integration process.

SIGNIFICANCE/CLINICAL RELEVANCE: An improved understanding of the signaling pathways that regulate zonal insertion formation in the adult will be crucial to developing new therapies to improve repair outcome. If the Hh pathway is harnessed therapeutically, it could result in a paradigm shift in the clinical treatment of these debilitating injuries, especially in more challenging scenarios that require reformation of the enthesis, such as rotator cuff repair.

REFERENCES: 1. Dyment et al., Dev Biol, 2015; 2. Kamalitdinov et al., JOR, 2020; 3. Hagiwara et al., Ann N Y Acad Sci, 2020; 4. Grcevic et al., Stem Cells, 2012; 5. Jeong, J et al., Genes Dev, 2004; 6. McKenzie et al., JOR, 2019; 7. Chen et al., PNAS, 2002.
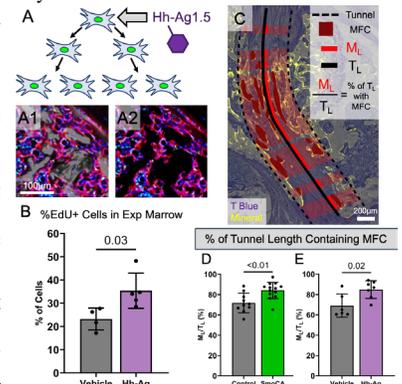
Cold plasma treatment at revision disrupts *S. aureus* immune avoidance mechanisms

Carly J. Smith[1], Amanda Watkins[2], Zoe Katz[1], Brianna Nisssley[1], Leslie Brewer[2], Thomas P. Schaer[2], Theresa A. Freeman[1*]

[1]Department of Orthopedic Surgery, Thomas Jefferson University, Philadelphia, PA
[2]University of Pennsylvania, School of Veterinary Medicine, Kennett Square, PA
theresa.freeman@jefferson.edu

Introduction: Biofilm-forming organisms pose a unique threat to orthopedic surgeries as implants are easily colonized, leading to complications including disability, amputation, and death. Antibiotic resistance complicates this issue and the development of non-antibiotic alternative approaches to treat bacterial infection are essential. Commercially available cold atmospheric plasma devices are emerging as an uncomplicated, non-antibiotic strategy to combat biofilm infection. Cold plasma devices generate a cocktail of electrons, reactive ions, UV radiation, and mechanical forces which have been used both on surfaces and tissues to eradicate bacteria. Additionally, studies show that cold plasma can have immunomodulatory and regenerative effects such as stimulation of macrophage and neutrophil activity, healing, and increased antioxidant defense responses [1, 2]. The goal of this study is to investigate the benefits of cold plasma treatment in an orthopedic model of *Staphylococcus aureus* (*S. aureus*) (MSSA) infection and surgical revision.

Methods: *Animals and Surgical Procedure:* At the index surgery (Day -7) male rats were anesthetized and a craniolateral incision between the vastus lateralis and the biceps femoris was created to access the femur. 1.7 mm titanium screws were placed at the proximal and distal ends, and a mid-diaphyseal empty drill hole was created to expose the medullary cavity. A collagen sponge impregnated with 250 µL of *S. aureus* ATCC 25923 at 1×10^6 CFU (infected) or saline (uninfected) was positioned over the screws and the empty hole. Seven days later, a revision surgery (Day 0) was performed through the previous incision. An 8-hole plate was secured using 1.7 mm titanium screws with 2 proximal and 2 distal to the open mid-diaphyseal hole. *Experimental Groups:* 3 groups of n = 5 each: Uninfected, Infection + Betadine, Infection + Plasma were humanely euthanized at either 4- or 14-days post-revision surgery. *RNA Analysis:* RNA sequencing and gene expression analysis (NovoGene) was performed on periprosthetic soft tissue from 3 rats/group. qPCR was used to confirm the results. Samples were run in triplicate. *Histology:* Tissue is fixed in 4% paraformaldehyde (PFA) (Sigma) for >24 before being embedded in paraffin blocks. 5 µM sections were stained with H&E, trichrome (fibrosis), toluidine blue (mast cells), and Brown and Hopps (bacteria) followed by image analysis (ImagePro Plus software, MediaCybernetics).

Results: Over the course of the study, neither treatment decreased the bacterial load (log CFU/ml) in infected animals. However, weight loss in infected rats treated with betadine averaged 2% by D14, while the cold plasma-treated rats had no change in body weight. In addition, we observed the draining lymph nodes at D14 in the betadine-treated group were more than double the size of uninfected controls, while those receiving plasma-treatment did not differ from uninfected controls. Histological staining of periprosthetic soft tissues with toluidine blue revealed significantly fewer mast cells at D4 with cold-plasma treatment, but comparable numbers between the groups were present by D14. To further elucidate the mechanism driving these differences, we performed RNA sequencing. KEGG analysis revealed that cold plasma treatment upregulated lysosome activity, leukocyte migration, and cytokine signaling at D4, indicating an increase in phagocyte and granulocyte activity. qPCR confirmed these findings.

Discussion: Cold plasma has been acknowledged as a potential treatment for bacterial infections [1, 2]. While we did not observe reduced bacterial infection, our results indicated that plasma treatment alters the local innate immune response to result in less inflammatory distress and improved body condition. It has been reported that *S. aureus* can induce IL-10 signaling to temper innate immune activity (confirmed by our qPCR data) [3]. Based on our current data, we conclude that cold plasma treatment may be a viable means to combat infection by way of innate immune response reprogramming to result in an improved outcome following revision surgery. Of note, cold plasma treatment can be easily incorporated into the surgical routine and can be combined with other treatments, such as antibiotics, and may synergize to eradicate infection.

Significance/Clinical Relevance: Cold plasma treatment is an exciting new tool to assist in combating orthopedic infection, and additional studies pursuing this treatment in conjunction with antibiotics or other means to control infection are ongoing.

REFERENCES:

[1] Smolková B et al., Critical Analysis of Non-Thermal Plasma-Driven Modulation of Immune Cells from Clinical Perspective. 2020 Aug
[2] Nguyen L et al., Cold atmospheric plasma is a viable solution for treating orthopedic infection: a review. 2018 Dec.
[3] Li Z et al., Immunomodulation and Disease Tolerance to Staphylococcus aureus. Pathogens. 2015 Nov.

Regulation of Fibroblast Mechanosensing under Inflammatory Stimulation by Type V Collagen

N. Patel*,[1], K. L. Spiller[1], L. Han[1], [1]Drexel University

Introduction: Fibroblasts are highly sensitive to the biomechanical and biochemical cues of residing niche [1]. During wound healing, inflammatory stimuli leads to aberrant collagen remodeling [2], and pro-regenerative stimuli leads to myofibroblast activation, resulting in excessive deposition of collagen I [1,3]. The fibrotic matrix, in turn, impacts the phenotypic shift of fibroblasts, contributing to a vicious cycle of scar formation [1,3]. Type V collagen, a minor regulatory collagen, plays a key role in regulating collagen I fibril assembly in vivo [4], and thus, could be a central player in this process. Indeed, atrophic scar formation is a prevalent symptom observed in patients with classic Ehlers-Danlos syndrome (cEDS), a connective tissue disorder caused by the mutation of *COL5A1* gene [3]. Understanding the role of collagen V in fibroblast mechanosensing can provide new insights into the cell-matrix cross-talk of fibrosis. This study aims to determine how deficiency of collagen V alters fibroblast response to external inflammatory and mechanical stimuli.

Materials and Methods: Adult human Dermal fibroblasts from normal human donors (HDFa) and cEDS patients (JaySen) were obtained from ATCC. Polyacrylamide (PAAm) gels with 2kPa (soft) and 64kPa (stiff) moduli were prepared, following established procedure [5]. After pre-culture in DMEM, cells were seeded on collagen I-coated PAAm gels in a 6-well plate at 50,000 cells/well for 2 days. Cells were then treated with tumor necrosis factor (TNF)-α (20ng/ml) to simulate M1-macrophage-induced proinflammatory response for 7 days, or left untreated as the control. After the culture, we performed immunofluorescence staining for collagen V (AB7046, Abcam), phalloidin for F-actin cytoskeleton (A12379, Thermo Fisher) and DAPI for nuclei (62248, Thermo Fisher).

Results and Discussion: The reduced collagen V expression in cEDS cells was confirmed by decreased collagen V staining relative to the normal control (Fig. 1a). Also, cEDS cells showed higher cell density and DAPI staining, indicating loss of collagen V may lead to accelerated cell proliferation. On the soft substrate, both groups expressed low amount of F-actin, and we did not notice substantial morphological differences between the normal and cEDS cells (Fig. 1b). However, when seeded on the stiff substarate, cEDS cells adapted a more elongated morphology . In alignment with this morphological change, F-actin cytoskeleton also became more aligned along the long axis of cEDS cells. The contrast was further aggravated when cells were stimulated with the inflammatory cytokine, TNF-α (Fig. 1b). Together, these results support that loss of collagen V could have a profound impact on fibroblast response to external biomechanical and inflammatory cues. It is possible that despite its low amount in native tissues, collagen V could mediate the type and levels of different integrins expressed by fibroblasts, and thus, participate in regulating the inflammation-mediated cell response during wound healing. Our ongoing studies aim to uncover the mechanobiological mechanisms by which collagen V regulates fibroblast behavior.

Conclusion: This study shows that loss of collagen V alters fibroblast response to inflammatory stimuli, providing a basis for studying collagen V in mediating fibroblast immunoresponse and fibrosis in wound healing.

References: [1] Hannan+ 2018, [2] Chou+ 1996, [3] Witherel+ 2021 [4] Wenstrup+ 2004, [5] Tse+ 2010.
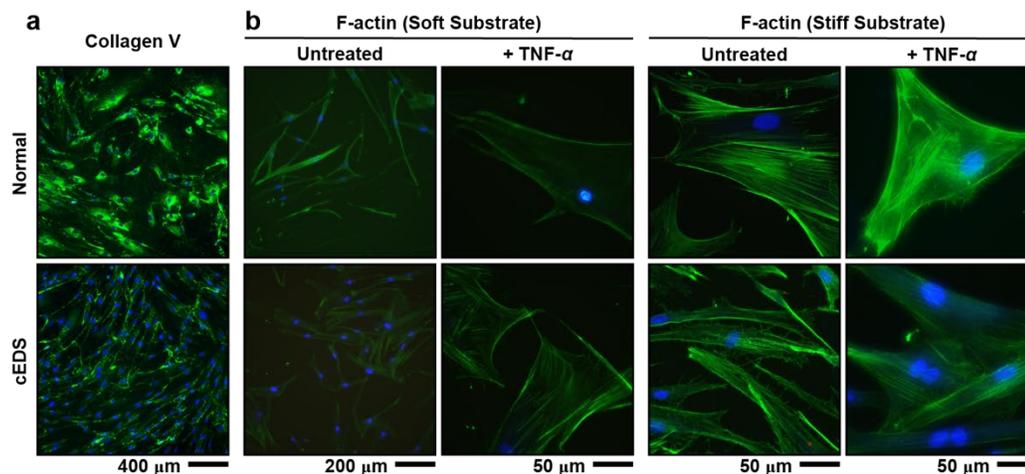
Fig. 1 a) Representative images of collagen V Immunofluorescence (green) and DAPI nuclear staining (blue) of normal and cEDS human fibroblasts (shown for untreated cells on stiff substrates). **b)** F-actin staining (green) and DAPI nuclear staining (blue) of fibroblasts grown on 2kPa/soft or 64kPa/stiff substrates, treated with or without 20 ng/mL inflammatory cytokine, TNF-α.

Genetic Modulation of IHH/PTHrP Signaling Influences the Development of Exostoses in a Mouse Model of Hereditary Multiple Exostoses (HME)

Sarah E. Catheline, PhD, Christina M. Mundy, PhD, and Maurizio Pacifici, PhD

Hereditary Multiple Exostoses (HME) is a congenital pediatric disorder in which benign cartilaginous outgrowths called osteochondromas or exostoses develop at 90-degree angles along the growth plates. In most HME patients, a mutation exists in *EXT1* or *EXT2*, Golgi-associated glycosyltransferases responsible for heparan sulfate (HS) synthesis and assembly onto HS-rich proteoglycans (HSPGs); HS chains are responsible for restricting growth factors within skeletal elements. Without proper HSPG formation, growth factors are freely accessible, which may drive aberrant chondrogenesis and osteochondroma formation. The signaling molecules essential to this process are unknown. One pathway of interest is the Indian hedgehog (IHH)/PTHrP signaling loop which is well documented in its ability to regulate growth plate activity; hedgehog proteins are readily bound by HSPGs to restrict their activity and may be over active after HS depletion. We hypothesize that this loop is both active during, and critical for, osteochondroma formation. To investigate, we used the inducible *AggrecanCreER*^{T2} allele to drive stochastic *Ext1* deletion and exostoses formation in chondrocytes and perichondrium cells at 5 weeks of age. Utilizing *Gli1-LacZ* and *Pthrp-LacZ* reporter strains, we observed that newly forming exostoses display a thin layer of flat, *Pthrp*+ cells on the leading edge of the exostosis, with numerous *Gli1*+ cells surrounding proliferating, Ki67+ cells within the perichondrium forming the exostoses 10 days following tamoxifen. These data confirm hedgehog is active during exostoses initiation. In order to determine whether hedgehog signaling is necessary and sufficient for their formation, we combined our genetic model with conditional deletion of the critical hedgehog receptor *Smo* to obtain Hedgehog loss of function (LOF), or with conditional deletion of *Ptch1*, a negative regulator of hedgehog signaling that results in gain of function (GOF). Histologically and via micro CT analysis, *Acan-Cre*$^{+/-}$*ER*^{T2}; *Ext1*$^{f/f}$; *Smo*$^{f/f}$ mice show a reduction in size and number of osteochondromas formed, and those that do form were disorganized relative to *Acan-Cre*$^{+/-}$*ER*^{T2}; *Ext1*$^{f/f}$ mutant mice four weeks following tamoxifen administration. In contrast, *Acan-Cre*$^{+/-}$*ER*^{T2}; *Ext1*$^{f/f}$; *Ptch1*$^{f/+}$ mice show an increase in both number and size of developing osteochondromas four weeks following tamoxifen administration relative to *Acan-Cre*$^{+/-}$*ER*^{T2}; *Ext1*$^{f/f}$ mice. Our current data implicate IHH/PTHrP signaling as a determinant of osteochondroma outgrowth and a target of therapeutic interest.

Transient Reduction in Lipid-Laden Bone Marrow Adipocytes during Pregnancy and Lactation and Full Recovery after Weaning

Wonsae Lee [1], Yihan Li [1], Shaopeng Pei [1], Justin Leggin [1], Leilei Zhong [1], Ling Qin [1], X. Sherry Liu [1]

[1] McKay Orthopaedic Research Laboratory, Dept. of Orthopaedic Surgery, Univ. of Pennsylvania, Philadelphia, PA; wonsae.lee@pennmedicine.upenn.edu

Disclosures: Nothing to disclose for all authors

INTRODUCTION: Bone marrow adipocyte (BMA) is a unique adipose tissue that has the potential for diverse functions, exhibiting a close relationship with bone homeostasis and marrow hematopoiesis [1]. Previous reports have shown an inverse relationship between BMAs and bone mass, which may link to competitive differentiation pathways of bone marrow mesenchymal progenitors towards an adipogenic or osteogenic lineage [2]. However, a contradicting and unique positive correlation between BMAs and bone mass was observed during reproduction and lactation in rats [3] and mice [4]. While bone mass and number of BMAs were significantly reduced during lactation, both recovered after weaning. Therefore, the objective of this study was to elucidate the cellular mechanisms behind the response of BMAs to pregnancy, lactation, and post-weaning recovery. We hypothesized that lipid-laden BMAs play a role as a fuel source during pregnancy and lactation to meet the increased metabolic demands of elevated skeletal remodeling.

METHODS: All animal experiments were IACUC approved. Adipoq-CreER/tdTomato mice received intraperitoneal injection of Tamoxifen (75 mg/kg/day) 3 times every other day at 6.5 weeks of age and recovered for 3 weeks to minimize the adverse effects of tamoxifen on female reproduction before being assigned to 5 groups (n=5-7/group): 14d Pregnancy, 1d Lactation, 12d Lactation, 14d Recovery, and age-matched Virgins. All animals were mated on the corresponding day of each designated stage and euthanized at 17 weeks of age (Fig 1A). Distal femurs were harvested for whole-mount embedding. Fifty-micrometer thick longitudinal sections were cut and stained with anti-perilipin and anti-endomucin antibodies before being imaged by a confocal fluorescence microscope. All following quantification parameters were calculated using a customized python code in the secondary spongiosa. Perilipin+ (green) cells were defined as mature adipocytes and their area % (Adi.A/BM), normalized number (Adi.N/BM), and individual size (Indiv_Adi.A) were quantified. An overlay of perilipin+ and tdTomato+ (Td+, red), resulting in yellow cells, were defined as pre-existing BMAs that derived from Td+ cells. From endomucin staining, vessel diameter (Vessel.D), area % (Vessel.A/BM), distance to the closest adipocyte (Adi.Vessel distance), and percentage of adipocytes that are in contact with marrow vessels (% zero distance Adi) were quantified. Lastly, TUNEL staining (n=3/group) was performed to identify adipocytes undergoing apoptosis. One-way ANOVA with Bonferroni *post hoc* corrections was applied and significant differences were set at $p<0.05$.

RESULTS: There was a decreasing trend in the area and number of adipocytes (perilipin+, green, Fig 1B) during pregnancy and lactation when compared to Virgins although the data did not reach statistical significance (Fig 1C-D). In 14d Rec group, both the area and number of adipocytes increased significantly compared to 14d Preg, 1d Lac, and 12d Lac (2.6-4.7-fold, 2.3-2.9-fold respectively). The individual size of BMAs showed a decreasing trend during Preg and Lac, and at 12d Lac. Their size was 52% and 38% smaller than that of Vir and 14d Preg, respectively (Fig 1E). In contrast, the individual size of BMAs in 14d Rec was 77% greater than the size in 12d Lac. While the total number of Td+ cells and % of perilipin+Td+ cells over Td+ cells did not differ (data not shown), the % of pre-existing (perilipin+Td+) adipocytes over perilipin+ cells in 12d Lac was 153% greater than that in 14d Preg (Fig 1F). No significant changes in vessel diameter were detected over a reproductive cycle (Fig 2A). However, 14d Rec had a 60% greater vessel area compared to 12d Lac (Fig 2B). The Adi.Vessel distance in 1d Lac and 14d Rec was 51% and 58% of that in 14d Preg (Fig 2C). The distance at 12d Lac tended to be greater than that of 1d Lac and 14d Rec ($p=0.08$). Furthermore, in the 14d Rec group, more adipocytes were in contact with marrow vessels than in 1d and 12d Lac groups (Fig 2D). No difference was detected in TUNEL+ BMAs among groups (data not shown).

DISCUSSION: During pregnancy and lactation, BMAs undergo a drastic change in their number, individual size and total area. The significant recovery at 14d Rec suggests that this is a transient change during pregnancy and lactation. Our results showing a significant reduction in the individual size of BMAs (Fig 1E) and no difference in TUNEL+ BMAs throughout pregnancy and lactation suggest that lipolysis of lipids within BMAs may be the main mechanism driving the reduction of BMAs during pregnancy and lactation. Because lipid-laden BMAs can actively respond to high metabolic, nutritional, hormonal, and environmental cues as an energy source [1], lipids from BMAs might break down and mobilize to neighboring cells where cellular energy is in demand, *i.e.*, skeletal remodeling sites. Following weaning, BMAs not only elevated in their number and size but also populated in closer proximity to vessels, potentially due to the high lipid deposition rate. The enlargement of BMAs indicates potential weaning-associated lipid hypertrophy. After intense metabolic stress induced by pregnancy and lactation, maternal bone marrow may start to store lipids via hypertrophic BMAs during post-weaning recovery in preparation for the next metabolic stress. Further lipidomic analyses may help to clarify detailed mechanisms of the lipid disappearance and reappearance and possible metabolic traits during a reproductive cycle. Taken together, our data elucidated responses of adipocytes, blood vessels, and their interactions within the bone marrow to different stages of a reproductive cycle and suggested that BMAs may respond to high metabolic demand during pregnancy and lactation through a lipolytic mechanism.

SIGNIFICANCE: This study elucidated the alterations in BMAs and marrow vessels when subjected to reproduction, lactation, and post-weaning recovery, highlighting the potential impact of BMAs on maternal and metabolic health.

REFERENCES: [1] Rendina-Ruedy E, *Cell Metab,* 2019. [2] Akune T, *J Clin Invest*, 2004, [3] Li Y, *ORS Annual Meeting*, 2021, [4] Bornstein S, *Endocrinol*, 2014.
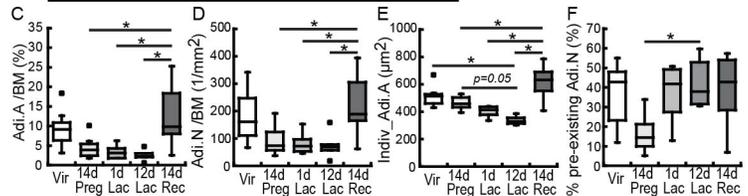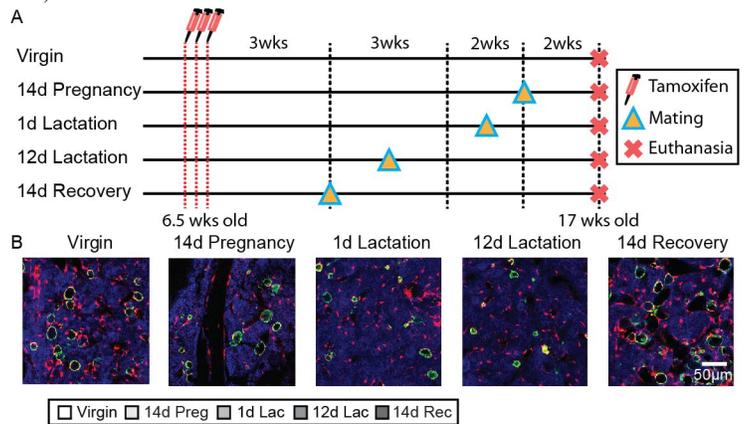
Fig 1. (A) Schematic of the experimental design. (B) Representative images of fluorescent immunostaining of perilipin (green), TdTomato (red), and DAPI (blue). Comparison of (C) adipocytes area %, (D) adipocytes number, (E) individual adipocytes area, and (F) percentage of number of pre-existing (yellow) adipocytes.
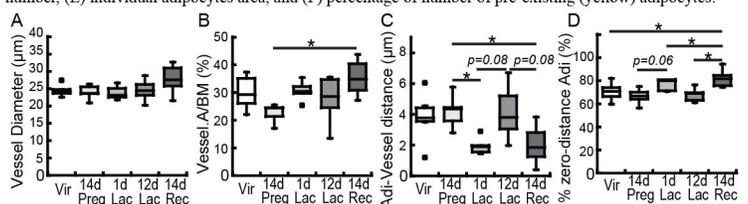

Fig 2. Comparison of (A) vessel diameter, (B) vessel area %, (C) distance between perilipin+ adipocytes and vessels, and (D) percentage of adipocytes in contact with vessels.

Delivery of Cyr61 Promotes Angiogenesis during Bone Fracture Repair

Annemarie Lang[1], Emily Eastburn[1], Carly Siciliano[1], Annapurna Pranatharthi Haran[1], Madhura Nijsure[1], Riccardo Gottardi[2], Joel D. Boerckel[1]
[1]Departments of Orthopaedic Surgery & Bioengineering, University of Pennsylvania, Philadelphia, PA,
[2]Children's Hospital of Philadelphia, Philadelphia, PA

INTRODUCTION: Compromised vascular supply and insufficient neovascularization are primary clinical challenges for bone repair and regeneration. Osteoblasts require close proximity to oxygenated capillaries and co-mobilize with new blood vessels to induce bone healing. Thus, injuries to bones with low peripheral vascular supply (e.g., tibia) and large bone defects with an obliterated vascular bed are prone to non-union. Previously, we found that interfragmentary mechanical stimuli can promote bone healing and also regulate neovascularization during bone regeneration [1]. Cysteine-rich angiogenic inducer of 61kD (Cyr61) is a matricellular growth factor whose expression is regulated by mechanical cues during fracture repair [2] and its delivery can enhance bone healing [3]; however, its cellular mechanism(s) of action in fracture repair are unknown. Here, we tested the effects of recombinant Cyr61 delivery on vascularized bone repair, chondrogenesis, osteogenesis, and angiogenesis.

METHODS: We performed three experiments. In experiment 1, we evaluated the effects of Cyr61 delivery on bone regeneration in vivo, with or without ambulatory mechanical loading. We modulated ambulation-induced interfragmentary motion by varying fixation plates stiffness (stiff vs. compliant external fixator, MouseExFix, RISystem; n= 6–8). We delivered Cyr61 (1 µg/defect) using photocrosslinked gelatin-fibrin hydrogels composed of 5% GelMA, 5 mg/ml fibrinogen and 0.2% LAP for photoinitiation. All procedures were conducted in accordance with UPenn IACUC regulations (protocol no: 806482). A total of 28 C57BL/6J female mice (Charles River) aged 12–16 weeks underwent surgery. The vehicle with or without Cyr61 was implanted into the gap before wound closure. Mice were euthanized 14 days post-fracture (dpf). We performed microCT analysis (Scanco µCT 45) and histology/immunofluorescence (Movat's Pentachrome; endomucin – Emcn = vessel; osterix – Osx = osteoblasts; F4/80 = multinucleated cells/macrophages). In experiment 2, we evaluated the effects of recombinant Cyr61 treatment on chondrogenesis and osteogenesis in vitro. For chondrogenic differentiation, human mesenchymal stromal cell (hMSC) pellet cultures were treated with different concentrations of Cyr61 (0–200 ng/ml) for 2 weeks, with or without co-supplementation with TGF-β1 to the chondrogenic culture medium. Analysis was performed by measuring the size of each pellet and performing Safranin-O staining. For osteogenic differentiation, hMSC were treated for 3 weeks with 0 or 100 ng/ml Cyr61 in osteogenic medium. qPCR was performed to analyze induction of osteogenic marker genes (RUNX2, ALP, COL1A1). Finally, in experiment 3, we evaluated the effects of Cyr61 treatment on vascular network formation in a 3D in vitro angiogenesis assay combing human umbilical vein endothelial cells (HUVECs) and hMSCs. Briefly, GFP+ HUVECs and MSCs (4:1) were embedded in gelatin-fibrin hydrogels and cultivated in vitro for up to 5 days with endothelial basal medium containing 0.1% FBS, with or without 100 ng/ml Cyr61. Images were taken at 3 and 5 days and the tube number and mean length were analyzed.

RESULTS: Experiment 1: Cyr61 treatment had no effect on fracture callus bone volume at 14 dpf, regardless of fixation stiffness. However, Cyr61 treatment increased formation of interfragmentary vascularized tissue and significantly increased Emcn+ vessel area under stiff fixation, compared to the vehicle control, but did not alter tissue formation or vascularization under compliant fixation. Quantification of F4/80+ macrophages exhibited similar trends as blood vessels, though differences were not statistically significant. Experiment 2: Cyr61 treatment had no effect on either osteogenesis or chondrogenesis in vitro. While osteogenic differentiation of MSCs increased endogenous Cyr61 mRNA expression, recombinant Cyr61 treatment did not alter osteogenic gene expression. Similarly, while pellet size was elevated in a dose-dependent manner in the absence of TGF-β1, combined treatment with TGF-β1 did not alter pellet size or chondrogenic glycosaminoglycan deposition. Experiment 3: Cyr61 treatment enhanced tubular network formation, with significantly elevated tube length at both 3 and 5 days.

DISCUSSION: We found that Cyr61 delivery promoted angiogenesis during fracture repair, but only under stiff fixation conditions. Previously, we showed that large interfragmentary strains, if applied early in the bone healing process, mechanically disrupt vascular ingrowth [1]. Thus, while potently angiogenic, both in vitro and in vivo, Cyr61 did not enhance vessel formation under mechanical conditions that were unfavorable for functional neovessel growth. Together we postulate that Cyr61 delivery represents a potential pro-angiogenic therapeutic for vascularized bone healing under conditions of limited blood vessel supply, such as tibial fractures and large bone defects, but does not promote cartilage callus formation or mineralization per se. As Cyr61 is a mechano-activated target of the YAP/TAZ mechanotransducers and functions as an integrin ligand, future studies are warranted to evaluate Cyr61 delivery under stimulatory and vessel-supporting mechanical loading conditions.

REFERENCES: [1] McDermott et al. 2019 *Sci. Transl. Med.*; [2] Lienau et al. 2005 *JOR;* [3] Frey et al. 2012 *Int. Orthop.*

Decorin Maintains Cartilage Surface Integrity and Chondrocyte Mechanotransduction During Aging

Mingyue Fan[1], Prerana Singh[1], Bryan Kwok[1], Biao Han[1], Thomas Li[1], Chao Wang[1],
Ling Qin[2], David E. Birk[3], Renato V. Iozzo[4], Robert L. Mauck[2], Lin Han[1]
[1]Drexel University, Philadelphia, PA; [2]University of Pennsylvania, Philadelphia, PA;
[3]University of South Florida, Tampa, FL; [4]Thomas Jefferson University, Philadelphia, PA.

Disclosures: RL Mauck (8, *JOR Spine*), no other disclosures.

INTRODUCTION: Aging is the most prominent risk factor for osteoarthritis (OA), which afflicts more than 10% of adults over 60 years of age [1]. Many efforts have been dedicated to elucidating the cellular hallmarks of aging [2]. In contrast, despite the importance of extracellular matrix (ECM) in cartilage biomechanical function and chondrocyte mechanosensing, there is limited knowledge regarding how aging impacts the integrity of ECM. Our recent studies found that decorin, a small proteoglycan, plays indispensable roles in regulating the integrity of aggrecan network in cartilage ECM [3] and mediating chondrocyte mechanotransduction [4] during post-natal growth. In post-traumatic OA, up-regulation of decorin delays the loss of fragmented aggrecan and thus attenuates surface fibrillation [5]. Decorin is actively expressed in both young and old human cartilage [6], indicating a potentially important role of decorin in regulating cartilage aging. This study tests whether decorin plays a crucial role in cartilage ECM maintenance during aging.

METHODS: *Animal model.* Cartilage-specific knockout of *Dcn* was induced by i.p. injection of tamoxifen to conditional decorin knockout mice (*Dcn* $^{flox/flox}$/*AcanCre*^{ER}, or *Dcn*^{cKO}) at 3 months of age, and the phenotype was evaluated at 9 months (9M) and compare to age-matched controls. Additional global decorin-null (*Dcn*$^{-/-}$) and wild-type (WT) mice were evaluated at 18 months of age (18M). *Histology* and *immunofluorescence (IF) imaging* were applied to sagittal sections to assess joint morphology, sulfated glycosaminoglycan (sGAG) staining and presence of collagen I, indicating surface fibrillation [7]. *SEM* was applied to measure collagen fibril nanostructure [5]. *AFM-nanoindentation* was applied to the condyle cartilage surface to quantify tissue modulus [3]. For *in situ intracellular [Ca^{2+}]$_i$ signaling*, freshly dissected tibial cartilage explants were labeled with intracellular calcium indicator Calbryte-520, and time-series of confocal images were taken in isotonic, hypotonic and hypertonic DMEM [4]. The responsive rate, %R_{cell}, was calculated as the fraction of responsive cells over a 15 min period. A non-parametric Mann-Whitney U test was applied to compare E_{ind}, and the proportion z-test was applied to compare %R_{cell}, between genotypes at each age and/or osmotic condition at $\alpha = 0.05$, followed by Holm-Bonferroni correction to account for family-wise errors.

RESULTS: In 9M *Dcn*^{cKO} mice, loss of decorin led to an overall reduction of sGAG staining in cartilage, as well as the appearance of a surface layer devoid of sGAGs (Fig. 1a). IF imaging further confirmed that this sGAG-depleted layer was rich in collagen I, evidencing surface fibrillation. Furthermore, the surface collagen fibrils formed highly aligned bundles along the mediolateral split-line direction (Fig. 1a). A similar but more severe phenotype was observed in 18M *Dcn*$^{-/-}$ mice, including more severely reduced sGAG staining, a thicker sGAG-devoid surface layer and the presence of collagen I on the surface (Fig. 1b). Applying AFM-nanoindentation, we did not detect significant changes of E_{ind} in 9M *Dcn*^{cKO} cartilage relative to the control. However, we found a substantially increased modulus in 18M *Dcn*$^{-/-}$ group, which was in stark contrast to our previously observed modulus reduction in 3-month-old *Dcn*$^{-/-}$ mice (Fig. 2a). This increase in modulus was also associated with a change in the nature of the indentation response. Specifically, we observed a linear *F-D* curve in 18M *Dcn*$^{-/-}$ mice (Fig. 2b), instead of the non-linear *F-D*$^{3/2}$ Hertzian indentation response typically observed for cartilage [3]. Also, for both 9M and 18M groups, loss of decorin led to a reduction in chondrocyte [Ca^{2+}]$_i$ responses in situ, as marked by significantly lower %R_{cell}, under both physiological (isotonic) and osmotically instigated (hypotonic and hypertonic) conditions (Fig. 3).

DISCUSSION: This study highlights a crucial role of decorin in maintaining the integrity of the cartilage surface during aging. The surface of healthy cartilage is characterized by a transversely isotropic mesh of thin collagen II fibrils [8], which plays an important biomechanical role in resisting shear forces and mediating boundary lubrication [9]. The absence of sGAGs and presence of highly aligned collagen I fibers (Fig. 1) clearly evidence cartilage surface fibrillation. Also, the non-Hertzian, linear *F-D* response in the 18M *Dcn*$^{-/-}$ group (Fig. 2) is a typical indentation response of fibrous tissues with inherent tensile pre-stress, such as the meniscus [10]. This surface fibrillation may be attributed to several mechanisms. First, decorin increases the retention of aggrecan in cartilage during post-natal growth [3], and the loss of sGAG staining observed here suggests that decorin continues playing this role during aging. Second, decorin also directly provides collagen interfibrillar spacing through its GAG chain [11]. Thus, the loss of decorin and aggrecan together may result in reduced biophysical resistance against collagen fibril fusion and alignment under shear forces during aging, thus accelerating surface fibrillation.

The reduction in chondrocyte [Ca^{2+}]$_i$ activities in both *Dcn*^{cKO} and *Dcn*$^{-/-}$ groups support a crucial role of decorin in regulating chondrocyte mechanotransduction during aging. As shown previously in immature and young adult *Dcn*$^{-/-}$ mice, the reduction of aggrecan caused by decorin loss alters the negatively charged pericellular environment of chondrocytes, leading to disrupted mechanosensing [4]. Our results here further show that decorin continues to play such a mechanobiological role during aging (Fig. 3). In addition, the alteration of the surface ECM structure (Fig. 1) could also have a profound impact on the mechanosensing of superficial layer cells. Indeed, the presence of collagen I fibers (Fig. 1) indicates possible dedifferentiation of superficial cells into a fibroblast-like phenotype that deposits collagen I. Our ongoing studies aim to pinpoint the mechanobiological roles of decorin in regulating superficial layer cell fate and signaling, which will provide justification for using decorin as a molecular therapy to modulate cartilage aging.

SIGNIFICANCE: This study identifies a novel role of decorin in maintaining cartilage surface integrity during aging by preventing surface fibrillation and regulating the in situ mechanotransduction of chondrocytes, supporting the potential use of decorin for ameliorating aging-induced cartilage degeneration.

REFERENCES: [1] Zhang+ 2010. [2] Loeser+ 2016. [3] Han+ 2019. [4] Chery+ 2021. [5] Li+ 2020. [6] McAlinden+ 2001. [7] Tschaikowsky+ 2022. [8] Vanden Berg-Foels+ 2012. [9] McNary+ 2012. [10] Li+ 2015. [11] Danielson+ 1997.
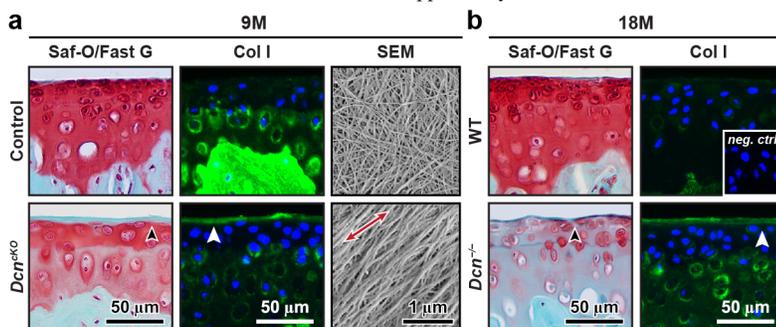
Fig. 1 a) Safranin-O/Fast Green histology, IF of collagen I and cartilage surface SEM images of *Dcn*^{cKO} and control mice at 9 months of age (9M). Red arrow: mediolateral direction. **b)** Safranin-O/Fast Green histology and IF of collagen I of *Dcn*$^{-/-}$ and WT mice knee joints at 18 months (18M). Black and white arrowheads in panels a) and b): lack of sGAG staining and presence of collagen I on cartilage surface ($n \geq 4$ animals for each age and genotype).
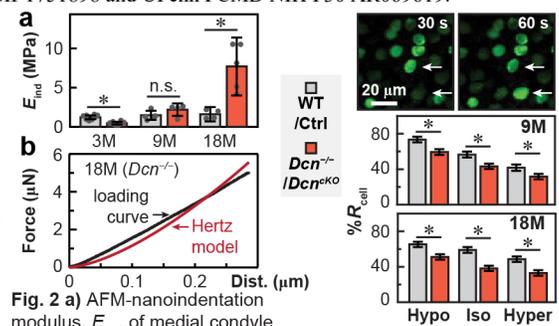

Fig. 2 a) AFM-nanoindentation modulus, E_{ind}, of medial condyle cartilage between Control vs *Dcn*^{cKO} at 9M, and WT vs *Dcn*$^{-/-}$ at 3M and 18M (mean ± 95% CI, $n \geq 4$, *: $p < 0.05$; n.s.: not significant). **b)** Representative *F-D* curve of 18M *Dcn*$^{-/-}$ cartilage shows non-Hertzian indentation response.
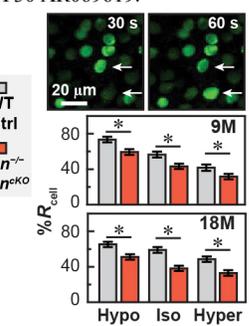

Fig. 3 Comparison of [Ca^{2+}]$_i$ cell responsive rate, %R_{cell}, between Control vs *Dcn*^{cKO} at 9M, and WT vs *Dcn*$^{-/-}$ at 18M (mean ± 95% CI, ≥ 300 responding cells from $n \geq 4$ animals, *: $p < 0.05$).

Sirtuin 6 is critical for maintaining intervertebral disc homeostasis during spine aging

Pranay Ramteke[1], Victoria Tran[1], Bahiyah Watson[1], Shira Johnston[1], John Collins[1], Richard Loeser[2], Makarand Risbud[1]

1. Thomas Jefferson University, Philadelphia, Pennsylvania, USA.

Introduction: Intervertebral disc degeneration (IVDD) is one of the main contributors for low back pain viz. the leading cause of disability worldwide[1]. Although environmental and genetic factors are the known etiological causes for disc degeneration, age is still the most significant risk factor. Recent findings report that senescence plays a major role in ageing as well as disc degeneration in human and mouse models[2]. Interestingly, Sirtuin 6 (SIRT6) a class two HDAC, has been shown to decelerate ageing across different species as well as have an anti-senescence effect[3]. However, its role in intervertebral disc degeneration is largely unknown. Therefore, the aim of this study is to explore the role of SIRT6 in intervertebral disc degeneration.

Methods: We studied the spinal phenotype of mice exhibiting conditional deletion of SIRT6 (cKO) in Acan-expressing cells (Acan^{CreERT2}SIRT6$^{fl/fl}$) at healthy and aged time points i.e., 12, 18 and 24 months. uCT analysis was performed to check effects of SIRT6 KO on physiological parameters of the disc and vertebral bones. SaF-O staining was performed on intervertebral discs sections and evaluated by at least six blind graders to generate Modified Thompson grading scores to characterize and measure degenerative phenotype. Picrosirius red staining was performed to check changes in collagen type. FTIR analysis was performed to determine aggrecan, collagen and proteoglycan content. Immunohistochemistry analysis was performed to measure senescence in the disc.

Results: uCT analyses of SIRT6 cKO mice showed significant changes in disc height (DH), vertebral height (VH) and disc height index (DHI) as compared to WT control mice. SaF-O staining and Modified Thompson grading of SaFO stained discs showed that SIRT6 cKo exhibit significantly higher grades of degeneration as compared to their respective age matched controls, especially in the AF (annulus fibrosus). Surprisingly, Picrosirius red staining showed no significant differences in the collagen content in SIRT6 cKO mice. FTIR analysis showed no significant changes in aggrecan, collagen or proteoglycan content of the cKO mice. Interestingly, immunohistochemistry analysis showed an increase in p21, a bonafide marker of senescence in SIRT6 cKO discs as compared to their respective controls.

Discussion: Higher modified Thompson grading scores for disc degeneration in SIRT6cKO mice suggest its fundamental role in disc homeostasis. Surprisingly, Picrosirius red staining showed no significant differences in the collagen fibrils, although AF tissue was the most affected in the disc compartment. Increased p21 in SIRT6 cKO mice suggests that senescence- the major etiological factor for disc degeneration, is regulated by SIRT6. Therefore, SIRT6 cKO accelerates disc degeneration via senescence.

Significance: In summary, our work provides new insights into SIRT6^{cKO} mediated disc degeneration at the pathological, cellular, and molecular levels, thereby defining the significance of epigenetic landscape in this unique tissue. Further exploration of these findings may lead to development of therapeutic targeting of SIRT6 to mitigate disc degeneration.

References:

1. Hartvigsen et al., Lancet Low Back Pain Series Working Group. What low back pain is and why we need to pay attention. Lancet. 2018 Jun 9;391(10137):2356-2367. doi: 10.1016/S0140-6736(18)30480-X. Epub 2018 Mar 21. PMID: 29573870.
2. Micco et al., Cellular senescence in ageing: from mechanisms to therapeutic opportunities. Nat Rev Mol Cell Biol. 2021 Feb;22(2):75-95. doi: 10.1038/s41580-020-00314-w. Epub 2020 Dec 16. PMID: 33328614; PMCID: PMC8344376.
3. Roichman et al., Restoration of energy homeostasis by SIRT6 extends healthy lifespan. Nat Commun. 2021 May 28;12(1):3208. doi: 10.1038/s41467-021-23545-7. PMID: 34050173; PMCID: PMC8163764.

YAP and TAZ Mediate Mechanical Regulation of Bone Development Ex Utero

Joseph Collins, Yasaman Moharrer, Cristian Parisi, Nathaniel Dyment, Niamh Nowlan, Joel Boerckel

Mechanical forces exerted *in utero* direct long bone development; however, the molecular mechanisms remain unclear. Here, we used *in vitro* mechanical stimulation of explanted fetal mouse hindlimbs to investigate the effects of mechanical loading on long bone morphogenesis. We previously showed that the mechanosensitive transcriptional regulators, YAP and TAZ, promote skeletal development by regulating endochondral ossification and primary ossification center (POC) development *in utero*[1]. We hypothesized that YAP and TAZ are required for mechanoregulation of fetal long bone morphogenesis *ex utero*.

We applied dynamic mechanical loading to explanted prenatal (E15.5) mouse hindlimbs, combined with two orthogonal approaches to ablate YAP/TAZ activity: global pharmacologic inhibition and conditional genetic deletion. Dynamic loading was applied at 0.67 Hz for 2 hrs, 3x per day, producing cyclic knee flexion to $14\pm4°$ (Fig A). Contralateral limbs served as static controls. All limbs were cultured in osteogenic media for 6 days. Statistical comparisons were made using two-way ANOVA and Holm-Sidak tests. We evaluated alkaline phosphatase activity as an indicator of osteogenic activity in two regions of interest: 1) whole femoral rudiment and 2) POC (Fig B). To globally inhibit YAP/TAZ activity, C57Bl6/J limb explants were cultured in $5\mu M$ verteporfin (VP) to block YAP/TAZ signaling, or vehicle (DMSO). To target osteoprogenitor cells and their progeny, we used Osx-conditional genetic YAP/TAZ deletion in three genotypes: $YAP^{fl/fl};TAZ^{fl;fl}$ (WT); $YAP^{fl/+};TAZ^{fl/fl};Osx$-Cre (cHET); and $YAP^{fl/fl},TAZ^{fl/fl};Osx$-Cre (cKO).

Global YAP/TAZ inhibition by VP had no effect on the bone volume of non-loaded limbs but abrogated load-induced bone formation and ALP activity, both in the POC and the whole limb rudiment (Fig C). In contrast, Osx1-conditional deletion of YAP and TAZ abrogated load-induced ALP activity in the POC (Fig D), but not the whole rudiment.

Both global inhibition and Osx-conditional YAP/TAZ deletion abrogated load-induced osteogenesis, implicating osteoblast lineage cells in YAP/TAZ-mediated mechanical regulation of bone development. Conditional YAP/TAZ deletion prevented load-induced osteogenesis in the region of Osx-expressing cell activity, whereas global inhibition prevented load-induced osteogenesis in the whole rudiment. Together, these orthogonal approaches identify YAP and TAZ as putative mediators of prenatal load-induced bone formation.
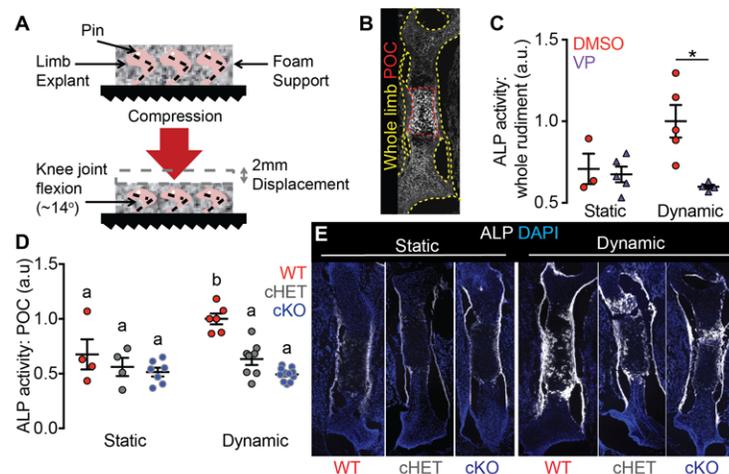
1.Collins et al ASBMR 2019.

Figure. A. Schematic of explant bioreactor. **B.** Regions of interest on explant femur section. **C.** Quantification of whole rudiment ALP activity. **D.** Quantification of POC ALP activity. **E.** Representative images of ALP and DAPI in explant femurs after 6 days of culture. POC - Primary ossification center; ALP - Alkaline phosphatase

NGF-TrkA Signaling in Dental Implant Osseointegration

Hattanas Kumchai[*], Ryan E. Tomlinson[*]
Department of Orthopaedic Surgery, Thomas Jefferson University, Philadelphia, PA, USA

Previous studies have shown NGF-TrkA signaling plays an important role in the establishment of sensory nerves during bone development and is required for a normal skeletal response to mechanical forces and injury. However, long bones have a different bone structure and healing environment compared to the maxilla and mandible. As a result, successful translation of NGF-TrkA therapy to dental implantation requires a complete characterization of NGF expression and innervation by TrkA sensory nerves during osseointegration of dental implants.

In this study, we utilized three validated reporter mouse lines (Thy1-YFP, TrkA-LacZ, NGF-EGFP) to analyze innervation and NGF-TrkA signaling during dental implant osseointegration in mice. Briefly, an osteotomy site was created in the alveolar bone 1 mm medial to the maxillary first molar tooth using a twist drill and hand wrench. A 0.6 mm diameter, 2 mm length titanium-alloy Ti-6Al-4V retention pin (Edenta) was secured in the osteotomy site. Soft tissue was approximated at the end of the surgery. Mice were euthanized at 7, 14, 21, and 28 days after the surgery. The maxilla was harvested intact and fixed overnight (10% NBF). Next, the implant and surrounding bone were analyzed radiographically with micro-computed tomography (Scanco uCT). In TrkA^{F592A}; Thy1-YFP mice, we used the membrane-permeable small molecule 1NMPP1 to inhibit TrkA signaling during implant osseointegration. In a separate study, Thy1-YFP mice received recombinant NGF injection (4 ug/g IP) prior to the implant surgery. We confirmed NGF efficacy by performing hot plate test, in which mice were placed on a 55 °C plate and their time to first reaction was recorded. In addition, the Mouse Grimace Scale was utilized to evaluate post-operative pain in mice. Decalcified sections of NGF-EGFP and Thy1-YFP mice were mounted in media containing DAPI, then imaged with a confocal microscope. Tissue harvested from TrkA-LacZ mice was X-Gal stained intact, then sectioned for brightfield microscopy.

By microCT, we observed progressively increased peri-implant bone around the dental implant up to day 28. In the TrkA-LacZ mice, we saw TrkA-expressing sensory nerve axons approach the peri-implant bone, with a significant peak at 21 days. In contract, NGF-EGFP fluorescence in the peri-implant bone progressively increased, with a peak value after 28 days. Importantly, TrkA^{F592A}; Thy1-YFP mice that received 1NMPP1 had significantly decreased peri-implant innervation whereas mice that received an injection of NGF had significantly increased peri-implant innervation expression along with significantly increased peri-implant bone volume fraction as compared to control. Although mice that received NGF injection had shorter latency time compared to control in hotplate test, they were not found to have differences in post-operative pain assessed by the mouse grimace scale during post-operative day 1, 3, 7, and 14.

In summary, TrkA-expressing sensory nerves and NGF expression in peri-implant tissue increases during implant osseointegration. Inhibition of TrkA signaling significantly decreased innervation, whereas increased NGF signaling increased innervation and improved osseointegration. Future studies will focus on leveraging these insights to improve patient outcomes.

Impacts of Type V Collagen Insufficiency on Cutaneous Wound Healing and Scar Formation

Y. Liu*,[1], C. Wang[1], D. C. Stewart[2], B. K. Brisson[2], D. E. Birk[3], S. W. Volk[2], L. Han[1]

[1]Drexel University, [2]University of Pennsylvania, [3]University of South Florida.

Introduction: Pathological wounds are a prevalent healthcare problem, affecting more than 40 million Americans [1]. Imbalanced healing often results in fibrotic scar formation, marked by excessive deposition and aberrant assembly of type I collagen fibers. Type V collagen, a minor fibril collagen, initiates the initial fibrillogenesis of collagen I [2], and thus, could be an important player in wound healing [3]. For patients with classic Ehlers-Danlos syndrome (cEDS), a genetic disorder caused by reduced COL5A1 expression, one major symptom is atrophic scar formation [4]. Understanding the role of collagen V in wound healing will provide new insights for improved cEDS patient care and new targets for regeneration therapies. This study aims to determine the impact of collagen V insufficiency on the wound healing and scar formation in vivo using collagen V heterozygous mice, $Col5a1^{+/-}$, an established animal model of cEDS [5].

Material and Methods: Two 6-mm diameter circular full-thickness dermal punch wounds were created on the lower dorsal skin of $Col5a1^{+/-}$ and wild-type mice at 7 weeks of age [6]. Both wound tissue and surrounding intact skin tissue were harvested on post-wound day (PWD) 14 and 21 [7]. We applied Picrosirius Red staining to assess scar size and collagen I fiber structure, and immunofluorescence (IF) imaging to assess the distributions of collagen V (1:200, Ab7046) and α-smooth muscle actin (α-SMA, 1:1000, Ab5694), a biomarker of myofibroblast activation. Freshly dissected skin tissue was cryotomed into 20-µm thick cross-sections in OCT for scanning electron microscope (SEM) imaging and atomic force microscope (AFM) analyses. For SEM, cryo-sections were treated with trypsin and hyaluronidase and imaged by 10kX. AFM nanoindentation was applied to quantify the micromodulus, E_{ind}, using a microspherical tip ($R \approx 5$ µm, $k \approx 0.03$ N/m) and a BrukerNano AFM in $1\times$ PBS, following established procedures [8]. We separated the moduli of intact epidermis, dermis, wound edge (WE), as well as granulation tissue at PWD14, and scar tissue at PWD21. Two-way ANOVA followed by Tukey-Kramer post-hoc test was applied to detect differences with region and genotype at the significance level of $\alpha = 0.05$.

Results and Discussion: The reduction of collagen V in $Col5a1^{+/-}$ murine skin was validated by the decreased staining of collagen V (shown for granulation tissue, Fig. 1a). With the reduction of collagen V, we observed an appreciable increase in the size of scar tissue (Fig. 1b, dashed line), which was in alignment with aggravated activation of myofibroblast, as illustrated by α-SMA staining (Fig. 1c). Also, at the nanoscale, for both genotypes, the scar tissue showed more aligned, densely packed collagen fibers relative to the intact dermis, illustrating the aberrant assembly of collagen (Fig. 2, arrowheads). Comparing to the WT control, both the intact dermis and scar tissue of the $Col5a1^{+/-}$ skin exhibited thicker collagen fibrils, indicating aggravated scar formation with the loss of collagen V. Furthermore, $Col5a1^{+/-}$ group also showed lower micromodulus relative to WT control throughout intact, granulation (PWD14) and scar tissues (PWD21) (Fig. 3), illustrating impaired biomechanical functions. Together, our results highlighted collagen V as a crucial constituent that regulates both matrix integrity and wound healing process of dermal tissue, supporting collagen V as a potential target for improved wound healing.

Conclusions: This study highlighted a crucial role of collagen V in regulating the healing process and scar formation in dermal wounds, establishing the basis for using collagen V as a potential therapeutic target.

References: [1]Birk+ 1990. [2]Wenstrup+ 2004. [3]DeNigris+ 2016. [4]Mak+ 2016. [5]Wenstrup+ 2006. [6]Müller-Röver+ 2001. [7]Volk+ 2011. [8]Han+ 2017.
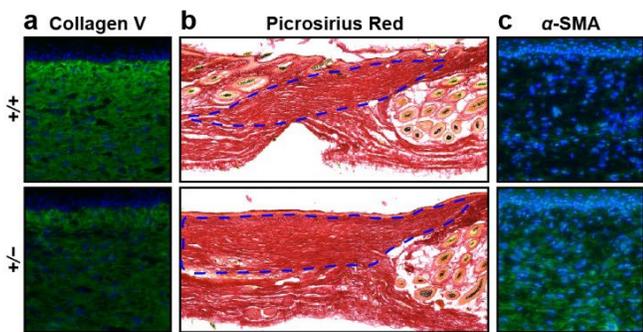
Fig. 1 a) Collagen V IF images, **b)** Picrosirius Red histology and **c)** α-smooth muscle actin (α-SMA) IF images of dermal scar tissue for WT (+/+) and $Col5a1^{+/-}$ (+/−) mice at PWD 21. Scale bar: 100 µm.
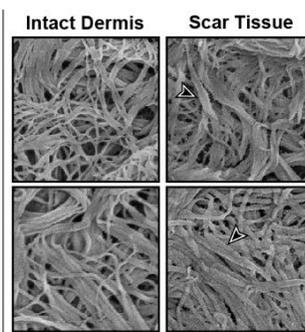
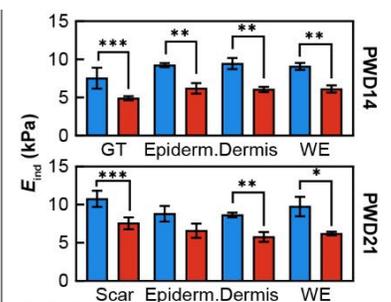**Fig. 2** SEM images of intact dermis and scar tissue for +/+ and +/− mice at PWD 21. Scale bar: 500 nm.

Fig. 3 Comparison of E_{ind} between of +/+ and +/− mice at PWD 14 and 21 (mean ± SD, n = 3, GT: granulation tissue, WE: wound edge, *: $p < 0.05$, **: $p < 0.01$, ***: $p < 0.001$).

Epigenetic Strategies for Preserving Chondrocyte Phenotype During *in vitro* Expansion

Yujia Zhang[1], Saeed B. Ahmed[1], Dong Hwa Kim[1], Zizhao Li[1], Lucy Hederick[1], Melike Lakadamyali[1], Robert L. Mauck[1] and Su-Jin Heo[1]
[1]University of Pennsylvania, Philadelphia, PA
yzhang98@seas.upenn.edu

Disclosures: Zhang (N), Ahmed (N), Kim (N), Li (N), Hederick (N), Lakadamyali (N), Mauck (5, 8), and Heo (5).

Introduction: Autologous chondrocyte implantation is one of the few promising biological treatment options for cartilage repair and/or restoration [1]. However, it is well appreciated that chondrocytes rapidly lose their phenotype (chondrocyte dedifferentiation) with *in vitro* expansion; that is, they cease expression and production of canonical markers that define the cartilage phenotype [2]. Thus, it is imperative to understand the underlying mechanism by which chondrocytes lose their phenotype during *in vitro* expansion and to use this knowledge to preserve their original phenotype for higher therapeutic efficacy in treating cartilage damage. Here, we assess how monolayer expansion alters the epigenetic status and nano-scale chromatin organization of chondrocytes, and demonstrate how application of epigenetic modifiers can restore chondrocyte-like epigenetic status, chromatin structure, and gene expression during *in vitro* expansion.

Figure 1. A: Immunofluorescent images and quantification of H3K9Ac and H3K27me3 (bar = 100 μm, n>95/group, +: p<0.001 vs. P1, *: p<0.001 vs. P2, #: p<0.001 vs. P4), **B:** Heat maps showing H2B localization density [bars = 5 μm (top) and 300 nm (bottom)] and quantitative analysis of chromatin condensation via super-resolution microscopy (n=5/group, ***: p<0.001 vs. P1).

Methods: Juvenile bovine chondrocytes were isolated from the femoral condyle and expanded on tissue culture plastic up to passage six (P0 to P6) in basal growth media (BM). To investigate how *in vitro* expansion alters histone modification status, immunofluorescence of acetylation of H3K9 (H3K9Ac, a marker of transcriptional activation) or tri-methylation of H3K27 (H3K27me3, a marker of transcriptional suppression) was performed at each passage, using a confocal microscope (Zeiss). Super-resolution STORM imaging (ONI) of histone-H2B (H2B) was carried out to determine nano-scale chromatin organization at P1 and P6 and analyzed using the Nanoimager software (ONI) and custom Voronoi-based clustering analysis in MATLAB [3]. Chromatin condensation parameter is determined by normalizing Voronoi density of H2B to the mean Voronoi polygon density in a nucleus [3, 4]. To examine whether treatment with epigenetic modulators regulates the observed epigenetic changes, cells were treated with various doses of Anacardic Acid (4 μM: AA4, 10 μM: AA10, 60 μM: AA60), a histone acetyltransferase inhibitor [5], for 24 hours prior to transition to P2 (**Fig. 2A**). Immunofluorescence of H3K9Ac, H3K27me3, and cell morphology (Phalloidin) data were obtained for each dose at P1 and P2 using a confocal microscope (Zeiss). Expression of chondrocyte markers

Figure 2. A: Schematic showing experimental setup, **B:** Cell area at P1 and P2 (normalized to P1 CTRL, n>75/group, *:p<0.05), **C:** Immunofluorescence levels for H3K9Ac and H3K27me3 (n>150/group), **D:** Quantitative data showing chromatin condensation via super-resolution microscopy (n=5/group), **E:** Gene expression at P1 and P2 (n=5/group) [*: p<0.05 vs. P1 CTRL, +: p<0.05 vs. P2 CTRL, #: p<0.05 vs. P1, AA: Anacardic Acid, P: Passage].

(Aggrecan: ACAN, SOX9, and Collagen Type-II: COL-II) was evaluated using qRT-PCR at P1 and P2. Effectiveness of this early treatment with AA was compared to later treatment (i.e., treating before P4 or P6). In addition, a potent epigenetic modulator, GSK343 (GSK, 2 μM: a histone methyltransferase inhibitor) [6] was also used in comparison to AA. Statistical analyses were performed using a student's t-test or ANOVA with Tukey's post hoc testing.

Results and Discussion: H3K9Ac staining increased with passage, while H3K27me3 staining decreased, suggesting that expansion increases transcriptional activation in chondrocytes (**Fig. 1A**). Indeed, it is known that chondrogenic-marker genes are down-regulated while other genes such as fibroblast-related genes are up-regulated with passage [7]. STORM analysis revealed a decreased H2B density in chondrocyte nuclei, which is consistent with the immunofluorescence data showing that chromatin becomes less condensed with passage (**Fig. 1B**). Since H3K9Ac levels increased and it is also known that chondrocyte dedifferentiation emerges during early passages (P1 and P2) [7], early treatment with AA at various doses (**Fig. 2A**) was first attempted to preserve epigenetic features. Early treatment with AA4 and AA10 blocked increases in cell area seen with passage (**Fig. 2B**). Interestingly, this early AA treatment also blocked changes in H3K9Ac and H3K27me3 with passage (**Fig. 2C**), as well as partially rescued the nano-scale chromatin condensation level (**Fig. 2D**). In addition, early AA treatment significantly increased expression of the chondrogenic markers (SOX9, ACAN, and COL-II) at P2 (**Fig. 2E**). Late treatment with AA was also performed in comparison to the early AA treatment. Although immunofluorescence data suggested that AA was successful in partially rescuing H3K9Ac and H3K27me3 levels at this later passage treatment (**Fig. 3A**), it did not restore expression of chondrogenic markers (**Fig. 3B**). Late treatments of GSK were also carried out; however, the GSK treatment did not have a significant impact on immunofluorescence levels nor gene expression levels (data not shown). Taken together, our data shows that *in vitro* expansion increases histone acetylation in chondrocytes and that inhibition of histone acetyltransferase during expansion blocks these changes and preserves the chondrocyte phenotype. Ongoing studies are focused on identifying how treatment with these epigenetic modifiers impacts the entire transcriptome and epigenome in chondrocytes and their therapeutic potential for translation.

Significance: By understanding the epigenetic alterations that occur during chondrocyte dedifferentiation with *in vitro* expansion, this work may accelerate the development of biologic approaches to generate chondrocytes with higher therapeutic efficacy for the treatment of damaged cartilage.
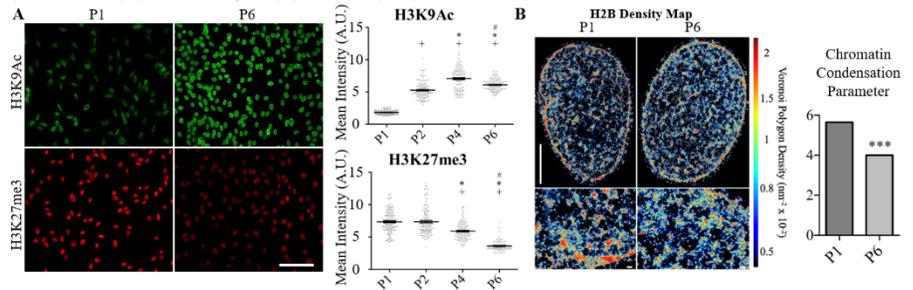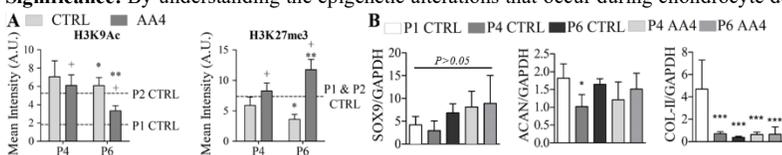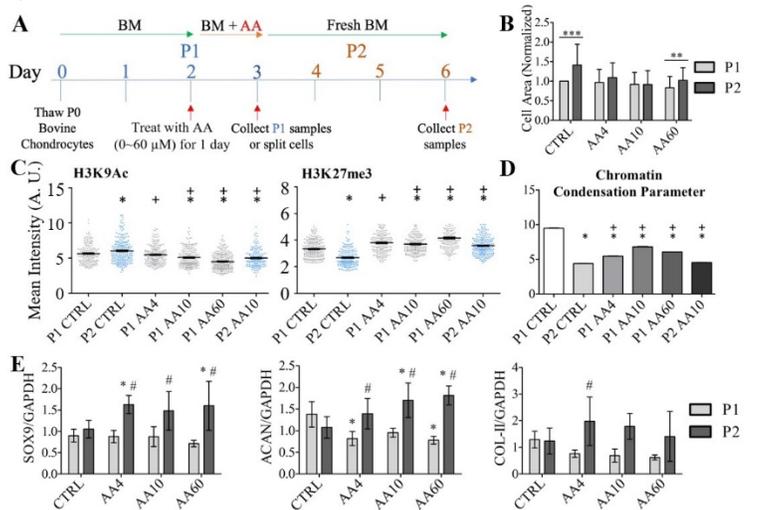

Figure 3 A: Immunofluorescence level for H3K9Ac and H3K27me3 (n>50/group, +: p<0.05 vs. CTRL, *: p<0.05 vs. P4, **: p<0.01 vs. P4), **B:** Gene expression at P1, P4 and P6 for CTRL and AA4 (n=5/group, *: p<0.05 vs. P1 CTRL, ***: p<0.001 vs. P1 CTRL).

YAP and TAZ Mediate Mechanoregulation of Embryonic Bone Formation and Bone Growth

Yasaman Moharrer [1], Joseph Collins[1], Cristian Parisi[3], April Hoggatt[2], Tala Azar[1], Ghazal Vahidi[4], Alexander Robling[2], X. Sherry Liu[1], Chelsea Heveran[4], Niamh Nowlan[5], Joel D. Boerckel[1].
[1]University of Pennsylvania, Philadelphia, PA, [2]Indiana University, Indianapolis, IN, [3]Imperial College London, London, UK, [4]Montana State University, Bozeman, MT, [5]University of College Dublin, Dublin, IE.
yasamanm@seas.upenn.edu

DISCLOSURES: Yasaman Moharrer (N), Joseph Collins (N), Cristian Parisi (N), April Hoggatt (N), Tala Azar (N), Ghazal Vahidi (N), Alexander Robling (N), X. Sherry Liu (N), Chelsea Heveran (N), Niamh Nowlan (N), Joel D. Boerckel (N).

INTRODUCTION: Bone adapts to mechanical signals. However, the mechano-regulatory mechanisms that direct bone formation are unclear. We recently determined that deletion of the mechanotransductive transcriptional regulators YAP (Yes-associated protein) and TAZ (transcriptional co-activator with PDZ-binding motif) mediate both embryonic and adolescent bone formation. Here, we sought to determine the roles of YAP and TAZ in mechanical load-induced prenatal bone formation and in postnatal bone growth.

METHODS: We performed acute, global pharmacologic inhibition of YAP and TAZ in E15.5 embryonic limb explants and 8 week-old mice using verteporfin (VP). VP inhibits YAP/TAZ-TEAD (TEAD is a binding domain) binding. Compared to genetic approaches, acute, global YAP/TAZ inhibition bypasses defects in developmental history, but influences all cells. Here, we performed two experiments on embryonic and growing mice, respectively. **Prenatal:** First, we evaluated the role of YAP and TAZ in mechanical load-induced bone formation in embryonic limb explants under dynamic bioreactor culture. We explanted prenatal (E15.5) hind limbs from C57BL/6 mice and applied dynamic loading (0.67 Hz), 3x per day for 6 days. Control limbs were simultaneously cultured without loading as static controls. To evaluate the roles of YAP and TAZ, we cultured explanted limbs in VP (5uM) or vehicle control (DMSO). To quantify rudiment mineralization, we generated 3D reconstructions of alizarin red-stained samples by optical projection tomography (OPT) and segmentation and 3D modeling software (ITK-SNAP and Rhinoceros). **Postnatal:** Second, we evaluated the roles of YAP and TAZ in postnatal bone formation. We injected male C57BL/6 mice with DMSO or VP (50 mg/kg, i.p.), 5 days per week for two weeks, beginning at 8 weeks of age. We evaluated bone formation by double fluorochrome labeling by Calcein and Alizarin complex one, injected i.p. at 9 and 2 days before sacrifice, respectively. We performed dynamic bone histomorphometry on coronal and transverse tibial sections. On transverse sections, we examined the extent of mineralized bone surface (MS/BS), mineral apposition rate (MAR), and bone formation rate (BFR) in both endosteal and periosteal surfaces using ImageJ and Osteomeasure. On coronal sections, we performed dynamic histomorphometry on trabecular bone and immunofluorescent staining. We measured fracture toughness by a three-point bending testing of notched femora at the rate of 0.001 mm/sec until failure. We measured fracture toughness from the maximum load (KIc-max) and fracture toughness from the yield load (KIc-initiation).

RESULTS: **Prenatal:** At this embryonic stage, mineralization in the long bones occurs in the primary ossification center. We found dynamic mechanical loading significantly increased mineralized length in DMSO-treated samples; however, YAP/TAZ abrogated load-induced bone formation (Fig. 1). **Postnatal:** YAP/TAZ inhibition significantly reduced periosteal MS/BS (Ps.MS/BS), but notably elevated endosteal MS/BS, though this effect was not statistically significant (Fig. 2). YAP/TAZ inhibition did not alter MAR or BFR on either periosteal or endosteal surfaces. A recent study on YAP/TAZ signaling in bone marrow blood vessels predicted that VP treatment in vivo could elevate bone formation through crosstalk from YAP/TAZ-inhibited endothelium.(Sivaraj et. al, Elife, 2020).Therefore, we next performed immunostaining for endomucin+ bone marrow blood vessels and observed the dramatic effects of VP treatment on vessel morphology. VP significantly reduced the vessels' area and the number of endomucin+ vessels. In addition, the fracture toughness test results showed that KIc-max and KIc-initiation values were similar among groups, although they were more heterogeneous in VP-treated femurs.

DISCUSSION: Here, we show that YAP and TAZ mediate both prenatal and postnatal bone mineralization. **Prenatal:** YAP and TAZ were required for mechanical load-induced rudiment mineralization ex vivo. **Postnatal:** YAP/TAZ inhibition reduced osteoblast activation on periosteal cortical bone surfaces. However, consistent with a recent report on YAP/TAZ signaling in bone marrow endothelium, YAP/TAZ inhibition did not reduce endocortical MS/BS and altered bone marrow vasculature, suggesting both cell-autonomous inhibition of osteoblast activation and non-cell-autonomous crosstalk with cells in the bone marrow.

SIGNIFICANCE/CLINICAL RELEVANCE: The mechanotransductive effects of YAP and TAZ can be disrupted in a diseased bone due to the altered mechanical environment during the disease development. Therefore understanding the mechanistic role of YAP and TAZ in regulating bone function is central to helping treat developmental bone diseases.
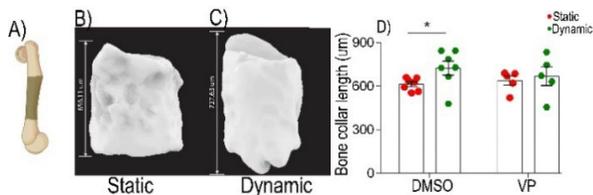
Fig. 1: **YAP/TAZ inhibition abrogates the effect of mechanical loading.** A) The darker region shows the mineralized portion of the rudiment B) and C) 3D reconstructed images of the mineral in static and dynamic loading conditions, respectively. D) Dynamic loading increases the collar length in DMSO-treated samples (*p<0.05), but not in VP-treated samples.
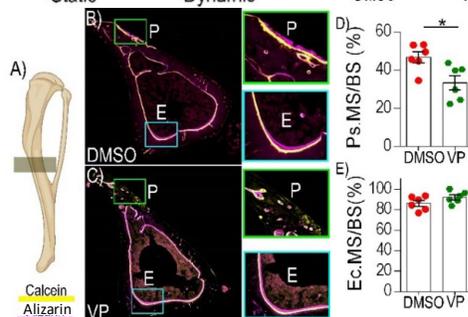
Fig. 2: **YAP/TAZ inhibition decreases the periosteal bone formation.** A) The darker region shows the location of the transverse sections. B) and C) Tibial transverse section for DMSO-treated and VP–treated samples at 10x magnification, respectively, "P" stands for the periosteum, and "E" stands for the endosteum, The mineralized bone is labeled with Calcein (yellow) and Alizarin (magenta). D) and E) VP-treated samples show a reduced bone MS/BS in periosteum (*p<0.05), but no change is observed in the endosteum.

CD206+ tendon resident macrophages and their crosstalk with fibroblasts and the ECM during tendon growth and maturation

Catherine A. Bautista[1], Anjana Srikumar[1], Elisia D. Tichy[1], Grace Qian[1], Xi Jiang[1], Foteini Mourkioti[1], Nathaniel A. Dyment[1]

[1] University of Pennsylvania

The tendon is composed of a heterogeneous cell population that includes resident macrophages. In this study, we characterize this population and its crosstalk with neighboring tendon fibroblasts and the extracellular matrix (ECM) during murine tendon development, growth, and homeostasis. Fluorescent imaging of cryosections revealed that F4/80$^+$ tendon resident macrophages reside adjacent to Col1a1-CFP$^+$ Scx-GFP$^+$ fibroblasts within the tendon fascicle from embryonic development (E15.5) into adulthood (P56). Through flow cytometry and qPCR, we found that tendon resident macrophages express several known macrophage markers, including *Adgre1* (F4/80), *Mrc1* (CD206), *Lyve1*, and *Folr2,* but not Ly-6C, and are labeled with the Csf1r-EGFP ("MacGreen") reporter. The proportion of patellar tendon Csf1r-EGFP$^+$ resident macrophages in relation to total cell number exponentially increases during early postnatal growth, from ~2% at P4 to ~8% at P56, while the density of macrophages per mm^2 remains constant. EdU labeling analysis of P1 patellar tendon sections showed that proliferation of resident macrophages within the tendon fascicle likely drives this increase in proportion. Gene expression analyses of P14 and P56 limb tendon resident macrophages demonstrated a clear divergence in phenotype from P14 to P56, with increased pro-inflammatory and anti-inflammatory cytokine expression at P56. At P56, gene expression of limb tendon resident macrophages diverges from that of tail tendon resident macrophages, suggesting differential phenotypes across anatomically and functionally different tendons. Ligand-receptor analysis suggests potential two-way signaling between tendon fibroblasts and resident macrophages. Tendon fibroblasts express high levels of *Csf1*, which encodes macrophage colony stimulating factor (M-CSF) that acts on the CSF1 receptor (CSF1R) on macrophages. RNA *in situ* hybridization of patellar tendon sections showed that *Csf1r*-expressing resident macrophages preferentially localize to *Csf1*-expressing fibroblasts. Lastly, we found that tendon resident macrophages express high levels of ECM-related genes, including *Mrc1* (collagen endocytosis receptor), *Lyve1* (hyaluronan receptor), *Lair1* (type I collagen receptor), *Ctss* (elastase), and *Mmp13* (collagenase), and internalize DQ Collagen in explant culture. Overall, our study provides insights into the potential roles of tendon resident macrophages in regulating fibroblast phenotype and the ECM during tendon growth.

NUCLEUS PULPOSUS REPLACEMENT MITIGATES IVDD IN A CAPRINE MODEL – A 3 YEAR STUDY

Leslie Brewer[1], Rachel Hilliard[1], Julie Engiles[1], Erik Brewer[3], Zachary Brown[3,4], Harrah Newman[2], Adriana Barba[1], Pete Wilson[3], Anthony Lowman[3], Dawn M Elliott[2], Thomas Schaer[1]

[1]University of Pennsylvania School of Veterinary Medicine New Bolton Center, Kennett Square, PA,
[2]University of Delaware, Newark, DE, [3]Rowan University, College of Engineering, Glassboro, NJ,
[4]ReGelTec Inc., Baltimore, MD

INTRODUCTION: Lumbar intervertebral disc degeneration (IVDD) impacts up to 90% of the aged population, with > 25% of Americans reporting low back pain. Early degenerative changes typically occur in the central nucleus pulposus (NP), where progressive dehydration from proteoglycan loss compromises mechanical function. We have developed a non-crosslinked injectable NP replacement hydrogel based upon a polyvinyl alcohol and polyvinyl pyrrolidine co-polymer, treated with polyethylene glycol to yield a thermally processible hydrogel (HY) with 59-66% water content. The hydrogel incorporates barium sulphate (BaS) for imaging contrast. The objective of this work was to utilize clinical exam, serial radiography, µCT, and histology to evaluate hydrogel disc replacements for IVDD over a three year follow up.

METHODS: Six adult goats (50-80kg) underwent chemonucleolysis with 1.5U Chondroitinase ABC (CABC) at levels L1-L2, L2-L3, and L4-L5 [1]. Two weeks later, discs L2-L3 and L4-L5 were injected with HY under fluoroscopic control via a 17g spinal needle. Animals were maintained for 6 weeks, 12 weeks, or 3 years with unrestricted exercise and daily evaluation for pain, gait symmetry, lameness, and signs of neurologic deficits. Monthly standing lateral radiographs were used to evaluate implant placement, disc space geometry and disc height index changes. At the completion of each cohort gross necropsy was performed, along with µCT of lumbar motion segments and histology of the discs and endplates.

RESULTS: Short-term neurologic deficits were observed in one animal, but no long-term lameness or neurologic deficits were observed. Longitudinal disc height index (DHI) analysis showed that HY-treated disc maintained their height throughout the study, while CABC-degenerated discs progressively decreased in DHI. µCT of the short-term cohorts showed evidence of moderate endplate erosions in the CABC-degenerated and HY-treated discs, with severe endplate changes associated with hydrogel extrusion. However, by the completion of the long-term cohort significant endplate changes were only present in the CABC-degenerated discs and no abnormalities were observed at levels with HY extrusion. HY-implanted discs exhibited improved overall histological grade compared to untreated discs. Mild to moderate degenerative change was observed in HY-treated discs in the short-term cohort. In the long-term cohort, chondrocyte-like cells were increased in both CABC-degenerated & HY-treated discs compared to controls. CABC-degenerated discs had increased degeneration, including foci of NP necrosis, and decreased AF fiber organization with increased proteoglycan staining through mid to outer AF layers. Endplates of CABC-degenerated and HY-treated discs have slightly wider zones of bone remodeling at the cartilage-bone but retain intact compact bone.

DISCUSSION & CONCLUSIONS: Our long-term clinical and *ex-vivo* findings suggest that minimally invasive, percutaneous nucleoplasty in degenerated intervertebral discs mitigates long-term disc degeneration and end-plate changes in this large animal model of IVDD. Disc height is maintained post-treatment, creating improved biomechanical function. BaS-enhancement of the HY enabled visibility on radiographs and fluoroscopy, which affords adequate intraoperative visualization during delivery and allows for long-term device monitoring. Ongoing work is focused on elucidating changes in the cellular / inflammatory signalling milieu and the development of imaging techniques to improve assessment of HY-treated and untreated degenerating discs.

REFERENCES: 1. Gullbrand+ *Osteoarthr. Cartil.* 2017; 2. Moore *Eur. Spine J.* 2006.

Deficiency of the pattern-recognition receptor CD14 modulates osteoclast differentiation *in vitro*

Lance A. Murphy[1,2], Baofeng Hu[1,2], Kevin G. Burt[1,2], Magnolia Wang[1], Vu Nguyen[1,2], Robert L. Mauck[1,2], Carla R. Scanzello[1,2]
[1]University of Pennsylvania, Perelman School of Medicine, Philadelphia, PA
[2]CMC VA Medical Center, Translational Musculoskeletal Research Center, Philadelphia, PA
Lance.murphy@pennmedicine.upenn.edu

INTRODUCTION: Osteoarthritis is often associated with bone changes such as subchondral sclerosis and osteophyte formation (1). Furthermore, it has previously been shown that CD14-deficient mice show less subchondral bone remodeling after joint injury in the DMM (destabilization of the medical meniscus)- model of OA (2). CD14 is a GPI-anchored surface protein known to be a co-receptor for several TLRs and is highly expressed in myeloid cell lineages including the precursors of osteoclasts (3,4). Therefore, we studied the osteoclast differentiation potential of bone marrow-derived precursors from CD14-deficient mice in comparison to congenic C57BL6 controls. It was hypothesized that there would not be a difference between strains in RANKL-dependent activation of osteoclast precursors at baseline, in the absence of TLR-stimuli.

METHODS: Cell isolation and culture: Bone Marrow was isolated from femurs and tibiae from 3 WT mice and 3 CD14 knockout mice. After 24 hours in suspension, cells were cultured in DMEM, modified with 10% FBS, 1% P/S, and 30 ng/mL M-CSF for 5 days to expand osteoclast precursors (monocytes). Cells were passaged on day 6 and plated at 50,000 cells per well in a 24 well plate in the presence or absence of RANKL (100 ng/mL).

Trap staining and image analysis: Cells were then stained for TRAP on days 3 and 4 after addition of RANKL. Cells were imaged at 10x with 5 images per well over 3 wells for each timepoint and characterized using ImageJ. Images were quantified for percent area covered of all cells as well as percent area covered after filtering out non-osteoclast cells based off of size, with the ratio of the two being the ratio of osteoclast area. Number of osteoclasts (cells with >3 nuclei) per 10X field was also quantitated. Multiple unpaired t-test were performed with Holm-Sidak correction.

Actin Ring staining and cell characterization over time: Cells were passaged on day 5 of expansion in MCSF and plated at 50,000 cells per well in 4-well glass bottom slides with 100 ng/mL RANKL. On days 3, 4, 5, and 6 after addition, the cells were fixed in 4% PFA and stained with Rhodamine Phalloidin (for F-actin) (and DAPI (for nuclei) (5). Cells were imaged at 10x using confocal microscopy with 4 wells per timepoint, and image analysis performed using CellProfiler (open source) to calculate area fraction of cells, average area per cell (cell size), and the intensity of DAPI per cell as a marker of number of nuclei. Differences between strains were tested with multiple unpaired t-test with Holm-Sidak correction.
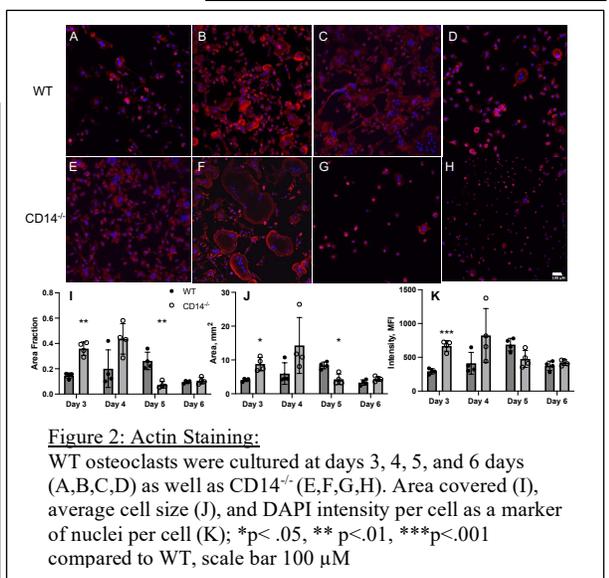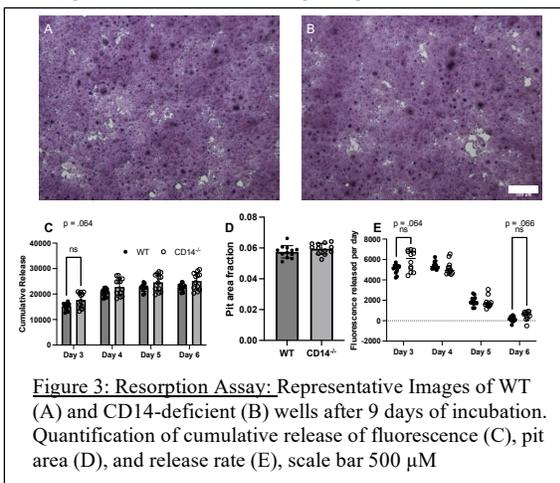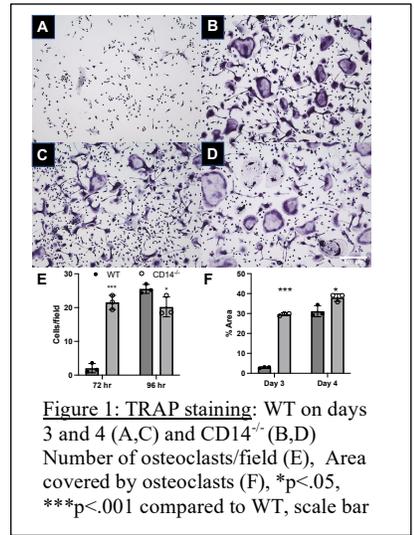
Calcium Phosphate Resorption Assay: A calcium phosphate-coated 24-well plate was obtained from Cosmo Bio USA. Fluorescently-labeled chondroitin sulfate was loaded on the plate for two hours per protocol, and rinsed with PBS. Precursor cells were plated at 50,000 cells per well in media with M-CSF and RANKL. Media was removed on day 3 and replenished with 1 milliliter of media with M-CSF and RANKL. 200 microliters of media was removed on days 4, 5, and 6 for analysis. Fluorescence of media was measured at exciting and emission of 495 and 519 nm, respectively. After 9 days, the wells were treated with 5% Sodium hypochlorite to remove the cells. The wells were then stained with 1% toluidine blue to visualize remaining calcium phosphate matrix, and imaged at 4x (3 images per well for a total of 12 samples in each group. CellProfiler was used to quantify pit area, which was averaged per well giving total sample number of 4 per group. Multiple unpaired t-test were performed with Holm-Sidak correction.
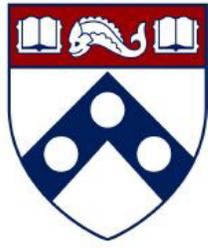
RESULTS SECTION: Representative TRAP staining in WT (Fig 1 A, C) and CD14^{-/-} cells (Fig 1 B,D) at 3 (A,B) and 4 (C,D) days after addition of RANKL. CD14-deficient cells showed more rapid differentiation than WT cells. When quantitated, numbers of osteoclasts (Fig 1E) and area of the plate covered by osteoclasts (Fig 1F) were higher in CD14-deficient cells on day 3 and day 4, although less difference on day 4. Image analysis of the actin stained images showed similar time-dependent trends (Fig 2 A-H). CD14-deficient cells covered more area of the plate on days 3 and 4 (Fig 2I) and were larger (Fig 2J), but by day 5 the trends reversed, with WT cells covering more area and being larger than the CD14-deficient cells. The DAPI intensity (surrogate for # of nuclei per cell) follows a similar trend (2K). The resorption assay showed that CD14-deficient cells release fluorescently-coated chondroitin sulfate more quickly in the beginning (Figure 3C,E), but cumulatively the WT performed similar functionally over time (Figure 3C,D).

DISCUSSION: Our results show that CD14-deficient osteoclasts precursors differentiate more quickly than WT cells, but ultimately the WT cells reached similar levels of confluency and size (6). Actin staining confirmed that the CD14-deficient osteoclasts differentiate approximately 24 hours ahead of WT cells in response to RANKL. While they form before the WT cells, they also die back before the WT cells. Because of this, we used the calcium phosphate-coated plate as a proxy for total function over cell lifespan, and we saw that despite early activation of CD14-deficient cells, the functionality of the cell lines were approximately the same over time. At the moment, it is unclear the mechanism that drives the early differentiation of CD14-deficient osteoclasts. It has been shown that TLRs 1-9 are present in osteoclast precursors and the activation of TLRs can either increase or decrease osteoclastogenesis (7). Less is known about CD14 signaling in osteoclast-precursors and how it affects osteoclastogenesis. To address this, we plan to compare osteoclastogenesis in the presence of specific TLR/CD14 stimuli and blockade in the future. **SIGNIFICANCE/CLINICAL RELEVANCE:** (1-2 sentences): We hope that understanding the role of CD14/TLR signaling in osteoclastogenesis, will lead to new therapeutic strategies for diseases characterized by pathologic bone remodeling.

REFERENCES: [1] Donell, S *EFORT* 2019; [2] Sambamurthy, N+ *PLoS ONE 2018*; [3] Zanoni, I+ *Front Cell Infect. Microbiol.* 2013; [4] Xue, J+ *Art Res Ther* 2020; [5] Kasonga, A+ *PLoS ONE* 2015; [6] Ikeda, K+ *Journ Biochem* 2015; [7] Ding P+ *Bone Res* 2022

Figure 1: TRAP staining: WT on days 3 and 4 (A,C) and CD14^{-/-} (B,D) Number of osteoclasts/field (E), Area covered by osteoclasts (F), *p<.05, ***p<.001 compared to WT, scale bar

Figure 3: Resorption Assay: Representative Images of WT (A) and CD14-deficient (B) wells after 9 days of incubation. Quantification of cumulative release of fluorescence (C), pit area (D), and release rate (E), scale bar 500 µM

Figure 2: Actin Staining: WT osteoclasts were cultured at days 3, 4, 5, and 6 days (A,B,C,D) as well as CD14^{-/-} (E,F,G,H). Area covered (I), average cell size (J), and DAPI intensity per cell as a marker of nuclei per cell (K); *p< .05, ** p<.01, ***p<.001 compared to WT, scale bar 100 µM

Miscellaneous Abstracts

CD-9 as a Novel Marker of Healthy Late-Stage Nucleus Pulposus Cells

Chenghao Zhang[1,2], Yian Khai Lau[1,2], Ling Qin[1], Thomas P. Schaer[1,2], George R. Dodge[1,2], Robert L. Mauck[1,2], Neil R. Malhotra[1], Lachlan J. Smith[1,2]
[1]University of Pennsylvania and [2]Corporal Michael J. Crescenz Philadelphia VA Medical Center, Philadelphia, USA
chenghao.zhang@pennmedicine.upenn.edu

INTRODUCTION: Intervertebral disc degeneration is a major cause of low back pain, the leading cause of disability worldwide [1]. Emerging cell-based therapies targeting the disc nucleus pulposus (NP), particularly those employing adult stem cells, have shown promise in preclinical studies [2]; however, efficacy has been limited by the inability of these therapeutic cells to sufficiently mimic the phenotype of native NP cells, including survival in the nutrient poor disc microenvironment and production of a proteoglycan-rich extracellular matrix (ECM). Recently, we provided the first evidence of emergent heterogeneity amongst NP cells in the postnatal mouse disc [3]. Specifically, we established the existence of putative early and late-stage NP cells, which exhibit distinct gene expression profiles reflecting unique functional roles. Late-stage NP cells highly expressed the surface marker CD-9 in addition to NP matrix-related genes suggesting they are essential to the development and maintenance of healthy NP tissue, and may possess optimal properties for NP regeneration. The objective of this study was to build on these findings and 1) Confirm that CD-9 positive NP cells co-localize to regions of high aggrecan expression in the postnatal mouse disc; 2) Establish the presence of CD-9-positive NP cells in other species, including goats and humans; and 3) Assess changes in the number of CD9-positive NP cells in a goat model of disc degeneration.

METHODS: _Single Cell RNA-Sequencing of Mouse NP Cells:_ With IACUC approval, notochord-derived NP cells were obtained postmortem from the discs of 30-day-old Shh-cre;R26R-tdTomato mice by fluorescence-activated cell sorting. Libraries were generated using the Chromium controller (10X Genomics) and sequencing was performed using the Illumina HiSeq platform. NP cell identity was confirmed by KRT19 expression [4], and cluster-specific relative aggrecan and CD-9 gene expression was determined using Seurat. Three replicate experiments were performed. _Immunofluorescent Imaging of Mouse Discs:_ Lumbar spines were isolated from Agc1[tm(IRES-CreERT2)]; R26R-tdTomato mice aged 30, 60, 90 and 120 days, and mid-sagittal cryosections were stained for immunofluorescent co-localization of CD-9 with aggrecan expression. _Flow Cytometry of Human and Goat NP Cells:_ Healthy NP cells from adult human (commercially sourced) and goat donors were immunolabeled with an anti-CD9 antibody the percentage of CD-9 positive NP cells in each sample was analyzed by flow cytometry. _Immunohistochemistry of Healthy and Degenerate Goat Discs:_ With IACUC approval, moderate severity degeneration was induced in the lumbar discs of adult goats via injection of 1U chondroitinase ABC [5]. After 12 weeks, degenerate (n=4) and adjacent healthy control (n=3) discs were harvested postmortem, fixed, decalcified and processed into paraffin. Sections were immunostained for CD-9 and imaged using bright field microscopy. The percent of CD-9 positive NP cells was quantified, with significant differences determined using an unpaired t-test.

RESULTS: _Co-Localization of Aggrecan and CD-9 in the Postnatal Mouse Disc:_ A total of 1116 notochord-derived NP cells with a median of 1445 genes/cell and a median of 4854 UMIs/cell were identified within the total sequenced cell population. Cluster-specific gene expression analysis confirmed mutual high expression of both CD-9 and aggrecan by late-stage NP cells (**Fig 1A**). Fluorescence imaging revealed emergent tdTomato-positive aggrecan-expressing cells localized to the peripheral region of the postnatal mouse NP, and immunofluorescent staining demonstrated that these same cells co-expressed CD-9 (**Fig 1B**). No CD-9 expression was observed in the annulus fibrosus. _CD-9 Expression by Human and Goat NP Cells:_ Flow cytometry analysis revealed that healthy adult human and goat NP cells were found to be 99.8 and 95.6% immunopositive for CD-9, respectively (**Fig 2**). _Immunohistochemistry of Healthy and Degenerate Goat Discs:_ CD-9 positive NP cells were observed in the NPs of both healthy and degenerate discs; however the percentage of CD-9 positive cells was significantly lower in degenerate compared to healthy discs (23% vs 79%, respectively, p<0.05, **Fig 3**).

DISCUSSION: CD-9 is a member of the tetraspanin superfamily of molecules and while its function in the disc as not been studied, diverse roles in other tissues have been reported include in growth, differentiation, cell adhesion, motility and regulation of inflammation [6]. CD-9 is also an established marker of extracellular vesicles [6]. In this study we provide evidence that CD-9 is a marker of late-stage NP cells in mice, goats and humans. In mice, CD-9 positive NP cells were found to co-express aggrecan, a proteoglycan that is an essential component of the healthy adult disc, where it maintains the hydration and swelling pressure of the NP. Loss of aggrecan is one of the hallmarks of early disc degeneration, and we provide initial evidence that the number CD-9 positive NP cells also diminishes with degeneration. Ongoing studies are focused on elucidating the biological role of CD-9 in the development and maintenance of the healthy NP, and examining CD-9 as surface marker for the isolation and enrichment of NP cells with high therapeutic potential.

SIGNIFICANCE: Cell-based therapies for disc degeneration hold significant promise for patients with chronic low back pain. The results of this study identify a novel marker of healthy adult NP cells and suggest target characteristics for therapeutic stem cells.
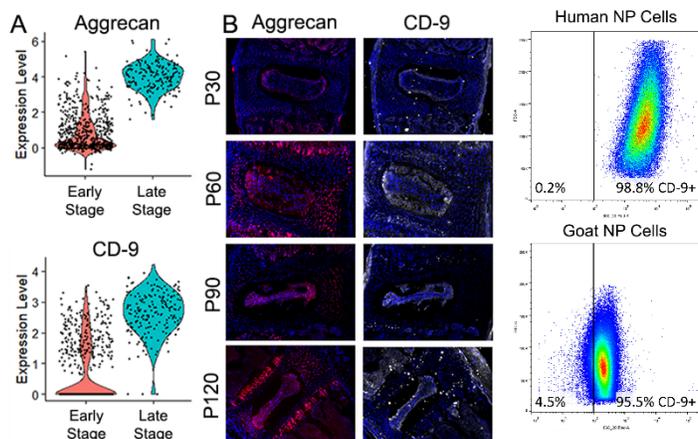
REFERENCES: [1] Vos+ Lancet 2015; [2] Smith+ JOR Spine 2019; [3] Zhang+ ORS Transactions 2022; [4] Mohanty+ J Cell Physiology 2020; [5] Gullbrand+ Osteoarthritis Cartilage 2017; [6] Brosseau+ Front Immunol 2018.

Figure 1. A. scRNA-Seq demonstrated that late-stage NP cells exhibit elevated expression of both aggrecan and CD-9 compared to early-stage NP cells in P30 mouse discs. **B.** Co-localization of aggrecan and CD-9 expression in the postnatal mouse NP.

Figure 2. Flow cytometry analysis demonstrated that the majority of adult, healthy human and goat NP cells express CD-9.
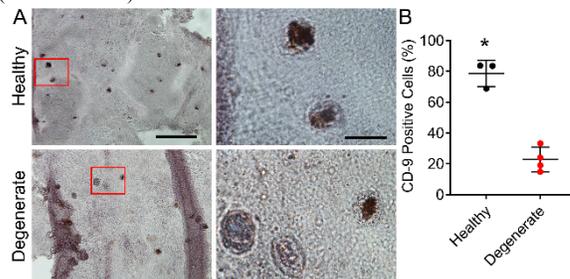

Figure 3. A. Representative immunohistochemistry showing CD-9-positive cells in the NP of adult healthy and degenerate goat discs. **B.** Quantification of CD-9 positive NP cells. Scale=100μm, inset=20μm; *p<0.05 vs Degenerate.

Effects of Organ Culture and Mesenchymal Stem Cell Delivery on Nucleus Pulposus Cell Extracellular Matrix Gene Expression and Cell Cycle Progression

Chenghao Zhang[1,2], Thomas P. Schaer[1], George R. Dodge[1,2], Neil R. Malhotra[1], Robert L. Mauck[1,2], Lachlan J. Smith[1,2]
[1]University of Pennsylvania and [2]Corporal Michael J. Crescenz Philadelphia VA Medical Center, Philadelphia, USA
chenghao.zhang@pennmedicine.upenn.edu

Disclosures: Chenghao Zhang (N), Thomas P. Schaer (1-PSI; 3B-ReGelTec, Peptilogics, Acuitive Technologies; 3C-PAX Therapeutics, OrimTech, SINTX Technologies, OsteoCentric Technologies, 4-ReGelTec, Acuitive Technologies, 5-DePuy Synthes, Alcyone Therapeutics, Acuitive Technologies, SINTX Technologies, Camber Spine, ReGelTec, 6-Heraeus), George R. Dodge (N), Robert L. Mauck (5-4Web Medical, 8-JOR Spine), Neil R. Malhotra (N), Lachlan J. Smith (8-JOR Spine, Connective Tissue Research; 9-ORS Spine Section, National MPS Society)

INTRODUCTION: Intervertebral disc degeneration is a major cause of low back pain, the leading cause of disability worldwide [1]. Emerging cell-based therapies targeting the disc nucleus pulposus (NP), including those employing adult mesenchymal stem cells (MSCs), have shown promise in preclinical studies [2]. Possible mechanisms of MSC-based repair and regeneration of the NP include paracrine signaling that suppresses inflammation, and enhances endogenous cell proliferation and extracellular matrix expression. Whole-disc organ culture is a powerful preclinical tool for investigating such mechanisms [3, 4]. However, even under ideal experimental conditions organ culture may not fully recapitulate the cellular microenvironment present *in vivo*, resulting changes to the phenotype of NP cells. The objective of this study was to use single cell RNA sequencing (scRNA-Seq) to investigate the effects of organ culture and MSC delivery on the cellular composition of the NP, and specifically, effects on extracellular matrix gene expression and cell cycle progression.

METHODS: With IACUC approval, lumbar spines were obtained postmortem from 6 male large frame goats, and discs were isolated and allocated to 3 experimental conditions: 1) NP cells freshly isolated from discs postmortem (no organ culture); 2) NP cells isolated after 7 days of whole disc organ culture; and 3) NP cells and MSCs isolated after 7 days of whole disc organ culture. For this final group, allogeneic adult goat bone marrow-derived MSCs (0.2×10^6 in 200μl saline) were injected into the NPs of discs on day 0. For all conditions, cells were isolated from the NP using a 5mm biopsy punch followed by collagenase digestion. For organ culture, bony end plates were removed and discs were cultured with intact cartilaginous end plates in basal media (DMEM +10% FBS) under limited swelling conditions [3]. For each condition, isolated cells from 5 discs were pooled, assessed for viability via trypan blue staining, and analyzed using scRNA-Seq. Libraries were generated using the Chromium controller (10X Genomics) and sequencing was performed using the Illumina HiSeq platform. Unsupervised clustering was undertaken using Seurat, and cluster-specific expression of matrix markers and cell cycle progression was performed using R software. Two replicate scRNA-Seq experiments were performed to confirm batch consistency, and data was pooled for analysis.

RESULTS: <u>Global scRNA-Seq Findings:</u> A total of 68,533 cells were sequenced (median 1284 genes/cell and 4904 UMIs/cell): 25,909 freshly isolated NP cells (94% viability), 18,657 NP cells after organ culture (86% viability), and 24,967 NP cells and MSCs after organ culture (74% viability). UMAP plots generated for each condition using identical analysis parameters identified 8 unique cell clusters (**Fig 1A**), with the percentage of cells present within each cluster differing between conditions (**Fig 1B**). <u>Extracellular Matrix Expression:</u> Aggrecan (ACAN) expression was highest in cluster 5 (**Fig 2**); the percentage of cells in this cluster was 19% for freshly-isolated NP cells, but decreased to 3% and 5% after organ culture, with and without MSCs respectively. Collagen 1 (COL1A1) expression was highest in cluster 3; the percentage of cells in this cluster was 7% for freshly isolated NP cells and 11% NP cells alone after organ culture, but increased to 29% for NP cells and MSCs after organ culture. SOX9 expression was highest in cluster 8, however this cluster was absent for both organ culture groups. <u>Cell Cycle Progression:</u> Globally, the percentage of cells in the resting (G1) versus the proliferating (S and G2M) phases was similar across the three study groups (**Fig 3A**). However, important cluster-specific differences in cell cycle phase were noted between groups (**Figs 3B** and **C**). Specifically, cluster 7 was comprised entirely of proliferating (S and G2M) cells. For freshly isolated NP cells, this cluster was absent, but comprised 3 and 7% of total cells after organ culture with and without MSCs, respectively.

DISCUSSION: In this study we provide evidence that organ culture and MSC delivery impacts extracellular matrix gene expression and cell cycle progression of NP cells. Organ culture models are used extensively as preclinical tools to study disc degeneration and therapeutic intervention [3, 4]. Here we show that while organ culture did preserve some phenotypic properties of NP cells, there were decreases in cell populations that highly express ACAN and SOX9. Interestingly, following MSC delivery, rather than enhancing expression of NP-specific ECM genes such as ACAN, there was an increase in cells expressing COL1A1. This supports the idea that preconditioning MSCs may be necessary for MSCs to exert optimal therapeutic effects on endogenous cells post-implantation. Emergent proliferating cells in organ culture may reflect adaptation of NP cells to the altered *ex vivo* nutritional microenvironment.

SIGNIFICANCE: MSC injections are a promising treatment approach for disc degeneration, and organ culture models are used extensively as preclinical tools. In this study we provide insights into how MSC injection and organ culture alter the cellular composition and phenotype in the disc.

REFERENCES: [1] Vos+ Lancet 2015; [2] Smith+ JOR Spine 2019; [3] Gawri+ Spine 2011; [4] Pfannkuche+ Connect Tissue Res. 2020.
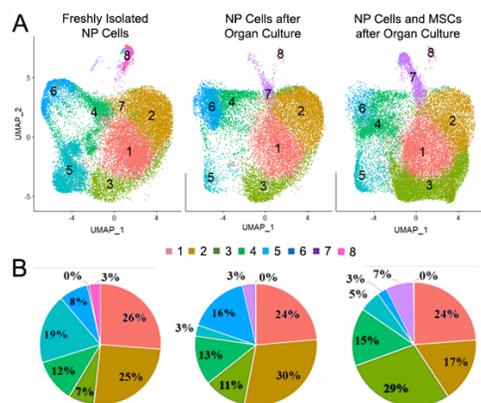
Figure 1. A. UMAP plots illustrating the presence of 8 distinct subpopulations (clusters) of cells in the goat NP. **B.** The percentage of cells in each cluster is markedly altered following organ culture with and without MSC delivery.

Figure 2. Cluster-specific expression of key extracellular matrix genes.

Figure 3. A. Globally, the NP contains both resting (G1) and proliferating (S and G2M phase) cells for all three experimental conditions. **B** and **C.** Cluster-specific differences in cell cycle progression across the three experimental conditions.

P49

Physiological Measurement of Nucleus Pulposus Oxygen, Glucose, and Lactate in a Large Animal Model of Disc Degeneration: Preliminary Findings

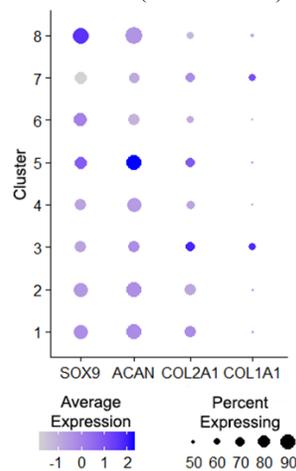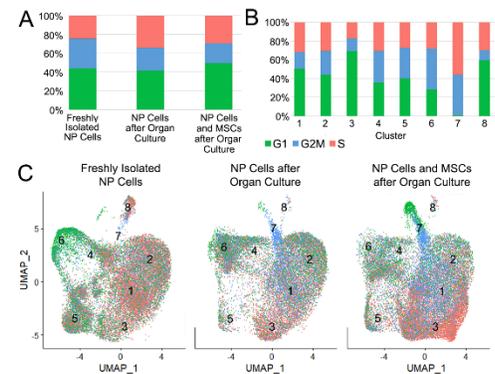Karthikeyan Rajagopal[1], Thomas P. Schaer[1], Chenghao Zhang[1], Kyle D. Meadows[2], Rachel Hilliard[1], John C. O'Donnell[1], George R. Dodge[1], Dmitriy Petrov[1], Dawn M. Elliott[2], Robert L. Mauck[1], Lachlan J. Smith[1], Neil R. Malhotra[1]

[1]University of Pennsylvania, Philadelphia, PA, USA, and [2]University of Delaware, Newark, DE, USA

Karthikeyan.Rajagopal@pennmedicine.upenn.edu

Disclosures: Karthikeyan Rajagopal (N), Thomas P. Schaer (PSI; ReGelTec, Peptilogics, Acuitive Technologies; PAX Therapeutics, OrimTech, SINTX Technologies, OsteoCentric Technologies, ReGelTec, Acuitive Technologies, DePuy Synthes, Alcyone Therapeutics, Acuitive Technologies, SINTX Technologies, Camber Spine, ReGelTec, Heraeus), Chenghao Zhang (N), Kyle D. Meadows (N), Rachel Hilliard (N), John C. O'Donnell (N), George R. Dodge (N), Dmitriy Petrov (N), Dawn M. Elliott (N), Robert L. Mauck (8-JOR Spine), Lachlan J. Smith (8-JOR Spine, Connective Tissue Res; 9-ORS Spine Section, National MPS Society), Neil R. Malhotra1 (N)

INTRODUCTION: Intervertebral disc degeneration is a common underlying cause of low back pain, the leading cause of disability worldwide [1]. Treatments for symptomatic mild to moderate disc degeneration are few, have limited long-term efficacy, and do not alter the disease course. In preclinical studies, delivery of mesenchymal stem cells (MSCs) to the disc nucleus pulposus (NP) has shown significant promise; however, characteristics of the local biochemical microenvironment have been shown to negatively impact MSC survival and therapeutic efficacy [2]. Quantification of this microenvironment, including changes in oxygen and nutrient availability as a function of degeneration severity, is critical to the development of effective MSC-based treatments. In situ measurement of tissue oxygen and metabolites using Licox monitoring and microdialysis, respectively, is successfully performed for patients with ischemic brain injury [3,4]. The goal of this study was to establish the feasibility of using Licox monitoring and microdialysis for the *in vivo* characterization of the NP microenvironment. This was achieved using a large animal model of disc degeneration in the goat lumbar spine, in which a spectrum of degenerative changes can be achieved following injection of chondroitinase ABC [5]. We hypothesized that monitors could be successfully placed in the goat NP, would not result in confounding structural damage to the disc, and could effectively detect changes in NP oxygen, glucose, and lactate as degeneration progressed.

METHODS: *Animal Model and Study Design:* With IACUC approval, under general anaesthesia, degeneration was induced in four lumbar discs (L23, L34, L45, and L56) of a large frame goat via chondroitinase ABC (ChABC, 2U in 200ul) injection into the nucleus pulposus (NP). *Imaging: In vivo* magnetic resonance imaging (MRI) of the lumbar spine was performed at 0 weeks (prior to initiation of degeneration), and 6 and 12 weeks. Images for quantitative T2 mapping were obtained, as well as T2-weighted images for subjective assessment of disc condition. Degeneration severity in discs that received ChABC *and* were subjected to serial oxygen and/or microdialysis probe insertions (L23, L34 and L45) was compared to the disc that received ChABC only (L56), and to healthy, intact control discs (L12 and L67). *In Vivo Measurement of Disc Oxygen, Glucose and Lactate:* Under fluoroscopic guidance, customized epidural needles were used to position the probes in the center of the NP. Oxygen levels were measured for 45 minutes in the L23 disc at 0 weeks (prior to ChABC injection) and 6 weeks using a Licox brain tissue oxygen probe (Integra). Glucose and lactate concentrations were measured in both the L23 and L34 discs at 12 weeks. Specifically, type 71 high cut-off brain microdialysis catheters (membrane length 10 mm, molecular cut-off 100 kDa) connected to CMA 107 precision pumps (M Dialysis AB, Sweden) were used to sample microdialysate from NP at a flow rate of 0.3 μl/minute at 30-minute intervals up to 150 minutes. Glucose and lactate concentrations in collected microdialysate were measured using high-sensitivity detection kits (Sigma, USA). The L45 disc level was used only for probe placement optimization.
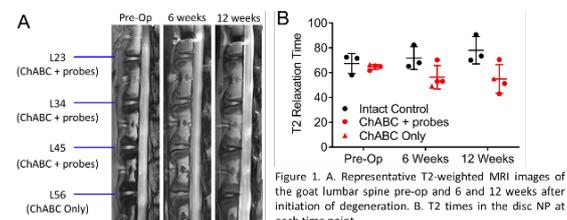

Figure 1. A. Representative T2-weighted MRI images of the goat lumbar spine pre-op and 6 and 12 weeks after initiation of degeneration. B. T2 times in the disc NP at each time point.
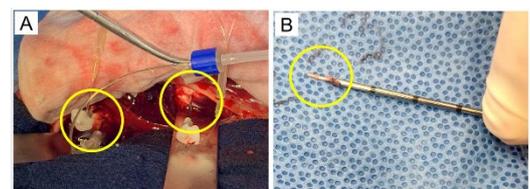

Figure 2. A. Surgical approach illustrating in vivo placement of MD microdialysis catheters in 2 goat discs. B. Catheter remains exposed and undamaged following retrieval from the disc.
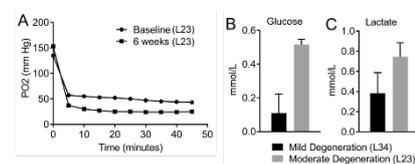

Figure 3. A. Oxygen measurements in the L2-3 disc at baseline and 6 weeks after initiation of degeneration. B. Glucose and C. Lactate measurements in the L23 and L34 discs 12 weeks after

RESULTS: *MRI Evaluation of Disc Degeneration:* Three discs injected with ChABC (L23, L45 and L56) exhibited progressive degeneration overtime at 6 and 12 weeks compared to baseline and intact controls, as seen on MRI (**Fig 1**). Importantly, introduction of the Licox and microdialysis probes did not appear to markedly exacerbate degeneration severity compared to the disc that received ChABC alone (**Fig 1**). *In Vivo Measurement of Disc Oxygen, Glucose and Lactate:* Licox probes and microdialysis catheters were successfully placed within the NPs of two adjacent discs (**Fig 2**). With respect to oxygen, Licox probe readings stabilized 10 minutes after final positioning in the NP (**Fig 3A**). At baseline, oxygen in the L23 disc plateaued at 44 mm Hg, while at 6 weeks this decreased to 24 mm Hg. Following a 90-minute equilibration period, glucose measured in microdialysates was 0.52 ± 0.03 and 0.11 ± 0.11 mmol/L (**Fig 3B**), while lactate was 0.75 ± 0.14 and 0.38 ± 0.20 mmol/L (**Fig 3C**) in the L23 and L34 discs, respectively (both average of 3 measurements).

DISCUSSION: In this study, we successfully adapted techniques for *in vivo* physiological assessment of NP oxygen and glucose in a clinically-relevant large animal model of disc degeneration. Compared to the brain, placement of fragile Licox probes and microdialysis catheters in the disc poses additional challenges, including a narrow, deep, surgical approach, greater tissue density, reduced tissue fluid, and lack of a bone entry point to secure the system. We established robust surgical techniques for stable placement of both probe types in the goat disc NP enabling repeated measurements. Importantly, the microdialysates collected can also be used to measure other metabolites and soluble proteins. While findings here were limited to a small number of measurements in this initial study, NP oxygen decreased with increased degeneration while, interestingly, more severe degeneration was associated with higher glucose and lactate levels. Several factors likely contribute to alterations in disc nutrition and oxygenation with degeneration, including cartilaginous endplate thinning and calcification and alterations in adjacent vasculature and NP cellularity. Ongoing studies will use this model in order to correlate alterations in NP oxygen and metabolites with concomitant structural, cellular, and molecular changes that occur with degeneration. Our long-term go is to leverage these findings and modulate the disc microenvironment to improve the performance of therapeutic stem cells.

SIGNIFICANCE: Intervertebral disc degeneration is a major cause of low back pain. Quantification of the *in vivo* cellular microenvironment of the degenerate disc is critical to develop effective stem-cell based disc regeneration strategies.

REFERENCES: [1] Vos+ Lancet 2015; [2] Smith+ JOR Spine 2019; [3] Wilensky+ J Neurosci Nur 2006; [4] Young+ Crit Care Nurs Clin North Am 2016; [5] Gullbrand+ Osteoarthritis and Cartilage 2017.

Brandon C. Jones[1,2], Hyunyeol Lee[1,3], Cheng-Chieh Cheng[1,4], Mona al Mukaddam[5], Hee Kwon Song[1], Peter J Snyder[5], Nada Kamona[1,2], Chamith S. Rajapakse[1,6], Felix W. Wehrli[1]

MRI quantification of bone water and phosphorus differentiates between osteoporotic status in postmenopausal women

Hypothesis: The mainstay of osteoporotic (OP) fracture risk prediction is bone mineral density (*BMD*), typically assessed by dual-energy X-ray absorptiometry (*DXA*). DXA measures areal density but cannot differentiate cortical bone (CB) from trabecular bone (TB), nor can it differentiate between the structural and material properties that determine bone mechanical competence, which is the chief determinant of osteoporotic fracture risk. CB comprises 80% of the whole-body skeletal mass and osteoporotic medications are known to have opposite effects on the CB/TB compartments. Furthermore, CB microarchitectural parameters can predict fracture independent of age, sex, height, weight, and BMD, and medications exist to improve CB porosity and thickness. Similarly, the degree of mineralization of bone (DMB) is reduced with disease but can be improved with treatment and may explain some treatment-related fracture reduction independent of BMD. While DMB quantification was historically only possible via biopsy, and CB microarchitecture is traditionally measured with high-resolution CT, advancements in solid-state MRI (SS-MRI) have enabled non-invasive quantification of water residing in pores (pore water (PW)) or bound to the osteoid's hydration sphere (bound water (BW)), as well as direct quantification of phosphorus (^{31}P) in bone mineral. PW, a measure of porosity, was shown in cadaveric studies to be strongly predictive of bone strength and density. BW, a measure of organic matrix density, is related to bone's ability to deform after yielding. MRI quantification of [^{31}P] was shown in animal models to be reduced with hypophosphatemia and improved with treatment, and feasibility of quantitative ^{31}P imaging in humans was recently demonstrated and shown to be predictive of total mineral content. Additionally, simultaneous measurement of [^{31}P] and BW can yield a non-invasive biomarker for DMB, i.e. the ratio of mineral over osteoid density [^{31}P]/[BW]. Therefore, the goal of the present work was to explore the potential of proton (^{1}H) and ^{31}P SS-MRI to provide insight into the microstructural and bone tissue material properties in patients with osteoporosis and matched reference subjects not meeting the criteria for *OP*.

Methods: 34 Postmenopausal women aged 50-75 years were recruited into two groups, 15 treatment-naïve-osteoporotic (OP) and 19 age-matched healthy non-osteoporotic (Non-OP). TW was quantified a UTE sequence and BW was quantified from an IR-rUTE sequence. PW was computed in a voxel wise manner by PW=TW-BW. Cortical area fraction (CAF) and CbTh were determined from segmentation.

Results: Representative images and colormaps are shown in Figure 1. The OP group had an elevated TW and PW density (*P*=0.02, *P*=0.005), as well as lower values for mineralization markers of [^{31}P] and [^{31}P]/[BW] (*P*=0.01, *P*=0.03) and bone morphological markers CbTh and CAF (*P*<0.001, *P*=0.007). Figure 2 details correlation plots between important MR parameters and tibia pQCT vBMD. Both DXA Total Hip BMD and distal tibia pQCT vBMD were inversely associated with TW and PW content (DXA: *r*=-0.55, *P*<0.001, *r*=-0.69, *P*<0.001; pQCT: r=-0.83, *P*<0.001, *r*=-0.84, *P*<0.001). DXA Total Hip BMD was positively correlated to BW, [^{31}P], [^{31}P]/[BW], CbTh, and CAF (*P*=0.03, *P*<0.001, *P*=0.008, *P*<0.001, *P*=0.006). pQCT vBMD was positively associated with CbTh (P<0.001). The data was suggestive of a relationship between pQCT vBMD and MR parameters of BW (*P*=0.11) and [^{31}P] (*P*=0.06), but it did not reach significance.

Conclusions: Results demonstrate that MRI assessment of CB microstructure and mineralization can provide useful insight into the ultrastructural implications of degenerative bone disease. This study demonstrates that information complementary to densitometry can be obtained with a single, integrated, multinuclear imaging protocol which includes CB microstructure, macrostructure and morphology, organic matrix density, and mineralization.
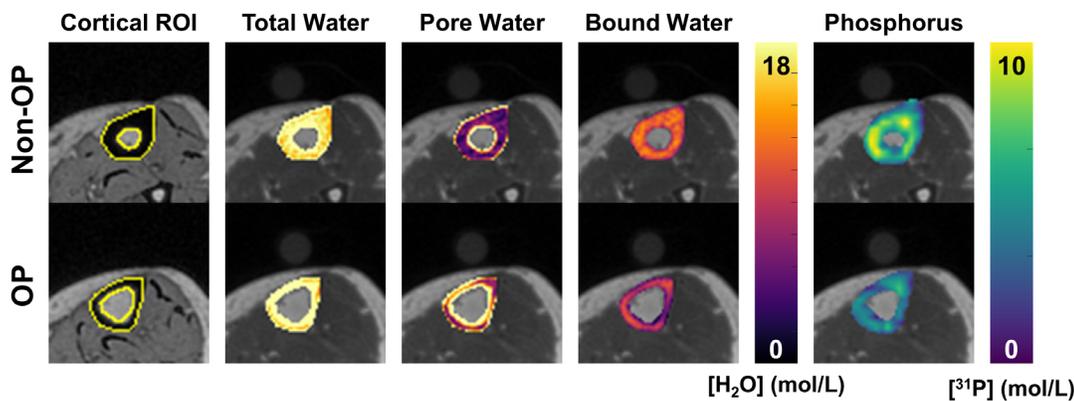
Figure 1: Representative cortical segmentation and quantitative parametric colormaps overlaid on UTE images for the same participants shown in Figure 1. (a) Yellow boundaries depict manually drawn contours of cortical bone overlaid on UTE echo 2 image, which has strong bone-tissue contrast. (b-e) Quantitative parameter maps for each MR parameters are overlaid on UTE echo 1 images.

Figure 2: Correlations of MRI biomarkers versus distal tibia pQCT vBMD. Line of best fit and confidence intervals are shown in black.
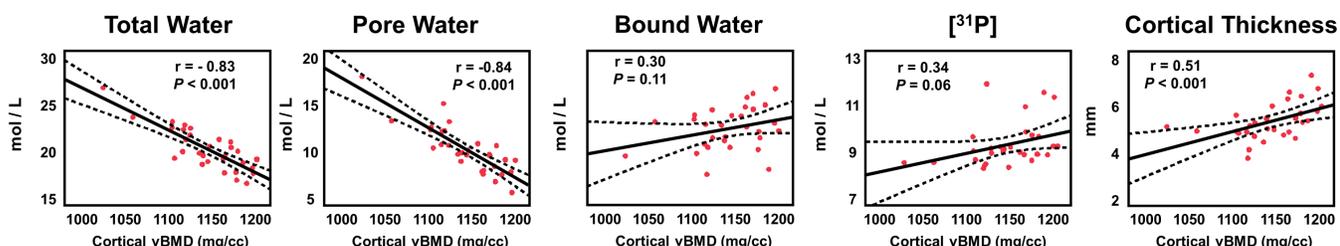
Dasatinib and Quercetin treatment reduces the incidence and severity of disc degeneration with evidence of Junb and Zfp3611 as regulators of cell fate

Emanuel J. Novais[1] and Olivia K. Ottone[1,2], Victoria A. Tran[1], Makarand V. Risbud[1,2]

[1]Department of Orthopaedic Surgery, Sidney Kimmel Medical College, Thomas Jefferson University, Philadelphia, PA, USA

[2]Graduate Program in Cell Biology and Regenerative Medicine, Jefferson College of Life Sciences, Thomas Jefferson University, Philadelphia, PA, USA

olivia.ottone@students.jefferson.edu

DISCLOSURES: The authors have no competing interests to disclose in relation to this work.

INTRODUCTION: Genetic background is one of the primary divers of disc degeneration, which ranks among the top causes of chronic back pain and disability worldwide. Importantly, there is a clear link between degeneration and senescence, independent of the aging process. In this study we characterized the senescence status of SM/J mice, a mouse model which experiences early onset spontaneous disc degeneration, and explored the ability of the drug combination Dasatinib and Quercetin (DQ) to prevent disc degeneration in these mice.

METHODS: Disc sections were evaluated by Safranin-O/Fast Green staining, Picrosirius Red polarized light quantitative microscopy, quantitative immunohistochemistry, and Fourier Transform Infrared (FTIR) imaging spectroscopy. RNA from nucleus pulposus (NP) and annulus fibrosis (AF) tissues was isolated from vehicle- and DQ-treated discs and used for microarray analysis. Plasma collected from vehicle and DQ animals was assessed for proinflammatory markers using MSD V-plex assays. Significance was measured using a student's t-test and χ^2 test, where appropriate, at a significance level of $p \leq 0.05$. Mice were kept according to protocols approved by the Institutional Animal Care and Use Committee (IACUC) of Thomas Jefferson University.

RESULTS: Noteworthy, SM/J discs showed increased levels of senescence relative to C57BL/6 mice as early as at 4 weeks. Accordingly, we treated SM/J mice beginning at 4 weeks of age and analyzed them at 17 weeks of age, when mice are skeletally mature and have established disc degeneration. DQ-treated mice demonstrated lower grades of degeneration and decreased levels of senescence markers p19ARF and p21. Interestingly, treated animals also showed preserved cell viability, cellular phenotype, and matrix content. Transcriptomic analysis showed disc compartment-specific effects of the treatment, but cell fate and vascular modulation were commonly modulated across tissue types. Additionally, cross model and tissue analysis identified Junb and Zfp36l1 down-regulators as key targets of DQ treatment in mice.

DISCUSSION & SIGNIFICANCE: This study further supports that senolytics may provide a novel approach to delay disc degeneration and suggests that Junb and Zfp36l are crucial mediators for this effect.

Nanoparticles 'Clicked' onto Nanofibrous Scaffolds for Meniscal Repair

Emily E. Sharp[2], Ryan C. Locke[1,3], Bian Jang[2], Tao Gui[1], Su Jin Heo[1], Nathaniel Dyment[1], Zhiliang Cheng[2], Ling Qin[1], Robert L. Mauck[1,2,3]

Dept. of Orthopaedic Surgery[1] and Dept. of Bioengineering[2], University of Pennsylvania; Musculoskeletal Research Center, Philadelphia VA Medical Center[3]

Click chemistry is a class of reactions wherein molecular pieces are easily joined together, like buckling two pieces of a seat belt.[1] In the context of tissue engineering, click chemistry can serve to fabricate innovative delivery mechanisms capable of regenerating damaged or diseased tissues via spatiotemporal-controlled release. Dense connective tissues, such as knee menisci, sustain demanding load-bearing functions via a complex arrangement of extracellular matrix proteins that surrounds and protects tissue specific cell types. Following injury, endogenous cells are unable to promote tissue regeneration and instead form less functional scar tissue. Thus, therapies that activate and recruit endogenous cells to promote tissue regeneration may significantly improve treatment and quality of life for millions of patients annually. Click chemistry-based delivery systems present a novel way of achieving these therapeutics. We previously showed that activation of Hedgehog signaling via a small molecule agonist, Purmorphamine (Pur), accelerated wound closure and attenuated cartilage erosion that results from meniscus injury.[2] Here, we overcome challenges to Pur delivery, such as rapid clearance and off-target toxicity, via delivery from polymeric nanoparticles (NPs) localized to the injury site by immobilizing NPs on a nanofibrous repair scaffold via click chemistry.

Rather than employing copper-catalyzed azide-alkyne cycloaddition as previously done,[3] we utilized strain-promoted azide-alkyne cycloaddition (SPAAC) to azide-functionalize electrospun polycaprolactone (PCL) nanofibrous scaffolds to click with DBCO-functionalized PEG-PCL NPs (prepared via oil-in-water emulsion). These azide-modified scaffolds, when compared to electropsun PCL controls lacking azide groups, selectively reacted with DBCO-conjugated fluorophores, validating the successful fabrication of a 'clickable' scaffold. Scratch assays using meniscus fibrochondrocytes revealed that Pur-loaded, DBCO-conjugated NPs increased the cell migration compared to free Pur delivery. We then implanted NP-conjugated scaffolds *in vivo* using a nude rat xenotransplant model. For this, adult porcine meniscal explants were incised to create a horizontal defect that was either left unfilled or filled with NP-conjugated scaffolds (Pur-loaded and empty). Using H&E staining, we observed a marked increase in cell infiltration with implantation of Pur-loaded NPs compared to empty controls.

This study validates a new approach to produce nanofibrous azide-functionalized PCL scaffolds via SPAAC click chemistry. The reaction between azide-modified PCL nanofibers and fluorophore-DBCO was highly specific, fast, repeatable, and stable over long-term. This indicates that azide-modified PCL scaffolds may be used to immobilize DBCO-modified NPs. When tested *in vivo*, Pur delivery via NP-conjugated scaffolds accelerated meniscal repair via increased cell infiltration. These data support the novel use of click chemistry-based approaches for sustained and localized delivery of small molecule drugs for dense connective tissue repair and, more broadly, musculoskeletal tissue repair.

References: [1]TCI Chemicals, "Click Chemistry." [2]Wei+ eLife 2021. [3]Lancuski+ ACS Appl Mater Inter 2012.

Stiffness and Structure-Tunable Extracellular Matrix-Based Multiphasic Nanofibrous Scaffold Systems for Rotator Cuff Enthesis Repair

Zizhao Li[1], Se-Hwan Lee[1], Dong Hwa Kim[1], Yujia Zhang[1], Richard Tran[2], Jason Burdick[3], Robert Mauck[1], and Su-Jin Heo[1]

[1]University of Pennsylvania, Philadelphia, PA; [2]Acuitive Technologies Inc., Allendale, NJ; [3]University of Colorado Boulder, Boulder, CO

DISCLOSURES: Li (N), Lee (N), Kim (N), Zhang (N), Tran (N), Burdick (N), Mauck (4, 5, 8), and Heo (5)

INTRODUCTION: The rotator cuff is critical to shoulder movement and shoulder joint stability [1]. Tears at the rotator cuff enthesis are often [1-2]. However, the surgically treated tendon-bone interface frequently re-tears due to undesirable scar tissue formation [3]. Currently, numerous new approaches for repairs are being investigated, including lab-designed tissue-engineered scaffolds [4]. Nonetheless, the limitations of current devices do not reflect zone-dependent structural, mechanical, and biological characteristics of native rotator cuff enthesis [5] (**Fig. 1A**). To address the shortcomings of current methods and to improve rotator cuff enthesis regeneration, here we develop a stiffness-tunable decellularized-bovine Achilles-tendon extracellular matrix-based nanofiber (DEMN) systems. The system is composed of two stages: Phase I [aligned DEMN with stiff methacrylate hyaluronic acid (MeHA) for the tendon-uncalcified zone regeneration] and Phase II [non-aligned DEMN with soft MeHA for the tendon-calcified zone regeneration]. Further, we investigate how the stiffness and alignment of DMEN systems impact juvenile bovine tenocyte (bJTC) phenotypes.
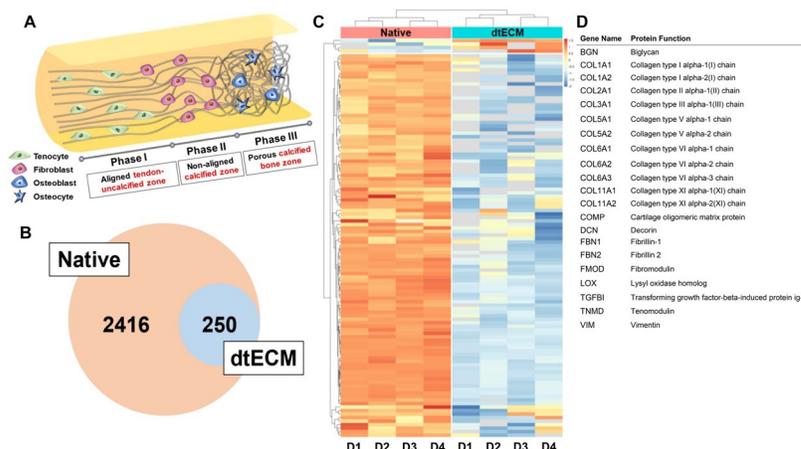

Fig. 1: (A) Schematics showing the zone-dependent structural and biological properties at the native rotator cuff fibrocartilaginous enthesis. **(B)** Venn diagram: unique proteins detected in either native (2416) or decellularized (250) tendon tissues. **(C)** Heat map and clustering analysis of the differential proteins identified in the native and decellularized tissues (n = 4 donors/group). **(D)** Protein mainly detected in native tissues (n = 4 donors). **(E)** Proteins mainly detected in decellularized tissues (n = 4 donors).

METHODS: Juvenile bovine Achilles tendons were decellularized using our established protocols using an SDS-based solution [6]. Proteomic analysis was carried out using Mass-spectrometry to determine how the decellularization process changes protein components in native tendon tissues (n = 4 donors/group). 'Soft' and 'stiff' decellularized tendon ECM (dtECM) nanofiber scaffolds were fabricated using our established protocols [6]. Briefly, to fabricate the 'soft' or 'stiff' dtECM scaffolds, dtECM was blended with 35% modified MeHA or 100% modified MeHA, respectively [6]. To form non-aligned (NAL) scaffolds, fibers were collected on a mandrel rotating with a surface velocity of <0.5 m/s, and for aligned (AL) scaffolds, fibers were collected at a high surface velocity (~10 m/s). 0.5% w/v Irgacure 2959 (Sigma) was used for the crosslink under UV light [6]. Passage 1 bJTCs were seeded on AL or NAL, stiff or soft dtECM scaffolds, respectively. F-actin staining and the CCK8 assay were used to assess cell morphology and proliferation rates on the scaffolds. The RT-PCR was used to determine the fibrogenic (Collagen-type 1 or 3), tenogenic (Tenomodulin, Tenascin-C), or chondrogenic (Collagen-2, Aggrecan) gene expressions in bJTCs seeded on the scaffolds and cultured in basal growth media for 7 days. Aligned 100 % modified (Stiff) MeHA alone nanofibrous scaffolds were used as control throughout all cell tests [7]. Statistical analyses were performed using one-way ANOVA with Tukey's post hoc testing.

RESULTS: The proteomic analysis determined 2416 unique proteins in the native bovine Achilles tendon with 250 proteins detected in both native and dtECM tissues (**Fig. 1B**). The clustering analysis revealed that the decellularization process significantly reduced the number of proteins compared to the native groups (**Fig. 1C**). Interestingly, the proteins related to collagen formations (such as COL1A1 and COL1A2), were mostly found in native tissues; however, the dtECM is primarily composed of CDC42 proteins, which are responsible for controlling various cellular functions such as cell division and migration [7] (**Fig. 1D-E**). Indeed, the dtECM components enhance both the bJTC attachment and proliferation on the nanofibrous scaffolds compared to cells on aligned 100 % modified (Stiff) MeHA alone nanofibrous scaffolds (Control, mostly cells are small and round on the MeHA alone scaffolds) (**Fig. 2A-C**). Cells on the 'stiff' dtECM scaffolds were larger than the cells on the 'soft' dtECM scaffolds and the cell aspect ratios were higher on the AL scaffolds than NAL scaffolds (**Fig. 2A-B**). Further, the stiffness and alignments of dtECM scaffolds regulate gene expression of bJTC. Cells on "Stiff" AL (for the Phase I regeneration) scaffolds express high levels of fibrous markers (Collagen-1/3; COL1A2 and COL3) (**Fig. 3**). Interestingly, the addition of dtECM components suppressed chondrogenic gene expression (Collagen-2; COL2 and Aggrecan; ACAN), while increased Tenomodulin (TNMD, a tenogenic marker) expression in bJTC, regardless of the fiber alignment (**Fig. 3**).

Fig. 2: (A) Representative F-actin staining images of P1 bJTC spreading on dtECM/MeHA nanofibrous scaffolds at day 3 (bar = 50 μm). (B) Relative bJTC areas and cell aspect ratios (*: p<0.005, vs. Control, ○: p < 0.005, vs Soft AL, +: p<0.005, vs Soft NAL, #: p<0.005, vs Stiff AL). (C) bJTC proliferation determined by CCK8 assay. [*: p < 0.005, vs. Day1, ○: p < 0.005, vs Day 3, n = 5 per group, mean ± SEM].

DISCUSSION: In this study, we successfully developed bioactive stiffness/structure-tunable decellularized-bovine Achilles-tendon extracellular matrix-based nanofiber (DEMN) systems. This work further investigated whether the DEMN systems can be optimized to recapitulate the zone-dependent biomechanical/chemical environments of the native rotator cuff enthesis to promote zone-specific rotator cuff enthesis repairs. From the proteomic analysis, we found that the dtECM material is mainly composed of CDC42 proteins that play an essential role to support cell spreading and ingrowth [7], and indeed it enhances tendon cell attachment and proliferation. In addition, we confirmed that the DEMN systems can control the cellular area, aspect ratio, and alignment on the scaffolds, and further via RT-PCR, we confirmed that DEMN systems can regulate the gene expression of tendon cells. Taken together, the novel DEMN system has great potential for the repair and regeneration of the rotator cuff enthesis, given its ability to recapitulate the zone-dependent biomechanical/chemical properties of the enthesis.

SIGNIFICANCE: Our advanced scaffold fabrication techniques combined with bioactive materials would result in novel frameworks that could best support rotator cuff enthesis repairs and musculoskeletal soft tissue regeneration.

REFERENCES: [1] Sambandam+, *World J Orthop* 2015; [2] Kuroda+, *Clin Orthop Relat Res* 2013; [3] Newsham-West+, *J Anat* 2007; [4] Chainani+, *Tech Orthop* 2016; [5] Chen+, *Prog Polym Sci* 2016; [6] Li+, *ORS Annual Abstract* 2022; [7] Kim+, *Biomaterials* 2016.

Fig. 3: Gene expression of fibrous, chondrogenic, or tenogenic markers to GAPDH in bJTCs at Day 7. [*: p<0.01, **: p < 0.001, ***: p < 0.0001, ****: p < 0.00001, n = 5/group, mean ± SEM].

Role of Energy Metabolism in Bone Mass Accrual

Mohd Parvez Khan[1], Giulia Lanzolla[1], Elena Sabini[1], Brittany M. Laslow[1], Lorenzo Arboit[1], Fanxin Long[2,1] and Ernestina Schipani[1]

[1]McKay Laboratory, Department of Orthopedic Surgery, Perelman School of Medicine, University of Pennsylvania, Pennsylvania, USA. [2]CHOP, Philadelphia, Pennsylvania, USA

Once thought to be a mere consequence of the cell state, metabolism is now known to play a critical role in dictating the cell fate. Glycolysis and oxidative phosphorylation (OxPhos) are the two main sources of intracellular ATP. Factors that promote osteoblast activity, such a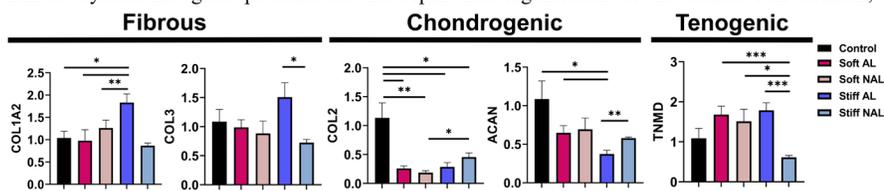s the Hypoxia-Inducible Factor 1α (HIF1), activate glycolysis. Notably, during *in vitro* osteogenic differentiation of mesenchymal progenitors, both glycolysis and OxPhos increase. The role of OxPhos in osteoblast biology *in vivo* is still mostly unexplored. To fill this gap of knowledge, we generated a mutant mouse lacking Mitochondrial Transcription Factor A (TFAM) in uncommitted mesenchymal progenitors and their descendants using PRX1-Cre (PRX;TFAM$^{f/f}$). TFAM regulates transcription of mitochondrial genes that encode thirteen subunits of the electron transport chain and thus controls OxPhos. Three-week-old PRX;TFAM$^{f/f}$ mice displayed a low bone mass phenotype with multiple spontaneous fractures. Our data indicate that mesenchymal TFAM is necessary for bone mass accrual. Impairment of OxPhos is the most powerful, consistent, and best characterized biological consequence of loss of TFAM across numerous cell types. However, TFAM also regulates duplication of mitochondrial DNA, and mitochondria have a variety of functions beyond OxPhos and ATP production. Therefore, to establish if the impairment of OxPhos, and thus the decreased intracellular ATP, is the primary cause of the PRX;TFAM$^{f/f}$ bone phenotype, we asked whether forced upregulation of glycolysis would prevent the low bone mass of PRX;TFAM$^{f/f}$ mice. For this purpose, we generated a double mutant mouse, lacking TFAM and overexpressing a constitutively stabilized HIF1 in the same cells, PRX;TFAM$^{f/f}$;HIF1dPA$^{f/f}$. Analysis of PRX;TFAM$^{f/f}$;HIF1dPA$^{f/f}$ bones revealed that increased HIF1 activity prevented the bone fractures occurring in PRX;TFAM$^{f/f}$ mutants. Building on those findings, we are currently testing the hypothesis that TFAM in cells of the osteoblast lineage is crucial for bone mass accrual by promoting OxPhos, and thus ensuring the proper levels of intracellular ATP. The successful accomplishment of these experiments will expand and deepen our knowledge of the role of energy metabolism, particularly OxPhos, in the regulation of osteoblast differentiation and bone mass accrual.

Engineering Bisphosphonate Lipid-like Materials for mRNA Delivery to the Bone Microenvironment

Lulu Xue[1], N. Gong[1], S. J. Shepherd[1], X. Han[1], X. Liao[2], M. G. Alameh[3], F. Long[2], D. Weissman[3], M. J. Mitchell[1]

[1]Department of Bioengineering [2]Department of Surgery, The Children's Hospital of Philadelphia [3]Department of Medicine, University of Pennsylvania, Philadelphia, PA 19104

Introduction: Bone microenvironment is a distinct and highly dynamic region, playing vital roles in orchestrated bone remodeling, hematopoiesis, immune function regulation, and tissue regeneration.[1] However, the blood-bone marrow barrier, poorly perfused bone sections, highly dense hierarchic structures, and low affinity between drugs and bone minerals, create challenging for therapeutics delivery into bone, therefore there is an unmet need for efficient and safe therapeutic approaches for targeted drug delivery to the bone microenvironment.[2] Here, we engineered a class of bisphosphonate (BP)-conjugated ionizable lipid-like materials and formulate a library of lipid nanoparticles (BP-LNPs) for systemic delivery of mRNA to the bone microenvironment.[3]

Materials and Methods: A library of 21 BP conjugated lipidoids were synthesized, formulated into BP-LNPs, and screened for luciferase mRNA delivery in HeLa cells. A library without BP were used as positive control. Outperformed BP-LNPs formulating with mRNA encoding for luciferase comparing with LNP in the

Figure 1. Schematic illustration of lipid nanoparticles (LNPs) containing BP lipid-like materials (BP-LNPs) to enable systemic delivery of mRNA to the bone microenvironment. After systemic delivery *via* intravenous injection, BP-LNPs coordinated with calcium ions in the bone microenvironment to enable specific bone targeting.

absence of BP were then intravenous administrated into C57BL/6 mice, and the luminescence activity of whole body, legs and spines were qualified to evaluate mRNA delivery efficacy. EGFP mRNA LNP were used to evaluated transfected cell types in the bone marrow. BMP-2 mRNA LNP were used to evaluate therapeutic delivery potentials.

Results and Discussion: Through an initial assessment from in vitro screening, 490BP-C14 LNP was identified as the lead formulation in this library. Compared to LNPs that did not incorporate BP-lipids, 490BP-C14 LNPs showed increased higher hydroxyapatite binding in vitro and affinity for bone fragments ex vivo. Following systemic delivery, LNP homing and mRNA transfection in the bone microenvironment significantly increased with LNPs incorporating BP lipid-like materials. In addition, 490BP-C14 LNPs showed increased transfection efficiency in diverse cell types in the bone marrow, especially monocytes (4-fold increase compared to LNP without BPs). BMP-2 secretion on the bone surface and in the bone marrow significantly increased after systemic BMP-2 mRNA delivery by 490BP-C14 LNPs.

Conclusions: We developed a facile and versatile approach to engineer a library of BP lipid-like materials that can be formulated into LNPs (BP-LNPs) for systemic delivery of mRNA to the bone microenvironment. The incorporation of BP lipid-like materials into LNPs demonstrates their potential in targeted mRNA delivery to bone, which can have applications in regenerative medicine, protein replacement, and gene editing therapies for bone and bone marrow.

Reference: 1. Croucher, *et al. Nat. Rev. Cancer.* 2016. 2. Mercier, *et al. Nat. Rev. Immunol.* 2012. 3. Xue, *et al. J. Am. Chem. Soc.* 2022.
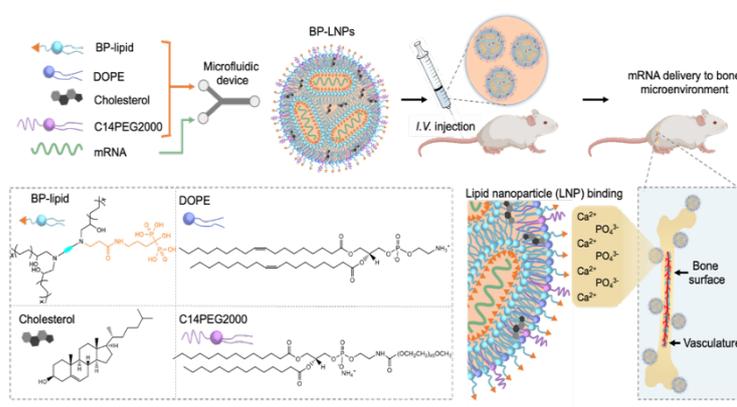
A Comparison of Three Cold Plasma Devices for Potential Clinical use in Preventing or Treating Surgical Site Infection during Orthopedic Procedures

Amanda Connelly[1], Rachel Grant[1], Ly Nguyen[1], Neil Zhao[1], Noreen Hickok[1], Theresa A. Freeman[1]
[1] Department of Orthopedic Surgery, Thomas Jefferson University, Philadelphia, PA
Theresa.Freeman@jefferson.edu

Introduction: Orthopedic infections are painful, life-altering, and life-threatening and current treatments to combat this problem are limited. Cold plasma presents novel means to overcome this issue and combat surgical site infections clinically. Cold plasma is an ionized gas composed of biologically active components such as charged particles, UV radiation, electric current, and reactive oxygen and nitrogen species which have been shown to be microbicidal. However, the composition and bactericidal efficacy of cold plasma can vary greatly, and a multitude of devices are available to generate plasma with differences in energy, frequency, power, carrier gas pressure and composition. The objective of this study is to characterize three different commercially available cold plasma devices, currently on the market. The J-Plasma device (Apyx Medical) is a helium plasma jet that uses radiofrequency energy, resulting in cold helium plasma that is delivered through an applicator wand. The Piezo Brush PZ3 (Reylon Plasma) generates plasma using direct dielectric barrier discharge (DBD) in air. The Plasma Care device (Terraplasma Medical) flows air through a surface micro discharge plasma and only the plasma charged air interacts directly with the treated surface. Thus, our aim is to identify which of these devices results in the most efficient bacterial killing with the least amount of tissue damage.

Methods: Bacterial Killing: Staphylococcus aureus (S. aureus ATCC 25923) biofilms were grown on PLA discs in TSB in a 24-well plate. Planktonic bacteria were removed prior to plasma treatment of varying times depending on the device. Following treatment, bacteria were isolated by a 15-minute sonication, serially diluted, plated onto Petri films, incubated overnight, and the colonies counted to determine log CFU/mL. Temperature and pH: Changes in the temperature and pH were recorded as each device was used to treat 5 mL of saline (0.9% NaCl) over time. Reactive species in Plasma Treated Liquid: 3 mL of saline was treated using each device, and the concentration of reactive species produced was determined using the Griess Assay (Sigma-Aldrich®) for nitrite (RNS), or the potassium iodide assay for H_2O_2 (ROS). Histology and Image Analysis: Equal size and thickness excised porcine skin were plasma treated to assess tissue damage. Treated samples were fixed in 4% PFA, processed for paraffin infiltration, embedded in paraffin, and sectioned. Tissue sections were stained using Masson's Trichrome and imaged using the Nikon Eclipse E800 light microscope and the Olympus MVX10 microscope. Depth of plasma penetration was measured using Image Pro Plus software (Media Cybernetics). Scanning Electron Microscopy (Hitachi TM-1000 SEM): S. aureus biofilm PLA discs prepared as described above were treated with each plasma device or received no treatment (control). Following treatments, the discs were fixed overnight in 4% PFA, then dehydrated in a graded series (70 - 100%) of alcohols (3 hours each) and air dried >24 hours before sputter coating with gold for SEM. qPCR: RNA from treated bacteria was isolated, quantified, made into cDNA and qPCR was performed for SodA expression. Statistical analysis: All individual experiments were performed in quadruplicate and done independently at least 2x. Data was transferred to GraphPad Prism 8 (GraphPad Software, San Diego) statistical software to identify outliers, determine significance, and graph results.

Results: Results from each of the analyses described above are presented in Table 1.

Table 1 – Summary of Results											
Plasma Device	Plasma Type	Gas Flow (L/min)	Treatment Time (sec.)	Δ°C	ΔpH	ROS (μM H_2O_2)	RNS (μM NO_2^-)	SEM Biofilm Disruption	ΔSodA Expression	Decrease in Log CFU/ml	Tissue Interaction / Penetration (mm)
J-Plasma	Helium Jet	4	30	67ºC	<1	330.17	260.53	Yes	1.88 ± 0.17	~2	Visible / 0.71 ± 0.17
Piezo Brush PZ3	DBD	~8	180	14ºC	2.5	112.71	1×10^8	Yes	-2.98 ± 0.22	~3	Visible / 0.22 ± 0.04
Plasma Care	Charged Air	N/A	60	1ºC	<1	ND	ND	Yes	ND	~4	None / 0.09 ± 0.01

Discussion: Our study comparing three commercially available devices find the Plasma Care device results in the largest overall decrease in bacteria, and the least amount of tissue damage. Additionally, it is the easiest to use, as it is cordless and rechargeable and does not require a gas canister.

Significance/Clinical Relevance: Surgical site infections in orthopedic surgery are an ongoing issue and cold plasma offers a simple to use non-antibiotic approach to combat surgical site infections clinically.

Cardiovascular effects of hyperpolarized xenon gas mixtures as used for dynamic lung MRI during general anesthesia in healthy pigs

Klaus Hopster[a], Kai Ruppert[b], Rachel Hilliard[c], Thomas Schaer[c]

University of Pennsylvania, [a]School of Veterinary Medicine, Department of Clinical Studies; [b]Perelman School of Medicine, Department of Radiology, Functional and Metabolic Imaging Group; [c]School of Veterinary Medicine, Institute for Medical Translation

Introduction Xenon (Xe) is a member of the noble gas group that was discovered in 1898 by William Ramsay and Morris Travers. Recently, xenon has shifted back into the spotlight for its use as a hyperpolarized gas to enhance and improve imaging. Hyperpolarized agents are used for certain nuclear magnetic resonance (NMR) spectroscopy and imaging (MRI) applications. The hyperpolarized gas can be used for void space imaging, including gas flow imaging or diffusion studies at the interfaces with other materials. Moreover, the Xe NMR signal is extremely sensitive to its molecular environment which allows for its use as an NMR/MRI contrast agent when dissolved in aqueous solution with functionalized molecular hosts that temporarily trap the gas. For these reasons, hyperpolarized xenon gas mixtures are used for dynamic lung MRI imaging in experimental and clinical settings in a variety of concentrations and mixture ratios. Although xenon is considered safe there are a few studies on the effects of xenon on hemodynamic function in animals and humans the results of which indicate hemodynamic alterations when xenon is inhaled. The goal of our study was to investigate the effects of Xe on the cardiovascular function of healthy, experimental pigs anesthetized with either isoflurane or ketamine.

Material and Methods Four healthy Yorkshire pigs were anesthetized twice using either isoflurane or a ketamine infusion. After instrumentation and equilibration baseline measurements were performed for 15 minutes including measurements of heart rate (HR), arterial blood pressure (aBP) and cardiac index (CI). Then, the rebreathing bag was exchanged and a 3-liter bag containing a 1:1 mixture of Xe and O_2 was attached to achieve a gradual increase in inhalant Xe concentrations. Inspiratory and expiratory concentrations of O2, isoflurane and N2 were measured and based on Dalton`s Law the amount of inspiratory and expiratory Xe was calculated. The cardiovascular measurements were continued during the Xe inhalation at similar intervals as previously described for another 15 minutes. Then the bag was switched back to the oxygen rebreathing bag for further 15 minutes before the experiment was concluded.

All variables were compared within the same group to the baseline value as well as between groups at the same timepoints using a two-factorial variance analysis for repeated measurements and Bonferroni correction for multiple comparisons. The correlation between the inspiratory xenon concentration and cardiovascular changes was compared using a linear regression. The level of significance was set to 5% ($p < 0.05$).

Results The inspiratory xenon concentration reached peak concentrations of up to 39%. In isoflurane anesthetized animals the Xe inhalation resulted in a significant decrease in HR, aBP and CI whereas in ketamine anesthetized animals the Xe inhalation did not change any measured cardiovascular parameters. There was a significant ($p<0.001$) negative correlation ($r^2 = 0.865$) between inspiratory xenon concentration and CI in isoflurane anesthetized animals (Figure 1).
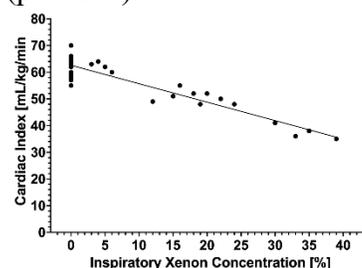
Discussion Xenon exerts its central effects via inhibition of n-methyl-d-aspartate receptors, and it has been reported that it can cause a noticeable decrease in HR. Isoflurane on the other hand can cause significant depression of the sympathetic nervous activity which results in hypotension. In addition, volatile anesthetics inhibit the influx of extracellular calcium in the cells by blocking calcium channels and therefore can cause negative inotropic effects of the myocardium resulting in low CI. These negative cardiovascular effects are usually compensated for by an increase in HR. Therefore, our results indicate that the addition of Xe during isoflurane inhalation reduces compensatory mechanisms leading to more negative cardiovascular effects.

Conclusion When anesthetizing animals with isoflurane and administering Xe in concentrations between 15% and 40% moderate to severe changes in aBP and CI need to be expected. A drop in HR can be considered an early warning sign and is poorly compensated for by the animal due to the negative inotropic and vasodilative effects of volatile anesthetics.

Identifying YAP target genes in periosteal cell proliferation by orthogonal RNA- and ATAC-sequencing

Madhura P. Nijsure[1], Miriam Baitner[1], Dakota Jones[1], Yasaman Moharrer[1], Annapurna Pranatharthi-Haran[1], Greg Szeto[2], Nathaniel Dyment[1], Joel D. Boerckel[1]

University of Pennsylvania[1], Allen Institute for Immunology[2]

Bone fracture repair initiates with periosteal cell proliferation, which coincides with activation of the transcriptional regulator, YAP. Deletion of YAP, and its paralog TAZ, from Osterix-expressing cells impaired periosteal cell proliferation[1]. How fracture-induced YAP activation promotes periosteal cell proliferation is unknown. In the nucleus, YAP does not directly bind to DNA, but forms a complex with other transcription factors to regulate transcriptional activity[2]. It is therefore important to identify both the YAP target genes and the associated transcription factor partners.

To this end, we used a mouse model that can express constitutively active YAP (YAP^{S127A}) upon treatment with doxycycline. We isolated periosteal cells from 4-day old fracture calluses and treated them with 1µM doxycycline *in vitro*. We then performed two orthogonal assays: Bulk mRNA sequencing (RNA-seq) and Assay for Transposase Accessible Chromatin with sequencing (ATAC-seq). Integrating these data sets, we quantified three features of the YAP-induced transcriptional landscape: 1. Differentially regulated genes (Fig A), 2. Genes with differentially accessible chromatin near their promoters, and 3. Genes containing consensus DNA motifs for known transcription factors (TF footprints) in differentially opened chromatin (Fig B). We short-listed proliferation-associated genes that satisfied 2 or more of these criteria as "orthogonally-confirmed target genes" (Fig C).

YAP^{S127A} induced differential expression of 376 genes (1) and differential accessibility, proximate to the promoter of 2668 genes (2). DNA motifs (3) most frequently opened by YAP^{S127A} were transcription factor footprints for TEAD, AP-1, Sox4/11/12, and Smad2/3 (Fig D). Integrating 1, 2 and 3, we found 85 orthogonally-confirmed target genes, from which we selected BMP4, IL-6, IL-11, CTGF and Cyr61 for independent quantification of temporal induction kinetics (Fig D). In each of these genes, at least one of the identified transcription factor footprints was present either in the promoter or in regions of differentially accessible chromatin. However, YAP-induced transcriptional kinetics were target gene-dependent, suggesting potentially divergent co-transcriptional mechanisms.

Together, we have orthogonally confirmed a set of proliferation-associated YAP target genes and transcription factor partners in periosteal cells during fracture repair.

References:

1. Kegelman+, JBMR 2020

2. Tian+, PNAS 2010

Knockdown of Decorin and Biglycan at Time of Tendon Injury Alters Gene Expression and Fibril Morphology

Ashley K. Fung[1,2], Thomas P. Leahy[1,2], Stephanie N. Weiss[1], Sheila M. Adams[3], Nathaniel A. Dyment[1], David E. Birk[3], Louis J. Soslowsky[1]
[1]McKay Orthopaedic Research Laboratory, University of Pennsylvania, Philadelphia, PA, [2]Department of Bioengineering, University of Pennsylvania
[3]Department of Molecular Pharmacology and Physiology, University of South Florida, Tampa, FL
afung@seas.upenn.edu

Disclosures: All authors have nothing to disclose.

INTRODUCTION: Tendon healing follows a typical wound healing process, including inflammatory, proliferative, and remodeling phases, though outcomes following tendon injury remain poor. The small leucine-rich proteoglycans (SLRPs), decorin (Dcn) and biglycan (Bgn), are critical regulators of fibrillogenesis and matrix assembly, but their specific roles in tendon healing are not fully understood. We previously showed that knockdown of Bgn or both Dcn/Bgn resulted in increased tendon modulus 6-weeks post-injury, suggesting improved function due to Bgn knockdown [1]. However, the mechanisms driving these differences remain unknown. Therefore, the objective of this study was to define the biological and structural regulatory roles of Dcn and Bgn in tendon healing using conditional knockdown of Dcn, Bgn, and both Dcn/Bgn at the time of injury. We hypothesized that induced knockdown of Bgn and both Dcn/Bgn would improve healing resulting in increased tendon extracellular matrix gene expression, reduced scarring, and superior fibril structure compared to wild-type mice.

METHODS: Study design: Female $Dcn^{+/+}/Bgn^{+/+}$ control (WT, n=44), $Dcn^{flox/flox}$ (I-$Dcn^{-/-}$, n=32), $Bgn^{flox/flox}$ (I-$Bgn^{-/-}$, n=32), and compound $Dcn^{flox/flox}/Bgn^{flox/flox}$ (I-$Dcn^{-/-}/Bgn^{-/-}$, n=32) mice with a tamoxifen inducible Cre (B6.129-Gt(ROSA)26Sortm1(cre/ERT2)Tyj/J, Jackson Labs) were used [2] (IACUC approved). At 120 days old, Cre excision was induced via two (injured) or three (uninjured) consecutive daily IP injections of tamoxifen. At time of induction, injured groups underwent bilateral patellar tendon (PT) injury surgery as described [3] and were sacrificed 1-, 3- or 6-weeks later. Uninjured groups were sacrificed at 150 days old. Gene Expression: PTs (n=4/group) were homogenized, and RNA was extracted. RNA was converted to cDNA, pre-amplified, and loaded into a Fluidigm 96.96 Dynamic Array. The 96 target genes included categories of collagens, non-collagenous matrix, matrix remodeling, cell-ECM proteins, and cell and inflammatory markers. ΔCt was calculated by subtracting the gene cycle threshold (Ct) from average Ct of the housekeeping genes ($Abl1$, $Rps17$). Histology: Knee joints (n=4/group) were fixed, decalcified, and paraffin sectioned in the transverse plane of the PT at 10μm. Sections were stained with toluidine blue, and scar tissue was measured in the wound site adjacent to the native tissue. Transmission Electron Microscopy: PTs (n=4/group) were isolated, fixed, and processed as described [4]. Sections were cut at 85nm, stained, and imaged at 60,000x in the wound area. Fibril diameter distributions were quantified. Statistics: For gene expression and scar area percentage, one-way ANOVAs with Tukey post-hoc tests were conducted at each timepoint. Fibril diameter distributions were compared using Kolmogorov-Smirnov tests. Significance was set at $p \leq 0.05$ and trends at $p \leq 0.1$.

RESULTS: Gene Expression: Dcn and Bgn expression demonstrated efficient knockdown at each healing timepoint. Dcn was significantly reduced (4-6 fold) in I-$Dcn^{-/-}$ and I-$Dcn^{-/-}/Bgn^{-/-}$ tendons compared to WT and I-$Bgn^{-/-}$ mice (**Fig 1A**). Similarly, Bgn expression was 4-6 fold lower in I-$Bgn^{-/-}$ and I-$Dcn^{-/-}/Bgn^{-/-}$ tendons (**Fig 1B**). Further evaluation of gene expression profiles revealed subtle changes during early tendon healing. At 1-wk post-injury, $Col12a1$, $Tnmd$, and $Igf1$ (**Fig 2A**) expression were significantly reduced in I-$Dcn^{-/-}$ tendons compared to WT. By 3-wks, $Igf1$ expression in the I-$Dcn^{-/-}$ group was significantly greater than WT tendons, contrasting the difference at 1-week. And by 6-wks, there was no difference in $Igf1$ expression between WT and I-$Dcn^{-/-}$ tendons, while expression was significantly higher in the I-$Dcn^{-/-}/Bgn^{-/-}$ group compared to WT tendons (**Fig 2A**). Contrasting the subtle changes at 1- and 3-wks post-injury, several significant gene changes during late tendon healing at 6-wks were observed in I-$Dcn^{-/-}/Bgn^{-/-}$ tendons. For example, there were no differences in $Fmod$ at 1 or 3 wks, but $Fmod$ was significantly increased at 6 wks compared to WT (**Fig 2B**). Similar trends were observed across several target genes, and those exhibiting increased expression in the I-$Dcn^{-/-}/Bgn^{-/-}$ group compared to WT at 6-weeks are listed in **Fig 2C**. Histology & Fibril Morphology: No differences in scar area percentage were observed at any healing timepoint (data not shown). However, fibril size distributions were significantly different between all groups at each timepoint with a shift towards smaller diameter fibrils in the I-$Dcn^{-/-}/Bgn^{-/-}$ at both 3- and 6-wks post-injury compared to WT and I-$Dcn^{-/-}$ (**Fig 3A,B**). Additionally, the fibril diameter distribution was narrower in I-$Bgn^{-/-}$ tendons compared to WT and I-$Dcn^{-/-}$ at 6-wks (**Fig 3B**).

DISCUSSION: Using our novel inducible models to minimize compensation typically present in traditional models, our findings support biological and structural regulatory roles of Dcn and Bgn during tendon healing, as evidenced by alterations in gene expression profiles and fibril structure. In addition to their structural roles in fibrillogenesis and matrix assembly, Dcn and Bgn regulate inflammation and growth factor activity [5]. Though only moderate changes were observed in 1- and 3-weeks post-injury, increased expression of several growth factors and matrix proteins at 6-weeks post-injury suggest that Dcn and Bgn play more critical roles during the remodeling phase of healing. This may be due to the role of Dcn and Bgn in regulating signaling pathways such as Igf, Pdgf, and Tgfb, which results in downstream effects on matrix synthesis and remodeling [6]. While no compensatory changes in Dcn or Bgn expression were observed, the most pronounced effects in the I-$Dcn^{-/-}/Bgn^{-/-}$ group indicate overlapping functions of Dcn and Bgn and that functional compensation may occur in the single knockdown models [7,8]. Contrary to our hypothesis, induced knockdown of Bgn in both the single and double knockdown groups resulted in a narrower distribution of fibril diameters at 6-weeks post-injury, which deviates from an uninjured distribution. Therefore, increased modulus in the I-$Bgn^{-/-}$ and I-$Dcn^{-/-}/Bgn^{-/-}$ groups is likely not due to superior fibril structure and may instead be driven by alterations in the non-collagenous matrix [1]. Future work is necessary to elucidate the roles of decorin and biglycan in regulating growth factor activity and evaluate the composition of the healing matrix.

SIGNIFICANCE: This study revealed regulatory roles of decorin and biglycan in altering gene expression and fibril structure during tendon healing, and elucidating these roles are necessary for understanding mechanisms that drive poor tendon healing.

REFERENCES: [1] Fung et al., ORS Annual Meeting, 2020. [2] Robinson et al., Matrix Biology, 2017. [3] Lin et al., J Biomech, 2006. [4] Dunkman et al., Matrix Biology, 2014 [5] Iozzo et al., J Biol Chem, 2011 [6] Hildebrand et al., Biochem J, 1994, [7] Corsi et al., JBMR 2002, [8] Wadhwa et al., Bone 2007
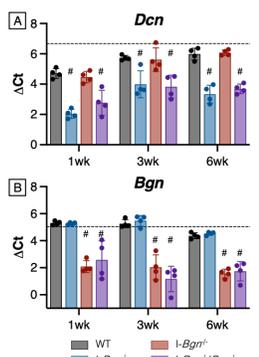
Fig 1: Induced knockdown of A) *Dcn* and B) *Bgn* expression resulted in a significant reduction in expression levels. (#: p≤0.05 from WT). Uninjured WT expression level is shown as a dashed line.
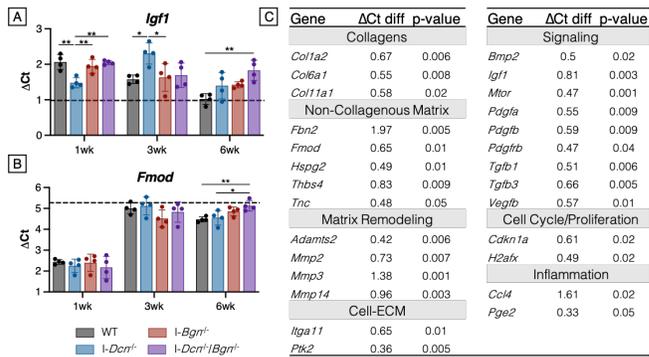

Gene	ΔCt diff	p-value	Gene	ΔCt diff	p-value
Collagens			Signaling		
Col1a2	0.67	0.006	*Bmp2*	0.5	0.02
Col6a1	0.55	0.008	*Igf1*	0.81	0.003
Col11a1	0.58	0.02	*Mtor*	0.47	0.001
Non-Collagenous Matrix			*Pdgfa*	0.55	0.009
Fbn2	1.97	0.005	*Pdgfb*	0.59	0.009
Fmod	0.65	0.01	*Pdgfrb*	0.47	0.04
Hspg2	0.49	0.01	*Tgfb1*	0.51	0.006
Thbs4	0.83	0.009	*Tgfb3*	0.66	0.005
Tnc	0.48	0.005	*Vegfb*	0.57	0.01
Matrix Remodeling			Cell Cycle/Proliferation		
Adamts2	0.42	0.006	*Cdkn1a*	0.61	0.02
Mmp2	0.73	0.007	*H2afx*	0.49	0.02
Mmp3	1.38	0.001	Inflammation		
Mmp14	0.96	0.003	*Ccl4*	1.61	0.02
Cell-ECM			*Pge2*	0.33	0.05
Itga11	0.65	0.01			
Ptk2	0.36	0.005			

Fig 2: A) I-$Dcn^{-/-}$ tendons exhibited an altered healing profile of *Igf1* expression with a significant decrease at 1-week and increase at 3-weeks post-injury compared to WT tendons. At 6-weeks post-injury *Igf1* and B) *Fmod* expression were significantly increased in I-$Dcn^{-/-}/Bgn^{-/-}$ tendons compared to WT tendons. (*p≤0.05, **p≤0.01) C) Target genes exhibiting increased expression in I-$Dcn^{-/-}/Bgn^{-/-}$ tendons compared to WT tendons at 6-weeks post-injury. The signaling category had the greatest number of differentially expressed genes. ΔCt diff represents the increase in mean ΔCt of I-$Dcn^{-/-}/Bgn^{-/-}$ compared to WT.
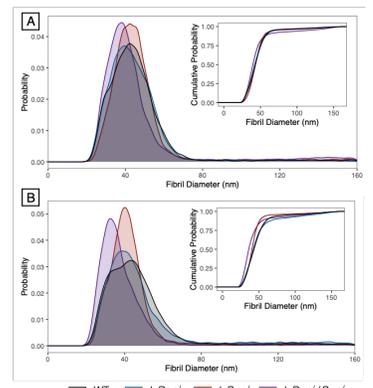

Fig 3: Probability density and cumulative distribution (inset) plots of fibril diameter demonstrated a moderate shift towards smaller fibril diameters in the I-$Dcn^{-/-}/Bgn^{-/-}$ group at A) 3-weeks and B) 6-weeks post-injury. I-$Bgn^{-/-}$ tendons also had a narrower distribution of fibril diameters at 6-weeks compared to I-$Dcn^{-/-}$ and WT tendons.

P60

The Prediction Of Lumbar Spine Surgery Outcomes Based On Computed Tomography- Finite Element Analysis of Lumbar Vertebrae

Rashad Madi[1], Thomas Statchen[1], Charis Gao[1], Dilini Ranaweera[1], Lihini Ranaweera[1], Anika Basu[1], Leilei Hao[1], Winnie Xu[1], Gregory Chang[2], Chamith Rajapakse[1]
[1]University of Pennsylvania, Philadelphia, PA, [2]New York University, New York City
Thomas Statchen: tstatch@seas.upenn.edu

Disclosures: None

INTRODUCTION: Lumbar spinal degeneration is a major cause of debilitating lower back pain in aging populations [1]. It is often characterized by narrowing of the vertebral canal causing compression of the spinal cord which eventually leads to lower back pain, leg tingling and numbness, and neurologic claudication. [1]. Surgical treatment may be indicated in certain patients that have persistent pain and activity impediment despite conservative treatment [2]. Surgical spinal decompression and instrumentation can lead to a wide array of complications known as adjacent segment disease (ASD), hence, increasing the rates of patient reoperation and morbidity [3]. Pre-op prediction algorithms can help decrease the rates of long-term ASD in high-risk patients. Our hypothesis is that computed tomography (CT) – finite element analysis (FEA) in pre op patients can help us predict which patients are at a higher risk of post op complications.
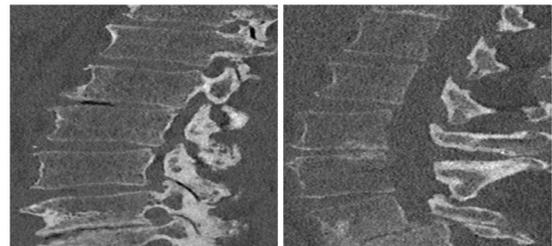

Figure 1: Representative images of CT scans of the lumbar spine used in analysis. The scan on the left is from a patient who experienced post-operative complications and the scan on the right is from a patient who did not experience post-operative complications.

METHODS: The pre-op CT scans of 104 patients were analyzed. The mean age and BMI of this population are 67 ±7.26 and 29.03 ±5.68 respectively and included 51.9% females and 48.1% males. Each lumbar vertebra from these 104 CT scans was segmented. Segmentations were performed using a novel image analysis software developed in Python. Scans were loaded into this software and a cubic region was segmented within the trabecular portion of each vertebra. The size of this cubic region was constant across all cases analyzed for each lumbar vertebra. Segmentations were excluded from analysis if they contained an implant or a non-bone region within the cubic segmentation. In total, the L1-L5 vertebrae were analyzed for 80 scans. 30 CT scans were from patients who experienced surgical complications (Cohort A) and the remaining 50 CT scans were from patients who did not experience complications (Cohort B). FEA was performed on each vertebra. A Student's t-test analysis was performed on the modulus values from the FEA, comparing the modulus values from patients with and without complications.[4]

RESULTS: The analysis of the segmentations of each lumbar vertebra indicated a statistically significant ($p < 0.05$) difference between the average modulus of the vertebrae from patients who did not experience complications and the average modulus of the vertebrae from patients who did experience complications (Table 1). Across all vertebrae the modulus of vertebrae in patients who did not experience complications was greater than the modulus of vertebrae in patients who did experience complications. The difference between the average modulus was highest for L4 and L5, with a difference of .185 GPa for L5 (p = .0105) and a difference of .149 GPa for L4 (p = .0064). In L3, the average modulus without complications was .680 GPa and the average modulus with complications was .554 (p = .0133). In L2, the average modulus without complications was .718 and the average modulus with complications was .578 (p = .0234). In L1, the average modulus without complications was .659 and the average modulus with complications was .557 (p = .0174).

Vertebra	Modulus (GPa)		p
	Complications	No Complications	
L1	0.557	0.659	0.0174
L2	0.578	0.718	0.0234
L3	0.554	0.680	0.0133
L4	0.611	0.760	0.0064
L5	0.617	0.802	0.0105

Table 1: Average Modulus (GPa) of Vertebra with p-value of Student's t-test.

DISCUSSION: Based on our results, the patient cohort A which had a lower bone modulus (GPa) in their L1 – L5 vertebra on initial pre-op presentation, had a higher rate of post-op complications compared to the patient cohort B with a higher bone modulus. Nowadays, as our population is aging, more patients are requiring spinal surgical interventions leading to higher rates of complications. [3] Pre – op segmentation analysis can help guide the spine surgeon's surgical judgement using non – invasive imaging analyses before preforming surgeries. This type of analysis help surgeons better weigh in the risks vs benefits of lumbar spinal surgery non – invasively before actually performing the surgery leading to a decrease in the complication rates.

Figure 2: Box plot comparing Complication and No Complication Modulus (GPa)

SIGNIFICANCE/CLINICAL RELEVANCE: In modern days, the development of advanced image analyses techniques will play a vital role in assessing patients' pre - surgical risks and helps them avoid unnecessary complications. If such imaging risk assessment analyses are implemented pre surgically, it will lead to a better surgical decision taking.

REFERENCES:
1) Wu L, Cruz R. Lumbar Spinal Stenosis. 2021 Aug 25. In: StatPearls. Treasure Island (FL): StatPearls Publishing; 2022 Jan–. PMID: 30285388.
2) Katz JN, Zimmerman ZE, Mass H, Makhni MC. Diagnosis and Management of Lumbar Spinal Stenosis: A Review. *JAMA*. 2022;327(17):1688–1699. doi:10.1001/jama.2022.5921
3) Burch MB, Wiegers NW, Patil S, Nourbakhsh A. Incidence and risk factors of reoperation in patients with adjacent segment disease: A meta-analysis. J Craniovertebr Junction Spine. 2020 Jan-Mar;11(1):9-16. doi: 10.4103/jcvjs.JCVJS_10_20. Epub 2020 Apr 4. PMID: 32549706; PMCID: PMC7274364.
4) Rajapakse CS, Magland JF, Wald MJ, Liu XS, Zhang XH, Guo XE, Wehrli FW. Computational biomechanics of the distal tibia from high-resolution MR and micro-CT images. Bone. 2010 Sep;47(3):556-63. doi: 10.1016/j.bone.2010.05.039. Epub 2010 May 31. PMID: 20685323; PMCID: PMC2926228.

Novel Approaches to Scaffold Biofabrication Utilizing Soft Computing

Ashkan Sedigh[*], Ryan E. Tomlinson[*]
Department of Orthopaedic Surgery, Thomas Jefferson University, Philadelphia, PA, USA

Bioprinting facilitates the generation of complex, three-dimensional (3D), cell-based constructs for various applications. Although multiple bioprinting technologies have been developed, extrusion-based systems have become the dominant technology due to the diversity of materials (bioinks) that can be utilized, either individually or in combination. However, each bioink has unique material properties and extrusion characteristics that affect bioprinting utility, accuracy, and precision. Therefore, optimization of the bioprinting parameters (e.g., print speed or bioink viscosity) is necessary to reach the desired outputs, such as high cell viability, appropriate cell function, or mechanical properties. In these studies, we advance several sophisticated soft computing approaches to develop and test dynamic models that can be used to improve bioprinting outcomes.

First, we introduced a new metric to quantify bioink performance termed the Bioprinting Precision Index (BPI). This quantification metric was used to optimize the input bioprinting parameters (bioink dilution percentage, speed, and pressure) in two common experimental bioinks. We estimate that printing with parameters optimized using BPI would increase the line width precision for collagen (+15%) and Pluronic F127 (+29%) as compared to the manufacturer's recommended printing parameters. Next, we utilized the ANFIS algorithm to develop a dynamic model scaffold bioprintibility prediction based on four input parameters (bioink concentration, printing pressure, speed, and bioink temperature) and a single output (scaffold printed linewidth range). We validated the bioprinting precision index (BPI) using a gelatin bioink with both standard and normalized printability factors. In order to utilize this predictive system in a biological process, we implemented a computational model to predict the bone mineralization volume. Here, we optimized experimental bone mineralization volume based on two inputs (cell culture period and cell suspension density). Furthermore, we demonstrate that system accuracy increases significantly by utilizing Type-2 Fuzzy systems as compared to Type-1 Fuzzy systems. Finally, we directly compared bioprinting to traditional casting in pre-fabricated molds for bone applications. In both scenarios, the bioink consisted of type I collagen (14 mg/mL) seeded with 5×10^6 MC3T3 osteoblasts per mL. For conventional fabrication, a 3D printed polycaprolactone (PCL) form was filled with the bioink. In comparison, we bioprinted the same scaffold using the bioink. Each construct was cultured for up to 28 days in osteoblast proliferation media (aMEM with 10% FBS and 1% P/S). Our microCT imaging and histological results reveal that the 3D bioprinted scaffolds have increased cell viability and greater bone mineralization.

In summary, our results demonstrate novel methods for improving bioprinting precision through in silico optimization of bioprinting parameters and post-processing procedures. Furthermore, we show that optimized bioprinting can yield superior results to traditional casting approaches for bone scaffold biofabrication. Future work will focus on utilization of bioprinting for specific applications that benefit from its high spatial resolution and cellular specificity.

The mechanobiology of hypoxia during bone fracture repair

Annemarie Lang[1], Cameron Koch[2], Joel D. Boerckel[1]
[1]Departments of Orthopaedic Surgery and Bioengineering, University of Pennsylvania, Philadelphia, PA,
[2]Department of of Radiation Oncology, University of Pennsylvania, Philadelphia, PA

INTRODUCTION: Two critical events early in fracture healing determine the course of repair: 1) potential lack of oxygen caused by blood vessel rupture and 2) mechanical instability. Cellular hypoxia-induced signaling and mechanotransduction are therefore thought to be critical to bone healing, but how crosstalk between these pathways impacts fracture repair is unknown. Our goal is to define how mechanical loading alters the identity and distribution of hypoxic cells in early fracture repair. Toward this end, we here validated a methodological pipeline to precisely sort for hypoxic and non-hypoxic cells, using murine bone marrow as a model. Oxygen concentration can be expressed as a percentage of the partial pressure of atmospheric O_2. At sea level, atmospheric pressure is 760 mm Hg; thus the partial pressure of oxygen (pO_2) in the atmosphere is 160 mm Hg. Prior measurements characterize bone marrow as "hypoxic" (i.e., 7.5 – 45 mmHg, or 1% – 6% pO_2) [1]. However, intracellular pO_2 can differ from that of the bulk environment, depending on local pO_2 and the oxygen consumption rate in a given cell. Further, methods to specifically sort and further characterize cells by their intracellular O_2 levels are limited. Nitroimidazoles such as EF5 are selectively reduced by nitroreductase enzymes under hypoxic conditions, resulting in the formation of EF5 adducts that can be visualized with fluorophore-coupled antibody [2]. Here, we establish EF5 staining as a precise method to delineate cells by levels of intracellular oxygen.

METHODS: We performed two experiments to assess cellular hypoxia in femoral bone marrow. In **experiment 1**, we isolated and cultured bone marrow cells under defined oxygen concentrations and evaluated intracellular EF5 by flow cytometry (n=4). Bone marrow cells were isolated from femora of C57BL/6J female mice and transferred into culture medium (MEM + 5% FCS supplemented with HEPES and bicarbonate as buffer system and 100 µM EF5 compound). Cells were cultured without CO_2 in aluminum chambers for 2h and the gas phase in the chambers was changed to 10%, 2%, 0.5%, 0.1% pO_2 using a series of gas exchanges with oxygen-free nitrogen (n= 4). Afterwards, cells were fixed and stained as described before while an aliquot of cells was used for RNA isolation and qPCR. In **experiment 2**, we performed flow cytometry of isolated bone marrow cells and cryohistological immunostaining *in situ*. Briefly, 12–14 week-old C57BL/6J female mice (Jackson Laboratory) were injected with 10 mM EF5 (Merck Millipore) and euthanized after 4 hours (n= 4). Femora were either directly cryo-embedded or flushed to isolate bone marrow cells. As a negative control for *in situ* EF5-labeling of cells with known high pO_2, we performed EF5 staining of the spleen (nominal pO_2 of 8-10%). To control for any nonspecific background staining, we also included bone marrow cells from non-EF5 treated animals (EF5-). For flow cytometry, cells were fixed with 4% paraformaldehyde directly after collection, and stained overnight with Cy5-conjugated anti-EF5 antibody (clone: ELK3-51; Merck Millipore). To distinguish between cells of the erythroid lineage (erythrocytes, pro-erythrocytes) and nucleated hematopoietic cells, we stained for Ter119 and CD45 (Biolegend), respectively. A BD FACSCanto II was used for flow cytometry and data was analyzed using FlowJo software. For immunofluorescence staining, sections were fixed in 4% paraformaldehyde, blocked with 5% goat serum, and stained 2h with Cy3 conjugated anti-EF5 antibody (clone: ELK3-51; Merck Millipore). All procedures were conducted in accordance with UPenn IACUC regulations (protocol no: 806482).

RESULTS: In **experiment 1**, murine bone marrow cells were cultivated under oxygen concentrations resulting in the presence of a EF5+ and EF5- cell fraction at 10% pO_2 and almost exclusively EF5+ cells at 0.1% oxygen. RNA expression analysis indicated an increasing expression of *Slc2a1* (HIF target gene) and *Ccn1* (YAP/TAZ target gene) under decreasing oxygen availability. In **experiment 2**, we were able to detect differences in cellular hypoxia by identifying EF5+ and EF5- cell populations as well as differences in the EF5 fluorescence intensity. Moreover, no EF5 positive cells were found in the spleen under normal conditions, although anoxia resulted in 100% EF5 positivity in spleen cells. Frequency quantification revealed that 51.25±5.39 % were positive for EF5 while 48.75±5.39 % of bone marrow cells were not positive for EF5. Immunofluorescence staining of the whole bone marrow identified regions with high and low EF5 signal intensity, indicating heterogenous intracellular hypoxia.

DISCUSSION: Our results indicate a substantial heterogeneity in intracellular hypoxia (equivalent to EF5 staining intensity) among bone marrow cells *in situ* but also when cultivated *in vitro* under defined oxygen concentrations. This underlines that intracellular pO_2 can differ from that of the bulk environment, depending on local pO_2, the oxygen consumption rate but also potential other unknown factors. Using this tool, we now aim to define how mechanical cues and hypoxia direct the course of bone fracture repair.

SIGNIFICANCE/CLINICAL RELEVANCE: Here we describe a unique methodology to pre-select hypoxic and non-hypoxic cells for sophisticated single-cell based analysis which will enable us to determine how *in vivo* mechanical cues direct intracellular hypoxia and mechano-signaling during bone fracture repair in future studies.

REFERENCES: [1] Spencer et al. 2014 *Nature*; [2] Koch, C. 2002 *Methods Enzymology*

Dysfunctional macrophage phenotype in fibrotic VML injury

Ricardo Whitaker and Kara Spiller, PhD.

Volumetric muscle loss (VML) is a debilitating condition resulting from the loss of a large portion of muscle tissue due to injury or disease. Current treatments are ineffective in restoring tissue function, due to the lack of understanding of cellular and molecular processes governing VML repair. Macrophages play a crucial role in VML outcome; however, a lot is still unknown about macrophage phenotype, kinetics, and interplay with other cells. More specifically, it is unknown whether changes in macrophage phenotype is a cause or consequence of fibrosis, and what trigger these changes. We hypothesized that the differences in local and/or systemic inflammation induced by different injury sizes cause early changes in macrophage phenotype, having long term consequences. We thoroughly characterized immune cell numbers and phenotype locally and systemically in a fibrotic versus non-fibrotic VML model.

Fibrotic injuries were generated by removing a portion of muscle tissue (quadriceps) from C57BL/6 mice via a 4mm biopsy punch, while non-fibrotic injuries were created using a 2 mm biopsy punch. At the site of injury, macrophages from fibrotic injuries expressed higher levels of inflammatory markers CD9, CD38 and CXCR4 but lower levels of CD86. On the other hand, fibrotic injuries had higher levels of M2 marker Arg1 at early timepoints, but lower levels of a CD163 and CD301b at later timepoints, as seen by flow cytometry analysis.

To further characterize macrophage phenotype, multiplex gene expression analysis (NanoString) for a custom panel of >220 genes was performed on FACS-sorted macrophages on Days 1 and 3 post-injury. At Day 1, macrophages from fibrotic injuries had a higher expression several M1 related genes such as *IL1a, CD9* and *CD86,* and M2 related genes such as *Arg1, CCL24* and CHIL3 compared to non-fibrotic injuries. Surprisingly, at Day 3, expression levels of approximately 77 % of all genes was downregulated in fibrotic injuries compared to non-fibrotic. Most significantly downregulated genes in fibrotic injuries were M2 related genes.

NanoString performed at the whole tissue level at Day 1, revealed 25 significantly different genes between fibrotic and non-fibrotic injuries. More notably, there was a significant decrease in *IGF1,* important in satellite cells maturation, and increase in *CXCL2* and *CXCL3,* crucial for neutrophil recruitment, in the fibrotic group compared to non-fibrotic.

Immune cell accumulation at the site of injury was markedly different between fibrotic and non-fibrotic injuries as well. Fibrotic injuries presented a significantly higher accumulation of neutrophils at Days 1 and 3 post injury, accompanied by an increase in systemic G-CSF levels. In addition, macrophage accumulation in the fibrotic injuries is significantly higher on Days 3 and 28 post injury.

Immune cell trafficking at main myeloid reservoirs (blood, bone marrow and spleen) showed little differences between fibrotic and non-fibrotic injuries at the first 7 days post injury. Bone marrow macrophages showed no phenotypic differences between fibrotic and non-fibrotic injuries. On the other hand, splenic macrophages in the fibrotic group consistently presented higher levels of inflammatory markers compared to non-fibrotic injuries.

Here we demonstrated that changes in macrophage phenotype occur soon after tissue injury, and before onset of fibrosis. This suggests that changes in macrophage phenotype drive fibrosis, and it is not a consequence of it. In addition, the hybrid phenotype identified deviates from stereotypical "M1" or "M2" phenotypes. Finally, these changes in phenotype are preceded by a high neutrophil influx, suggesting neutrophils as possible mediators in macrophage modulation.

SOX4 inhibits trabecular bone formation in adult mice

Marco Angelozzi, Anirudha Karvande, and Véronique Lefebvre

Translational Program in Pediatric Orthopaedics, Department of Surgery, Division of Orthopaedics, The Children's Hospital of Philadelphia, Philadelphia, PA 19104

The development and adult maintenance of strong bones are critical for healthy life, but these processes can be negatively influenced by aging, genetic and environmental factors. Thus, the identification of molecular and cellular pathways involved in bone formation and adult homeostasis is crucial to developing therapies for bone-afflicting conditions. The SOXC genes (i.e., *SOX4*, *SOX11* and *SOX12*) belong to the SRY-related HMG box-containing transcription factor family. Mouse models have shown their involvement in many developmental processes, including embryonic skeleton growth and patterning. In humans, heterozygous variants inactivating *SOX4* or *SOX11* cause neurodevelopmental syndromes associated namely with mild skeletal dysmorphism, and GWAS have linked *SOX4* to osteoporosis. Although the latter findings hint at roles for SOXC in postnatal and adult bones, these roles remain elusive. To address this knowledge gap, we generated mice inactivating the SOXC genes individually ($Sox4^{OsxCre}$, $Sox11^{OsxCre}$ and $Sox12^{OsxCre}$) or simultaneously ($SOXC^{OsxCre}$) in the osteoblast lineage and analyzed them from pubescence to late adulthood. μCT showed that $SOXC^{OsxCre}$ mice have thinner long bones than controls due to reduced cortical thickness and marrow area. This difference depends on the three SOXC genes and tends to fade away with aging. More strikingly, $SOXC^{OsxCre}$ mice have a higher trabecular bone mass, largely due to an increase in trabecular number, and this phenotype is far more prominent in females than males. $Sox4^{OsxCre}$, but not $Sox11^{OsxCre}$ or $Sox12^{OsxCre}$, mice show the same phenotype, indicating *Sox4* as the main determinant. Accordingly, *Sox4*, but neither *Sox11* nor *Sox12*, is expressed in late hypertrophic chondrocytes, bone marrow cells, osteoblasts, and osteocytes. *Sox4* inactivation in chondrocytes ($Sox4^{AcanCreER}$ and $Sox4^{Col10Cre}$) did not increase trabecular bone mass, excluding a contribution of chondrocyte-derived osteoblasts to the phenotype of $SOXC^{OsxCre}$ mice. Further analyses showed that $SOXC^{OsxCre}$ mice have more osteoblasts and a higher bone formation rate in early adulthood, and fewer osteoclasts later. These changes align with downregulation of *Mdk*, encoding an inhibitor of bone formation (midkine), and upregulation of *Tnfrsf11b*, encoding an inhibitor of RANKL-stimulated osteoclastogenesis (osteoprotegerin). Taken together, our data identify SOX4 as a pivotal inhibitor of bone formation and promoter of bone resorption, and thus as a potential therapeutic target for bone loss conditions.

Ergonomic External Endoscope Attachment Device For Smaller Hands

Grace Buckwalter, Carmel Alexander, Christalle Wilson, Joshua Pletcher, Rania Bakhri, Ruth Ochia
Department of Bioengineering, Temple University, Philadelphia, PA

Introduction: Endoscopic surgeries are used as a noninvasive surgical method which reduces large incisions and post operative healing time [1]. However the devices used in these surgeries were designed with larger hands in mind. A study performed at different general surgery programs showed that the average glove size for women was 6.5 with men being 7.5 [1]. As there is an increase in the number of female medical personnel who typically have smaller hands, it poses a problem as they are not able to perform procedures as easily as their counterparts with larger hands [1]. This is due to the over extension smaller handed operators experience from utilizing the control knobs with their thumbs. Ultimately, this results in hand and upper extremity discomfort with the use of these instruments [2]. Additionally it showed that women are more likely to use two hands to use a device [1]. This places female surgeons at a disadvantage as many surgeries require the surgeon to use each hand for a separate instrument. Female surgeons are more likely to receive treatment for their hands and 85% of them attributed their symptoms of numbness, fatigue, stiffness and pain due to the design of endoscopic instruments [3]. Furthermore, the extensive training physicians receive makes it difficult for new endoscopic technologies to become adopted in medical communities [4]. We propose a size-inclusive endoscope attachment that allows medical personnel with smaller hands to more effectively complete surgical procedures without disrupting the time and effort physicians spend learning the current endoscope design.

Materials and Methods: The primary objective is to have the endoscope accommodate health professionals with smaller hands. Any solution will have to address timeliness for changing the adjustable parts, inclusivity of the standard size, interfacing with current endoscopic instruments, and maintaining familiarity with current colonoscopy practices. In addition, the device is used without additional discomfort, can be used with only one hand, and it should be relatively inexpensive.
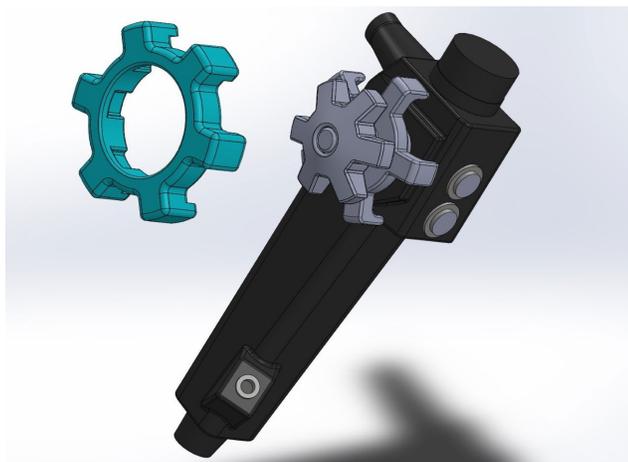
Results and Discussion: We feel that the most optimal design is a two component external grip attachment, which is made of silicon and stretches over the rotating knobs of the endoscope. The addition of the external attachment that is shaped to the control knobs includes more grooves to operate the knob, reducing the distance the thumb travels to utilize them. Each component of the device will attach to the perimeter of both control knobs, allowing them to rotate freely from each other. This will reduce the risk of injury throughout operation. It also eliminates the requirement to relearn the muscle memory of the device, as physicians are able to decide if the attachment is needed. A potential issue with this device is it is another device to sanitize or dispose of after each use, which is costly and time consuming [5].

Figure 1. Proof of concept displaying external gripper device in green, interacting with the current endoscope design

Conclusion: Our external gripper device provides medical personnel with small hands a more ergonomic option, allowing them to operate current endoscopes more efficiently. As we mentioned earlier, our proposed attachment will not interfere with physicians who do not have any problems with current endoscopic devices. A study on the effectiveness of our proposed grip attachment is recommended to evaluate its potential to become adopted into medical communities.

References: [1] Adams, D. M., et al.. (2008). *Surgical endoscopy*, *22*(10), 2310–2313. [2] Berguer, R., & Hreljac, A. (2004). *Surgical endoscopy*, *18*(3), 508–512. [3] Sutton, E., et al. (2014). *Surgical endoscopy*, *28*(4), 1051-1055. [4] Khanicheh, A., & Shergill, A. K. (2019, June 4). *Endoscope design for the future*. Techniques in Gastrointestinal Endoscopy. [5] Denny, N. A., et al.. (2019). Operating room waste reduction. *AANA J*, *87*(6), 477-482.

Fatigue Loading of Mouse Achilles Tendon Explants Leads to Degenerative Changes Without Collagen Denaturation

Krishna Pedaprolu[1], Spencer Szczesny[1,2]
[1]Department of Biomedical Engineering, The Pennsylvania State University, University Park, PA
[2]Department of Orthopaedics and Rehabilitation, The Pennsylvania State University, Hershey, PA
kup225@psu.edu

Disclosures: Krishna Pedaprolu (N), Spencer Szczesny (N)

INTRODUCTION: Tendinopathy is a debilitating condition that is characterized by the presence of abnormal calcium, lipid, and cartilaginous deposits[1], which lead to weakening of the tissue[2]. It is hypothesized that these abnormal deposits are produced by tendon cells in response to fatigue damage and changes in biophysical cues. While the response of tendons cells to biophysical cues has been studied on artificial substrates, *in vitro* studies fail to replicate various critical *in vivo* conditions (e.g., cell-cell communication, cell-matrix interactions). For these reasons, the exact biophysical stimuli (e.g., altered matrix structure and tissue strains) responsible for tendon degeneration in the native tendon environment remain unknown. Therefore, the objectives of this study were to develop an explant model of fatigue-induced tendon degeneration and to determine the altered structural cues that accompany degeneration in mouse Achilles tendons. Based on prior data suggesting that atmospheric oxygen levels (20%) are supraphysiologic[3], we hypothesized that more physiologic oxygen levels (3%) would be more appropriate for studying tendon degeneration in an explant model. Additionally, given that previous studies of energy storing tendons (like Achilles tendons) found collagen disorganization[4] but little collagen denaturation[5] in response to fatigue loading, we hypothesized that fatigue loading mouse Achilles tendon explants would lead to cellular degeneration in the absence of collagen denaturation.

METHODS: Achilles tendons were extracted from male C57BL/6 mice (17 ± 2 weeks) euthanized under an approved IACUC study. *Explant Model:* Mouse Achilles tendon explants were statically loaded at ~0.2 MPa for 24 hours in culture medium (low glucose DMEM, 5% fetal bovine serum, 1% penicillin and streptomycin, 200 mM Glutamax, 25 mM HEPES, 1 mM magnesium ascorbyl phosphate) at 30°C to acclimate them to culture conditions. The explants were then loaded to 5 MPa for 12 hours each day for 4 days (total of 86,735 cycles) in either atmospheric (20% O_2, n =6) or physiological oxygen levels (3% O_2, n =7). The same number of control samples were placed under static load (~0.2 MPa) for the same duration. At the end of loading, samples were frozen in liquid nitrogen, cryogenically homogenized and processed for RT-qPCR. *Structural Analysis:* Achilles tendons extracted from freshly frozen mice (n=7) were cyclically loaded to a peak load of 5 MPa (20% of UTS) till rupture. An additional three samples were heat denatured in PBS at 57°C for 25 mins to act as positive control for collagen denaturation. These tendons were cryosectioned at a thickness of 20 μm and incubated overnight with collagen hybridizing peptide (CHP) that specifically binds to denatured collagen and then washed thrice with distilled water. A confocal and multiphoton microscope were used to image CHP and collagen fibers (via second harmonic generation), respectively. Freshly harvested/static controls were used to determine the threshold to eliminate background for quantifying the percentage area of positive collagen denaturation. Collagen disorganization was defined as a >30° difference in fiber angles (quantified via FFT) between neighboring subregions of 18 μm x 18 μm. *Data analysis:* Gene expression of fatigue loaded samples was normalized to static samples and the median fold change in expression was compared to a hypothetical median of 1 using a Wilcoxon signed ranked test. Differences in percentage area of CHP staining between fatigue loaded and heat denatured samples, and collagen disorganization between static and fatigue loaded samples were compared using a student's t-test with Welch's correction. Unless otherwise noted, statistical significance was set at $p<0.05$.

RESULTS SECTION: Under atmospheric oxygen levels (20%), fatigue loading of mouse Achilles tendons did not lead to difference in expression of any of the genes (except *IL-1β*) compared to the static controls (Fig. 1). However, physiological oxygen conditions (3%) led to downregulation of matrix genes (*COL1A1* (p<0.1), *COL3A1*) and upregulation of catabolic genes (*MMP3, MMP13*), inflammatory genes (*IL1β, IL6, PTGS2*), and non-tenogenic genes (*SOX9, RUNX2* (p<0.1), *LPL*). Samples that were fatigue loaded till rupture demonstrated minimal collagen denaturation (3.2 ± 2.7%) that was significantly lower than heat denatured mouse Achilles tendons (97.1 ± 3.6%, p < 0.0001) (Fig. 2) but resulted in significantly more collagen disorganization (17.4 ± 5%) compared to the static samples (7.7 ± 1.6%, p < 0.005) (Fig. 3).

DISCUSSION: We developed an explant model of fatigue-induced tendon degeneration in the form of downregulation of matrix genes, and upregulation of proteinases, inflammatory markers, and non-tenogenic markers. While previous tendon explants models also exhibit increases in proteinases and inflammatory markers[6], this is the first model to exhibit upregulation of non-tenogenic markers, which is observed in *in vivo* models of tendon degeneration[7] and is likely responsible for abnormal matrix deposits. We found that the fatigue induced degeneration only happens under physiological oxygen levels and that atmospheric oxygen levels renders the cells mechano-insensitive, possibly because atmospheric conditions themselves already induce a baseline degenerative response in tendons[3]. This study underscores the importance of maintaining physiological culture conditions in explant models. Interestingly, fatigue-induced degeneration occurred in the absence of substantial collagen denaturation in mouse Achilles tendons. This suggests that collagen denaturation is not an initiator of degeneration in Achilles tendons. Furthermore, the lack of collagen denaturation in mouse Achilles tendons with fatigue loading is in agreement with studies of other energy storing tendons (e.g., SDFT).[5] In contrast, we did measure collagen fiber disorganization with fatigue loading, suggesting that this altered biophysical cue might be a contributor to the initiation of tendon degeneration. Future studies will investigate the causal relationship between collagen fibril disorganization and degeneration by correlating the spatial localization of tissue damage and gene expression. Additionally, the mechanotransduction mechanisms that underlie the degenerative response will be investigated using pharmaceutical agents to perturb various signaling pathways.

SIGNIFICANCE/CLINICAL RELEVANCE: The structural cues responsible for initiation of tendinopathy are unknown. Our explant model of tendon degeneration provides a powerful approach to understand the role of fatigue loading and structural damage in driving tendon degeneration. For example, our data suggest that collagen denaturation is not responsible for aberrant tendon cell behavior. Future studies using our explant model will test whether collagen disorganization and other structural cues initiate degeneration as well as the underlying mechanotransduction mechanisms.

REFERENCES: [1] Kannus et al., J Bone Joint Surg Am, 1991; 73(10):1507-25 [2] Archambault et al., J. Orthop. Res., 2007; 25(5):617-24 [3] Wunderli et al., Matrix Biol; 2020, 89:11-26. [4] Fung, et al., J. Biomech., 2010, 43(2), 274-279 [5] Herod, T. W et al., Acta Biomaterialia, 2016; 42, 296–307 [6] Devkota, et al., 2007, J. Orthop. Res., 25.8: 1078-1086. [7] Zhang, J et al., PLoS ONE, 2013; 8(8), e71740 [7] Szczesny, SE et al., J. Biomech., 2018; 71, 251–256
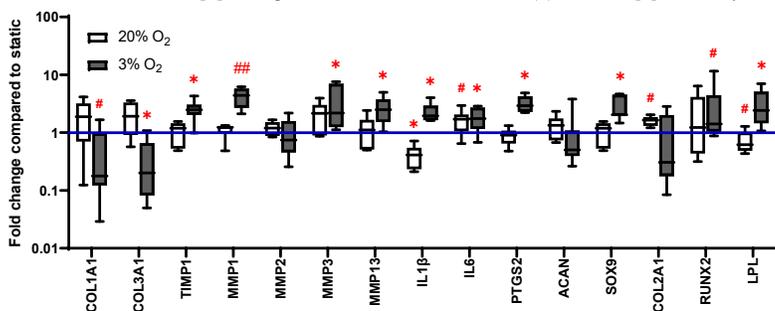
Figure.1. RT PCR Gene expression of fatigue loaded samples in 20% or 3% O_2 levels normalized to static controls. ✳: p<0.05, #: p<0.1, ##: p= 0.125 (n=4)
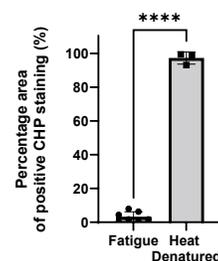
Figure.2: The percentage of collagen denaturation in fatigue loaded samples is lower than heat denatured samples mouse Achilles tendons. ✳✳✳✳: p<0.001
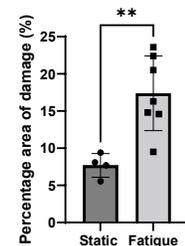
Figure.3: The percentage of collagen disorganization in fatigue loaded samples is higher than statically loaded samples mouse Achilles tendons. ✳✳: p<0.01

Development of Explant Model to Investigate ACL Reconstruction Mechanobiology

Lauren Paschall[1], Erdem Tabdanov[2], Aman Dhawan[3], Spencer Szczesny[1,3]

[1] The Pennsylvania State University, Department of Biomedical Engineering, Hershey, PA
[2] The Pennsylvania State University, Department of Orthopeadics and Rehabilitation, Hershey, PA
[3] The Pennsylvania State University, Department of Pharmacology, Hershey, PA

Introduction: Anterior cruciate ligaments (ACLs) are one of the most commonly torn ligaments and affects more than 200,000 people in the United States each year[1]. Given the lack of spontaneous tissue repair, reconstruction of the ACL is the gold-standard treatment. During ACL reconstructions, a tendon graft replaces the torn ACL. Graft options for reconstructing the ACL come in the form of autogenous and allogenic tendons. In the general patient population, outcomes are similar between graft types; however, the reruptre rate in non-irradiated allografts are 3-4 times higher than autografts in young active individuals[2,3]. Data suggest that differences in clinical outcomes between graft types is due to increased mechanical loading[4]. Therefore, we hypothesize that poor allograft performance in young individuals is because of an altered response to mechanical loading leading to impaired post-surgical remodeling. To investigate a potential mechanobiological deficit in allograft reconstructions, we intend to use a bioreactor to apply stress to ACL reconstructions within a controlled environment. Therefore, the goal of this project was to validate the use of an explant model to investigate the mechanobiological response of allografts to mechanical loading.

Methods: Following IACUC approval, 10 New Zealand white rabbits underwent unilateral autograft ACL reconstructions and were euthanized 8 weeks post-op. Autografts were harvested and placed in a tensile bioreactor with culture media kept at 37℃. After 18 h of acclimating the ACLs to explant culture, the bioreactor cyclically loaded the samples to 2 MPa at 0.5 Hz for 8 h. Since unloading is detrimental to tendon homeostasis[5], control samples will be placed in the bioreactor for the same duration but under a minimal (0.1 MPa) static load. Cell Viability: After loading, the autografts were stained with 2 μl/ml fluorescein diacetate (FDA) and 5 μl/ml propidium iodide (PI) in PBS for 10 min to visualize live and dead cells, respectively. Volumetric image stacks were acquired at multiple locations using an inverted confocal microscope. The images were thresholded to determine regions of positive labeling, and cell viability was determined by dividing the area of FDA signal by the total (FDA + PI) signal. _Gene Expression:_ Autografts were immediately removed after loading, rinsed with ice cold RNase free-water and flash frozen in liquid nitrogen. Total RNA was isolated, and cDNA was synthesized from 10 ng of the total RNA. Real-time PCR was performed using Taqman probes to measure expression of anabolic (_COL1A1, COL1A2, LOX, COL3A1, TGFβ1, ACTA2, TIMP1, TIMP3_), catabolic (_MMP1, MMP2, MMP10, MMP13_) and inflammatory (_IL-1β, PTGS2_) genes with _ACTB_ as a reference. _Statistics:_ Quantification of gene expression was performed via the delta-delta Ct method (after correcting for primer efficiencies) relative to the statically loaded condition with one sample Wilcoxon tests to determine differential expression. Significance for all tests was set at $p < 0.05$.

Results: Cell viability was comparable between autografts and the native ACL between the loading (71% and 79% respectively) and static (63% and 78% respectively) groups. For the statically loaded samples, autografts (n = 4) trend to higher gene expression of anabolic (COL1A1, COL1A2, COL3A1) and catabolic (MMP2, MMP10) genes and lower expression of anabolic genes (LOX, TIMP1) compared to native ACLs ($p = 0.06$).

Discussion: This study validated that our explant model is sufficient to investigate the mechanobiological response of allografts. First, we demonstrated that the cell viability was comparable between autografts and the native ACL. This suggests ACL reconstructions remain viable during static and cyclic loading in the bioreactor. Second, preliminary data demonstrates that statically loaded allografts trend to increased expression of anabolic and catabolic genes suggestive of increased remodeling potential. This matches literature that the tendon graft goes through a remodeling phase to resemble the native ACL. Furthermore, when autografts are cyclically loaded, preliminary data suggests that there is a differential gene expression. Together, this suggests that this loading protocol is appropriate for mechanically stimulating ACL reconstructions and to investigate the possible discrepancies between allograft and autograft reconstructions to mechanical loading.

References: [1] Garett+ J Bone Joint Surg 2006 88(3):660–667 [2] Barett+ Arthroscopy 2010 6(12):1593–1601 [3] Singhal+ Am J Sports Med 2015 3(10):2501–2509 [4] Borchers Am J Sprts Med 2009 37:2362-7; [5] Galloway+ J Bone Joint Surg Am 2013 95(17):1620-8

HXe MRI evaluation of pulmonary function in a rabbit model of thoracic insufficiency syndrome

R. Hilliard[1], Veridiana Nadruz[1], K. Ruppert[2], F. Amzajerdian[2], Y. Xin[2], H. Hamedani[2], L. Loza[1], T. S. Achekzai[2], R. J. Baron[2], I. F. Duncan[2], H. Profka[1], Y. Qian[2], S. Kadlecek[2], A. Fusco[1], K. Hopster[1], H. Douglas[1], B. Sinder[3], B. Snyder[3,4], T. P. Schaer[1], P. J. Cahill[3], R. R. Rizi[2]

[1]University of Pennsylvania, School of Veterinary Medicine, Kennett Square, Pa, [2]University of Pennsylvania, Philadelphia PA, [3] Children's Hospital of Philadelphia, Philadelphia PA, [4]Harvard Medical School, Boston Children's Hospital, Boston, MA

Disclosures: No author disclosures

INTRODUCTION: Thoracic Insufficiency Syndrome (TIS) represents a novel form of postnatal pulmonary hypoplasia and restrictive respiratory disease that occurs in children (<10 yrs.) with congenital or acquired anomalies of the spine and thorax. Accompanying the early onset scoliosis (EOS) is a 3-D malformation of the thorax limiting the volume for the lungs to grow (1). Decreased pulmonary function is a consequence of mechanical inhibition of diaphragmatic excursion and inspiratory expansion of the rib cage which limit the mass transfer of air via convection (ventilation) as well as dysmaturity of the evolving lung parenchyma that adversely effects gas (O_2, CO_2) exchange at the alveolar level (respiration). Humans are born with only 15% of their total alveoli; rapid alveolarization, accompanied by microvascular development, occurs within the first year, but continues until 3-5 yrs. (6). We have developed a rabbit model of TIS by tethering the rib cage in very young rabbits to create a thoracogenic scoliosis to parametrically evaluate the effect of thoracic deformity on the growth and development of the lung and impact on pulmonary function (2). Similar to children, with increasing deformity there was a decrease in lung mass, functional residual capacity and forced vital capacity (7). While these metrics portray mechanical pulmonary function, they do not reflect microscopic function (2). Similar to humans, rabbit alveoli multiply post-natal until age 14 wks; radial alveolar counts (RAC) were decreased in the tethered rabbits. However, histomorphometric measurements of RAC require biopsy of lung parenchyma and is not translatable to human studies. Hyperpolarized xenon magnetic resonance imaging (HXe MRI) has been shown to accurately measure regional ventilation and gas diffusion (4), revealing in clinical studies of dyspneic patients alveolar-capillary diffusion deficits when other pulmonary function metrics were normal (5). The purpose of this pre-clinical pilot study is to demonstrate the ability of HXe MRI to non-invasively measure lung respiratory pathophysiology in the TIS rabbit model to diagnose decreased gas exchange as a consequence of diminished alveolar permeability induced by restricted lung growth.
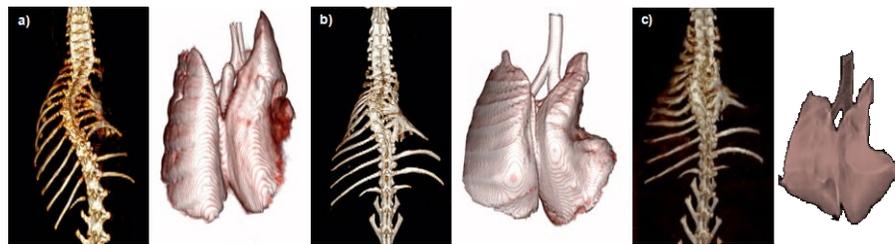

Figure 1. *3D CT reconstruction of the thorax (left) and the lungs (right) in rib-tether rabbits (a) @ 6 weeks, (b) @ 28 weeks, (c) @ 2 years after surgery demonstrating spine and thoracic deformity that restricted right lung growth.*
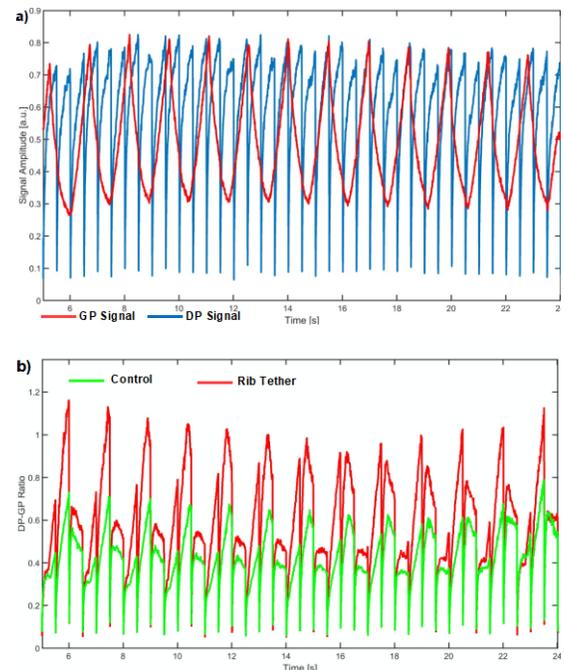
METHODS: Constriction of the right hemithorax (TIS) and spine deformity (EOS) was induced by tethering the rib cage in seven 6-week-old female New Zealand white rabbits (2). Two additional rabbits served as age-matched controls. All protocols were approved by the University of Pennsylvania IACUC. Under general anesthesia, a longitudinal incision was made along the caudal angle of right ribs 1-9; the periosteum of each rib incised and elevated. A figure-8 ligature was used to tether ribs 2-9, slowly bringing them into apposition. A transthoracic tube was incorporated to alleviate post-operative pneumothorax followed to layered closure. Computed tomography (CT) was performed and the rabbits were recovered, provided oxygen as needed for 24-48 hours. Repeat CTs were for 2 years post-op to measure lung volume, spine and thoracic deformity. HXe MRI was performed under general anesthesia in a TIS rabbit @ 30 weeks post-op (skeletal maturity) and a control rabbit using 1.5 Tesla magnet and custom xenon-129 transmit/receive birdcage coil (Stark Contrast). Enriched xenon gas (87% xenon-129) was polarized using a prototype commercial system (XeBox-E10). A gas mixture of 20% oxygen and 80% HXe was administered for 15 breaths at 6mL/kg tidal volume. Alveolar septal wall thickness is calculated from dissolved phase (DP) dynamics in entire lung during multi-breath acquisition: DP magnetization is saturated every 500 ms, septal wall thickness is derived during subsequent recovery (Fig. 2)

RESULTS: Three rabbits died intraoperatively, another of unknown causes @ 4 months post-op. Serial CTs performed in the surviving rabbits exhibited Cobb angles ranging from 20-62°. While scoliosis severity varied between rabbits, once established, it did not change with age (Fig. 1). HXe MRI revealed that throughout the respiratory cycle the dynamic ratio of xenon dissolved in the parenchyma and the alveolar gas phase was 20-80% higher in the TIS rabbit than in the control rabbit (Fig. 2). Physiologic septal wall thinning was retarded in the TIS rabbit: septal wall thickness = 18.0 +/- 2.1 μm constricted lung, 14.7 +/- 1.0 μm contralateral lung, compared to an average of 12.5 μm in the control rabbit.

DISCUSSION: This pre-clinical pilot study demonstrated that HXe MRI can diagnose respiratory pathophysiology at the parenchymal level beyond the increased stiffness of the constricted thorax impeding ventilation (3). These results indicate that relative to a healthy rabbit, the septal walls of alveoli are generally thicker, especially for the restricted lung. Septal thinning and subsequent capillary restructuring are critical for normal lung maturation and function (6). The thickened septa suggest that extrinsic constriction during post-natal lung growth not only affects lung mass/volume, but also the evolution of the microvasculature during maturation of the juvenile lung that directly affect gas exchange. Serial MRI and confirmatory histopathological evaluations (RAC) throughout skeletal maturity will allow further characterization of TIS pathophysiology and help elucidate an optimal age for surgical interventions to mitigate respiratory dysfunction.

SIGNIFICANCE/CLINICAL RELEVANCE: We developed a clinically relevant rabbit model of TIS that demonstrates: 1) acquired anatomic thoracic deformities induce pulmonary hypoplasia by extrinsically restricting lung growth; 2) using hyperpolarized [129]Xe gas, HXe MRI can measure the extent that thoracic deformity induced in young rabbits predicts pulmonary dysfunction at skeletal maturity. This will allow better understanding of how structural anomalies are associated with impaired respiration (oxygenation) and ventilation (removal CO_2) and the effect of timing on interventions to preserve lung function and development.

Figure 2. *A) Representative xenon gas phase (GP) and dissolved phase (DP) dynamics in entire lung during multi-breath acquisition. The DP magnetization is saturated every 500 ms and its subsequent recovery is monitored to obtain the alveolar septal wall thickness. B) Associated dynamic DP-GP ratio in rib-tethered and age-matched control. Throughout the respiratory cycle, the DP-GP ratio in the rib-tethered rabbit is substantially higher than in the healthy control.*

REFERENCES: 1) Yang+*Pediatrics* 2016; 2) Olson+*PLoS One* 2015;Olson+*Spine* 2018; Ruppert+*Sci Rep*. 2019; Grist+*Radiology* 2021; Burri+*Biol Neonate*. 2006; Kovar + *J Appl Physiol* 2002

An essential telomere protein for muscle stem cell function and regeneration during homeostasis, disease, and aging

Ji-Hyung Lee[1] and Foteini Mourkioti[1,2,3]

[1]Department of Orthopaedic Surgery, Perelman School of Medicine, University of Pennsylvania, Philadelphia, PA 19104, USA.

[2]Department of Cell and Developmental Biology, Perelman School of Medicine, University of Pennsylvania, Philadelphia, PA 19104, USA.

[3]Penn Institute for Regenerative Medicine, Musculoskeletal Program, Perelman School of Medicine, University of Pennsylvania, Philadelphia, PA 19104, USA.

Skeletal muscle exhibits extraordinary regeneration after muscle injury and this ability exclusively depends on the activity of residential stem cells called muscle stem cells (MuSCs). Disruption of MuSC action leads to impaired muscle regeneration and it is observed in several muscle disease such as muscular dystrophies and muscle aging. Telomeric repeat binding factor 2 (TRF2) is a DNA binding element of shelterin complex, which protects telomere from undesired DNA damage responses and recombination. TRF2 has been reported to have both telomeric and extra-telomeric functions with cell type and tissue specific manner. However, nothing has been studied about the TRF2 as a regulator of MuSCs behavior. We found that TRF2 expression was dynamically changed in MuSCs during muscle regeneration. Intriguingly, TRF2 was downregulated in both dystrophic and aged MuSCs without affecting the expression of other shelterin component, TRF1. MuSC-specific removal of TRF2 severely impaired muscle regeneration and DMD progression deteriorated by TRF2 deletion in MuSCs of mdx mice. *In vivo* imaging of Pax7-positive cells illustrated that MuSC population was declined by TRF2 deletion in MuSCs. However, acute cell death was not observed in TRF2 knockout MuSCs implying that stem cell depletion is independent from cellular apoptosis. Proliferation test showed that loss of TRF2 inhibits MuSCs propagation after muscle injury. These results demonstrate that TRF2 is an an indispensable factor for adequate MuSC function and muscle regeneration. Findings from this study propose TRF2 as an intrinsic gatekeeper of appropriate MuSC function and provide new strategies to overcome skeletal muscle disease.

Identification of *Fgfr3* enhancers, potential targets for achondroplasia therapy

Angela Fernandez-Iglesias, Arnaud Molin, Marco Angelozzi, Abdul Haseeb, Andrew Bloh and Véronique Lefebvre

Translational Research Program in Pediatric Orthopaedics, Division of Orthopaedic Surgery, Department of Surgery, The Children's Hospital of Philadelphia, PA 19104

FGFR3 encodes a cell surface receptor tyrosine kinase for fibroblast growth factors (fibroblast growth factor receptor 3) that plays essential roles in various processes. Most notably, it is highly expressed in growth plate chondrocytes, where it limits cell proliferation and accelerates terminal differentiation. Heterozygous variants that increase its activity cause achondroplasia (ACH), the most common form of dwarfism in humans, and homozygous variants that inactivate it cause a rare syndrome of overgrowth (CATSHL, Camptodactyly-Tall Stature-Scoliosis-Hearing Loss). To date, no surgical or pharmacological treatments satisfactorily correct these diseases and related ones. Alternative treatments thus need to be developed. Studying transcriptional mechanisms that control chondrogenesis, we previously identified an enhancer that is located 29 kb upstream of *Fgfr3* (*E29*), is highly conserved in vertebrate genomes, and is avidly bound by the master chondrocyte transcription factors, SOX9 and SOX5/6. These data and encouraging progress in the development of gene therapies for many diseases led us to hypothesize that *E29* may chiefly contribute to *Fgfr3* expression in growth plate chondrocytes and that its deletion could be a safe and efficient way to treat achondroplasia. To obtain functional information on this enhancer, we constructed reporter plasmids containing the enhancer upstream of a minimal *Col2a1* or *Fgfr3* promoter and the firefly luciferase gene. We transiently transfected the plasmids in rat chondrosarcoma-derived RCS cells, which display a faithful growth plate chondrocyte phenotype, including high expression of *Fgfr3*, and in human embryo kidney epithelium-derived HEK-293 cells, which weakly express *FGFR3*. We observed that *E29* was sufficient to powerfully activate either promoter in RCS cells, and that it was weakly active in HEK-293 cells unless the cells were forced to express SOX9 and SOX5/6. To determine the importance of *E29 in vivo*, we used the Crispr/Cas9 gene editing strategy to knock it out in mice. We derived two mouse lines that carried the expected deletion. Both *E29*^{del/+} and *E29*^{del/del} mice were viable and looked externally normal. X-rays showed normal axial and appendicular bone lengths at juvenile and adult ages, and histological analysis showed normal growth plates. Expression profiling by quantitative RT–PCR in homozygous mutant juveniles showed that *Fgfr3* RNA levels were reduced by 50% in long bone and thoracic cage cartilage, were reduced by 30% in brain, and were unchanged in kidney and lung. The expression of the nearby genes (*Tacc3*, *Letm1* and *Tmem129*) was unchanged. This partial reduction in *Fgfr3* expression explains why *E29*^{del/del} mice, like *Fgfr3*^{+/-} mice, were able to develop a normal skeleton. Taken together, our findings show that *E29* acts as a cis-regulatory region that significantly contributes to *Fgfr3* expression in cartilage and brain, but also call for further investigations to identify additional enhancers that act along with *E29* to drive *Fgfr3* expression. Our next aims are to identify these enhancers and to determine whether the deletion of E29 alone or these other enhancers in a mouse model for achondroplasia mitigates the effects of the disease. If true, gene therapy approaches could be considered in the future that would delete or block the activity of these enhancers in patients with achondroplasia.

Reduced expression of immune response genes to S*taphylococcus aureus* biofilm in periprosthetic tissue despite unresolved infection

Amanda R Watkins[1], Carly Smith[2], Brianna Nissley[2], Lauren Israel[2], Leslie Brewer[1], Thomas P Schaer[1], Theresa A. Freeman[2]
[1]University of Pennsylvania, Department of Clinical Studies New Bolton Center, School of Veterinary Medicine, Kennett Square, PA. [2]Department of Orthopedic Surgery, Thomas Jefferson University, Philadelphia, PA

Treatment for recalcitrant orthopedic infection may require removal of the implant and antibiotic treatment to resolve the infection, usually in 2 stages. A single stage revision or DAIR (debridement, antibiotics, and implant retention) would be preferred if the infection could be more easily resolved, as it would decrease treatment time, anesthetic events, health care costs and time to functional rehabilitation (1). Unfortunately, eradication of a biofilm is difficult as it provides a barrier against host immune cell surveillance and antibiotic efficacy (2). In addition, *Staphylococcus aureus* (*S. aureus*) biofilms have been shown to actively evade the immune response by increased anti-inflammatory signaling including alternative activation of macrophages and increased expansion of myeloid derived suppressor cells (MDSC) which suppress T cell function (2, 3). The goal of this study was to investigate the progression of the immune response in a rat model of a one stage revision with an unresolved infection, in an effort to understand the host periprosthetic tissue immune response throughout the revision process. A one stage revision model was used wherein male Sprague-Dawley rats were anesthetized and two screws were placed in the femur and then a collagen sponge impregnated with 250 µL *S. aureus* ATCC 25923 at 1×10^6 CFU (INF) or saline (CON) was positioned over the screws. Seven days later a revision surgery (Day 0) was performed through the previous incision. Both screws were removed and an 8-hole RatFix (RISystem) plate was secured using 4 screws. At either 4- or 14-days post-revision surgery (n=10/timepoint, 5 INF, 5 CON) the rats were humanely euthanized and the hardware and tissue surrounding the incision were aseptically collected for histology, microbial analysis and RNA sequencing. Infected rats developed substantial abscessation, swelling and increased fibrotic tissue around the implant that was clinically unresolved at D14. Infection was confirmed by bacteria (5.6±0.84 CFU) recovered from screws at revision surgery (D0). At D4, contamination of the periprosthetic soft tissue was 6.9±0.29 CFU, and the hardware was 6.5±0.63 CFU with no significant difference at D14. Analysis of RNA seq data indicated substantial changes in gene expression between the CON and INF groups at both D4 and D14. Immune response genes in the INF group at D4 were markedly increased compared to CON. However, gene groups representing MHC antigen presentation, complement activation, interleukins, cell death, and the innate and adaptive immune response of the INF D14 group trended towards that of the D14 CON group, despite continued infection. Analysis of immune cell signature genes revealed that neutrophils, monocytes, macrophages, T cells and unexpectedly MDSCs were all down regulated at D14 when compared to D4. However, MDSCs do remain upregulated from CON at both D4 and D14. CD5L, a protein known to promote an anti-inflammatory phenotype in macrophages, (4) was found to be upregulated 10-fold at D14 compared to D4. Interestingly, we also identified upregulation of the PD-1 signaling, a pathway known for its role in promoting immune avoidance in cancer by downregulating T-cell proliferation. Activation of PD-1 signaling and upregulation of the M2 macrophage marker CD5L are potential mechanisms controlling the decreased host immune response despite the continued presence of *S. aureus* biofilms. Investigation of the role of MDSCs, and macrophages is ongoing. Future directions also include performing deep sequencing of the periprosthetic tissue to evaluate pro/eukaryotic crosstalk within the tissue.

REFERENCES: (1) Foster AL et al., Single-stage revision of MRSA orthopedic device-related infection in sheep with an antibiotic-loaded hydrogel. 2020 (2) Gries CM, Kielian T. Staphylococcal Biofilms and Immune Polarization During Prosthetic Joint Infection. 2017 (3) Heim CE et al., Myeloid-Derived Suppressor Cells Contribute to Staphylococcus aureus Orthopedic Biofilm Infection. 2014 Feb (4) SanJurjo et al., CD5L promotes M2 macrophage polarization through autophagy-mediated upregulation of ID3. 2018

BIOFILM FORMATION IN *STREPTOCOCCUS EQUI* SUBSP *EQUI*

Rachel Hilliard[1], Ashley Boyle[1], Thomas P Schaer[1]
[1]*University of Pennsylvania School of Veterinary Medicine New Bolton Center, Kennett Square, PA*

INTRODUCTION: *Streptococcus equi* subsp *equi* (*S. equi*) is a gram-positive bacteria that causes a contagious upper respiratory tract (URT) infection in equids. Up to 40% of horses remain chronically infected with *S. equi* following a clinical outbreak, persistently shedding bacteria for months to years. It is postulated that persistent *S. equi* infection may be caused by the bacteria assuming an antimicrobial-tolerant phenotype, which has evolved to create a particularly tenacious biofilm within the mucin layer of the URT. If confirmed, *S. equi* may provide a useful model for biofilm treatment and prevention on surgical implants in the mucosal microenvironment. The objective of this study was to determine whether *S. equi* forms a biofilm when grown in an *in vitro* environment analogous to the equine URT.

METHODS: Equine synovial fluid and plasma was harvested aseptically from healthy horses. To test *in vitro* biofilm formation, either tryptic soy broth (TSB), equine synovial fluid ("SynF"), or 15% equine plasma solution with 1% dextrose ("Plasma") was inoculated with 1×10^6 CFU/mL *S. equi* 26014. The inoculated samples were incubated at 37°C until approximately late-exponential phase, (6 hours for TSB or 24 hours for SynF and Plasma), in a microaerophilic environment on a shaker. At the completion of the incubation, 2/3 wells of each media were treated with 10x the minimum inhibitory concentration (MIC) of ceftiofur. The samples were incubated for another 18 hours, then centrifuged, washed, and treated with Proteinase K to dissolve the biofilm. Serial dilutions were performed and plated on sheep's blood agar for colony counts. To test adherence to surfaces analogous to the guttural pouch, 1×10^6 CFU/mL *S. equi* 26014 were inoculated onto collagen-coated plates containing Plasma solution. The samples were incubated for 48 hours in a microaerophilic environment, then 2/3 wells were treated with 10x MIC penicillin. Five hours later, each well was washed to remove non-adherent bacteria, treated with Proteinase K, and serial dilutions were performed as above. The ultrastructural architecture and 3-D morphology of the biofilms were visualized via scanning electron microscopy (SEM) and confocal microscopy (CM). For SEM, *S. equi* was grown in SynF or Plasma as described for 36 hours, then fixed, sputter coated, and analyzed with a FEI Quanta 250 SEM. For CM, *S. equi* was grown in SynF or Plasma for 36 hours as described above, then stained with BacLight Green (cells), wheat germ agglutinin (carbohydrates), and SYPRO (proteins). The samples were fixed and analyzed using a Leica SP8-MP two-photon confocal microscope.

RESULTS: *S. equi* successfully grew in both SynF and Plasma, forming grossly visible aggregates by 24 hours post-inoculation. These aggregates displayed antimicrobial recalcitrance, with no significant difference in CFU count after antimicrobial treatment as compared to controls, while planktonic bacterial in TSB displayed decreased growth. In addition, *S. equi* grown in a plasma and collagen-rich environment (representative of the URT) displayed the ability to form an adhesive film resistant to washing and antimicrobial treatment. SEM showed a network of densely packed cocci chains. In SynF these chains resided within a fibrinous extracellular matrix, and in Plasma formed densely packed, three-dimensional structures. CM revealed a biofilm matrix rich in proteins and carbohydrates.

DISCUSSION: To our knowledge this is the first *in vitro* assay demonstrating *S. equi* forming bacterial aggregates consistent with biofilm, with associated hallmarks of biofilm such as antimicrobial recalcitrance, adherence, and complex extracellular matrix structures. The SynF and Plasma media used contain nutrients, proteins, and other host factors similar to those found in the clinical environment, such as interstitial fluid and nasal secretions.[3] Biofilm-producing bacterial present in the mucosal microenvironment have evolved mechanisms to evade immune defenses present in the mucin barrier[5]. Using this *in vitro S. equi* assay, we can test treatments to combat these recalcitrant bacteria that can be applied to orthopedic implants in mucosal areas, such as those used in URT and oral surgeries. We recently demonstrated platelet-lysate restoring antimicrobial susceptibility in an equine infectious arthritis model.[4] Our upcoming experiments will focus on testing similar compounds against *S. equi*.

REFERENCES: 1. Todd *J Comp Path Therap* 1910; 2. Gilbertie+ *PlosOne* 2019; 3. Cardile+ *BMC* 2014; 4. Gilbertie+ *J Orthop Res*. 2020; 5. Linden+ *Nature* 2008;

Sequentially Applied Posterolateral Off-Set Tethers Induce and Correct Spinal Deformity in a Growing Porcine Model

Madeline Boyes[1], Axel C Moore[3], Benjamin Sinder[2], Rachel Hilliard[1], Dawn Elliott[3], Brian Snyder[4], Patrick Cahill[2], Thomas Schaer[1]

[1]University of Pennsylvania School of Veterinary Medicine, Kennett Square PA, [2]Children's Hospital of Philadelphia, Philadelphia PA, [3]University of Delaware, Newark, DE [4]Boston Children's Hospital, Boston MA

Introduction: Treating adolescent idiopathic scoliosis (AIS) in skeletally immature patients aims at three-dimensional deformity correction and complete lung development without compromising spinal and chest growth. Aside the classic approaches of non-operative management operative interventions typically involve instrumenting and fusing affected vertebrae, transforming a flexible curved spine into a straight rigid construct. In recent years several growth-friendly surgical procedures have been introduced in clinical practice: growing rods, Shilla procedure, vertebral body stapling, posterior dynamic deformity correction device and anterior vertebral body tethering (1). Non-fusion surgical treatments attempt to correct spinal deformity, while preserving flexibility, by mechanically modulating spine growth through the application of a flexible tension band along the convexity of the scoliosis to asymmetrically inhibit growth along the "longer side of the spine". Using a preclinical large animal model (Yucatan minipig) we test the hypothesis that applying an asymmetric load along the growing spine can induce growth modulated spinal deformity that affects both osseus and non-osseus tissues

Methods: With IACUC approval, spinal deformity was induced in 8-10 wk-old female Yucatan minipigs N=4. Lateral offset connectors were attached to T11/T12 and L3/L4, leaving 5 levels un-instrumented. An asymmetric axial load and bending moment was applied via a 1.7 mm diameter braided cobalt chrome "tether" that spanned the T12 to L4 lateral offsets (Fig 1). After a substantial curvature was reached, the cable was cut in one pig to remove the asymmetric load and demonstrate definitive growth modulated spinal deformity. Three days later a second tether was attached on the opposite side. Bi-weekly CT and/or radiographs of the spinal deformity were performed to quantify progression and subsequent correction over time.

Results: The posterolateral offset tether successfully produced an average Cobb angle of 46° by 12-14 wk . Cutting the cable decreased the Cobb angle by 10°, showing a stable growth deformity and not stored elastic nor viscoelastic strain. Applying a tether to the opposite side led to progressive deformity correction over an additional 22 weeks. The final Cobb angle in the animal undergoing a corrective 2nd surgery was 4.3° during continued spinal growth as measured by vertebral body length over time (Fig 1).

Conclusion: This pilot experiment supports the hypothesis that persistent asymmetric loads applied to the growing spine can induce growth modulation. We are currently working to decouple osseus and non-osseus tissue growth modulation. Our future work aims to elucidate the relationship between load, time, and deformity progression, and the underlying mechanobiology.

Significance: In agreement with the Hueter-Volkmann Principle, we demonstrate that a posterolateral offset tether can be applied in a growing spine to create and correct spinal deformity.

References: 1. Bizzoca D, Piazzolla A, Moretti L, Vincenti G, Moretti B, Solarino G. Anterior vertebral body tethering for idiopathic scoliosis in growing children: A systematic review. World J Orthop. 2022 May 18;13(5):481-493. doi:10.5312/wjo.v13.i5.481.
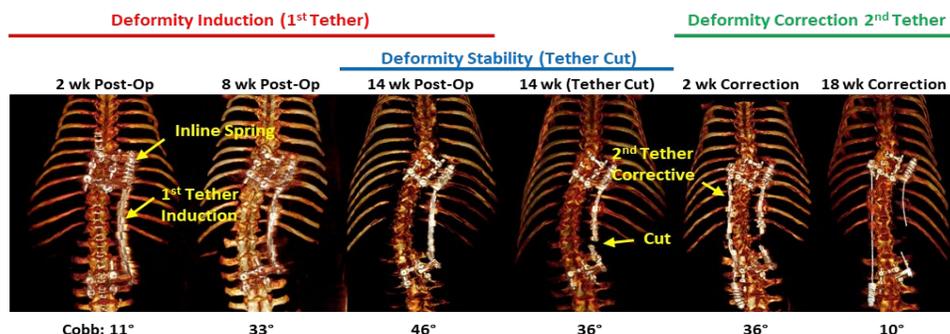
Figure 1: A posterolateral offset tether progressively increased spinal curvature to 46° in a Yucatan minipig. After cutting the 1st tether, 36° of the induced curvature remained, suggesting most of the curve was due to spine deformity and not active tether tension. Finally, to test whether this induced deformity could be corrected, a 2nd tether was placed on the opposing side of the spine. With continued growth, the 2nd tether corrected the spinal deformity between the instrumented levels down to 10° after 18 wk.

Mechano-active Rho signaling through YAP/TAZ suppresses chondrogenic gene expression

Ryan Daniels[1,2], Dakota Jones, PhD[1], Ryan Locke, PhD[1], Lorielle Laforest[1], Robert Mauck, PhD[1]

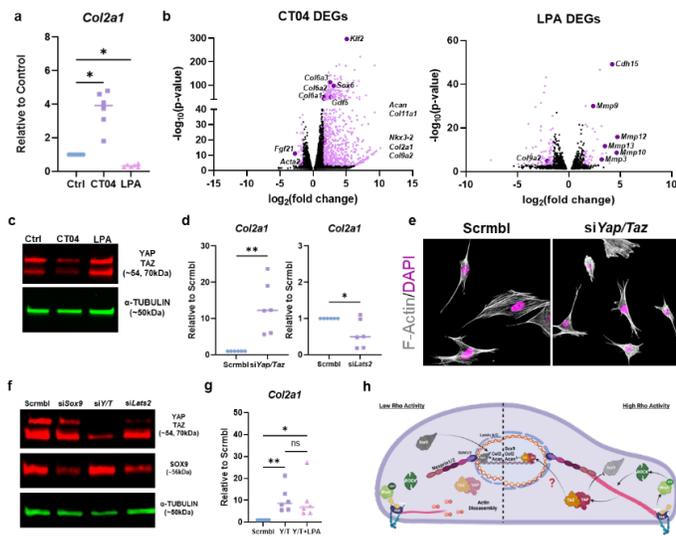1 University of Pennsylvania, Philadelphia, PA 2 Howard Hughes Medical Institute Gilliam Fellowship, Chevy Chase, MD

Figure 1: (a) qPCR showing changes in Col2a1 expression in ATDC5 cells treated with Rho inhibitors (CT04) and activators (LPA), n=6. (b) RNA-seq of ATDC5 cells treated with with CT04 or LPA , n=3 (c) Immunblots for Yap/Taz in ATDC5 cells treated with CT04 or LPA. A-tubulin used as a loading control. (d) qPCR for Col2a1 in ATDC5 cells with knockdown of Y/T or Lats2, n=6. (e) Immunostaining of filamentous actin and DAPI in ATDC5 cells treated with a non targetting (scrambl) siRNA and Y/T siRNA. (f) Immunoblot for Sox9 and Y/T in ATDC5 cells treated with siRNA to Sox9, Y/T, and Lats2. A-tubulin used as a loading control, n=6 (g) qPCR for Col2a1 in ATDC5 cells treated with siRNA to Y/T with or without LPA, n=6. (h) Hypothetical model of how Rho signaling impacts chondrogenic gene expression through Yap. *=p<0.05, **=p<0.01

Mechanotransduction is the process by which cells convert biophysical stimuli into a biochemical response[1]. The cytoskeleton, namely filamentous actin, which is partly regulated by elevated Rho signaling, plays a crucial role in transducing external biophysical forces to the nucleus to alter gene expression[1]. How mechanobiology impacts articular chondrocyte (AC) phenotype has long been an area of interest, given that seminal work showed that ACs dedifferentiate with elevated Rho signaling and actin stress fiber formation[2]. However, there exists a gap in knowledge as to the exact molecular mechanism by which increased Rho signaling negatively regulates chondrogenic differentiation. Yap is a primary mechanoactive transcription co-regulator that regulates the differentiation of multiple mesenchymal cell types. Recently, Yap has been identified as a potential downstream protein of Rho that may negatively regulate chondrogenic differentiation[3]. We hypothesized that Rho signaling negatively regulates chondrogenic differentiation through nuclear translocation of Yap, acting as a transcriptional co-repressor.

To assess changes in chondrogenic differentiation, we assayed for differences in hallmark chondrogenic markers (*Sox9*, *Col2a1*, and *Acan*) using ATDC5 cells, a common chondroprogenitor cell line cultured in a media that promotes an AC-like phenotype[1]. With Rho signaling inhibition, via purified C3-transferase (CT04), we noted a marked increase in chondrogenic gene expression (**Fig 1a**) and RNA-seq identified elevation of multiple genes involved in AC differentiation (*Gdf5*, *Nkx3-2*, and *Col6a1-3*, **Fig 1b**). Conversely, increasing Rho signaling with LPA decreased chondrogenic gene expression (**Fig 1a**) and increased expression of a number of MMPs (**Figure 1b**). Rho inhibition also decreased YAP/TAZ protein (**Fig 1c**). Based on this, we next used siRNA to knockdown both *Yap* and *Wwrt1* (TAZ) or their endogenous inhibitor, Lats2. Combined knockdown of *Yap/Taz* (Y/T) increased chondrogenic gene expression and SOX9 protein (**Figure 1d, f**) and qualitatively decreased cell spread area (**Fig 1e**). *Lats2* knockdown, on the other hand, decreased chondrogenic gene expression (**Fig 1d**). Finally, to assess the requirement of Yap in mediating the negative effects of Rho on chondrogenic gene expression, we knocked down Y/T and treated cells with LPA. Here, we found that when Y/T were knocked down, induction of rho signaling with LPA could no longer decrease chondrogenic gene expression (**Fig 1g**).

Taken together our data further elucidate the molecular mechanism by which Rho signaling regulates chondrogenic gene expression. Our data showing that the removal of Y/T abrogates the inhibitory effects of Rho on chondrogenic gene expression. This supports the hypothesis that, in chondrocytes, nuclear Yap acts as a mechanoactive transcriptional repressor of chondrogenesis. Current studies are exploring Yap as a transcriptional corepressor by studying binding to Sox9 using ChIP-seq and DNA FISH (Oligopaint).

Citations:
1. Driscoll, T. P. et al. Biophys J. (2015)
2. Woods, A. & Beier, F. J. Biol. Chem. (2006)
3. Vanyai, H. K. et al. Development dev. (2020)

The role of telomeric protein repeat binding factor 2 (TRF2) in cardiac development and disease

Sienna Pyle[1,2], Foteini Mourkioti[1,2,3]

[1] Department of Orthopaedic Surgery, Perelman School of Medicine, The University of Pennsylvania, Philadelphia, PA, USA.

[2] Bioengineering Graduate Program, The University of Pennsylvania, Philadelphia, PA, USA.

[3] Department of Cell and Developmental Biology, Penn Institute of Regenerative Medicine, Musculoskeletal Regeneration Program, Perelman School of Medicine, The University of Pennsylvania, Philadelphia, PA USA.

Cardiomyopathy refers to any disease of the heart muscle that impairs the ability of the heart to deliver blood to the body. Interestingly, telomere dysfunction has been associated with multiple modes of cardiomyopathy, yet the involvement of telomeric proteins such as telomeric repeat binding factor 2 (TRF2) in cardiac physiology and disease is currently unknown. We found attenuated levels of TRF2 in cardiac tissue from human patients with cardiomyopathy, suggesting that this protein has an important role in human cardiac diseases. To investigate the cardiac role of TRF2, we generated mice with cardiomyocyte specific deletion of both copies (TRF2^{CardiacKO}) or one copy (TRF2^{CardiacHet}) of TRF2 by crossing TRF2$^{Fl/Fl}$; Ai9$^{Fl/Fl}$ mice with αMyHC-Cre mice. We found TRF2 to be essential for cardiac development, with TRF2^{CardiacKO} resulting in embryonic lethality. TRF2 was also found to be haploinsufficient for heart function and survival into late adulthood. There were no significant changes in cardiomyocyte proliferation and death, while telomere length remained unaltered in both TRF2^{CardiacKO} and TRF2^{CardiacHet} mice, showing the unique function of TRF2 independent of telomeres in cardiomyocytes. Recent studies implicate the importance of epigenetic mechanisms in cardiomyocyte function, and cardiac development and remodeling during heart failure. Interestingly, we demonstrated that, besides its role as a telomeric protein, TRF2 also has extra-telomeric functions in cardiomyocytes via interactions with lamin, promoting optimal expression of genes associated with cardiac contractility. Our findings define a previously unrecognized role associated with TRF2 in developing and adult diseased hearts, and link how TRF2 guides chromatin reorganization in cardiomyocytes.

In vivo validation of a continuous gradient porous scaffold for osteochondral defect repair in a rabbit model

Kyra W.Y. Smith[1,2], Soheila Ali Akbari Ghavimi[2], Stephanie Logterman[2], Paul M. Gehret[1,2], Gioacchino Conoscenti[3], Valerio Brucato[3], Vincenzo La Carrubba[3], J. Todd Lawrence[2], Riccardo Gottardi[1,2]

[1]University of Pennsylvania, Philadelphia, PA, [2]Children's Hospital of Philadelphia, Philadelphia, PA, [3]University of Palermo, Italy
smithkw@chop.edu

Disclosures: Nothing to disclose

INTRODUCTION: Osteochondral defects, characterized by damage to the articular cartilage and the subchondral bone, are a major health concern affecting 60% of patients who undergo knee surgery [1]. Current standards of care include microfracture, which only creates fibrocartilaginous scar tissue, or osteochondral transplant, which suffers from limited donor supply [2]. Tissue engineering thus represents an exciting alternative, but a key hurdle is the tendency of engineered cartilage to ossify [3]. To overcome this limitation, we developed a porous osteochondral scaffold in which specific pore sizes are tailored to promote chondrogenesis on one side and osteogenesis on the opposite side. The scaffold is made of Poly(L-Lactide) (PLLA) and the pore dimensions vary along a continuous gradient to prevent delamination from the cartilage side (~70μm pore diameter, pro-chondrogenic) to the bone side (~200μm pore diameter, pro-osteogenic). We used an established biphasic bioreactor [4] that allows parallel chondrogenic and osteogenic differentiation of each side of the osteochondral constructs which were then tested *in vivo* in an osteochondral defect rabbit model.

METHODS: *Engineering of the osteochondral constructs:* Scaffolds of PLLA were fabricated by Thermally Induced Phase Separation to form a continuous gradient of pore sizes along the sample thickness (*Fig. 1A*), as described in a previous ORS abstract by Gottardi et al. [5]. Cylindrical scaffolds (diameter=4mm, height=6mm) were uniformly seeded with 200K rabbit mesenchymal stem cells (MSCs) harvested from the marrow of rabbit donors and expanded in growth medium (DMEM, 2% Penicillin/Streptomycin/Fungizone (PSF), 10% Fetal Bovine Serum (FBS)). Seeded scaffolds were placed in the biphasic bioreactor for osteochondral differentiation (*Fig. 1B*). The small pore side of the scaffold was perfused in the upper chamber of the bioreactor at flow rate of 1.4μL/min with chondrogenic medium (DMEM, 2% PSF, 10ng/mL TGF-β3, 1% insulin-transferrin-selenium (ITS), 50 μg/mL L-ascorbic acid 2-phosphate (AA), 40μg/mL L-proline, 0.1μM dexamethasone), and the larger pore side was perfused in the lower chamber at the same rate with osteogenic medium (DMEM, 2% PSF, 10% FBS ,0.1μM dexamethasone, 50μM AA, 10mM β -glycerophosphate, 10nM 1α, 25-Dihydroxyvitamin D3).

Osteochondral constructs characterization: Constructs were assessed for chondrogenic and osteogenic morphology via Alcian Blue and Alizarin Red staining, respectively (*Fig. 1D,E*). The top third (cartilage) and the bottom third (bone) of the constructs were separated and analyzed via RT-qPCR for chondrogenesis (*COL2A1, ACAN, SOX9*) and osteogenesis (*RUNX2, IBSP, SPP1*) (*Fig. 1F,G*), or underwent mechanical testing (bulk modulus: 20% compression at 0.01%/s, dynamic modulus: 10 sinusoidal compressions at 1Hz) using a custom compression tester at the Penn Biomechanics Core (*Fig. 1C* [6].

In vivo implantation of engineered osteochondral constructs: Bilateral osteochondral repair was performed on 21 female rabbits (New Zealand White, 3.5-4.5kg) for a total of 42 knees (IACUC: Children's Hospital of Philadelphia). The experimental groups were: (i) empty defects (negative control), (ii) acellular scaffolds, (iii) non-differentiated MSC-seeded scaffolds, (iv) pre-differentiated engineered osteochondral constructs (see previous section). In brief, the trochlea was exposed, a surgical drill was used to create a cylindrical osteochondral defect 4mm wide and 6mm deep, and the scaffold was press-fit into the defect with the large pore side (bone) facing the marrow cavity and the small pore side (cartilage) facing the joint space. After three months, the rabbits were euthanized, the knees were examined for gross appearance, integration, and repair, then excised for microCT and histology to assess differentiation and integration, and for RNAscope to assess spatial distribution of gene expression across the implanted constructs.

RESULTS: Pre-surgical characterization of the scaffold shows that after differentiation, there is significant difference in both the bulk and dynamic moduli between the chondral and osseous regions of the scaffold, approaching native articular cartilage values (*Fig. 1B*). Strong glycosaminoglycan presence and expression of chondrogenic genes was observed in the chondral region (*Fig. 1D,F*), while strong calcium production and expression of osteogenic genes was observed in the osseous region (*Fig. 1E,G*). At the end of the three-month healing period, rabbits were ambulating normally and showed no signs of pain or distress. Healed osteochondral defects exhibited complete defect closure and integration in the cell-seeded and differentiated groups, and non-closures in most empty and acellular groups (*Fig. 2*). Additionally, differentiated scaffolds display shiny white surfaces typical of hyaline cartilage. There was only one scaffold extrusion event. Ongoing examinations by microCT show both cartilaginous and trabecular repair in healed defects, proving successful biphasic morphologies, and initial gene expression distributions in the *in vivo* model suggest specific chondrogenic and osteogenic differentiation analogous to *in vitro* results.

DISCUSSION: Our continuous pore gradient scaffold avoids the risk of delamination common with biphasic models and promotes dual chondro- and osteogenic differentiation to align with the osteochondral bilayer in the knee. Small pores promote chondrogenic differentiation by mimicking mesenchymal condensation [7], while large pores promote osteogenic differentiation [8]. Construct maturation within the dual-flow bioreactor allows the simultaneous differentiation of each tissue types within a monolithic structure ready to be implanted. Application of the scaffold to an *in vivo* rabbit model confirms success of scaffold integration and osteochondral tissue healing suggesting significant promise for clinical translatability.

SIGNIFICANCE: With this work we explored the use of local pore geometry to replicate developmental processes that drive chondrogenesis thus establishing a powerful approach for robust cartilage engineering. The effectiveness of our engineered osteochondral construct to repair a rabbit osteochondral defect shows tremendous promise for this technology to heal osteochondral defects and provide a solution to a major health problem.

REFERENCES: [1] Graham, *Orthop. Nurs.*, 237-239, 2017. [2] Howel et al., *Curr. Rev. Musculoskelet. Med.*, 60-66, 2021. [3] Saka et al., *Regen. Med. Res.*, 2019. [4] Ianetti et al., *PLoS One*, 1-25, 2016. [5] Gottardi et al., *ORS Proceedings*, 2016. [6] Patel et al., *Tissue Eng. Part C Methods*, 593-608, 2019. [7] Nava et al., *J. Appl. Biomater. Funct. Mater.*, e223-e229, 2016. [8] Lin et al., *Int. J. Mol. Sci.*, 326, 2019.
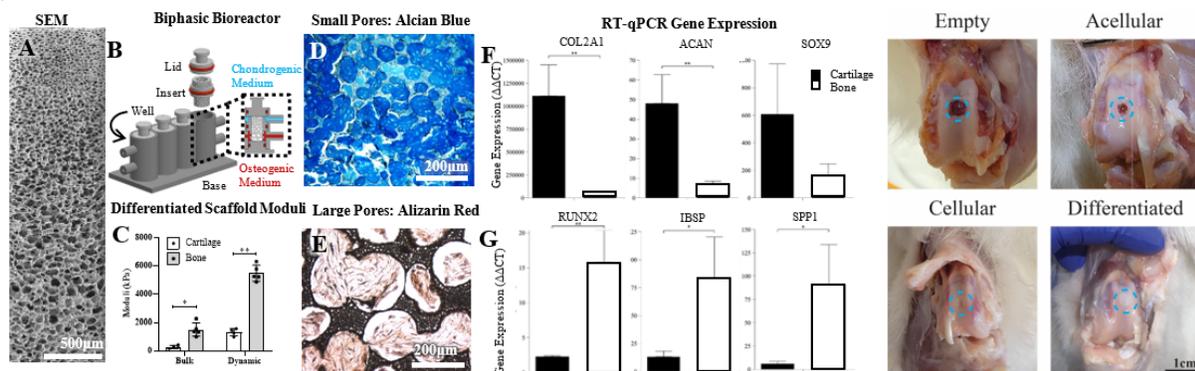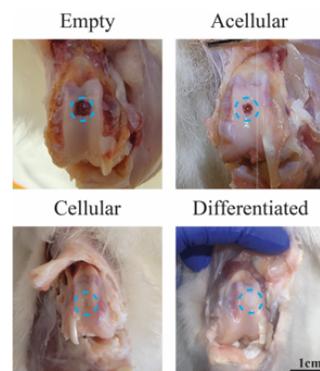
Figure 1: **A)** SEM of the pore gradient scaffold. **B)** Biphasic bioreactor set-up. **C)** Differentiated scaffold moduli. **D)** Alcian blue staining for GAGs of chondral region. **E)** Alizarin Red staining for calcium of osseous region. **F)** Chondro- and **G)** osteogenic gene expression for both construct sides. *Figure 2:* Post-euthanasia macroscopic appearance of scaffold integration and defect closure.

Deep-Learning Strategies for Automated Fibril Segmentation in Embryonic Tendons

Authors: Benjamin Peterson, Spencer Szczesny
[1] Department of Biomedical Engineering, Pennsylvania State University, University Park, PA
[2] Department of Orthopaedics and Rehabilitation, Pennsylvania State University, Hershey, PA

Introduction: Ultrastructural imaging of tendons can provide critical insight into their structure-function relationships. While powerful, conventional ultrastructural characterization tools (i.e., TEM & SEM) only provides information on two-dimensional parameters, leaving three-dimensional relationships up for debate. In contrast, 3D characterization tools (i.e., serial block-face SEM; SBF-SEM) can provide critical insight regarding the 3D arrangement of the collagenous ultrastructure. However, while powerful, the large amount of data generated makes processing datasets challenging. Segmentation, the process which identifies specific objects of interest, is especially challenging and most labs still rely on manual segmentation. However, recent advancements in machine learning architectures (i.e., U-Net[1]) have emerged which are designed especially for biomedical imaging datasets. Furthermore, commercial software packages have begun to integrate these tools, enabling their use within the biomedical community. Despite these advantages, no published study has leveraged these tools to study tendon and its collagenous ultrastructure. Thus, the objective of this study was to implement Deep Learning strategies to automate the segmentation collagen fibrils from SBF-SEM images within embryonic tendons. We aimed to leverage these tools to investigate how structure-function relationships are acquired during tenogenesis with the goal of applying this knowledge to tissue engineering and regenerative medicine strategies.

Materials & Methods: Fresh embryonic chicken limbs were skinned and Achilles tendon removed at embryonic days 16 and 20 (E16 & 20). Limbs were fixed in 2% paraformaldehyde/2.5% glutaraldehyde with 2mM calcium chloride in 0.15 cacodylate buffer (pH 7.4). After 3 days samples were removed, Flexor digitorum brevis II tendons were isolated, and stained/resin embedded utilizing standard protocols within the field[2]. Transverse cross-sections were scanned in series under 2.5 kV in low-vacuum pressure (35 - 40 Pa) using an Apreo VolumeScope. E16 tissue samples were imaged under a 3072 x 2048 px field with a pixel size of 4nm/px. E20 tissue samples were imaged under a 4096 x 4096 px field with a pixel size of 2 nm/px. Representative regions of interest were manually segmented to train Deep Learning model, utilizing a 2.5D U-Net architecture. After training (~10 – 13hr) the model was applied to the entire data set and manually inspected to ensure accuracy of the segmented objects of interest. Additional training sets and/or data augmentations were incorporated into the model as needed. Resulting fibril masks were watershed and then processed in FIJI using the Analyze Particles function to calculate distribution of fibril diameters and total volume fraction as a function of development.

Results & Discussion: When validated with manually segmented training sets, all models identified fibrils with an accuracy of 95% or greater. With development, a progressive increase in fibril volume fraction was observed ($p < 0.001$; data not shown), and consistent with prior reports in the field[3]. A look at individual fibril morphologies reveals an increase in mean fibril diameter ($p < 0.001$) with maturation (**Fig. 1**). Notably, there was a shift from a unimodal to bimodal diameter distribution between E16 and E20 tissues. This rise in small diameters fibrils at later developmental timepoints may contribute to an increase in multiscale loading behavior observed during these developmental timepoints[4]. Importantly, we demonstrated the capacity to measure 5 – 10 times more objects than in prior studies[3,5,6] via deep learning strategies, improving our measurement of system heterogeneity and minimizing human bias. Current on-going work aims to utilize these Deep-Learning tools to create volumetric reconstructions of the collagenous network in its native configuration. This work will provide crucial insights into the 3D arrangement of collagen fibrils and how they contribute to the multiscale mechanical capabilities of tendon tissue.
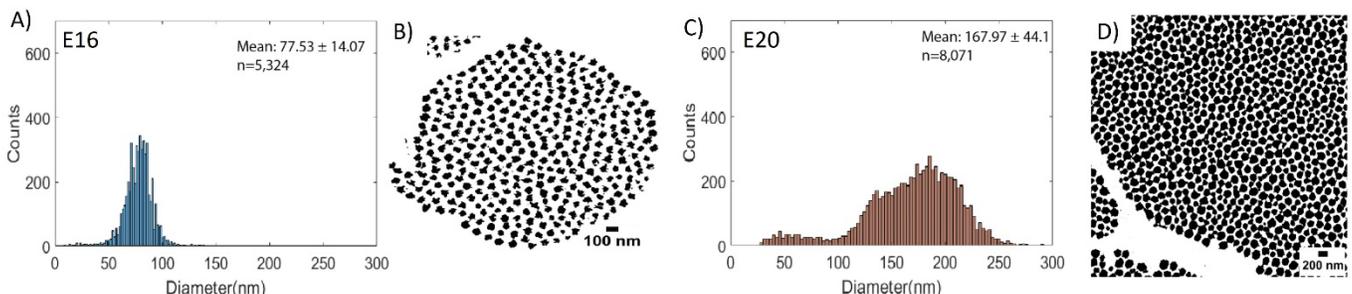

Figure 1: Collagen fibril diameter distributions (bins =100) as a function of development. **A)** E16 fibril diameter distribution (n = 5,324), with **B)** representative masks generated via automatic segmentation. **C)** E20 fibril diameter distribution (n = 8,071), with **D)** representative masks.

References

1) Ronneberger et al. (2015), MICCAI pg 234-241
2) Starborg et al., (2013) Nat. Protoc. 8:1433-1448
3) Kalson et al., (2015), eLife doi.org/10.7554/eLife.05958
4) Peterson et al., (2021), Front. Cell Dev. Biol (2471)
5) McBride et al., (1998), Int. J. Biol. Macromol. 10:1994-200
6) Svensson et al., (2017), Acta Biomat. 50:293-301

Optical Photothermal Infrared Assessment of Plastic-Embedded Bone Composition

Alexandra F. Arnold, Isha Dev, William Querido, Nancy Pleshko
Department of Bioengineering, Temple University, Philadelphia PA.

Introduction: Bone quality and strength rely on nanoscale building blocks on the order of ~500 nm [1]. Thus, analysis of bone composition at high spatial resolution is crucial to elucidate the nanoscale origins of normal and impaired bone quality. Recently, a new modality of infrared spectroscopy, optical photothermal infrared (O-PTIR) spectroscopy, has been developed to allow data collection with sub-micron resolution [2]. Here, our goal was to evaluate the novel application of O-PTIR spectroscopy and imaging and to optimize sample preparation for assessment of bone tissue sub-micron composition.

Methods: Cross-section of mouse femurs embedded in blocks of poly(methyl methacrylate) (PMMA) were investigated. Minimal preparation was required other than cutting the initial block to ~3mm thickness to expose the bone surface. Infrared spectral data were acquired using the state-of-the-art mIRage infrared O-PTIR microscope (Photothermal Spectroscopy Corp) with a spot size of 500 nm. Data were collected from cortical bone regions to assess the primary vibrations associated with PMMA and with the protein and mineral phases of bone [3]. Mapping of tissue components was done based on peak heights related to these components, as previously described [4] and shown in Figure 1b

Results: Embedded bone could be easily visualized and evaluated using the O-PTIR spectroscopic microscope (Figure 1A). O-PTIR spectra from cortical bone showed only minor influences of PMMA, presenting all typical peaks related to tissue compositional properties (Figure 1B). Spectral imaging and RGB overlay of the single peak height distributions illustrated the opposite distribution of PMMA and bone tissue protein and mineral (Figure 1C), demonstrating the feasibility to assess composition of PMMA-embedded bone samples with no PMMA spectral influence. In fact, by obtaining hyperspectral images of cortical bone, we could gather a vast data collection comprising thousands of spectra acquired at 500 nm spatially-defined regions. Quantification of spectral features from this data can provide a rich and detailed assessment of several nanoscale compositional properties of bone tissue, informing not only on average properties, but also on their distribution (heterogeneity) throughout the tissue area (Figure 1D).

Conclusions: This is a pioneering approach, which could become widely adopted as it brings a great advantage to bone research: it enables high-resolution assessment of tissue composition in thick and intact bone samples without the need for challenging thin-sectioning of calcified bone. Application of O-PTIR spectroscopy and imaging to investigate bone properties will fill an important gap in revealing bone sub-micron compositional properties associated with skeletal diseases such as osteoporosis.

References:

1. Reznikov et al. Acta Biomaterialia. 2014; 10(9):3815.
2. Zhang et al. Sci Adv. 2016; 2(9):e1600521.
3. Boskey and Camacho. Biomaterials. 2007; 28:2465.
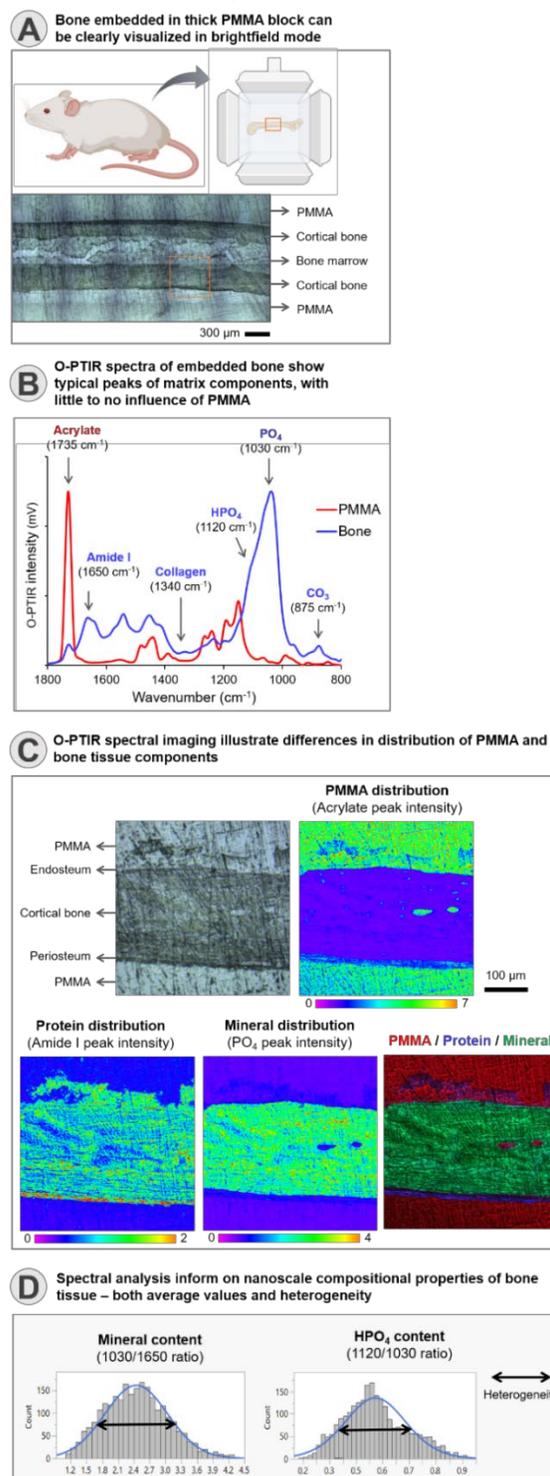4. Querido et al. Molecules. 2021; 26(4):922.

Disclosures: N/A

Figure 1: O-PTIR spectroscopy and imaging of bone embedded in thick PMMA blocks. Color bar reflects intensity of peaks and ratios.

Leveraging Hydrogel Viscoelasticity and Heterogeneity to Promote Cell Migration in Meniscal Repair

Karen L. Xu[1], Robert L. Mauck, Ph.D. [1], Jason A. Burdick, Ph.D[1,2]

[1]University of Pennsylvania, Philadelphia, PA [2]University of Colorado Boulder, Boulder, CO

The meniscus is a load-bearing structure that supports knee stability and motion, and has a limited capacity for repair after disease or damage [1]. Untreated torn menisci often result in the rapid progression of osteoarthritis in adult patients due to changes in joint loading, underscoring the critical need to develop therapeutics that promote meniscus repair. Towards this, we design hydrogel materials with biophysical cues that promote important cellular behaviors for meniscal healing, namely migration, proliferation, and ECM deposition [2]. Specifically, we pursued the combination of: (1) tissue viscoelasticity, which has been shown to support cell migration within hydrogels [3] and (2) tissue heterogeneity, which can influence bulk properties and local cellular microenvironments.

To introduce these features, we develop an interpenetrating network (IPN) in which one component promotes elasticity and gel stability (covalent network), while the other promotes viscous energy dissipation (physical network) (Fig 1A). The covalent network consists of gelatin crosslinked via the addition of transglutaminase. The physical network consists of adamantane-modified hyaluronic acid and cyclodextrin-modified hyaluronic acid, where the adamantane and cyclodextrin form dynamic guest-host complexes. As we increase the physical network present in our IPN (0% to 3%), the loss modulus (viscous component) increases (e.g., 1.68 Pa for 0%, 66.89 Pa for 1%, 321.42 Pa for 3%) while maintaining an equivalent storage modulus (elastic component) of ~405.47 Pa, suggesting that the IPN modulates hydrogel viscoelasticity.

Important for our study, the mixing of the networks during IPN formation introduces microstructural heterogeneities akin to those found in native tissue, as visualized with fluorescent gelatin (Fig 1B). While gelatin networks alone are largely homogeneous, the IPNs
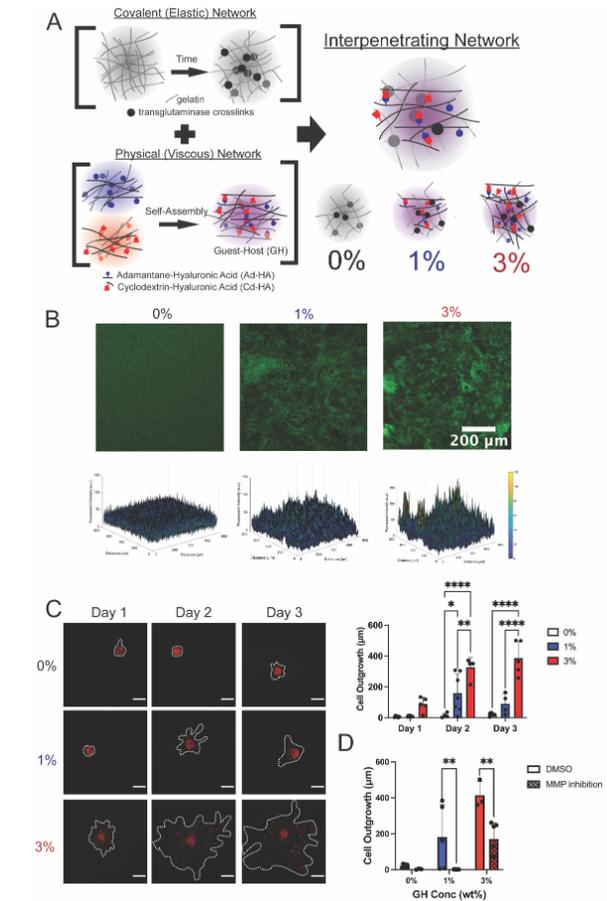

Fig 1. (A) Schematic of interpenetrating network (IPN) formation. (B) Confocal images (top panel, FITC-gelatin) and corresponding intensity profiles (bottom panel) of IPNs. (C) Images and quantification of MFC outgrowth from spheroids. (D) Quantification of MFC outgrowth from embedded spheroids at day 3 with the addition of an MMP inhibitor ($*p \leq .05$, $**p \leq .01$, $***p \leq .001$, $****p \leq .0001$, scale=200µm).

exhibit increased heterogeneity in structure. Despite the inherent heterogeneity of tissues and importance on cell microenvironment, this feature is largely unexplored. Ongoing work includes further characterizing the heterogeneity of our IPN through atomic force microscopy and Raman studies.

Importantly, the combined attributes of viscoelasticity and heterogeneity increase meniscal fibrochondrocyte (MFC) migration into hydrogels, as measured by MFC spheroid embedding and cell tracking (Fig 1C). This cell infiltration does not rely solely on degradation, as inhibiting matrix metalloproteinase (MMP) activity still supports cell infiltration at terminal time points (Fig 1D). Further, migrating MFCs are positive for markers of proliferation. Ongoing studies include exploring matrix deposition coincident with migration.

To further explore the mechanisms behind cell migration in 3D heterogeneous environments, particularly where microscale presentation of adhesion ligands and mechanics are changing, ongoing work includes blocking specific cell interactions (e.g., adhesion, mechanosensing) with the covalent (e.g., integrin binding) and physical (e.g., CD44 interactions) components of the IPN, visualizing cell migration paths during culture, and investigating cell migration from tissue explants. Gaining a greater understanding of the basis behind cell migration and other critical steps involved in tissue healing will enable a more targeted design of therapeutics that promote repair of connective tissues such as the meniscus.

Citations:
[1] de Albornoz, P.M. et al, Muscles Ligaments Tendons J, 2012 1 10-8.
[3] Chaudhuri O et al, Nature. 2020 584 535-46.
[2] Mauck RL et al, Ann Biomed Eng. 2015 43 529-42.

Effects of the Application of a Thoracolumbar Posterolateral Tether on Osseous and Non-osseous Tissues in a Porcine Model of Scoliosis

Axel C Moore[3], **Madeline Boyes[1]**, Benjamin Sinder[2], Rachel Hilliard[1], Dawn Elliott[3], Brian Snyder[4], Patrick Cahill[2], Sriram Balasubramanian[5], Thomas Schaer[1]
[1]University of Pennsylvania School of Veterinary Medicine, Kennett Square PA, [2] Children's Hospital of Philadelphia, Philadelphia PA, [3]University of Delaware, Newark, DE [4]Boston Children's Hospital, Boston MA, Biomedical Engineering, [5]Drexel University, Philadelphia, PA

INTRODUCTION: Scoliosis is a multi-planar spine deformity that presents predominantly as a lateral curve in the coronal plane >10°. In children and adolescents, the etiology of scoliosis is most often idiopathic. Stokes hypothesized that spinal deformities progress as a "vicious cycle" in which asymmetric stresses and strains applied to the growing spine induce deformity of both osseous and non-osseous tissues, causing growth modulation in agreement with the Heuter-Volkmann Principle (1). This concept was validated clinically, demonstrating that spine deformity progresses as a function of skeletal age: during periods of high growth, spine deformity evolves primarily through the intervertebral disc (IVD), whereas towards the end of growth, the deformity increases primarily through the vertebrae (VB) (2). Interventions to correct scoliosis that preserve spinal growth and motion are based on predictably modulating spinal growth. Currently, it is unknown how asymmetric loading alters the growth of IVD relative to the VB. The goal of this study is to identify the relationship of osseous and non-osseous tissues during progressive spinal deformity with asymmetric loading by use of a posterolateral tether. In this proof-of-principle study we investigate the influence of mechanics in spinal deformity progression by applying a bending moment to a straight spine in an otherwise healthy, growing pig.

METHODS: With IACUC approval, 3 Yorkshire pigs were instrumented with each a thoracic and lumbar construct consisting of pedicle screws, lateral rods, and crosslink connectors. A CoCr cable, connected to lateral offset connectors was placed spanning the two constructs. This offset tether created a lateral bending moment and an initial scoliosis that progressed as the pig matured **(Fig. 1).** Two un-instrumented Yorkshire pigs were used as controls. Anatomical changes to the IVD and VB as a function of time were measured with serial CT scans at -2, 0, 4, 6, 8, 12, and 19 weeks post-op and MRI at 5, 19, and 22 weeks post-op. CT scans were used to quantify lateral wedging and longitudinal growth along the line of curvature between the instrumented levels. Two MRI sequences were utilized, a T1-weighted FLASH sequence to evaluate IVD volume and a T2-weighted CPMG echo sequence to evaluate IVD T2 relaxation time. The T2 relaxation time, which is positively correlated with hydration and is decreased in IVD degeneration, was calculated for the IVD nucleus pulposus.
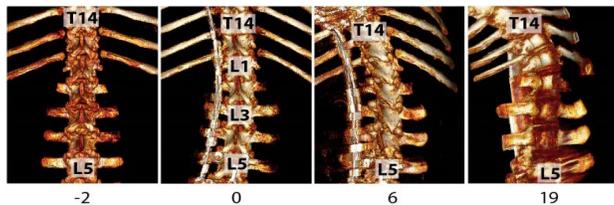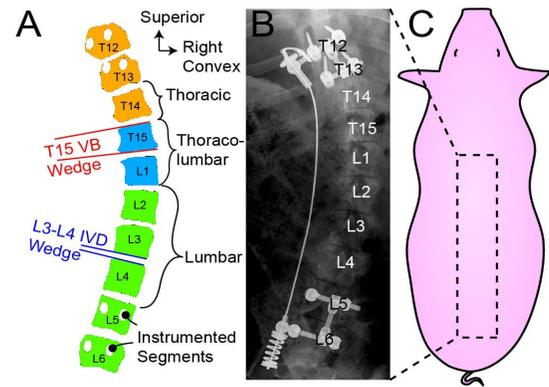

Figure 1: (A) Schematic, (B) radiograph, and (C) pig model showing instrumentation and curvature at 6 weeks post-op. Avoiding instrumented levels, analysis was conducted from the inferior side of T13 to the superior side of L5. Color coding indicates the thoracic (orange), thoracolumbar junction (blue), and lumbar (green) regions.

Figure 2: CT reconstructions in weeks post-op demonstrating progressive curvature.

RESULTS:
Serial imaging (3D CT reconstructions) demonstrate progression of spinal deformity and vertebral growth modulation due to the tether **(Fig 2).** At the time of instrumentation, a 17° Cobb angle was produced via IVD wedging **(Fig3A,B).** At 6 weeks, deformity progression was approximately equally distributed between the thoracolumbar (45%) and lumbar (41%) regions **(Fig 3A)** with VB wedging accounting for 60% of the total deformity **(Fig 3B)**. From 12-19 weeks post-op, the spine deformity transitioned from nearly equal contributions of IVD and VB to only VB **(Fig 3B)**. At 19 weeks post-op, the spine developed a 41° Cobb angle.

DISCUSSION: In this preliminary study, asymmetric spine loading in a porcine model using a posterolaterally placed tether provoked asymmetric spine growth. Early-stage deformity was shared between the IVDs and VBs. However, from 12-19 weeks post-op the deformity transitioned to be primarily located in the VBs. The growth of the IVDs and VBs appear to be impaired when compared to the controls.

CLINICAL SIGNIFICANCE: We have developed a clinically relevant in vivo animal model to mimic scoliosis. Serial CT and MRI imaging allowed differentiation of mechanical deformation of the soft tissues from modulated growth, which manifest as changes in the composition, structure, and geometry. This model will allow biomechanical, biochemical, and biological adaptations to be studied. Moreover, this model is being developed to predictably apply corrective treatments for scoliosis.
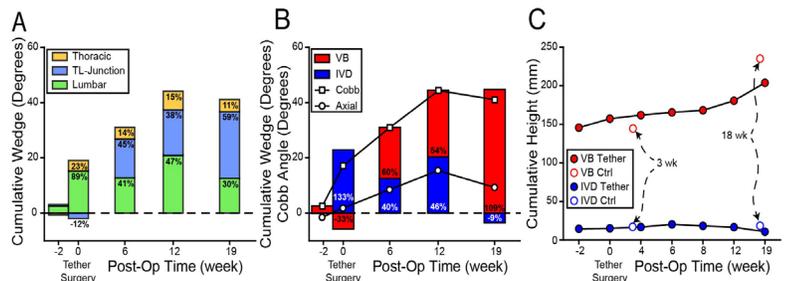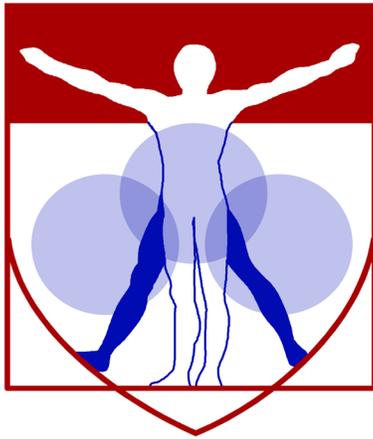

Figure 3: Sum of segmental IVD and VB wedge angle by (A) anatomical region and (B) tissue type with Cobb angle and axial rotation shown in B. Regions defined in Fig 1: positive = right curve and counterclockwise rotation. (C) Sum of VB and IVD height between instrumented segments. Control pigs at equivalent age are shown at 3 and 18 weeks post-op.

REFERENCES: (1) I. A. F. Stokes, *Eur. Spine J.*, 16:1621–1628, 2007. (2) Will, RE et al., *Spine* 2782–2786, 2009. (3) Schlager, B et al., *Biomechanics of the Spine*, 2018.

Notes